Clogging in micro-channels : from colloidal particle to clog

Benjamin Dersoir

N° d'ordre : **ANNÉE 2015**

THÈSE / UNIVERSITÉ DE RENNES 1
sous le sceau de l'Université Européenne de Bretagne

pour le grade de

DOCTEUR DE L'UNIVERSITÉ DE RENNES 1

Mention : Physique

Ecole doctorale Sciences De La Matière

présentée par

Benjamin DERSOIR

Préparée à l'unité de recherche UMR UR1 CNRS 6251
Institut de physique de Rennes
UFR Sciences et Propriétés de la Matière

Intitulé de la thèse
La physique du colmatage : de la particule colloïdale au bouchon.

Thèse soutenue à Rennes
le 24 Mars 2015

devant le jury composé de :

Patrice BACCHIN
Professeur – Université Paul Sabatier Toulouse / *rapporteur*

Jean-Baptiste SALMON
Chargé de recherche CNRS – LOF Bordeaux / *rapporteur*

Anke LINDNER
Professeur – ESPCI Paris / *examinateur*

Marc TRAMIER
Ingénieur de Recherche – IGDR Université de Rennes 1 / *examinateur*

Luc OGER
Directeur de recherche CNRS – IPR Université de Rennes 1 / *directeur de thèse*

Hervé TABUTEAU
Chargé de recherche CNRS – IPR Université de Rennes 1 / *co-directeur de thèse*

Résumé

Introduction

Ce manuscrit commence par une introduction qui comprend l'état de l'art sur les processus d'obstruction en général. La formation de bouchon est un problème récurrent et presque inévitable lors de l'écoulement de solutions de particules diluées dans des milieux poreux. A cause de la complexité du processus de colmatage, des études récentes se sont concentrées plus spécifiquement sur les caractéristiques du bouchage à l'échelle du pore, principalement au sein de dispositifs microfluidiques. Ces études ont identifié les conditions dans lesquelles les particules adhèrent sur les parois des canaux. Elles ont aussi mise en évidence que le colmatage est le résultat de dépôts successifs de particule unique ; le nombre moyen de particules qui peut passer dans un pore avant qu'il ne soit obstrué dépendant du rapport entre la largeur du canal et le diamètre de la particule. Cependant, la grande incertitude sur ce nombre de particules rend le modèle que très peu prédictif. De plus, on ne sait toujours pas comment, à partir du processus initial de déposition de particules à la paroi, les particules s'accumulent dans le pore, les unes sur les autres et finissent par le boucher. Les mécanismes de croissance d'agrégats, à partir de la surface du pore, sous écoulement ne sont toujours pas connus. L'idée générale de ce travail est de visualiser et d'étudier l'écoulement de particules colloïdales au sein de matériaux poreux modèles (canaux microfluidiques), dont la taille des pores est proche de celle des objets transportés. Nous pouvons ainsi déterminer quelle est la part de la physico-chimiques, de l'hydrodynamique et des interactions particule/particule et particule/paroi, sur les différentes étapes du colmatage de matrices poreuses. Nous déterminerons les conditions d'adhésion des premières particules à la paroi du pore, puis la manière dont croissent les agrégats à partir de cette première couche. Finalement, nous étudierons comment la croissance des agrégats, et leur rencontre, conduisent au colmatage du pore.

Matériels et méthodes

Dans un deuxième chapitre, nous donnons les définitions des différents phénomènes physiques impliqués dans la capture de particules et dans l'agrégation colloïdale. Nous faisons une brève présentation des différentes techniques d'imagerie utilisées dans ce travail. La microscopie en champ clair nous a permis de déterminer les propriétés géométriques du bouchon ainsi que sa dynamique de formation à l'échelle du pore. Grâce à l'utilisation de particules fluorescentes, nous sommes capables de déterminer la position du centre des particules de manière très précise, lorsque que ces dernières sont disposées sur une seule couche. De plus, en utilisant des temps d'exposition longs et une modulation périodique du signal d'excitation, nous pouvons visualiser les trajectoires des particules sous forme de

traînées dont l'intensité varie avec le signal d'excitation, dont nous pouvons extraire des informations de position et de vitesse. Pour des empilements de particules, nous avons recourt au microscope confocal. Ce dernier permet en effet d'avoir accès à la position du centre des particules dans des empilements denses. A l'aide de ces données, nous pouvons fournir des informations structurales sur les agrégats en cours de formation et sur le bouchon, une fois formé dans le pore.

Colmatage 2d

Dans un troisième chapitre, nous abordons le processus de colmatage en situation de fort confinement (degré de confinement : $1.1 < H / D < 1.7$, avec H la hauteur du pore), appelé dans la suite colmatage 2d ; qui correspond au cas où les particules s'écoulent dans un pore de faible rapport d'aspect, bien plus large que haut. Dans cette situation, l'interaction particule-mur est dominante devant l'interaction interparticulaire. Nous avons tout d'abord fait une description du processus de colmatage à l'échelle du pore, en nous attachant à décrire les caractéristiques géométriques du bouchon une fois formé, ainsi que sa dynamique de formation. Nous avons identifié les deux régimes de colmatage de ce type de filtre, et ceci, en fonction de la géométrie, du réservoir et du pore, et des conditions hydrodynamiques. Soit le colmatage à lieu à l'entrée du pore (régime dit de « ligne »), soit il se produit plus profondément dans le pore (régime « invasion »). La transition entre ces deux régimes se produit pour un débit critique, au-delà duquel le nombre de particule qui passent dans le pore avant de le colmater augmente très rapidement.

Nous avons ensuite déterminé tous les processus à l'origine du colmatage du pore, à l'échelle de la particule, et ceci, grâce à l'utilisation en parallèle de deux techniques d'imagerie. Le microscope confocal nous a fourni la position des particules, alors que la techniques des traînées nous a permis de définir la dynamique de capture des particules par la paroi ainsi que la provenance de ces dernières, en amont du filtre, dans la zone dite de capture. Dans le régime ligne, les particules sont capturées juste à l'entrée de la constriction par l'un des deux murs horizontaux. Nous avons montré que la probabilité associée à ce type de capture diminue de manière exponentielle avec le débit ; cette évolution correspondant exactement à celle de la zone de capture. Par ailleurs, dès que quelques particules sont déposées, on ne peut plus négliger les interactions hydrodynamiques avec ces dernières. Ces interactions augmentent la probabilité de capture en augmentant la taille de la zone de capture. Les particules déjà déposées repoussent les particules en les déplaçant vers l'une des parois du pore, de sorte que ces dernières viennent se déposer proche d'elles. Il se forme ainsi des agrégats allongés de petites tailles, perpendiculairement à la direction de l'écoulement. Ces derniers finissent par être connecté et on obtient un bouchon sous forme de ligne. Au fur et à mesure que le débit augmente, les particules se déposent de plus en plus profondément dans le pore, tout en restant toujours à proximité de son entrée. L'augmentation du débit conduit à la formation de « lignes » de colmatage plus en plus tortueuses. Le régime d'invasion

du pore commence dès que le centre des particules capturées est, en moyenne, à une distance supérieure à deux diamètres de l'entrée du pore. La majorité des captures par les parois du pore sont indirecte. Elles découlent des interactions hydrodynamiques entre particules mobiles et immobiles dans le pore. De manière similaire à ce qu'on a observé dans le régime ligne, ces interactions favorisent le dépôt des nouvelles particules à proximité de celles qui sont déjà à l'arrêt ; ce qui contribue à la croissance des agrégats. Nous avons mis en évidence que leur taux de croissance ne découle que des interactions binaires. La particule qui se déplace à proximité d'un agrégat va être capturée uniquement par une particule, la plus proche, située sur le bord de l'agrégat. Il en découle que le taux de croissance des agrégats dépend principalement du débit et non de la taille et de la forme des agrégats. Dans ce régime d'invasion du pore, le taux de croissance des agrégats est plus grand que la probabilité de capture directe à l'entrée du pore. Le pore est finalement colmaté en moyenne à une distance, par rapport à son entrée, égale à la largeur du pore. Finalement, nous avons pu établir un diagramme de fonctionnement du filtre qui dépend uniquement du débit Q et du rapport des largeurs WR/W, où WR et W sont respectivement les largeurs du pore et celle de la zone dite de réservoir, située de part et d'autre de l'entrée du pore. Les particules qui proviennent de cette zone participent au colmatage du pore dans le régime invasion, en se déposant presque uniquement à l'intérieur du pore. Tant que la largeur de cette zone réservoir, WR est plus petite que la largeur du pore, W, la transition entre les deux régimes de colmatage se produit pour les plus grands débits mesurés. Pour $1<WR/W<4$, plus ce rapport est grand, plus le débit d'apparition du régime d'invasion est faible. Le nombre de particules déposées dans le pore croît avec ce ratio de largeur ainsi que les agrégats. Pour $WR/W > 4$, le débit à la transition est constant et est indépendant du ratio. Dans ce cas, les particules peuvent être capturées partout dans le pore, sauf à l'entrée, vu que la majorité des particules proviennent des zones de réservoir.

Colmatage 3d

Dans le chapitre IV, nous avons abordé le colmatage de pore 3d, dont la hauteur est égale à la largeur du pore. Nous avons fourni une description détaillée de l'ensemble du processus de colmatage, à la fois à l'échelle du pore et à l'échelle de la particule. L'approche à l'échelle du pore, basée sur des images en champ clair, nous a permis de déterminer l'influence de la géométrie du pore, du confinement, du débit du fluide et des forces colloïdales sur le processus de blocage. Nous avons observé tout d'abord que de petites modifications de la géométrie du pore, notamment la courbure de son l'entrée, peuvent changer grandement les conditions de formations de bouchon. Nous avons mis en évidence que pour que les bouchons puissent se former dans le pore, ce dernier doit être suffisamment long, avec une longueur au moins égale à la largeur du pore W. Cette longueur minimale correspond aussi à l'extension, dans la direction de l'écoulement, de bouchons stables, L_{clog}. Nous avons aussi montré que pour former de tels bouchons, il faut qu'un certains nombres de particules, N*, soit passé dans

le pore avant que ce dernier soit colmaté. Dans la suite, nous avons étudié l'évolution de ces deux paramètres, N* et L_{clog}, avec les conditions hydrodynamiques et les forces colloïdales. Nous avons montré qu'il y a deux régimes de colmatage suivant la valeur de la pression imposée. Dans un premier régime, aux faibles pressions, N* et L_{clog} restent constants, alors que dans le deuxième régime, aux pressions plus élevées, les deux quantités augmentent avec la pression. Dans ce dernier régime, l'écoulement peut détacher les particules qui sont en contact qu'avec une seule paroi du pore. L'augmentation de N* correspond au fait qu'il faut que plus de particule passe dans le pore pour que certaines soient capturées de manière permanente et permettent ainsi la croissance des agrégats. Par la suite, nous nous sommes focalisés sur le premier régime de colmatage. Nous avons montré qu'alors que Lclog augmente linéairement avec le degré de confinement, W/D, N* augmentent aussi mais de manière beaucoup rapide, suivant une loi de puissance avec un exposant égal à sept. Par ailleurs, nous avons mis en évidence que la modification de la partie répulsive du potentiel d'interaction, de type DLVO, entraîne les plus grandes variations de N*. Plus la répulsion interparticulaire est grande, plus grand est ce nombre, ce dernier suivant une augmentation linéaire avec la force ionique de la suspension. Cependant, l'évolution de N* avec W/D reste inchangée lorsqu'on modifie la force ionique. Nous en avons conclu qu'il y avait deux contributions distinctes à l'évolution de N* avec le degré de confinement. La première est purement géométrique alors que la seconde dépend uniquement des caractéristiques du potentiel DLVO. En zoomant à une échelle plus fine, celle des particules, grâce au microscope confocal, nous avons pu montrer qu'en effet, la structure des bouchons obtenus dans différentes conditions de salinité était assez similaire, au moins pour ce qui concerne la fraction volumique moyenne ainsi que la distribution des contacts dans le bouchon. Le changement rapide de N* avec la force ionique est directement relié à la probabilité de capture des particules par les agrégats qui croissent sur les parois du pore. Pour une force ionique importante, dont la valeur est juste inférieure à la concentration critique de coagulation, la barrière répulsive est relativement faible ; et par conséquent la force de traînée nécessaire pour passer au-dessus de cette barrière l'est également. Ceci permet une capture même aux faibles vitesses d'écoulement et, en quelque sorte, élargi la zone de capture autour d'une particule appartenant à un agrégat, permettant une croissance plus rapide des agrégats. Dans le cas opposé, pour les faibles forces ioniques, la barrière électrostatique est importante et la probabilité de capture est petite, puisque que les particules utilisées dans cette étude, des PS (polystyrène) et des PMMA (polyméthacrylate de méthyle), ont une charge de surface relativement grande.

Nous avons pu aussi déterminer la dynamique de formation du bouchon à l'échelle de la particule pour un confinement important (H/D =3). Nous avons mis en évidence que la construction du bouchon se déroule, dans ce cas, en deux étapes. Dans un premier temps, les particules se déposent sur les parois du pore. Dès que deux ou trois particules sont capturées à l'entrée du pore, le mode de capture indirect domine la déposition. Toute nouvelle particule qui entre dans le pore, va forcément interagir, de manière hydrodynamique, avec celles déjà

déposées. Les nouvelles particules ainsi capturées se déposent toujours à proximité de ces particules immobiles. Nous avons donc une croissance d'agrégat « monocouche ». Nous avons constaté que seulement deux ou trois agrégats croissent en même temps dans le pore. Mais au fur et à mesure de leur croissance, un seul finit par croître plus rapidement que les autres, souvent en formant des réunions avec les autres. Quand cet agrégat principal couvre la paroi du pore, à partir de l'entrée de ce dernier et dans la direction de l'écoulement, sur une distance de l'ordre de la hauteur du pore (la longueur la plus petite), on assiste à la déposition de particules sur la monocouche de particules en contact avec la surface du pore. On observe en effet que la capture de la première particule à cet endroit correspond systématiquement au début de la deuxième et dernière partie de la formation du bouchon. Au cours de ce régime, le taux de capture de particule augmente puisque la section disponible du pore est significativement réduite. Nous avons aussi confirmé que pour un confinement aussi important, la fraction volumique moyenne du bouchon est un peu plus importante que pour des conditions de confinement moins drastiques étudiées précédemment (H/D=3 vs. H/D=6). Ceci est dû principalement au fait qu'en milieu très confiné, la plupart des dépositions de particules se déroulent sur la paroi du pore, où la fraction volumique est plus la élevée puisque on est sur une surface, à deux dimensions. Finalement, quel que soit le degré de confinement, les bouchons présentent une structure ténue, typique des gels colloïdaux, qui résultent de la croissance et la réunion d'agrégats.

Perspectives

Notre étude expérimentale nous a aidés à identifier plus clairement comment la dynamique de colmatage et les propriétés structurales des bouchons dépendent de la géométrie du pore, des conditions hydrodynamiques et de force colloïdales. Cependant, beaucoup d'aspect du processus de colmatage restent peu ou pas explorés. Tout d'abord et de manière générale, il faudrait avoir une meilleure connaissance de la dynamique de capture des particules soit par la paroi, soit par les agrégats. Pour cela, il est possible d'augmenter la fréquence de modulation du signal fluorescent pour détecter des variations de vitesses plus faibles en même temps que la position des particules en mouvement. La dynamique de formation des bouchons à l'échelle de la particule doit être aussi étudiée de manière beaucoup plus systématique pour déterminer entre autre les caractéristiques de la croissance des agrégats à partir d'une surface sous écoulement. En ce qui concerne les forces colloïdales, une étude approfondie de l'impact des forces d'adhésion doit être menée. Nous avons observé, au cours d'expériences préliminaires à l'échelle du pore, que la modification des forces de van der Waals entraîne des variations relativement importante de la longueur des bouchons et de la dynamique de formation des bouchons. Une extension naturelle de ces travaux est l'étude du colmatage dans un réseau de pores interconnectés à deux dimensions.

Remerciements

Je tiens d'abord à remercier mes directeurs de thèse Hervé Tabuteau et Luc Oger. Luc, merci pour ta disponibilité et ta bienveillance. Hervé, merci de m'avoir laissé l'opportunité de m'épanouir dans cette thèse en me laissant libre de développer des solutions techniques et d'analyse qui orienteront la suite de ma carrière. Parce qu'il existe des rencontres stimulantes qui nous incitent à donner le meilleur de nous-même, je tiens à remercier Janine Emile de m'avoir présenté Hervé.

Des remerciements dans la langue de Shakespeare s'imposent pour ceux qui m'ont accueilli à l'Université d'Edimbourg :

I would like to thanks Wilson Poon and Jochen Arlt for welcoming me at the University of Edinburgh and for their wise advices on colloidal systems and microscopy. Thanks to Andrew Schofield for the production of the PMMA particles and his support and advices on colloidal solutions and dyes during my stay. Finally, thanks to Dario, Adriano and Giovanni for bringing some of the Italian sun under the Scottish rain.

Je tiens à remercier les membres du jury : Patrice Bacchin et Jean-Baptiste Salmon pour leur lecture attentive de mon manuscrit et leurs remarques avisées ; Anke Lindner de m'avoir fait l'honneur de présider mon jury de thèse ; ainsi que Marc Tramier d'avoir examiné ce travail.

Un grand merci à tous les membres de l'Institut de Physique de Rennes et particulièrement à tous ceux qui au cours des quatre années où j'ai étudié à Rennes avant ma thèse ont su m'insuffler leur passion pour la physique. Merci à John, Louis, Matthieu, Hélène, Mickaël, Antoine, Federico, Martin, Alexandre, Thao, pour les bons moments et notamment la Pologne pour certains.

Pour terminer, je tiens à remercier ma famille et mes amis pour leur soutien. Merci à mes parents de m'avoir permis d'effectuer ces longues études dans les meilleures conditions. Finalement, merci à Kahina, toi qui partage ma vie depuis 10 ans maintenant et qui m'a toujours soutenu durant toutes mes études et sans qui je ne serais surement pas là aujourd'hui.

A toi avec qui j'ai rendez-vous dans un an moins le quart…

Chapter I - Introduction

A. State of the art

1. Dynamical jamming

The transport of mobile agents in networks is ubiquitous in various different areas, ranging from functional structure of the living organisms (cells, skin and lung) up to mechanical operations (air and water filtration, particles sorting). Usually, and whatever the length scale, if there is a low density of mobile agents in the network, the traffic is fluid. This remains true as long as those mobile agents interact neither with each other nor with the network or the surrounding media. On the contrary, those interactions promote the creation of localized blockages which might end up stopping the transport [1],[2]. To prevent the clogging and optimize the transport, it is crucial to understand the underlying mechanisms of the blockage in bottlenecks, so frequently observed in many fields such as engineering, medicine and architecture. The clogging of industrial silos and conduits by granular materials, which completely stop the production, can cause important economic losses. In the oil and gas industry, the clogging of pipelines by clay particles is a major issue. For instance, it is not possible to transport continuously oil and gas together in the same pipeline along the sea floor. Indeed, water and natural gas form hydrates under high pressure and low temperatures that clog the pipelines. Clogging also modifies the efficiency of filters due to the increase of hydrodynamic resistance [3]. Flow of concentrated colloid suspension is either continuous or exhibit velocity fluctuations because of the permeation flux of the solvent through the arches formed by the particles network [4]–[7]. In the natural aquifer, clogs modify the permeability whose the control is essential for the well extraction and also to quantify pollutant mobility [8]–[10]. In ecological engineering, for instance, we use subsurface flow treatment to remove pollutants from wastewaters in wetlands. Even though this solution has many advantages (low energy and maintenance cost) the efficiency of the process evolves in time mainly because clogs are formed within the porous medium [11]. In the automotive industry, the carbon deposit affects the combustion engine performance.

Clogs of humans or animals are also very important. In real panic situation, for instance, people trying to leave a room through a single exit, generate intermittent clogging in the exit (Figure 1-A). Group of individuals can escape in an irregular manner and vast majority of the crowd cannot flow continuously outside [12], [13]. It was possible to observe the dynamical features of a genuine escape panic of mice attempting to escape out of a water pool [14]. The mice also escaped via the exit in bursts of different sizes, which depend mainly on the exit width.

Today, all the above mentioned examples are not described in a general framework of clogging with extensive variables, like for the jamming transition [15]. However, those different systems share

some common features. There must be a critical density of particles per unit area in the vicinity of the narrowing in order to observe clogging in silo [16] (Figure 1-B), in suspensions [4], [17] (Figure 1-C), and crowd dynamics [18]. The clogging always corresponds to the formation of an arch. Therefore, the contact properties, such as friction and pressure, between objects play a major role in the process. This was further evidenced by putting respectively obstacles or columns just in front of the outlet in silos [19] and in rooms [13], [20], [21]. Even though the placement of an obstacle before the possible clog location seems against intuition, it releases locally the pressure and helps to prevent the clog formation. In general, we can consider all those systems as a concentrated assembly of "hard spheres", in the sense that, when they come into contact they push each other and are not stuck permanently. The many body interactions are responsible of the arches formation corresponding to the clogging.

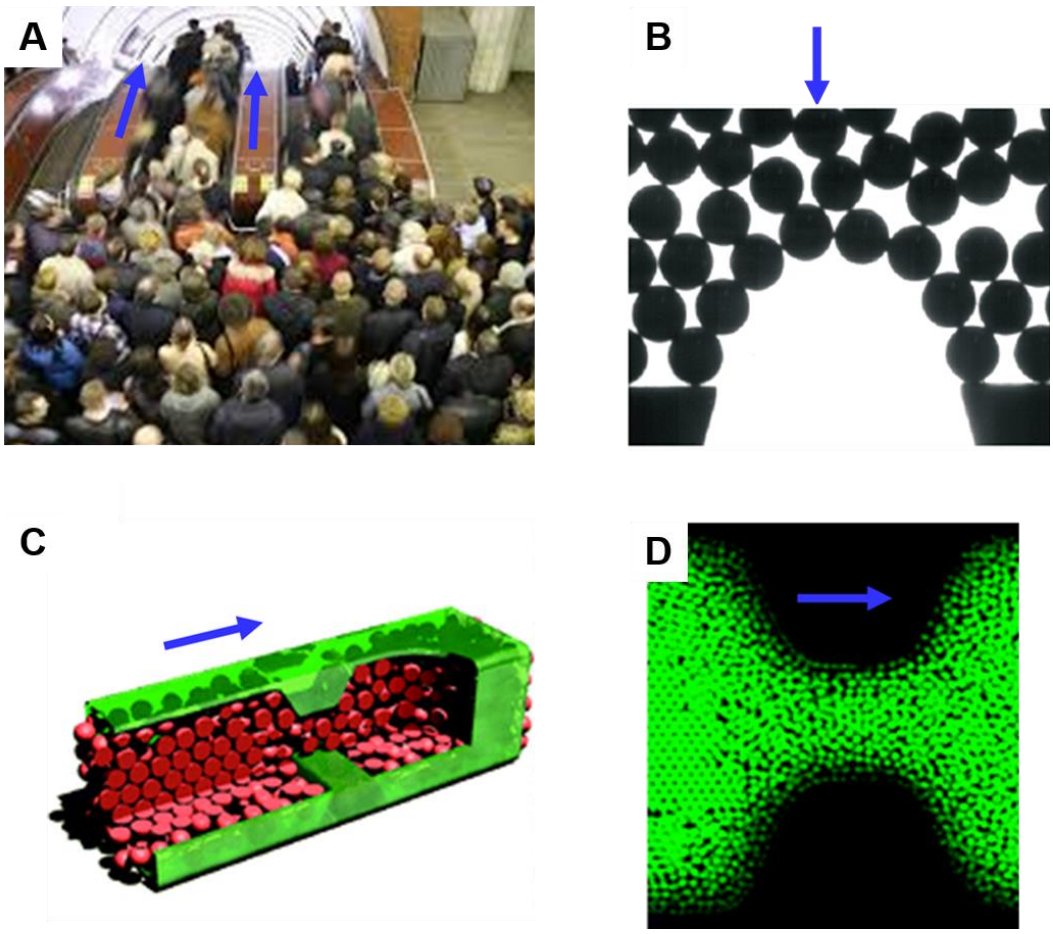

Figure 1: Different clogging situations. The blue arrow indicates the flow direction. A-The crowd tries to ride the escalator all together. They formed temporarily a clog in front of the escalator. B- Grains get blocked before the outlet of a 2d silo [22]. C- Flow of a concentrated suspension of hard sphere colloids within a constriction. The flow in the narrowing induces a densification of the suspension, upstream of the constriction, which leads to the formation of crystalline domains [5].

2. Clogging in porous media

At the opposite extreme, we also observe the clogging process when diluted suspensions, with (living or inert) particles sizes from the nanometre range to the millimetre, flow through some sorts of porous media. In this case, clogging results from the adhesion of those particles on the pore walls and their consecutive aggregation, due to attractive forces at short distance. Again, there are many natural and industrial examples. Fatty substances can progressively clog arteries. This build-up of fatty material that forms plaques on the inner wall of the arteries reduces locally the blood flow. The flow can also detach some parts of this deposit, which then travel in the bloodstream and block a smaller artery. Clogging is also important for the efficient remediation processes, because microbial growth can greatly modify the flow conditions and the transport [23]. During the separation of colloidal particles from fluids (ground water treatment, deep-bed filtration in oil recovery, catalysis) pore clogging inevitably happens and stops the process.

Experimental studies address two aspects of the particle accumulation in the porous structure: particle retention and channel clogging. The retention of particles prior to clogging is estimated by measuring the particle content at the outlet of the porous medium [24], [25]. The vast majority of these studies report on colloidal and non-colloidal particles deposition in complex porous structure such as columns of packed beads [26] and fibres [24] or membranes with different sizes of cylindrical pores [27]. The colloidal particles are also often polydisperses such as clay particles [28], [29] due to the large amount of colloids required by macroscopic experiments. Yet while these experiments give the opportunity to monitor filtration and clogging under field conditions, the complexity of the results makes it difficult to gain a good understanding of the underlying physical mechanisms. Others studies have investigated colloid deposition and clogging within 3D model porous media to simplify the problem, using either X-ray-micro-tomography [30]–[32] or static light scattering in refractive index matching conditions [33]**.** Authors are able to show that the structure adopted by the particles in the clogged pore is rather heterogeneous. However, those techniques cannot provide the structure at the particle level and we cannot study at all the dynamics of the clogging process. Based on these observations, several groups have focused on the flow of dilute colloidal suspensions within model porous media (microfluidics devices), at the pore scale. This technique allows visualizing the flow within the pore, define where exactly the porous structure is clogged and also quantify the dynamics of the colloidal particles [34], [35].

Most of those studies have shown that clogging generally occurs when the flow becomes confined [3], [27], [36]–[41]. The porous medium is clogged either at its entrance or within the first rows of pore throats, depending on the pore width W to colloid diameter D ratio, W/D, thereafter called in this thesis *the degree of confinement*. We have a good illustration of this phenomenon in figure 2. When the particles are larger or almost equal to the size of the pores they form a deposit on the

medium surface known as a *filter cake* (figure 2d where W/D ≈ 1).When the particles are generally smaller than the pores sizes, deposition occurs within the internal structure of the medium (figure 2B-C, 1.8 < W/D <2.5). Strikingly, for a very small increase of the ratio (figure 2A, W/D >2.5), we only observed interception and attachment of particles by the pore walls.

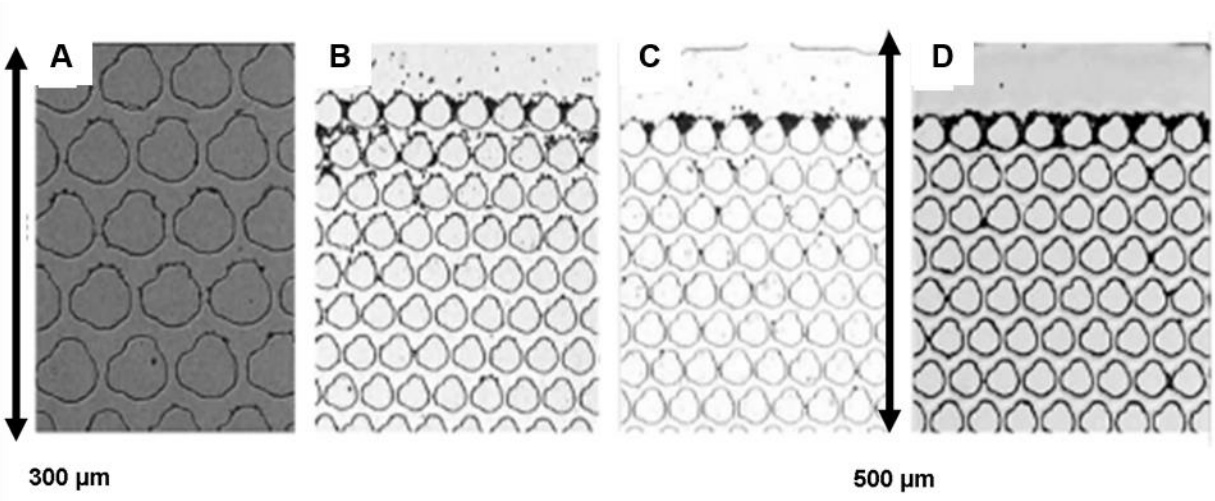

Figure 2: Images of a model porous medium in which flow a diluted colloidal suspension with the same flow velocity (60 mDarcy) (from ref. [37]). In each case, the particle size is different: 3 µm in (A), 4 µm in (B), 5 µm in (C) and 7 µm in (D).

At the microscopic scale, i.e. at the particle level, pore blocking can be either instantaneous or more frequently be progressive, depending on the volume fraction of the suspension and the ratio of confinement. The cake formation is based on two primary mechanisms, referred to as *complete blocking*, shown in Figure 3-A (a sieving process that occurs when the particles are larger than the pore sizes) and *bridging* (Figure 3-B). Bridging occurs when the pore size is larger than the particles. This phenomenon occurs particularly when the particle volume fraction (ϕ) in solution is high. Several particles, as the individuals in front of the exit door in the previous section, attempt to pass simultaneously into the pore entrance, but fail to do so and form an arch at that place. We can easily destroy this arch, stabilised by the flow, if the velocity and/or flow directions change rapidly (back flush). The standard clogging mechanism is less severe and more progressive (Figure 3-C). Particles, which are smaller than the average pore sizes, are captured within the pore, on its surfaces. Their accumulation leads to the reduction of the cross section (increase of the hydrodynamic resistance) of the pore and eventually clogs it.

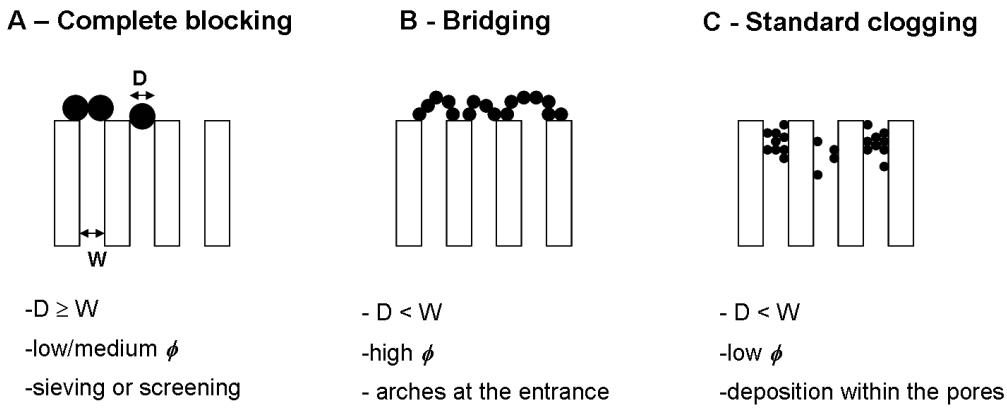

Figure 3 : Different mechanisms of clogging which depend mainly on the degree of confinement W/D and the particle volume fraction in solution ϕ.

3. Experimental studies of the clogging process at the pore scale

a. Complete blocking

One often encounters the complete pore blocking during the fractionation process, which separates particles of different sizes by microsieving. Ben Hassan et al. [42] followed the deposition of monodisperse and bidisperse particles, all being larger than the pore size, on a sieve in dead end filtration mode (flow perpendicular to the microsieve surface). They monitored the growth of the filter cake, layer by layer. They were able to determine its morphological features (local structure, thickness and porosity) and correlated those ones to the reduction of pressure recorded during the cake build-up [42], [43]. Brans et al. [44] have focus on the behaviour of binary colloidal mixture in cross flow filtration (flow is parallel to the membrane surface). The mixture consisted in particle whose size was larger than the pore size and the other smaller. They observed that the larger particles always plug the pore exactly in its centre, whereas the smaller ones deposit on the pore edges (Figure 4). They found that the clogging by bridging increases with the particle concentration.

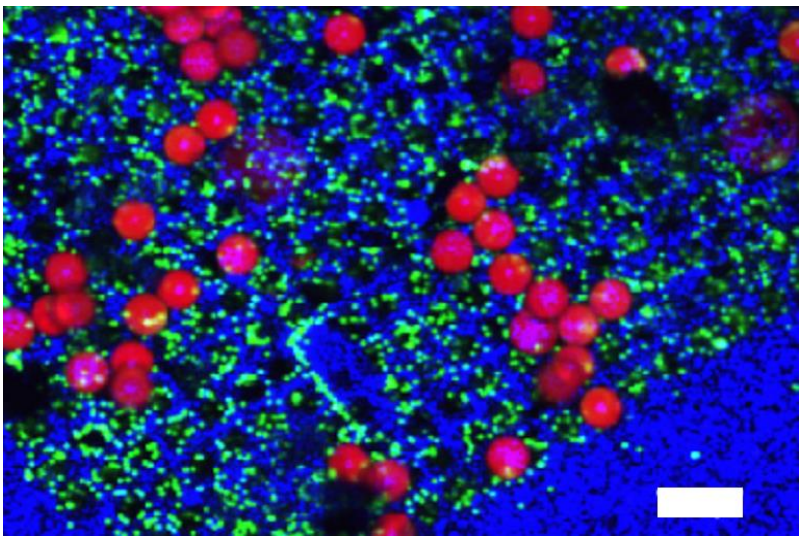

Figure 4 : Confocal image of a microsieve during fractionation of bidisperse suspension (initial volume fraction of 1µm (green) and 9.7 µm (red) particles in solution are respectively 5.3 10^{-7} and 2. 3 10^{-5}, 30 minutes after the beginning of the experiment. The grid is in blue colour.

b. Bridging

Clogging by bridge or arch formation occurs when (micro) sieves or tubes have a pore diameter larger than the particle size. Roussel et al. [16] shown that millimetre beads, suspended in a fluid, can come together in the same time and clog a pore grid (ref Figure 5a). Sharp and Adrian [36] also observed, with way smaller particles sizes (50µm), an arch like shape within a tube (Figure 5b). For even smaller particle (200 nm), and within the same range of degree of confinement [3], [4], pore bridging was also evidenced by Ramachandran and Fogler [45], (Figure 5c). They showed that above both, a critical concentration and a critical flow rate, pore clogging is always due to hydrodynamics bridging. Above this critical flow rate, no deposition of individual particles on the pore wall is possible but the hydrodynamic forces at the pore entrance can overcome the repulsive part of the DLVO barrier for both the inter-particle and the particle-wall potentials. Particles can thus adhere on one another and on the pore walls in the same time and form in this way an arch. More recently, Bacchin's group [46]–[48] found similar results (Figure 5-D) when latex microparticles flow through a PDMS[1] microchannel composed of an array of parallel and rectangular elongated pores (W/D=4). They varied the flow rates of injection of the suspensions and their volume fraction. They can gather all their results in a single graph (Figure 6-A) when one can easily identify in which conditions clogging occurs or can be avoided. For volume fraction values lower than $5x10^{-4}$, irrespective of the flow rate, there is no clogging. Above this value, the critical velocity, from which clogging shows up, decreases with the volume fraction of the suspension.

[1] PDMS: Polydimethylsiloxane a polymer widely used for the manufacture of microfluidic chips.

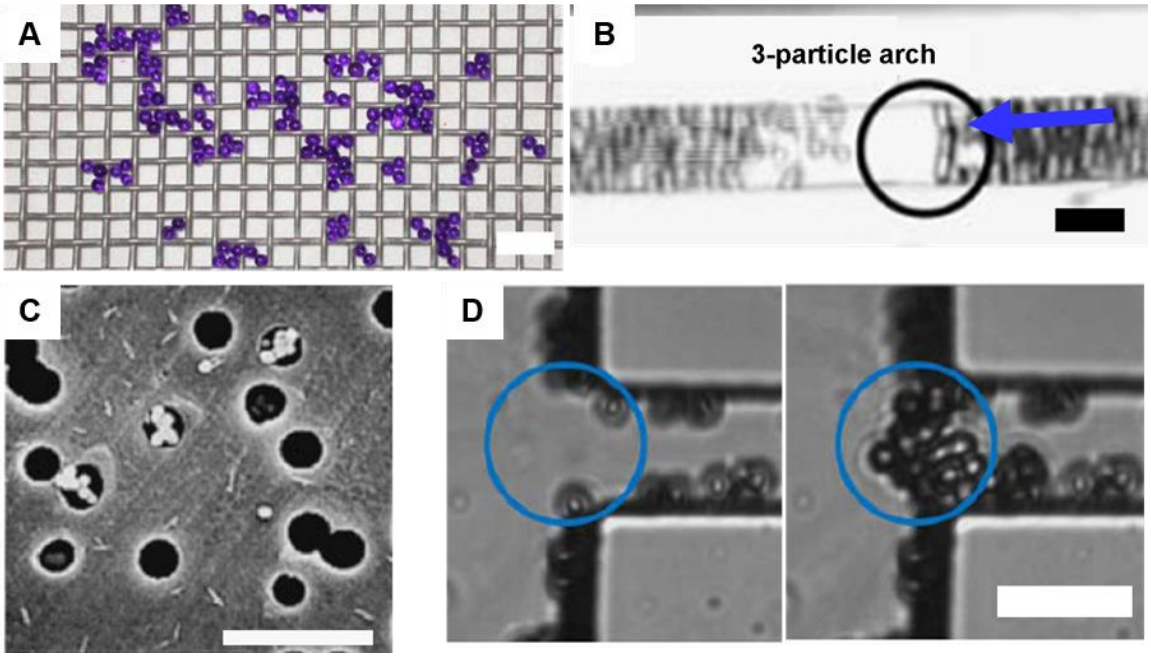

Figure 5 : A- 3 mm beads lying on a grid (5 mm pore size). Pore can be blocked by two, three or four particles. Scale bar is 1cm [16]. B- Clogging of a 150 µm inner diameter circular tube by three 50 µm particles which form an arch [36]. Scale bar is 150 µm. Particles accumulated upstream of the clog. C- Pores of a track-etched membrane clogged by bridges of 0.2 µm latex particles [27]. Scale bar is 3µm. D- Two consecutives images of a pore with a width of 20 µm clogged by 5µm particles [48]. After a limited deposition on the pore walls (left), an arch suddenly occurs 5s later (right). Scale bar is 20 µm.

They also showed that slight changes of hydrodynamic conditions, the volume fraction and the ionic strength lead to different morphologies of deposits. Latex microparticles can form arches, clusters or dendrites (Figure 6-B). In the clogging regime, when there are arches within several pores, particles start to accumulate on top of them and overflow on both sides, on the neighbouring pores, which clog more rapidly. Some adjacent clogged pores can merge in this way, forming a big aggregate, called here *cluster*. Those structures grow on top of the pores, upstream of the flow. Those clusters also merge to give birth to the filter cake. When the ionic strength increases up to a concentration of 0.1 M KCl, particles are more easily captured even for low volume fraction. This ionic strength value is quite high but just a bit smaller than the critical coagulation concentration (0.2 M). This addition of salt to the solution allows forming dendrite-like aggregates on the edge of the pores on the overall range of the volume fraction. It is worth noting that, even though the aggregation is facilitated in this regime, pores are not clogged.

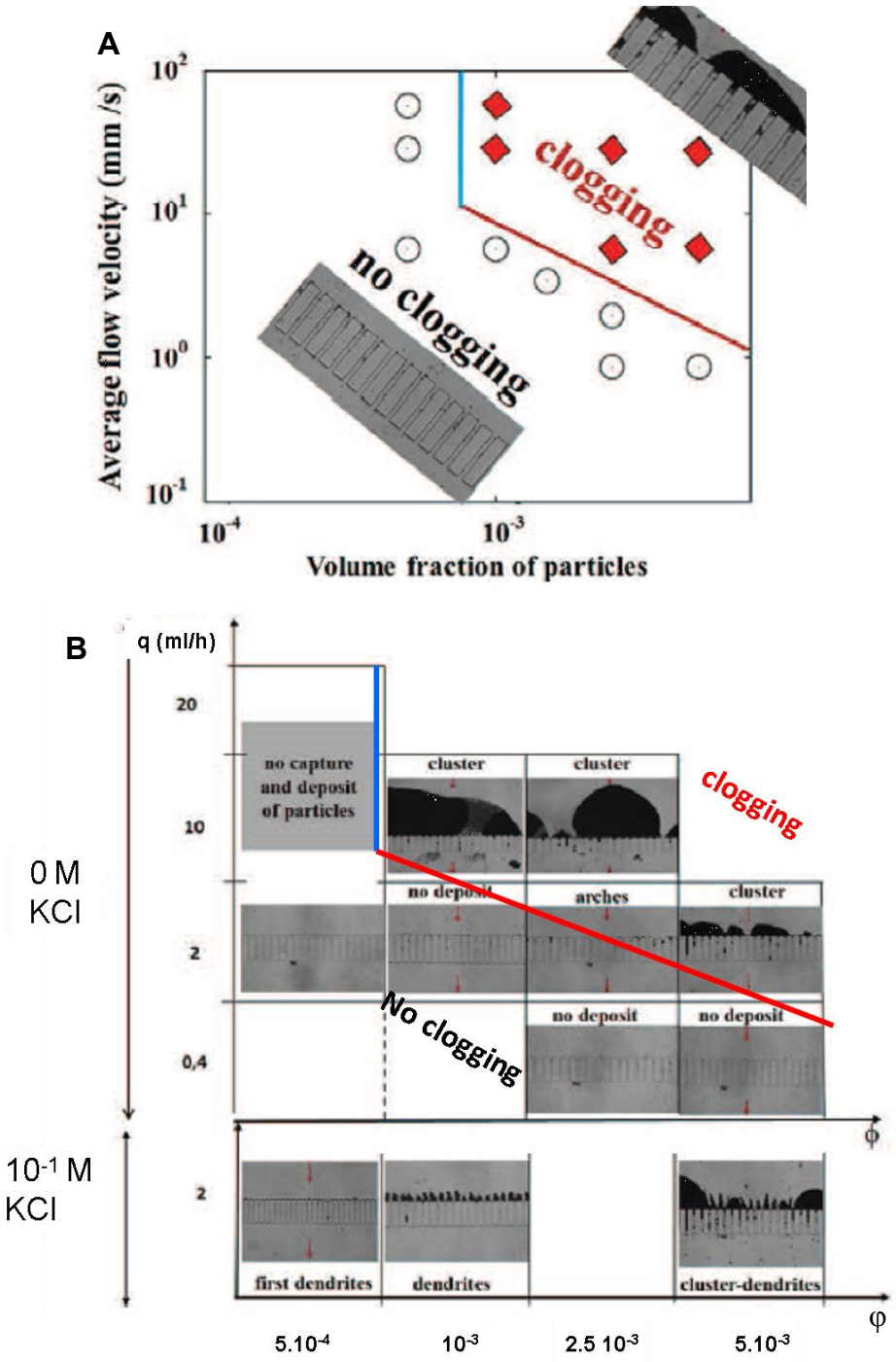

Figure 6 : A- Experimental conditions leading to the pore clogging after 90 minutes of injection of a latex microparticles suspension. The open circles correspond to homogeneous transport and the filled diamonds to the blocked pores (clogging). For each regime, there is a picture of the model filter. B- Different deposit morphologies of 5 µm latex particles within the model filter for various flow rates, volume fraction of the colloidal suspension and the ionic strength of the solution. After the filtration started, for q ⍰ 2 ml/h and q > 10 ml/h, we take images 90 and 40 min, respectively.

c. Standard clogging: progressive building-up

We can also clog pore more gradually, resulting from the adhesion and the accumulation of individual particles within the pore. Most of the time, we have indirect hints that the pore is on its way to be blocked, usually by looking at the variation of the pressure at the level of the porous medium. Recently, some groups have unambiguously correlated those pressure variations with the formation of clogs at the pore scale, and the consecutive growth of the filter cake, at the entrance of simplified model porous structure [46]–[49]. There is no study, up to now, that addresses the dynamics of the overall clogging process at the pore scale and even less at the particle level. Each study has focused on one peculiar moment of the clogging history. In the following, we will briefly review those diverse advances, going from the first particle deposited to the final blocking.

i. The first particle

At the very beginning of the process, the pore wall capture a first particle. Only few studies deal with the dynamics of the particles deposition near the entrance of a pore.

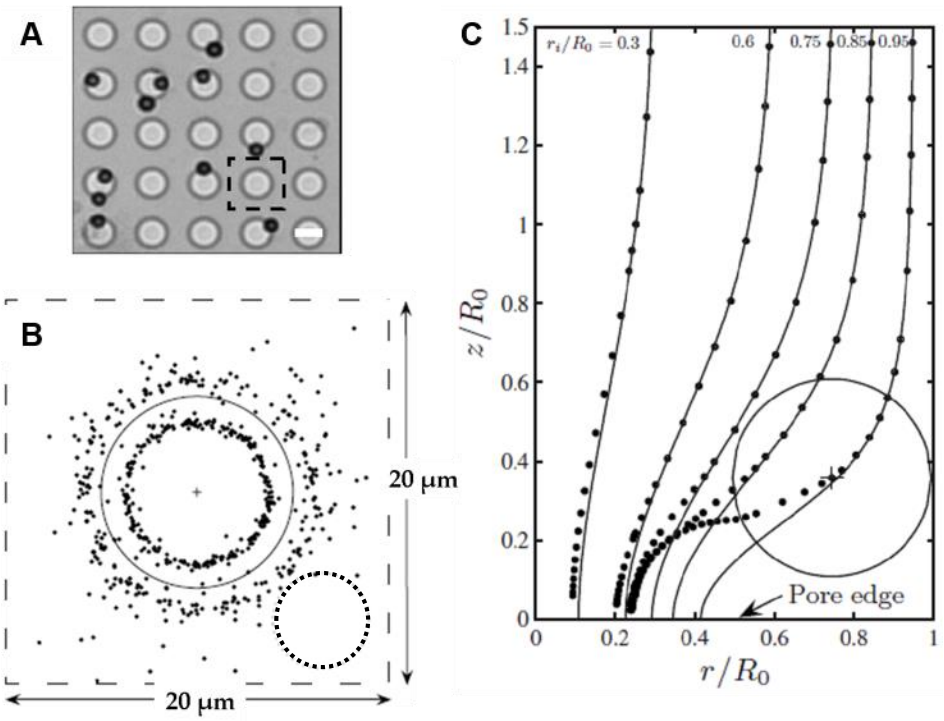

Figure 7 : A-Image of the microsieve membrane with 5.2 µm colloidal particles captured at the edges of the 10µm pores (scale bar is 10µm). B- Typical results for the first captured particle positions (dots) around the pore entrance. The solid circle is the pore edge and the dotted circle in the bottom right corner corresponds to the area of a particle. C- Five particle trajectories in an axisymmetric flow near the pore entrance (circles). The continuous lines come from an analytical model that uses enhanced drag coefficient due to the presence of the wall. We show the most off centred particle at one of its positions.

Lin et al. [50] has shown that, in the case of microsieve, the first particle stops at two preferred locations just at the edge of the pore, irrespective of the flow rates and the pore geometry (Figure 7-A and B). They used a hydrodynamic model, which takes into account the modifications of the drag forces when particles come very close to the pore wall, to determine the captured particle trajectories (Figure 7-C). Very recently, one author of the same group [51] refined the computation of particles trajectories, by including the van der Waals attraction at short distance. In this configuration, the author results do not match exactly with those found in the previous study. They attributed this small difference to a rolling motion, either just after the capture, or after the presence of impurities or local roughness. They called for additional experimental studies of the real time capture dynamics to remove any kind of ambiguity.

ii. Single layer versus multilayer formation

Ramachandran and Fogler[45] determined in which conditions multilayer of particles can be formed within the pore. They distinguished two types of colloidal suspensions. One which is stable against aggregation, i.e. there is an electrostatic barrier that does not allow the particles to come too close to each other to form an aggregate, and the other one not. In this latter case, multilayer formation is usually observed, the deposit on the pore wall having an irregular shape [52], [53]. In the stable case, we form only a monolayer if the velocities of the particles are below a critical value. The way the first layer of particles is formed depends directly on the so-called shadow effect [54] (Figure 8). Downstream of a particle that is already captured at the pore surface, there is an excluded area where the deposition probability of a new incoming particle is reduced (Figure 8-A and B). The size of this excluded area increases with the approach velocity, low ionic strength conditions, due to the electrostatic repulsion between the particles, and the particle size [55], [56]. When the particle velocity can be higher than the critical velocity, according to Ramachandran and Fogler, the second layer can be formed (Figure 9- A and B).

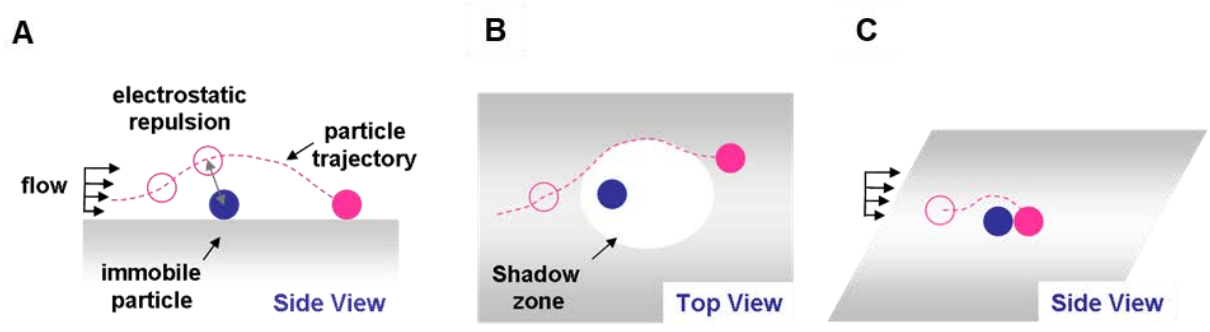

Figure 8 : Schematic description of the shadow effect which is affected by the flow properties, the electrostatic repulsion and the particle size, inspired by Ko and Elimelech [54]. A particle flowing around an immobile one and getting stopped downstream particle in side view (A) or in top view (B). There is an excluded zone (white zone in B named *shadow zone*) in which the flowing particle cannot be deposited. C- Full trajectory of the flowing particle from upstream of the immobile one to its still position, just downstream, forming a doublet.

They said that the ability to have a multilayer deposition within the pore is directly related the interaction between a flowing particle and a deposited particle. The immobile particle can captures the flowing one if it can overcome the electrostatic barrier of the DLVO inter-particle potential, thanks to the hydrodynamic force. Indeed, when the inter-particle separation is of the order of a particle radius, lubrication forces dominate [57]. The slow drainage of liquid between the two particles as they come closer to each other causes this lubrication interaction. Lubrication forces come into play at approximately the same separation distances at which double-layer interactions and van der Waals attraction become appreciable. Ramachandran and Fogler [45] have also shown that the value of the critical velocity, related to the multilayer formation, depends on the ionic strength of the suspension. In their scenario, there is no indication of the final position of the flowing particle, which the stopped one just captured. They have only focused on the conditions of the aggregation process under flow without looking at the structure of the aggregate (doublet). However, there are experimental evidences [58] that after its interception, the flowing particle rolls upon the immobile particle until it gets stuck just downstream (Figure 8-C). Actually, this is the most stable position for the particle under flow. Thus, the capture of a particle by an immobile one can only lead to the formation of a monolayer.

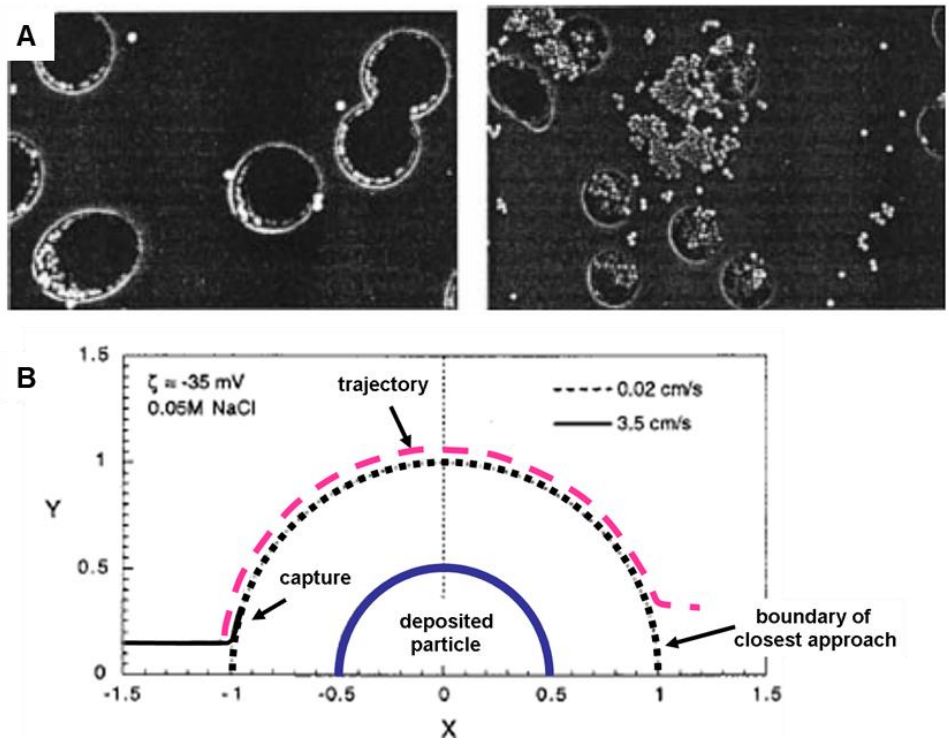

Figure 9 : A- SEM images for flow velocities through the microsieve membrane of 0.05cm/s (left) and 0.73 cm/s (right), corresponding to the monolayer deposition and the multilayer deposition, respectively. B- Calculated trajectories of the flowing particle near the immobile one, for an ionic strength of 0.05M and two velocities. For the smaller one (pink dashed line) the particle flows around the still particle without touching it. For the higher velocity, the flowing particle trajectory intersects the boundary of the closest approach (dotted black semicircle) and thus we capture it.

iii. From the first particle to the clog

More recently, Wyss et al. [3] put forward the inertial retardation effect to explain the deposition on a curved surface of the pore entrance used in their study. Indeed, particles tend to maintain their trajectories except when the streamlines bend, near a constriction, for instance, where a local difference between the liquid and the particle velocity field appears. The authors supposed there are successive particle irreversible depositions, which end up by clogging the pore, after we deposit this first particle. Wyss et al.[3] did not give any detail on the conditions of capture of a particle on top of another one, nor how a layer deposits on top of the previous one. They just say, like Ramachandran and Fogler did, that we capture a particle when this one come close enough to an already deposited one, in order to be trapped by the attractive van der Waals part of the inter-particle potential. They have shown that in the dilute regime, the clogging process is independent of the volume fraction and the flow rate (Figure 10-A). The clogging occurrence depends exclusively on the average number of particles, N*, that pass through the pore prior clogging. This number follows a power law of the degree of confinement W/D as defined above (Figure 10-B). There is a simple relationship between the average time of clogging t* (t*~ 1/Qϕ) and N*: $N^* = t^* Q\phi / V_p$, with V_P the particle volume and Q the flow rate. They also proposed a model that accounts for the variation of N* with the degree of confinement (Figure 10-B).

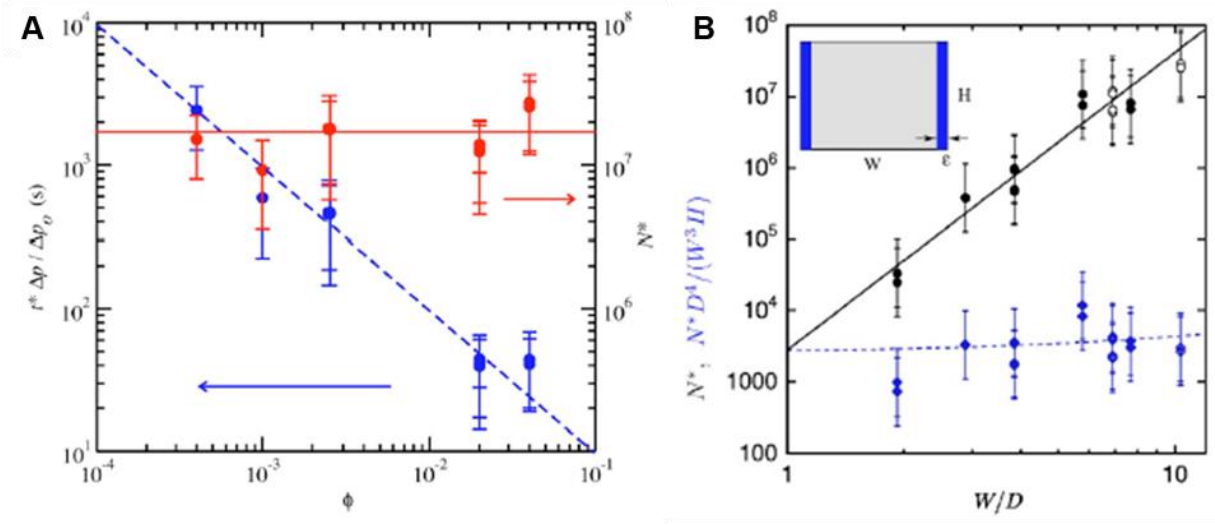

Figure 10 : A- Variation of the average clogging time t* and N* with the volume fraction of the flowing colloidal suspension. Clogging times are normalized by the relative pressure difference. This rescaling eliminates the dependence on the flow rate, and indicates that a fixed volume has to pass through the pore prior to its clogging. The straight dashed line is a power law fit with a slope of -1. The solid red line is a constant value. B- Number of particles, N*, that passes through a pore before clogging as a function of the degree of confinement W/D (black circles). The solid line a power law fit of the data with an exponent equal to 4. N* is also rescaled according the proposed model (blue diamonds). The blue dashed line is a linear fit showing that the rescaled data are independent of the ratio between pore and particle size.

Mustin and Stoeber [38] have used almost the same design and also particles coming from the same suppliers than Wyss et al. They confirmed that the clogging process is independent of the flow rate and the volume fraction. However, they found that pore could be clogged in different manners. The pores can clog either by successive particle depositions or by a single particle, with a diameter larger than the pore size. They also observed pore clogging by a combination of both clogging processes. The cross section of the pore first decreases, as particles accumulate within them, and finally a larger particle finishes the process (Figure 11). Even though the colloidal suspensions are really monodisperses, a very low concentration of larger particles always exists. In a very recent paper, Sauret et al. [39] were able to measure the concentration of those large particles, which also block their devoted microfluidic device, by measuring the time interval between two clogging events.

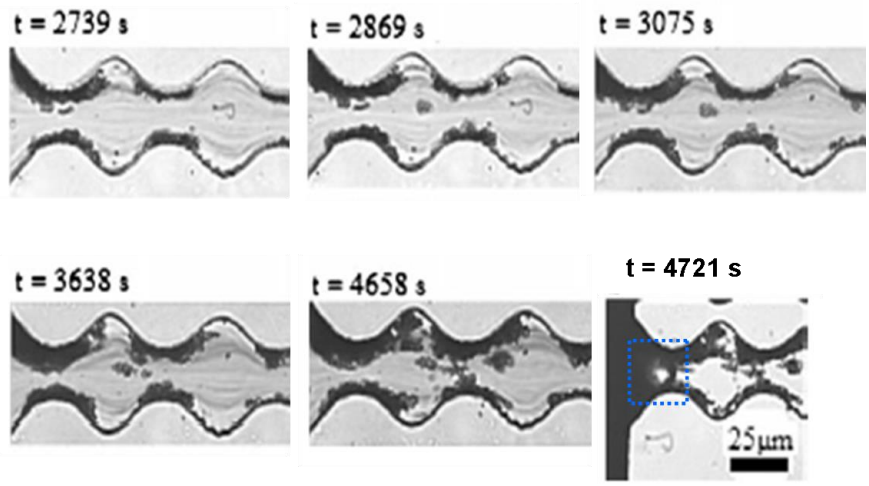

Figure 11 : Images of the progressive accumulation of particles within a pore (first five images). In the last image, a particle (within the blue dotted square) with a diameter as large as the pore size is stuck at the entrance.

B. Thesis outline

We have seen that using model and simplified porous media had led to a better understanding of the clogging process. The visualization at the pore scale has allowed to define unambiguously all the relevant physical parameters related to this complicated process. However, this approach is still rather new and thus used only by few groups, which have worked with rather different experimental conditions (porous media type, flow rate, geometry and colloidal suspensions….). Thus, we end up with three different clogging scenarios. The pore either clogs progressively, due to successive particles accumulations, or almost instantaneously, blocked by a few particles that form an arch at its entrance. A pore can also have its cross section progressively reduced by particle accumulation until a big particle or an aggregate suddenly blocks the rest of the pore. For those three cases, the dynamic of the overall clogging process not been observed. We have only images on the clogged pore, at the end of the process. Moreover, from these images, the structure and thus the mechanical stability of the clog cannot determined.

The main goal of the present work is to fill this gap in providing a detailed description of all the different steps of the clogging process of a pore by a diluted colloidal suspension. We will start to define the conditions (chemical, hydrodynamics and confinement) for the deposition of the particles on the pore surface. Then we will determine how aggregates start to growth from this first layer of particles in contact with the walls. Finally, we will study how the aggregates growth leads to the complete blockage of the pore.

The thesis starts with the definition of the various physical concepts involved in the particle capture and colloidal aggregation (Chapter II -A). We make also a brief presentation of the different imaging techniques (bright field, fluorescence and confocal) and analysis methods, used in the remaining parts of this document (Chapter II -B). In the Chapter III -, we consider the clogging process in very high confinement (degree of confinement: $1.1< H/D < 1.7$, with H the pore height), named thereafter *2d clogging*, which corresponds to the case where particles are flowing through a slotted pore (Figure 12-A). In this case, the interaction between the particles and the pore surface is dominant over the inter-particle interaction. We first define the main features of the clogging at the pore scale (Chapter III -A). Then, we determine the different particle capture mechanisms on the pore wall and quantify the influence of the flow rate, the size of the geometrical features of the pore and DLVO forces on the probability of particle capture (Chapter III -B). In the following, Chapter IV -, we consider the case of the 3d clogging case. In the first part of this chapter, we study the clogging within square cross section pores with a width W, (Figure 12-C). We study the influence of the degree of confinement, which can vary between 1.5 and 10, the pore geometry, the DLVO forces and the flow rates on the clogging dynamics, at the pore scale. Then in a second part, we study the case of a suspension flowing through an elongated pore with a rectangular cross section ($W>H$), with a degree of confinement around to 3.5 (Figure 12-B). We consider the influence of both, the particle-wall and the inter-particle

interaction on the clogging process. We detail all the steps of the process at the particle level in this "moderate" confinement regime, thanks to high-speed confocal microscopy. We provide the rate of particle capture and the structure of the growing aggregates as the clog grows, from the first deposited particle on the pore surface up to the complete pore blocking. We also provide the structure of the clog front at the end of the process, at the particle level, for both confinement studied. We end each chapter by a discussion of the results and a conclusion. Finally, we present the outlook and future work that will follow this work.

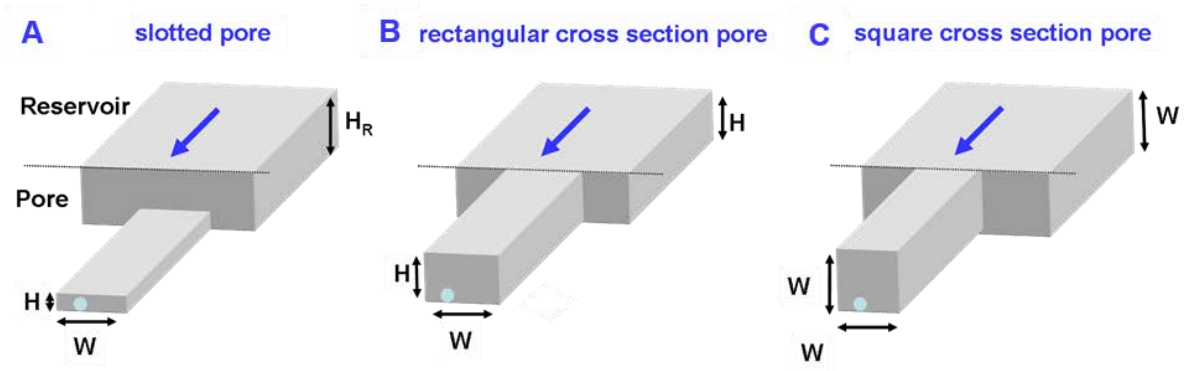

Figure 12 : Both types of pore geometry used in this thesis.

Chapter II - Materials and methods

In this chapter, we will present the specific systems, the methods and experimental setup used to obtain the results presented in this thesis. First, we will define the various physical concepts involved in the particle capture, colloidal aggregation and particle flow in a microfluidic device. Then, we will present the different imaging techniques and analysis used throughout this work. We then will present the method of fabrication of the microfluidic devices using photolithography. Next, we will characterise the colloidal suspension that we will be using throughout this work and discuss how the suspension are prepared. We took special care to the preparation of the colloidal solution to avoid any contamination of the suspension (dust residues, aggregates, larger particles). Finally, we will present a typical experimental setup.

A. Colloids and microfluidics

In this section, we will review the theoretical tools that are necessary to understand the flow of colloidal particles in a microchannel and their interaction with the medium (pore walls) and between each other. We will first describe the colloids and the colloidal forces. Then we will describe the hydrodynamics of the fluid and the suspension in confined microfluidic channels and the relevant dimensionless numbers that characterise such a flow.

1. Colloids

Colloid comes from the Greek word κολλα meaning glue, and originate from the tendency of colloids to agglomerate in solution. This sticky behaviour was the first characteristic of colloidal system identified and is of major interest in our study. The aggregation of colloidal particles arise from an attractive force (Van der Waals) entering a competition with repulsive forces as Coulombic and steric forces.

a. Interaction between colloidal particles

The DLVO (DERJAGUIN, LANDAU, VERWEY and OVERBEEK) theory captures the interactions between colloidal particles in a fluid. It describes these interactions as a sum of VAN DER WAALS attraction, electrostatic repulsion and BORN repulsion at short distance (few nanometres).

i. Van der Waals forces

Van Der Walls (VdW) forces result from the interaction of fluctuating dipoles in each atoms. For two spheres of radii a separated from a small distance h, VdW attraction potential [59] is:

$$\Phi_a = -\frac{Aa}{12h\left(1+\frac{11.12h}{\lambda}\right)}$$

where A is the Hamaker constant, it depends on the characteristics of the different medium ($A = 10^{-20}J$ for polystyrene in water) and λ is the retardation length ($\lambda \approx 100\ nm$).

To calculate the Hamaker constants of the particle used in this work, we used the McLachlan's equation:

$$A = \frac{3}{4}K_BT\left(\frac{\epsilon_1-\epsilon_3}{\epsilon_1+\epsilon_3}\right)\left(\frac{\epsilon_2-\epsilon_3}{2+\epsilon_3}\right) + \frac{3\pi\hbar v_e}{4\sqrt{2}}\frac{(n_1^2-n_3^2)(n_2^2-n_3^2)}{(n_1^2+n_3^2)^{\frac{1}{2}}(n_2^2+n_3^2)^{\frac{1}{2}}\left[(n_1^2+n_3^2)^{\frac{1}{2}}+(n_2^2+n_3^2)^{\frac{1}{2}}\right]}$$

where v_e is the orbiting frequency of the electron, ε is the material dielectric constant, n is the material refractive index with subscripts 1,2 and 3 referring to the particle, the walls and the medium. For inter-particles interaction, it simplifies as:

$$A = \frac{3}{4}K_BT\left(\frac{\epsilon_1-\epsilon_3}{\epsilon_1+\epsilon_3}\right)^2 + \frac{3\pi\hbar v_e}{8\sqrt{2}}\frac{(n_1^2-n_3^2)^2}{(n_1^2+n_3^2)^{3/2}}$$

This potential close to contact grows as the inverse of the separation distance leading to rapid overcome of thermal energy (K_BT) and irreversible aggregation. However, a strong repulsion force completely forbids the interpenetration of particles, the Born repulsion.

ii. Born repulsion

At short distances, a strong repulsion rises from the impossibility for the electronic clouds of the atoms constituting the particles to interpenetrate. The potential ϕ_B associated with this repulsion also called BORN repulsion (a.k.a PAULI repulsion), can be expressed as follow:

$$\phi_B = \frac{A}{37800}\left(\frac{\sigma_c}{a}\right)^6\frac{1}{R}\left\{\frac{R^2-14R+54}{(R-2)^7}+\frac{60-2R^2}{R^7}+\frac{R^2+14R+54}{(R-2)^7}\right\}$$

where σ_c is the collision diameter (4Å) and R is the centre-to-centre particle separation ($R = h/2a$).

BORN repulsion forbids interpenetration of colloids but does not prevent irreversible aggregation. One way to prevent from aggregation is to add charges to the particles to create a Coulombic repulsion between them.

iii. Electrostatic repulsion

In a polar solvent, ionisable groups on the surface of colloids will dissociate forming charged micro-ions. In this case, the formation of a diffuse double layer of counter ions surrounding the particles due to COULOMB attraction maintains the electro-neutrality of the solution. The double layers of particles close together cannot interpenetrate yielding to a repulsive electrostatic force. The resulting potential Φ_e can be obtained by solving the POISSON-BOLTZMANN equation in the limit of a weak electrostatic potential using DERJAGUIN approximation:

$$\Phi_e = 2\pi A \frac{\sigma^2}{\epsilon \kappa^2} ln(1 - e^{-\kappa h})$$

Where ϵ is the solvent dielectric constant, σ is the surface charge density and κ^{-1} is the screening length that represents the size of the double layer and known as the DEBYE-HÜCKEL length:

$$\kappa^{-1} = \left(\frac{\epsilon \epsilon_0 K_B T}{e^2 \sum_i z_i^2 n_i} \right)^{\frac{1}{2}}$$

where e is the electron charge, ϵ_0 is the permittivity of the vacuum, K_B is BOLTZMANN constant, T is the temperature of the system, z_i is the valence of the *i*-type of counter ion and n_i is the corresponding number density.

The DEBYE-HÜCKEL length varies as the inverse of the square root of the counter ions concentration. Increasing the electrolytes concentration in solution leads thus to the decrease of the screening length. Therefore, the addition of salt in the solution is widely used to tune the electrostatic forces in colloidal systems. A colloidal suspension remains stable i.e. does not aggregate under thermal agitation until a critical concentration of electrolytes called the critical coagulation concentration (CCC). In the further, we will always work below the CCC to prevent the formation of aggregates in the suspension prior to the experiment.

We have characterised the inter-particle interaction, but particles can also interact with the medium i.e. the microchip walls. In the following, we will define the colloidal interaction between a particle and a flat surface (pore walls).

b. Interaction between particles and walls

Within a microfluidic channel, particles can interact with the channel walls when they approach the wall close enough (about 10-50 nm). In this case the VAN DER WAALS interaction particle-wall is:

$$\Phi_{a_{p-m}} = -\frac{A}{6h}$$

where h is minimum distance between the particle surface and the wall.

As walls can present also some surface charges, electrostatic repulsion arise in a similar manner than between particles. In this case, the associated potential is:

$$\Phi_{e_{p-m}} = \frac{2\pi a}{\kappa\epsilon}\left\{(\sigma^2 + \sigma_m^2)\left[d - \frac{\ln(e^{2d\kappa}) - 1}{2\kappa}\right] + \frac{\sigma\sigma_m}{\kappa}\ln\left(\frac{1 + e^{-d\kappa}}{1 - e^{-d\kappa}}\right)\right\}$$

where $\sigma_m$is the charge density on the wall surface.

Although exact calculation of this interaction is difficult as it depends also on the geometry of the system, Ramachandran and Fogler [60] shown that the repulsion between particles and wall was weaker than between particles (Figure 13). This implies that the particle will more likely stick onto the wall than between each other. This is not always the case. The wall can be more charged than the particles. In this configuration, once a particle is captured by the wall it will be more probable for an incoming particle to be captured by the still particle rather than by the wall.

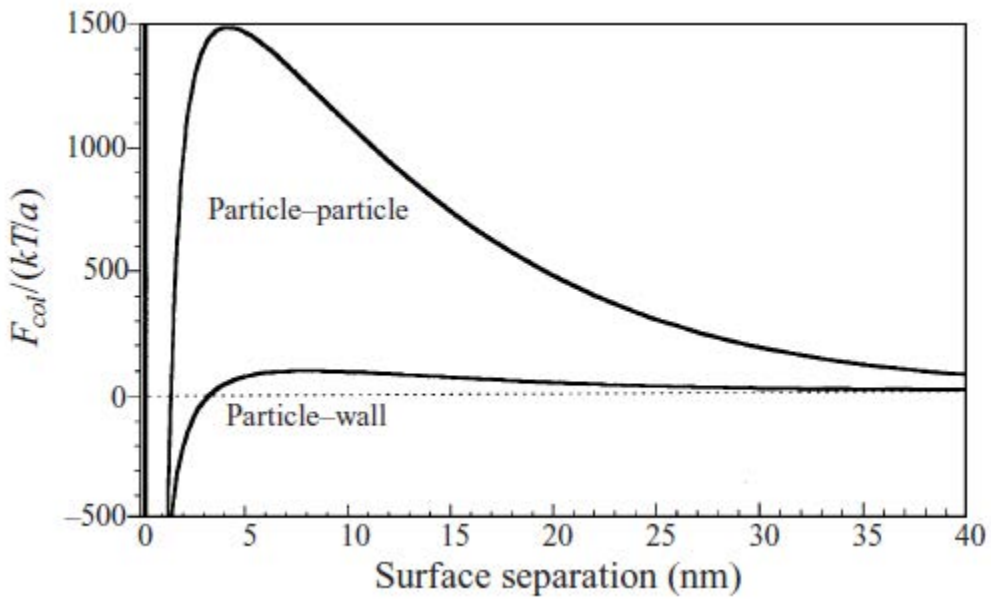

Figure 13 : Comparison of interaction forces between two colloidal particles and between a particle and the channel's walls with respect to the surface separation. Take from Ramachandran et al. [60]. F_{col} is the sum of the forces of the DLVO theory.

We have defined the colloidal forces that exists between particles and between the particles and the channel walls in a static case. However, in our experiment, the particles are advected through the microchannel. It is therefore necessary to describe the hydrodynamic forces responsible for the particle flow in the channel.

2. Microfluidics: Hydrodynamics in micro-channels

In this section, we will describe the flow of fluid in a microfluidic channel. We will define the relevant dimensionless number characterising the flow in such channel. We will then see how this flow transports such particles. Finally, we will see how the hydrodynamics can bring the particles close enough to the channel walls to experience colloidal interaction with the channel surfaces and possibly deposit.

a. Flow in channel of rectangular cross section at low Reynolds number

In a hydrodynamic flow, two modes of momentum's transport coexist: advection and convection. Depending on the flow's characteristics, both modes are not of the same order of magnitude. The comparison of those two quantities gives rise to a dimensionless parameter called ***Reynolds number***:

$$Re = \frac{Ul}{\nu} \qquad (1)$$

where l is the characteristic length of the flow, U is the characteristic velocity and ν is the kinematic viscosity of the fluid.

Because of the micron size of the channels and the low-pressure regime with which we are working, we will only consider flows at low Reynolds number. Typically, the width of the channel is about ten microns and the velocity of the fluid is of the order of centimetres per seconds. Thus, for a flow of water ($\nu = 1.005 \times 10^{-6} m^2.s^{-1}$at 20°C), the Reynolds number does not exceed 10^{-1}.

The ***Stokes equation*** governs the flow of a Newtonian fluid[2] at low Reynolds number:

$$\rho F_i - \frac{\partial p}{\partial x_i} + \mu \frac{\partial^2 u_i}{\partial x_j^2} = 0$$

where u_i is the velocity component along the i direction, p is the pressure, μ is the viscosity[3] of the fluid, ρ is the density of the fluid and F_i is the external forces component along the i direction.

Because of the way they are made (cf. Chapter II -C Micro-fabrication – soft lithography) micro-channels usually have a rectangular cross section as shown on Figure 14.

[2] Newtonian fluid: fluid which viscosity does not depends on the constraints applied.
[3] The viscosity μ and the kinematic viscosity ν are linked by the relation : $\nu = \rho/\mu$

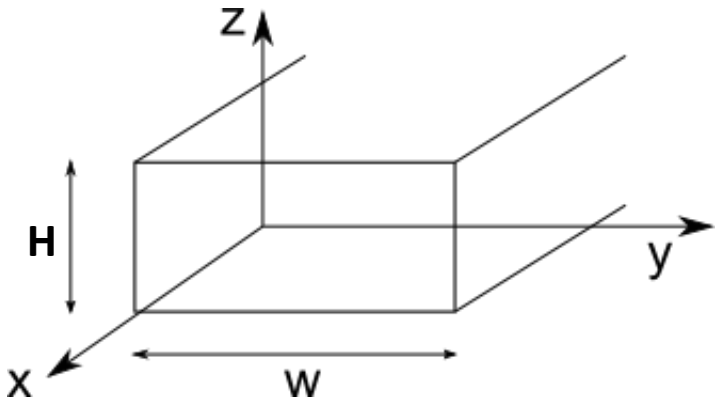

Figure 14 : Cross section of channel with aspect ratio W/H.

Solving the Stokes equation for this geometry gives the following expression for the fluid velocity field inside the channel:

$$u(y,z) = \frac{4\Delta P}{\mu W L}\sum_{n=1}^{\infty}\frac{(-1)^{n+1}}{\beta_n^3}\left[1-\frac{\operatorname{csch}(\beta_n z)}{\operatorname{csch}\left(\beta_n \frac{b}{2}\right)}\right]\cos(\beta_n y)$$

where $\beta = (2n-1)\frac{\pi}{W}$ and csch is the hyperbolic cosecant.

The volumetric flux through the cross section is defined as:

$$Q = \int_{-W/2}^{W/2}\int_{-H/2}^{H/2} u(y,z)\,dy\,dz$$

which leads to:

$$Q = C\frac{\Delta P H^3 W}{\mu L}$$

where C is the friction coefficient that link the flux to pressure drop ΔP with respect to the aspect ratio $\chi = \frac{W}{H}$. For a square section channel ($\chi = 1$) C=4x10^{-2} and find its asymptotic value of 1/12 corresponding to a plane Poiseuille flow.

b. Hydrodynamic resistance of the channel

Flow through micro-channels at low Reynolds number exhibits analogy with electrical circuits. In this analogy, the pressure corresponds to the tension and the flux is the current intensity. This analogy leads to an Ohm's law for flow in micro-channels expressed as:

$$\Delta P = RQ$$

where ΔP is the pressure drop along the channel and Q is the flux through the channel. This relation introduces a hydrodynamic resistance R for the channel. To define this resistance, one need to solve the Stokes equation for a flow in a rectangular channel of section:

$$R = \frac{\nu L}{C(\chi) H^3 W}$$

The hydrodynamic resistance depends linearly with the length of the channel but mainly depends on its section. Reduction of the channel width increases dramatically the hydrodynamic resistance.

The analogy with electrical circuits does not limit itself to the Ohm's law. It can be shown that as in electrical circuits, the Kirchhoff's law applies. This property is appreciable when it comes to complicated networks. For example, by placing channels in parallel, the same flux can be achieve in every channels by setting the pressure drop.

c. *Particle transport in micro-channels*

Every object moving in a liquid undergoes a viscous friction from the fluid flow, called the hydrodynamic ***drag force***. It can be found for low Reynolds flow from the Stokes equation that for an isolated particle the drag force, F_D, is:

$$F_D = 6\pi\mu a U \qquad (2)$$

This remains true as long as the particle displacement is small compared to the inter-particle separation (i.e. small displacements or low particle concentration). Close to a wall, this friction force is strengthened [61].

As for the fluid, we can estimate the relative contribution of the viscous force. The Reynolds Number, Re, associated to the colloidal particle is then:

$$Re = \frac{\rho_f a U_p}{\mu}$$

where U_p is the particle velocity.

Colloidal particles because of their small size also experience a stochastic diffusion due to random collision of fluid molecules, the so-called ***Brownian motion***. The mean square displacement, $\langle x^2(t) \rangle$, of a colloidal particle due to Brownian diffusion over time is then:

$$\frac{1}{2}\langle x^2(t) \rangle = \frac{K_B T}{6\pi a \mu} t$$

where $K_B T / 6\pi a \mu$ is the diffusion coefficient associated with this motion.

The respective contribution of diffusion and advection is measured making the ratio between the energy due to the motion of the particle inside the fluid and the average thermal agitation ($K_B T$). This ratio defines a dimensionless number called ***Peclet number,*** Pe:

$$Pe = \frac{6\pi a\, \mu W\, U}{K_B T}$$

where W is the width of the channel inside which the particle is moving at speed U.

For low Pe, Pe<<1, the motion of the particle is dominated by the Brownian motion and particles will be able to move around their streamlines. On the other hand, for Pe>>1, particles are fully advected by the fluid. In this manuscript we always use density matched colloidal solutions. Therefore, the particles do not sediment during the experiments. The particle Reynolds number is similar to the flow Reynolds number as the particle and pore size are comparable. We have neglected inertial effects that would make the particles depart from the fluid streamlines when those ones start to be highly curved, close to the pore entrance or close to another particle that is stuck on the pore surface. Those inertial effects are quantified by the Stokes number, St, which is the ratio of the particle viscous relaxation time to a typical time scale related to the flow within the pore entrance:

$$St = \frac{2a^2 \rho_p U}{9W\mu}$$

where ρ_p is the density of the particles. For the range of flow, we used the greatest Stokes number lie between 10^{-10} and 10^{-5}.

d. Capture of a particle by a solid surface

The term “particle capture” refers to the physical process by which suspended particles come into contact with a solid surface and adhere to it. In a typical filtration experiment, we define the capture of particles by a single collector, which can be a sphere, or a cylinder, which are respectively the main component of the sand bed and fiber filters. The figure below is a sketch of the particle capture by such a collector. Classically, there are three different mechanisms of particle capture [62] : (i) inertial compaction, when the particle inertia causes deviation from the streamlines and contact with the collector, (ii) diffusional deposition, when Brownian motions help to reach the collector surface; and (iii) direct interception, for particle centers that follow the streamlines and contact is made due to the finite size of the particle. In our case, as the colloidal particles are charged and the suspensions density matched, the relevant capture mode is the direct interception. However, this capture mode has to be refined to take into account the lubrication, the van der Waals force and the double layer repulsion [63]. Indeed, when a particle comes very close to the surface it experiences repulsion due to both the hydrodynamic resistance and electrostatic double layer. This causes the particle to go across streamlines. A detailed description of the equation of the particle trajectories when the

collector size is much bigger than the particle diameter has been provided by Spielmann [63]. Up to now, this calculation has not been refined to take into account the curvature of the collector, which modifies the hydrodynamics and the van der Waals forces.

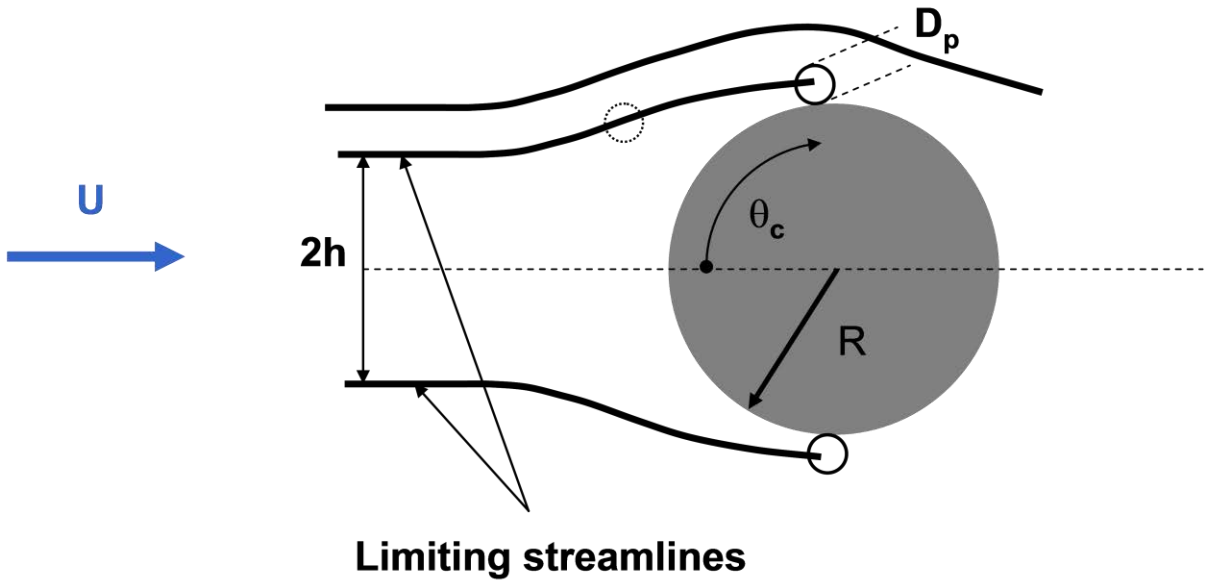

Figure 15: Capture of a particle in the interception mode. All the particles centres which lie in between the two limiting streamlines are captured by the collector (full grey circle). Outside of this zone, particles are not captured. The scheme is purposely not at the scale.

B. Imaging and image analysis tools

1. Microscopy of colloidal particles

a. Optical microscopy

In this section, we will present briefly the conventional optical microscope, essential to image objects within micrometre range, used in both bright field and fluorescence imaging, and its limitations, which leads to the need of confocal microscopy.

i. Bright field microscopy

Bright field microscopy is the conventional optical microscopy. Specimen is illuminated with white light coming from a halogen lamp (or LED) focused through a condenser lens onto the sample. The differences of absorbance by the sample creates the contrast in the resulting image, thus the quality of illumination dictates the quality of the images obtained. The optimal configuration for the microscope is called Köhler illumination, it guarantees sharp images and uniform illumination, information on how to achieve Köhler illumination can be found in [64]. Figure 16 shows the ray paths through the microscope. The objective produces a magnified image of the sample at infinity and the eyepiece further magnifies it and creates an image on to the imaging device (camera, or user's eye). This set-up assumes that the tube length of the microscope (i.e. the objective eyepiece distance) is fixed and chosen for the couple objective-eyepiece. In fact, a third lens, called the tube lens, is added between those two lenses to decouple the eyepiece and the objective (infinity-corrected microscope), thus the axial position of the objective becomes unimportant and moving only the objective allows focusing.

The diffraction and refraction determine the resolving power of a microscope. Refraction occurs at the interface between the medium surrounding the objective (air, water or oil for immersion objective) and the coverslip (glass). According to Snell-Descartes's law, a difference in refractive indices as $n_{\text{medium}} < n_{\text{glass}}$, results in a deflection of the out coming ray and thus in less light entering the objective lens. The cone of light entering the objective defines the numerical aperture (NA) of an objective as:

$$NA = n \times \sin(\theta)$$

where $\boldsymbol{n}$ is the immersion medium refractive index and $\boldsymbol{\theta}$ the angle of the cone of light. The numerical aperture can be highly enhanced by use of oil immersion objective.

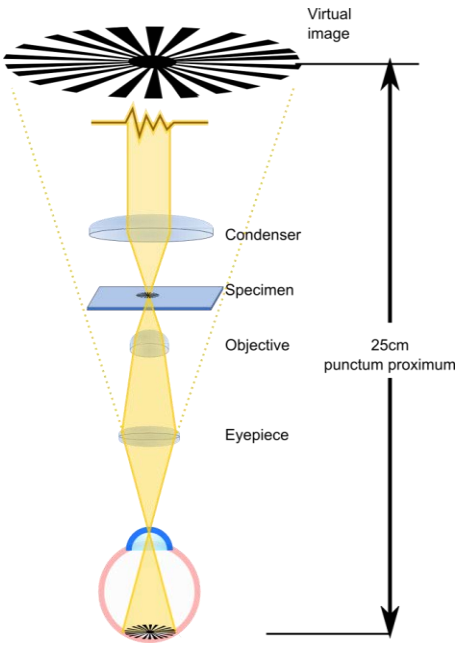

Figure 16 : Diagram of conventional optical microscope imaging process. A magnify virtual image of the specimen is created by the optics combination at a distance corresponding to the punctum proximum of the observer eye.

The use of immersion oil matching the refractive index of the glass reduces the refraction and thus enlarges the NA. Diffraction also limits the resolving power of the microscope. Fraunhofer diffraction tells us that the image of a single point by the microscope projection on the focal plane (PSF) is the Airy pattern as shown in Figure 17-A&B and is a function of the form:

$$\text{Intensity} \propto \left(\frac{2\mathrm{J}_1(r)}{r}\right)^2$$

Where r is the radial coordinate in the focal plane and $\mathrm{J}_1(r)$ is the first order Bessel function of the first kind.

The intensity distribution of two points closed together is the superposition of their two PSF[4] (Figure 17-C and D), for those two points to be resolved by the microscope they need to be sufficiently far apart as shown in Figure 17-D. The Rayleigh criterion states that the two points can be resolved if their maxima are at a distance larger than twice the position of the first minimum of the PSF. For lateral resolution r, this can be expressed as:

$$\mathrm{r} = \frac{0.616\lambda}{\mathrm{NA}}$$

where λ is the wavelength of the illuminating light.

[4] PSF: point spread function

We can extend this criterion in the axial direction to define the axial resolution:

$$r \propto \frac{n\lambda}{NA^2}$$

Note that the axial resolution is lower than the lateral resolution. Taking into account that thicker the sample the more it absorbs and lower is the resolution, imaging in the sample's volume is difficult to achieve in bright field microscopy. The image of a colloidal particle given by the microscope is the convolution of the sphere response to illumination light (or emission for fluorescent particles) with the microscope's PSF, the resulting pattern is called the sphere spread function (SSF) as defined by Jenkins and Egelhaaf [65].

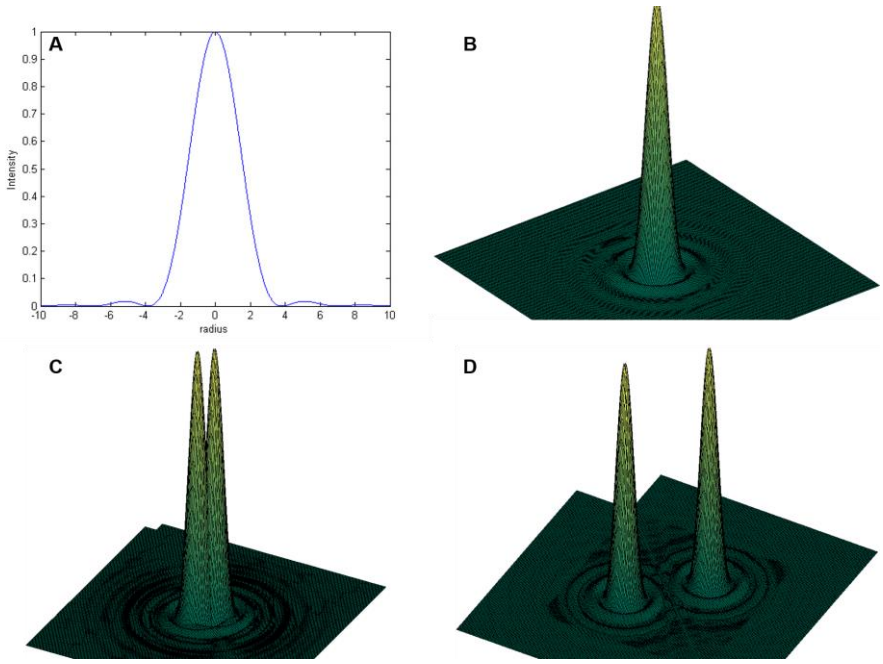

Figure 17 : A- Normalized Intensity of the Airy pattern across a diametrical section. B- Airy pattern of a single point. C- Diffraction patterns of two points not resolved by the imaging system according to Rayleigh criterion. D- Diffraction patterns of two points resolved by the imaging system.

Bright field microscopy allows to image colloids in microchannel. In such images, the contrast originates from the differences in light absorption of the different media. However, in the systems we are using, all components are transparent to optical light, resulting in poor image contrast. One way to enhanced the image contrast is to use fluorescently dyed particles and to image them using fluorescence microscopy.

ii. Fluorescence microscopy

We can achieve high improvements in image contrast using the fluorescence of the sample. A specimen intrinsically fluorescent or targeted tagged with a fluorophore can be imaged using its own emission. Fluorescence results from the absorption of radiation at a specific wavelength by the

fluorophore that becomes excited and returns to its original state by emitting light at a larger wavelength after losing part of its energy through non radiative vibrational relaxation as shown on Figure 18-B. We illuminate the sample with a collimated light, filtered at the wavelength absorbed by the fluorophore. A dichroic mirror, selected for those specific wavelengths, splits the emitted light from the illumination light. The dichroic mirror is designed to reflect any wavelength shorter than a threshold value and to transmit longer wavelength. The dichroic mirror transmits all wavelengths larger than its threshold value; therefore, the emission filter must filter emitted light from any residual light. Principle diagram of fluorescence microscopy is shown on Figure 18-A. Despite its ability to collect only the light coming from the labelled object, fluorescence microscopy collects light coming from the whole volume illuminated in the sample, therefore, the contribution coming from the out-of-focus planes increases the noise in the sample's image. To suppress light coming from those out-of-focus planes a further improvement is required, that is confocal microscopy.

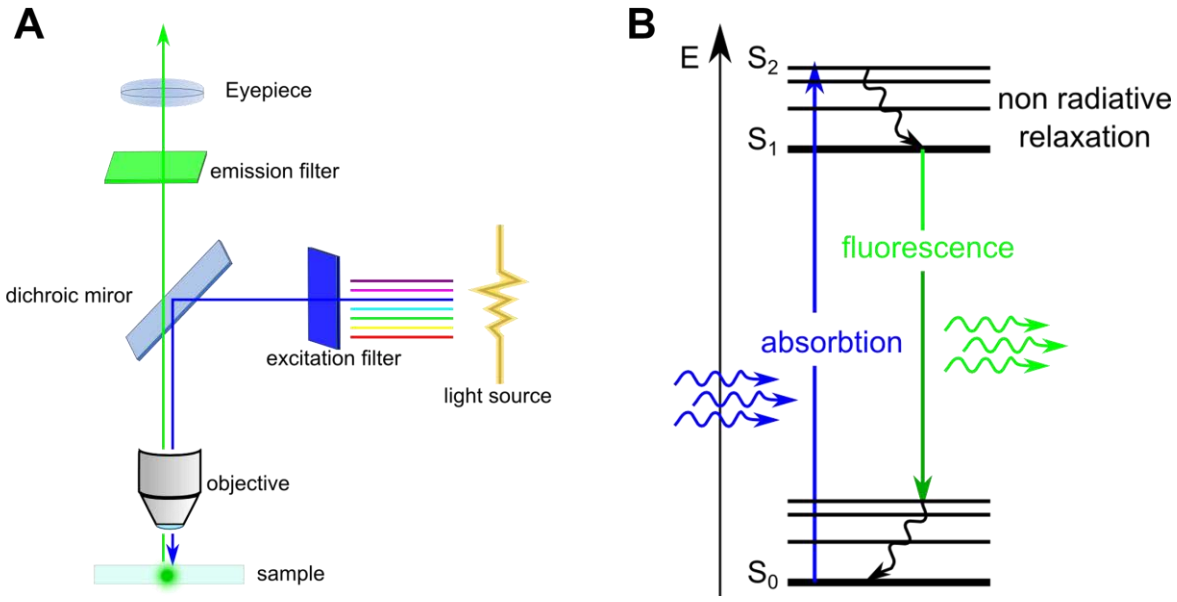

Figure 18 : A- Diagram of fluorescence microscope. B- Diagram of the fluorescence process

Fluorescence microscopy allows then a huge improvement in image contrast, as particles emitting fluorescence are bright objects on a dark background. However, this type of microscopy does not provide improvement on the image resolution and does not allow precise imaging of colloids in volume. Both improvement requires the use of confocal microscopy.

b. Confocal microscopy

iii. Laser scanning confocal microscope

Described for the first time by Minsky in 1957 [66], confocal microscopy is nowadays a well-established tool for studying colloidal particles. It was designed as an improvement of conventional

fluorescence microscope where the illumination where restricted to a small volume in the sample by using a pinhole in front of the illumination lamp, then the sample was imaged point by point by a detector with a pinhole in front and moving the sample. The pinhole in front of the detector turns it into a point-like detector and is placed on the conjugate focal plane (hence confocal) of the illumination volume allowing to suppress light coming from out-of-focus planes as shown on Figure 19. We call ***Optical sectioning*** this ability to reject out-of-focus light that allows us to image within bulk sample with a good axial resolution.

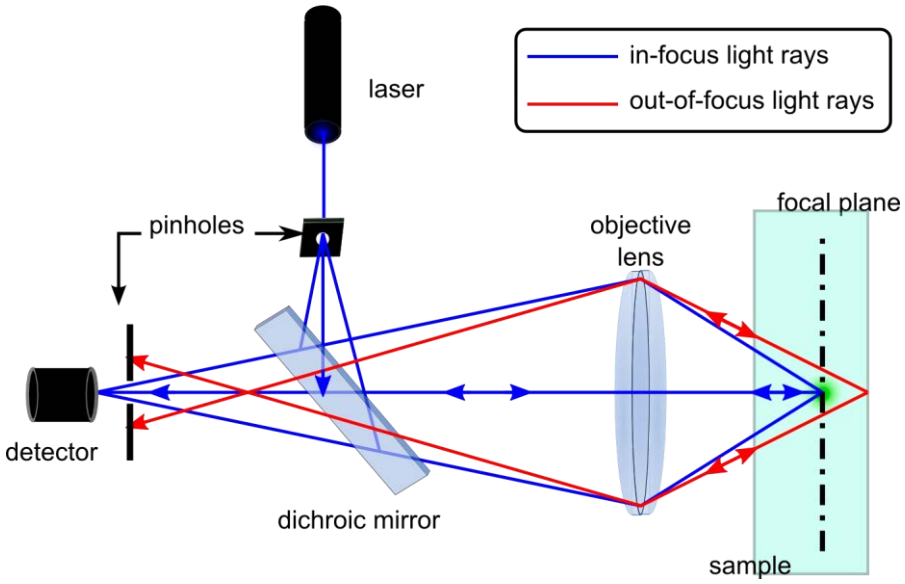

Figure 19 : Schematic light path through a confocal microscope illustrating the out-of-focus light rejection.

Now, the use of laser as light source and high numerical aperture objectives significantly increases small volume illumination. Mapping of the sample is also easier and faster thanks to scanning mirrors, which allows imaging of plane up to a frequency of 8 kHz for resonant galvanometer scanning mirrors. Those improvements give to the modern confocal microscope the name of Laser Scanning Confocal Microscope (LSCM). Diagram of a LCSM is shown on Figure 20; laser light shines through a pinhole (confocal aperture) and then a dichroic mirror bounces it toward a pair of scanning mirrors (scanning X and Y direction respectively) to be finally focused into the sample by a high numerical aperture objective. Emitted light from the sample travels through the same path but is not reflected by the dichroic mirror (see § Chapter II -B.1.ii Fluorescence microscopy), and is filtered by the pinhole in front of detector. Detectors are usually photomultiplier tubes (PMT).

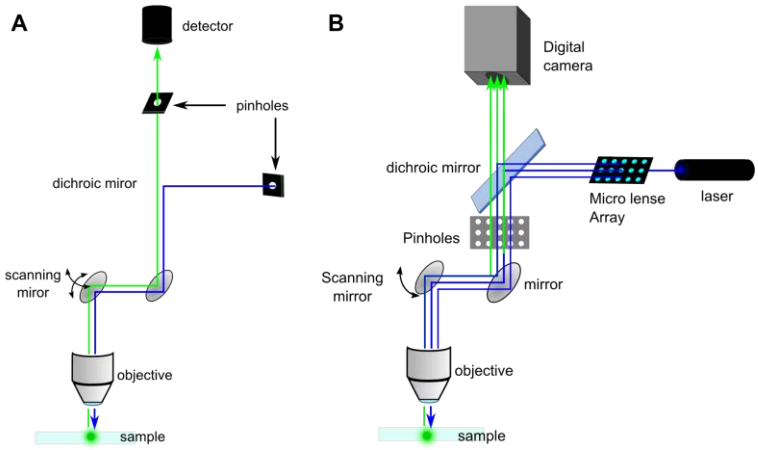

Figure 20 : A-Diagram of a Laser Scanning Confocal Microscope (LSCM). The illuminating light from the laser is shown in blue and emitted light coming from the sample in green. B- Diagram of the multi-array scanning microscope "VT-infinity"

LSCM provides improvements on the lateral resolution and allows to image separately different planes in the sample volume. However, the point-by-point acquisition and the scanning of each planes imply a large acquisition time to form an image of the sample in 3 dimensions. With this technology, imaging our microchannel can take up to 3 min. This imaging system provides the best resolution but it is not well suited for studying fast evolving phenomenon over time. To achieve high-speed imaging without compromising too much the resolution we used an array scanning confocal microscope.

iv. Array scanning microscope: VT-Infinity

One can achieve high-speed confocal imaging by several ways. The most common is the use of resonant scanning confocal microscope. It is a regular point scanning confocal where the scanning mirrors are replaced by resonant scanning mirrors, achieving thus a scanning of 30 frames per seconds (fps) at standard PMT full resolution (512x512 pixels) and up to ~400 frames per seconds on a cropped area (152x32 pixels). Even though it is way faster than the maximum frame rate of 4 fps achieved in full frame with a standard point scanning confocal it is still far from the nowadays standards for "high-speed" imaging (e.g. 12,500 fps at 1024x1024 for the Photron fastcam sa-x2). To get faster imaging the others alternatives systems get rid of the PMT to capture light with digital cameras (usually CMOS or EMCCD) with the best ratio imaging speed / sensibility and scan multiple points at the same time. The oldest technology is the spinning disk confocal microscope. The multiple scanning point are achieved from a single laser beam split by a series of micro-lenses on the surface of a first disk and then passing through a series of pinhole on a second disk (Nipkow Disk) and sent onto the sample. Emission is then descanned through the Nipkow disk and recorded by the digital camera. An alternative to the spinning disk consists of using the same principle of coupling a micro-lenses array with an array of pinholes, but instead of scanning the sample using a spinning disk,

scanning is made by a conventional scanning galvanometer mirror. It is the technology used in the Visitech's VT-Infinity confocal unit (illustrated on Figure 20-B). The use of galvanometer mirror to scan and descan through the pinhole is less restrictive in term of alignment than the two spinning disks and allow a wider use of pinhole sizes. It is thus more flexible. With this system, we are able to image a microchannel in less than 2s, which is a huge improvement over the LSCM (~90 times faster). However, this improvement comes with a prize. With this system, the physical size of the camera pixels determines the resolution. To get the best resolution/sensibility/speed we used a Hamamatsu Orca flash 4.0 black and white camera.

We have presented the different image acquisition techniques that we will be using throughout this work. It is important to get the best images out the experiment to ensure the best conditions for image analysis latter on. The main image analysis process we will be using is the precise location of the particle in the images. Precise location can only be achieve on fluorescence or confocal images where the particles are clearly identifiable on the image (bright object on a dark background). In the latter section, we will present the steps of image analysis leading to this precise location.

2. Image processing: finding particles coordinates

Locating precisely the particles in an image or within a stack of images- is of central interest for our work. To achieve a reliable identification of the particles we used the algorithm developed by Crocker and Grier [67]. This algorithm uses the fact that particles are spheres to find their centroid coordinates by identifying the local maxima in the intensity profile of each particle. We will describe this method applied firstly to a 2 dimensional image and then generalized to a 3 dimensional confocal stack of images.

a. Finding particles in 2 dimensions

Calculation of the image of a spherical colloid (i.e. its intensity profile) given by fluorescence microscopy or confocal microscope is still a real theoretical challenge, but it can be roughly thought as a Gaussian surface of revolution as suggested by Crocker and Grier [67]. Thus, we will assume that the ideal image of a particle is a Gaussian blob. The real image obtained with a microscope is naturally not this ideal image; it suffers from inherent noise and distortions coming from the optics of the microscope and mainly from the camera. The first step to identify particles centre is thus to restore the "ideal" state of the image.

i. Image filtering

A typical confocal image, as shown in Figure 21-A, exhibits some noise and its corresponding intensity profile (Figure 21-B) deviates then from the ideal Gaussian shape.

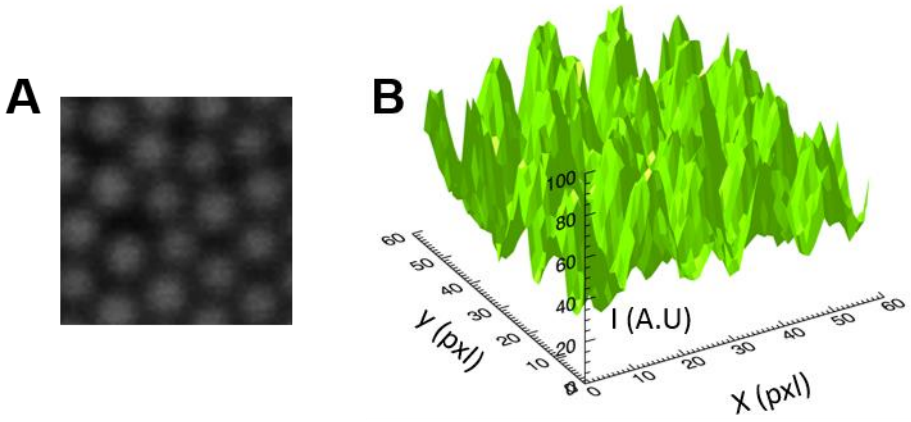

Figure 21 : A- "Real" image of spherical colloids from confocal microscope. B- Intensity surface plot of the image in (a).

Applying a spatial band-pass filter smooth the image and subtracts background off. Uneven illumination and non-uniformity among camera's pixel often causes contrast gradients in the image and long wavelength modulation in the background brightness. For typical colloidal images, where the features are small and well separated, the background can be determined simply by averaging intensity over a region defined as larger than twice the radius of a single sphere but smaller than inter-sphere separation. A background image can be then obtained by a convolution of a boxcar average over the defined region. Short wavelength modulations are due to the noise created by the camera. Such noise is purely random and has a short correlation length of about a pixel. A convolution of the image with a Gaussian surface of revolution of half width 1/2 pixel (Gaussian blurring) allows to get rid of this noise. We apply both convolutions to the images to perform the band-pass filtering. The difference between the noise-reduced and background images giving us an image close to the ideal one. After this filtering, each particle should become a single rounded peak, the local maximum corresponding to the centre of the particle. Figure 22-A shows the effect of the band-pass filtering on the original shown in Figure 21 , and the corresponding intensity profile.

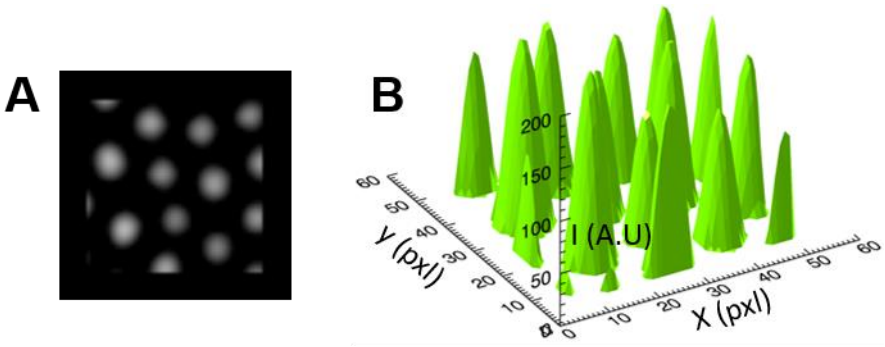

Figure 22 : A- Image shown in Figure 21-A spatially band-passed. B- Corresponding intensity profile.

ii. Features extraction

Once we filtered the image, the next step is to extract from the image the possible particle matches. Assuming that the image of the particle has a maximum intensity at its centre, we identify candidate particle locations as the local brightness maxima within the image. We search the pixels that have no brighter neighbours in a distance corresponding to a particle diameter. This step provides an estimate of particle location with nearest pixel accuracy. Refinement is required to achieve sub-pixel accuracy.

iii. Location estimates discrimination and refining

The features extraction method is slightly too sensitive and especially with dilute sample where you have large areas without particle, it may find local maxima due to residual noise. Therefore, next step is to remove those false matches; fortunately, those false matches are much fainter than the particles. One easy way to remove them is thus to apply a brightness cut-off keeping only the matches with a brightness greater than a threshold value. As shown in Figure 23, one can easily distinguish good matches from noise using the brightness of the found candidate. We clip the found coordinates using a brightness threshold under which the candidate is considered as noise and then removed.

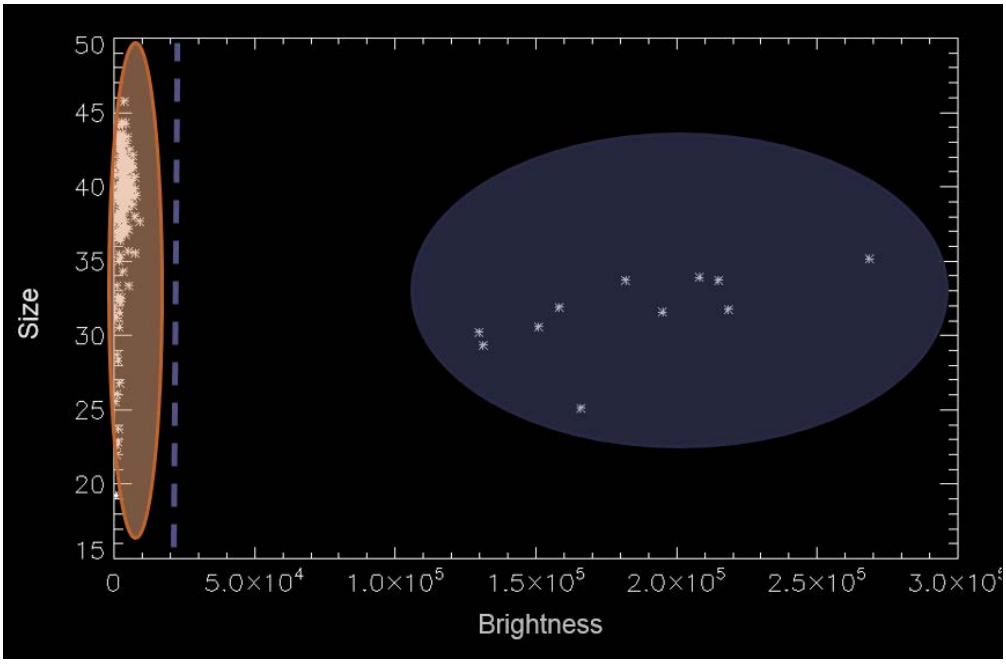

Figure 23 : Plot of size and brightness for identified particles. Good matches are circled in blue, false in orange. Dashed purple line is the clipping threshold.

The step of features extraction provides the position of the particles with pixel resolution. To further increase the precision toward sub-pixel accuracy, a refinement is necessary. To do so we need to rely on the a priori knowledge of the shape of the particles on the image. Imaging of spherical colloids does not affect the spherical symmetry of the particle. We can thus use this symmetry to refine the

position of the particle using a brightness-weighted centroid. Identifying the centre of mass of the intensity profile of the pixel surrounding the possible centre results in a precision in location around 30-40nm.

b. Finding particles in 3 dimensions

We can retrieve three dimensions coordinates in a confocal z-stack. Z-stack consists of imaging the sample at different focuses. Figure 24 illustrates a typical z-stack where images where taken by changing the height of the sample with a piezo z-stage by 0.5 µm between each image.

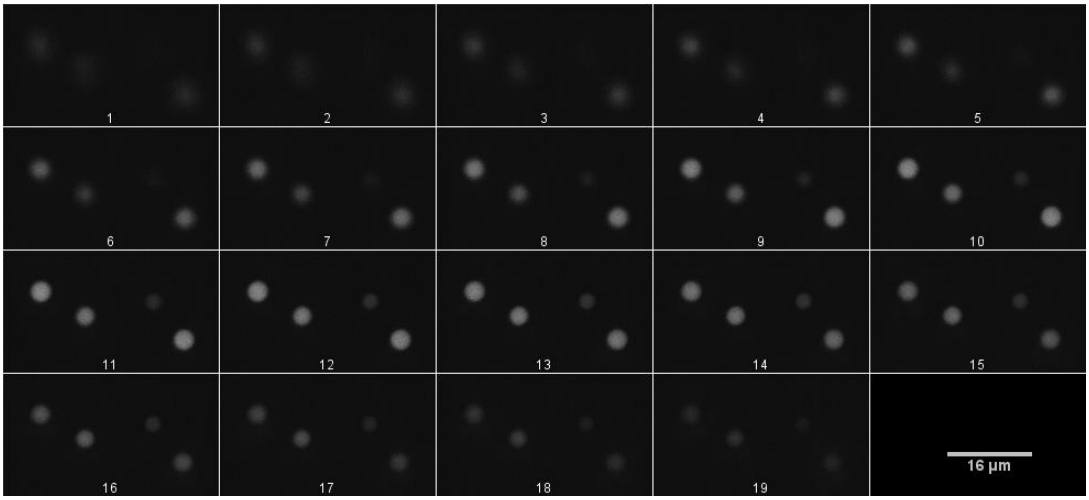

Figure 24 : Confocal z-stack of 4µm colloids (Δz=0.5 µm between 2 images).

iv. Extension of the 2d features extraction to 3d

On each of the image constituting the z-stack, we perform the 2d tracking algorithm and while looping over the particles we calculate centroid refinements, moments m_0 and m_2 of each candidate image's brightness, in a circular region of radius w as follow:

$$m_0 = \sum_{i^2+j^2 \le w^2} I(x+i, y+j)$$

and

$$m_2 = \frac{1}{m_0} \sum_{i^2+j^2 \le w^2} (i^2+j^2) I(x+i, y+j)$$

where (x, y) are the coordinates of the centroid.

In a given frame of the z-stack, particles form a roughly elliptical cluster in the (m_0, m_2) plane. For each particle, we collect the probability distribution $P(z_i | m_0, m_2)$ for it to be within dz of z_i given its

moments m_0 and m_2. Summing this probability function for each frame in the z-stack allows estimating the particle's vertical position. This method finds the z coordinate of the particle with an error 10 times larger than the location in the x-y plane. Figure 25 illustrates the centre location of one of the particles in the z-stack shown in Figure 24.

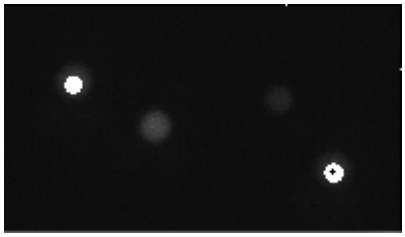

Figure 25: Centre location in a z-stack. The overlaid white circle indicate the proximity of the particle centre in the z-direction and the black dot, that the centre is located in this z plane.

v. Refining: the Sphere Spread Function (SSF)

Centroid refinement is the most widely used refinement technique for particle location estimation. However, even though it is successful in most scenarios, the precision of particle centre location is not always the best. In particular, with particles whose size is close to the resolution of the imaging apparatus (i.e. like colloids) the image centroid does not necessarily overlap with the particle centre. It is particularly true when particles are close together so that their spread functions overlap. In this work, we will look at particles within a clog that are touching each other. Then we need to use another refinement method to overcome issues in the centroid method. We choose SSF refinement method developed by Jenkins [65].

As the centroid method, the SSF refinement relies on a priori knowledge the SSF (see § Chapter II - B.1.i). When imaging immobile or slowly moving particle (which is our case) we can reconstruct an experimental SSF by averaging over the image of each particles. A typical SSF reconstruction is shown on Figure 26. This experimental SSF allows accounting properly for experiment dependant imperfections as index mismatch for example.

After determination of the experimental SSF, we can refine the particle location by searching the location that matches best the SSF within a window around the found position. We compare every pixel value in the SSF to every value in the image window to form a chi-square hypersurface. This χ^2 presents a minimum at the particle's location that can be find with sub-pixel accuracy by determining the minimum in the three directions and interpolating for a large number of point lying within half a pixel around the minimum of χ^2.

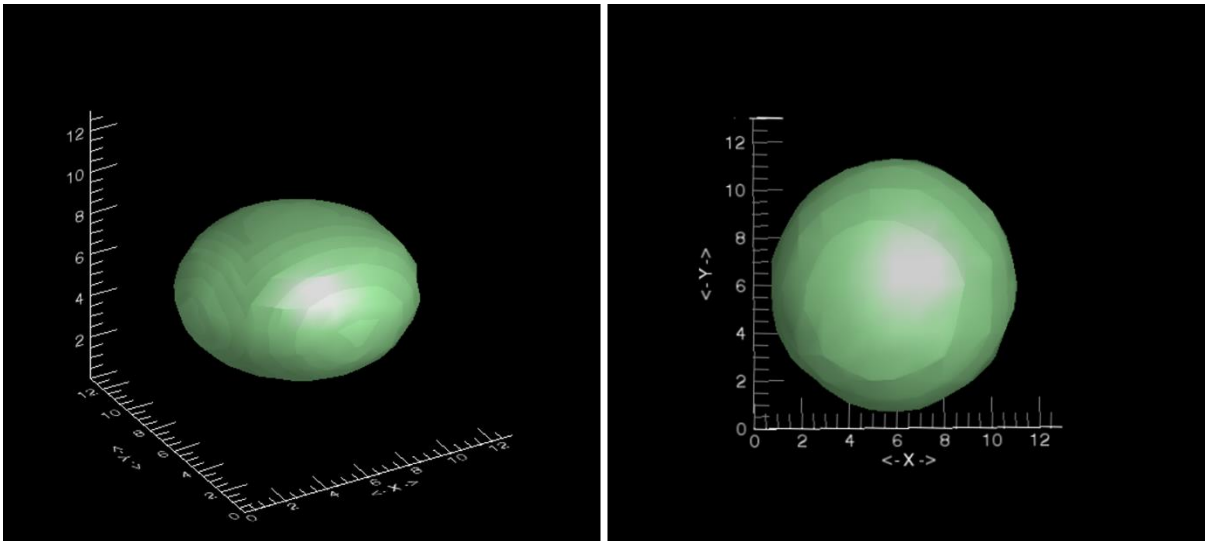

Figure 26: Experimental 3D SSF reconstructed from confocal imaging of 1.1µm PMMA particles (units in pixels).

This image analysis technique allows precise location of the particle in the image. We can extend it to track the particle trajectories over time. However, this method requires many images acquired at high speed. Over an experiment lasting typically 30min and with about 10^6-10^8 particles flowing through the channel over this time, this method can be heavy in terms of computational time. We thus used this method to locate immobile particles (captured in the channel). To follow particle trajectories in the channel we used a more efficient technique in term of computational time, the particle streak method.

3. Particle Streak Velocimetry

Particle streak velocimetry is one of the oldest image based velocimetry. It was introduced by Fage and Townend in 1932 [68]. Key idea of the streak velocimetry is the imaging of moving particles over a large exposure time resulting in the imaging of the motion blur of the particle. Thus, it can give information of the mean velocity along the path visible during the exposure time. Introduction of digital imaging enhanced this method by allowing quantitative measurement of the intensity recorded. Therefore, one can code temporal information along the path by changing the intensity of illumination during exposure [69].

a. Measurement set-up

The setup used to record streak particle trajectories is built up using a fluorescence microscope. A LED, which allows a high frequent intensity modulation, provides fluorescence illumination. We use a blue LED (Thorlabs) emitting at 470 nm modulated using a DC2100 high-power LED Driver (Thorlabs) allowing frequency modulation up to 100 kHz. Strike patterns are recorded with the Orca Flash 4.0 sCMOS camera (Hamamatsu) over an exposure time of 200 ms. The intensity variation frequency is chosen to ensure that at least 5 modulations during the travel of the particle throughout

the channel. We performed image processing and analysis in Matlab using the image processing toolbox.

b. Feature extraction

i. Segmentation

The first step in this analysis process is to identify streaks in the image. Fluorescence images provides an ideal framework for streak image processing as the signal to noise ratio is of the order of 50 with correct illumination. Extraction of particles from background is therefore quite straightforward. We convert the grayscale image to a binary image using the right threshold and identify connected components in the binary image as features. The second step is to identify the streak among those features. There are two kinds of features found by our process: streaks and immobile particles (particles deposited in the channel). Figure 27 shows those two features, features in Region of Interest (ROI) A (yellow) are strikes and those in ROI B (green) are deposited particles. We can separated those two kinds of features using their shapes and brightness. Immobile particles are circular and the brightest features whereas streaks are elongated and fainter than immobile particle. Comparing the total brightness and the eccentricity[5] of the features allows to identifying without ambiguity the streaks. The segmentation process provides us a bounding box enclosing the identified streaks and the orientation of the main axis of the streak. We will use it to define the region of the image where we will fit the streak to find its centreline.

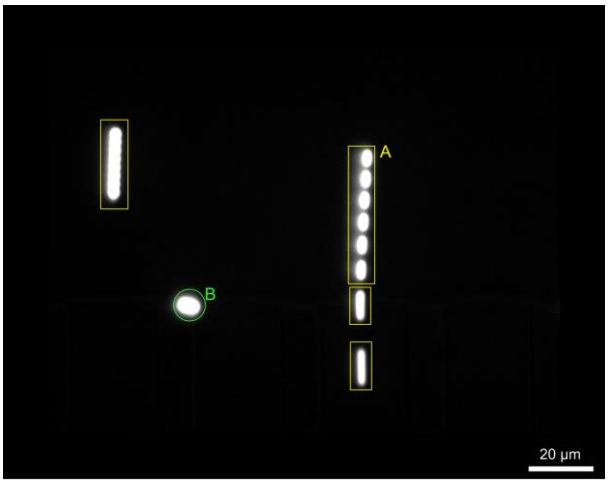

Figure 27 : Typical frame from streak experiment. ROIs: A - Strike features; B - Deposited particles.

[5] Eccentricity is the ratio of the minor axis length and the major axis length of the ellipse fitting the object. An ellipse whose eccentricity is 0 is actually a circle, while an ellipse whose eccentricity is 1 is a line segment.

ii. Iterative centreline extraction

In this step, we use the region of the image containing the streak to analyse, to extract the centreline with sub-pixel accuracy. This region is shown as the yellow box on Figure 28-A. It performs a Gaussian fit of the strike signal from a cross sectional line, denoted as B in Figure 28-A with elements $B_i, i = 1 \dots N$, using a non-linear Levenberg-Marquard fit. We use an offset Gaussian-bell-curve as model:

$$g(x) = S + A * \exp\left(-\frac{(x-\mu)^2}{2\sigma^2}\right)$$

where S is the offset, A is the amplitude, σ is the width and μ is the maximum of the Gaussian bell.

Initial guess (tilde variables) for those parameters is:

- $\tilde{S} = \min(B_i, \forall i)$
- $\tilde{A} = \max(B_i, \forall i) - \tilde{S}$
- $\tilde{\mu} = \frac{\mathrm{N}}{2}$
- $\tilde{\sigma} = \mathrm{N}/4$

Fit along B is shown on Figure 28-B. We repeat these steps line by line until complete extraction of the strike. Finally, we link the strikes split on different images to one another. The result is a list of sub-pixel precise location of the centreline and intensities associated that allows the trajectory reconstruction (Figure 28-C). The spatial coding of the illumination variation (Figure 28-D) gives us access to the velocity measurements.

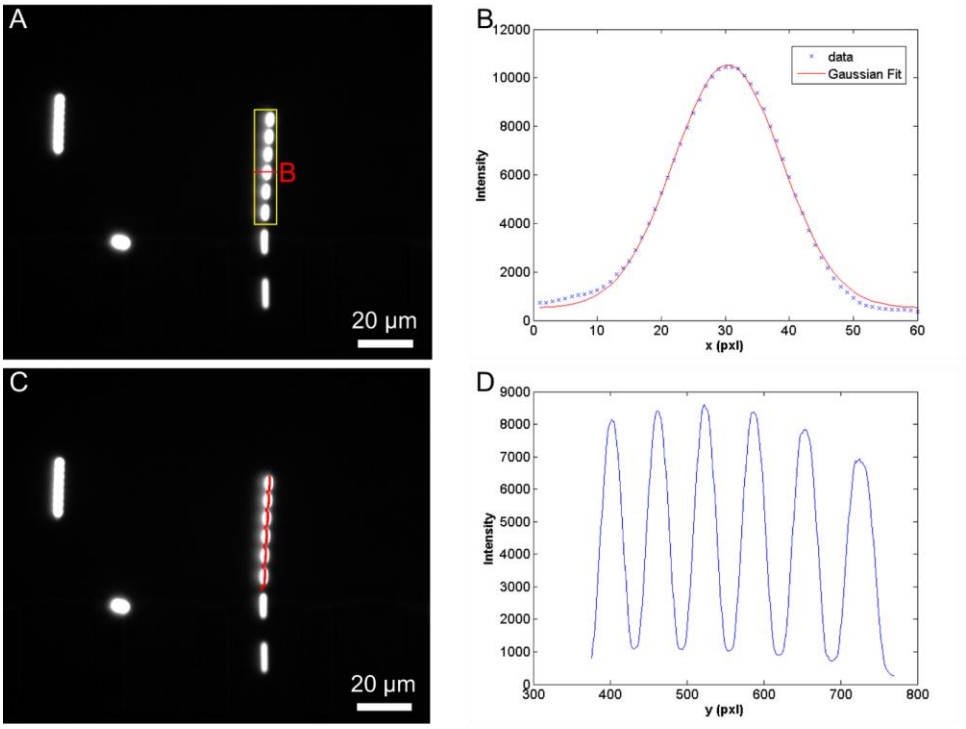

Figure 28 : A - Strike feature identification; B- Gaussian Fit of the signal along red line in A; C - Trajectory reconstruction from Gaussian fit; D - Intensity signal along strike reconstructed in C.

c. *Velocimetry form frequency analysis*

The illumination variation allows the coding of higher temporal frequency than the exposure time along the streak. Lower level velocimetry consists of the extraction of the spatial movement of the particle during one illumination pulse using a square illumination variation. This results in an evaluation of the mean velocity along this part of the trajectories. We extract this information from the intensity variation along the path (Figure 28-D). Figure 29 shows a reconstruction of velocity along a trajectory.

Using a sinusoidal variation of the illumination one can extract more precise information about the velocity of the particle, in each point of its trajectory. This can be achieved using a Hilbert Huang Transform [70] based on the correlation between the instantaneous speed in x-y plane and the spatial frequency:

$$v_{x-y}(y) = \alpha \frac{F}{f(y)}$$

where α is the scaling factor (pxl/mm), F is the modulation frequency of the illumination and $f(y)$ is the instantaneous spatial frequency at the centre of the streak at position y.

Figure 29: Velocity reconstruction along a streak trajectory using square pulse illumination

C. Micro-fabrication - soft lithography

Micro-fabrication is the way we generated the microfluidic devices used throughout these thesis. Soft-Lithography method that we used [73] relies on two separate process. Photolithography is the first process in the production of our microfluidic devices. It creates the master used to cast the PDMS device. This master is made from a photoresist (SU8, a photocurable epoxy) cured with UV light through a chrome mask on which the desired motive is printed. This process requires a few steps (Figure 30):

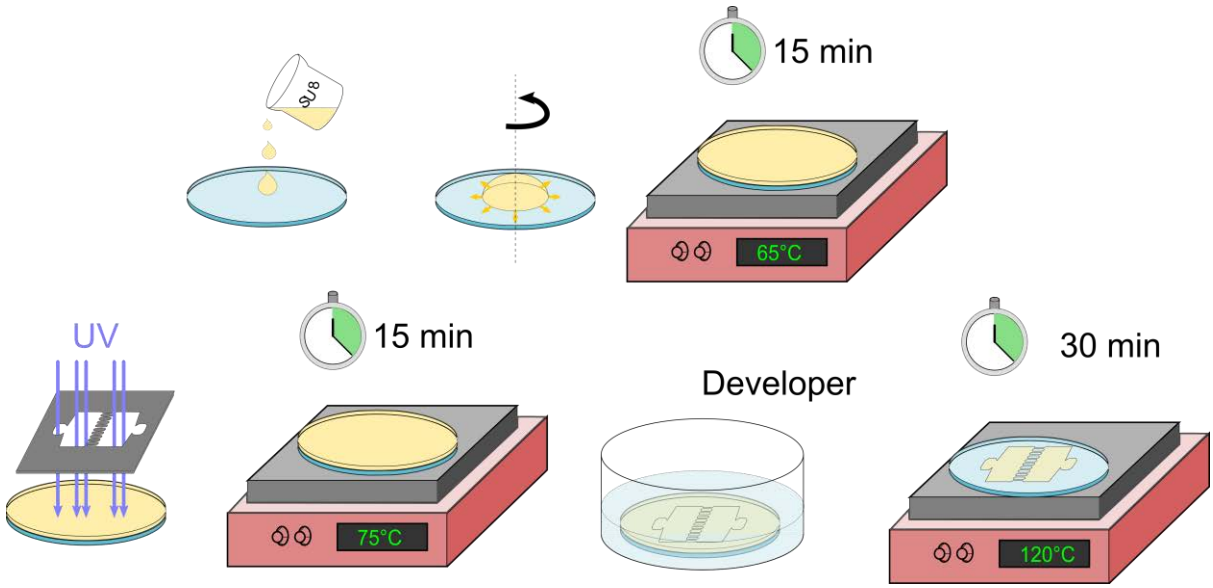

Figure 30 : Schematic illustration of the SU8 soft-lithography process

First, a thin, uniform film of resin is spin-coated on a glass wafer (see Figure 30). The resin is a polymer resin called SU8 (microchem). It exists in different formulations (different viscosity) which allows one to build a uniform film from a few microns thick to a few hundreds. The thickness is determined by the characteristics of the resin given by the manufacturer and the speed of spinning, the fastest spinning and the thinnest is the layer. Typical rotation speeds range from 1000 to 5 000 rpm. To obtain the desired thickness (i.e. the final channels height) we usually span a wide range of rotation speed around the values given by the manufacturer. At the end of the process, we use a mechanical profilometer to measure the real height and only the wafers at the desired height are kept. Then, this uniform layer is baked for 15 min at a temperature increased from 50 °C to 65 °C by 5 °C steps every 5 min. This step is called ***soft baking***; it allows the solvent to evaporate from the resin prior to exposition to the UV.

The next step consists of curing the desired areas of the resist to create our pattern. To do so, we expose the wafer to collimated UV light through the chrome mask with an aligner. The exposure time is crucial; it depends on the resin used and the thickness of the layer. The manufacturer provides an equivalent dose of UV light required for good curing. The correct exposure determines the viability of the process and the verticality of the walls. Indeed, a too short exposure will result in an incomplete curing of the patterns. In the worst scenario, it results in the vanishing of the patterns during the developing. Too much exposure will result in leaking of the UV under the masked areas and therefore in trapezoidal shapes. Figure 31 illustrates the influence of exposure time. To conserve the right geometry and achieve straight walls we need to fine tune the exposure time. To do so, we never process a single wafer, we usually create a batch of 3 to 5 wafers with the same spin coating speed (same height) and vary their individual exposure time around the known optimal value and choose the best one.

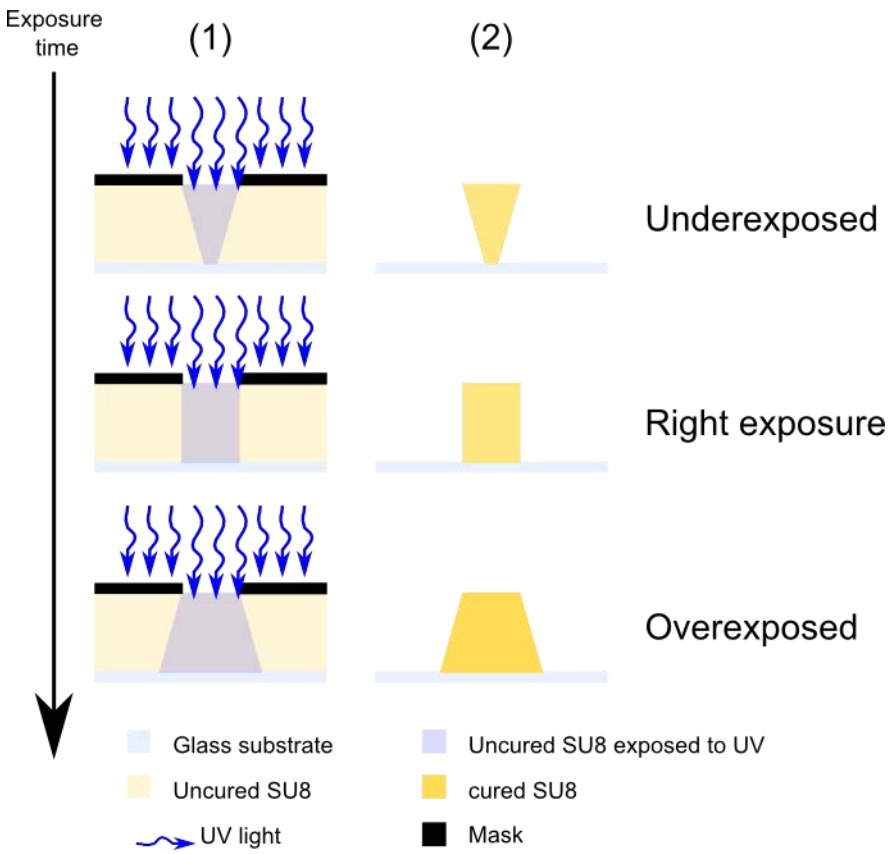

Figure 31: Influence of exposure time in soft lithography. (1) Exposed area for the different exposure times and resulting structures after development (2).

We then baked the wafer once again for 15 min at 75 °C after rising the temperature from 50 °C to 75 °C by 5 °C steps every 2 min. This step is called the ***post-exposure bake*** and reduces the standing wave phenomena caused by interferences of the incoming UV light. We remove then the non-exposed resin using a developer, for SU8 the correct developer is PGMEA (Propylene glycol monomethyl ether acetate). We place the wafer in a bath of developer for about 5 min then rinse it with clear PGMEA and finally rinse it with isopropanol to stop the developing process. We then dry the wafer with clean nitrogen. The final step consist of a final bake, the ***hard bake*** to solidify the remaining resin and make the master more durable. It also reduces the surface cracks. Typically, we hard bake the wafer for 30 min at 120 °C.

The actual microfluidic is made by replicating the SU8 master with an elastomer. PDMS (polydimethylsiloxane) is the most commonly used elastomer for microfluidic devices fabrication. PDMS is a silicone polymer which formula is $\mathrm{Si(CH_3)_2O}$. The mains benefits of PDMS are its ability to conform to the substrate over a large area, its facility to unmould and that it is homogeneous, isotropic and optically transparent over a wide range of wavelengths (300 nm to 2200 nm). The PDMS we used is Sylgard 184 from Dow Corning. It was prepared as a mixture of ratio 1:10 in weight of curing agent, uniformly mixed and degased in a vacuum chamber for 15 min. The PDMS is then

poured over the master wafer in a petri-dish and degased again for another 15 min. We then put the petri-dish in an oven at 65 °C for 1h30 for PDMS to cure. After peeling off we obtain a faithful replica of the SU8 master in PDMS. We punch holes into the PDMS to allow connection of inlet and outlet. Finally, to seal the PDMS device, we use a microscope coverslip coated with a thin layer of PDMS. Irreversible bond between PDMS and coverslip is achieved by exposing both surfaces to oxygen plasma. Under plasma treatment, the repeated units of $–O-Si(CH_3)_2-$ of PDMS develops silanol groups (-OH). For both PDMS and glass, these reactions yield Si-O-Si bonds when brought to formal contact. These covalent bonds form an irreversible seal between the chip and the coverslip. Such seal can withstand up to 3 bars of air pressure. As the silanol groups are polar in nature, they make the exposed surface highly hydrophilic and the exposed parts of the device not bounding remains hydrophilic until after 48 h where recovery take place [74]. We can reduce this recovery time to a day placing the device in the oven at 65 °C and to three hours at 120 °C.

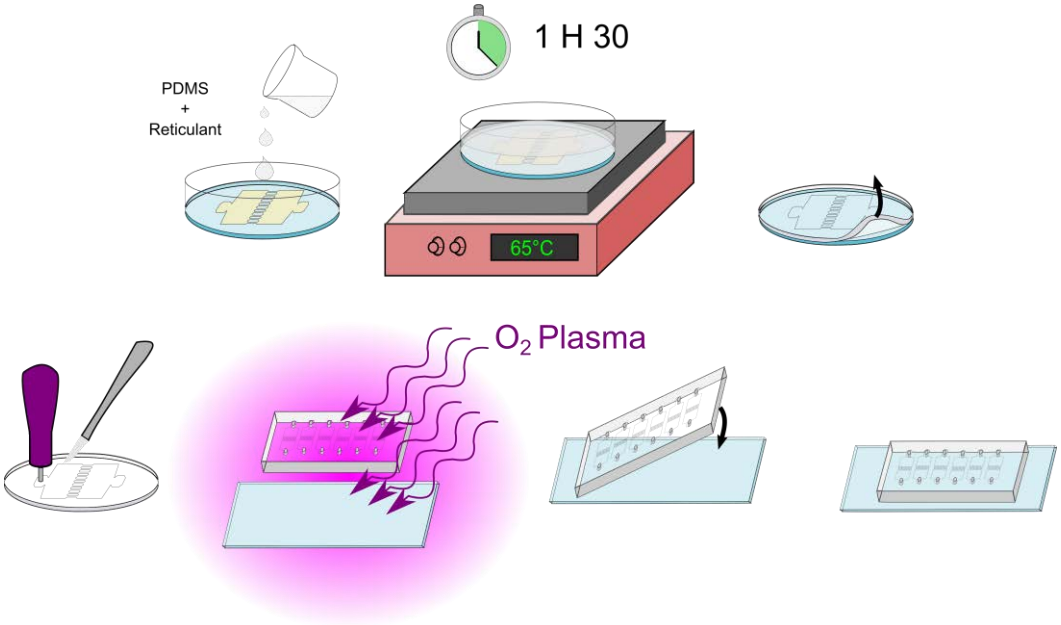

Figure 32 : Schematic illustration of the procedure of PDMS replica moulding.

D. Sample preparation and experimental set-up

a. Sample preparation

We used two sets of colloidal particles in this work. The first set is a set of polystyrene particles (PS) bought from Invitrogen (diameters: 1 to 4, 6 and 10 µm). They are stabilized by surface charges coming from sulphate groups, with in average a surface charge of 3.4 µC/cm² corresponding to a zeta potential of 30-35mV. The second set consists in poly-methyl-acrylate (PMMA) colloids. Those particles where synthetized at the university of Edinburgh by Dr. Andrew B. Schofield. They are synthetized following the method describe in [71]. The PMMA particles are dyed with NBD (4 chloro-

7 nitrobenz-2 oxa-1,3 diazote) which is excited at 488 nm and has a maximum in emission at 525 nm. PVP chains that bear negative charges stabilize them. Their sizes were measured using a granulometer Mastersizer 2000 (diameters: 1.13, 1.43, 1.81, 4.09 µm). Their zeta potential was measured to be 70 mV.

Buoyancy matching is necessary to avoid sedimentation during the experiments. We can achieve it simply by matching the fluid density with the bulk density of the suspended particles. Index matching on the other hand is only required for confocal imaging. Index matching of polystyrene in aqueous solution with perfect buoyancy matching is impossible because polystyrene as a high refractive index (n=1.59) but a small density (1.055 g/cm^3). Therefore we only buoyancy matched the polystyrene solution. We achieve this matching using a water / heavy water (D_2O) mixture with a ratio of 45% and 55% (by weight) respectively. The Hamaker constant for PS particles in water D_2O mixture is $A=1.88\text{x}10^{-20}$ J. PMMA particles allow a better compromise between buoyancy and refractive index matching as its refractive index is lower (1.49) than polystyrene and its density greater (1.18 g/cm^3). Thus we achieved a perfect buoyancy matching using a mixture of water, glycerol and urea with a close matching of the refractive index ($n_{solution}$ = 1.42). The solution is made with water and 30% of glycerol and 37% of urea in weight. We also add 10^{-2} mMol of EDTA (ethylenediaminetetraaacetic acid) to prevent from bacterial growth in solution. In this solution, the Hamaker constant for PMMA particles is $A = 7.87\text{x}10^{-21}$ J.

The volume fraction of the polystyrene particles is known from the manufacturer. On the other hand, the volume fraction of the synthetized PMMA particle is unknown at first. Precise measurement of the volume fraction is a difficult task [72] but can be done using some assumptions. Thus, we used two different methods to define the volume fraction of the PMMA solutions. The easiest way to measure the volume fraction of a sample is to weight the mass of colloids after drying. To do so, we put few millilitres of solution of unknown volume fraction in a glass vial of known weight. We then put the vial in a drying oven for a few hours. Once all solvent has been evaporated, we weight the mass of the vial. Subtracting the initial weight of the vial gives us the total weight of colloids in our initial volume of solution. Thus, we obtain the concentration in weight of particles, knowing the radius of the particles allows us to calculate the volume fraction of the initial solution. For best accuracy, we have to carry out this operation on at least 3 different vials.

One solution to obtain a solution at a given volume fraction is centrifugation. After long enough centrifugation, particles will all settle in an amorphous pack. Assuming that it achieves the so-called “random close packing” (RCP) density, we can then redisperse the particles in a known volume. Knowing the volume fraction of the RCP ($\phi_{RCP} = 0.64$) and the volume of solvent added we can obtain a solution at known concentration. This method is widely used in the field of colloids but is still subject to the controversy existing around the RCP [72].

b. Experimental set-up

The typical experimental set up we will be using in this work is schematised on Figure 33. It consists of a microfluidic device built as described in the previous paragraph. In this device, we inject a solution of colloidal particles. The injection is achieved by applying a pressured drop between the inlet and outlet of the device. This pressure drop is created by applying pressure in both the vial containing the colloidal suspension that is connected to the device inlet and a lower pressure on the disposal vial connected to the outlet of the device. The pressure in both vials is regulated by a compressed air regulator. The regulators we used are OB1 from Elveflow and MFCS from Fluigent that both allow quick response time and stability to the applied pressure.

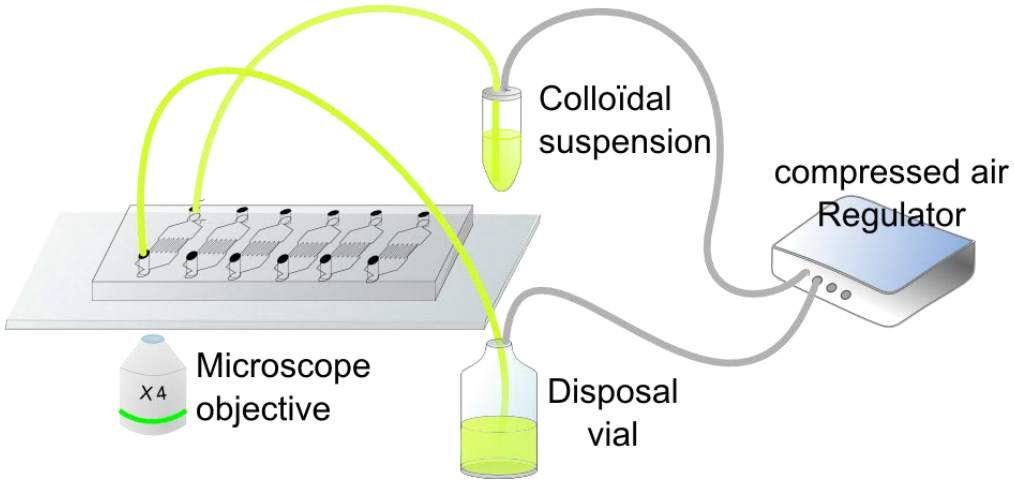

Figure 33: Experimental set-up. The colloidal suspension is injected in the microfluidic device applying a pressure drop (ΔP) between the inlet and outlet of the microchip.

Chapter III - Clogging in a 2d pore

In this chapter, we investigate the clogging phenomenon on the simplest scenario possible, the “2d” case (“slotted pore” in Figure 12), when the particle is confined in one direction or dimension. We look first at the macroscopic aspects of clogging at the pore scale, varying the geometrical features of the channel. In a second part, we zoom in at the particle scale and we evaluate the variation of the capture efficiency of the pore as it get clogs (evolution of number of deposited particle over the number of particles that already flow through it, N*) with the different geometrical features. Thereafter, we present all the different capture mechanisms, and the corresponding probabilities, which lead to the pore clogging. Finally, we explain the different pore clogging regimes we have observed using those mechanisms.

A. General features at pore scale

1. Geometrical features of the device

In a serie of preliminary experiments, we start to investigate the clogging of a 2d porous medium which was made of a main channel followed by a serie of parallel constrictions (pores), the height of the medium H being the same everwhere (Figure 34). Actually it is the microfluidic equivalent of an Hele-Shaw cell with a very thin gap in between the top and the bottom parts. Before each constriction or pore, of width W, we consider that particles can accumulate in a part called hereafter *reservoir*, which has a width W_R. We used pores with a slotted shape, with their widths greater than their height. In the entire chapter, we flow through the chosen device diluted suspensions (particle volume fraction : $5x10^{-5}<\phi<10^{-4}$) of PMMA microparticles using a pressure difference between the inlet and the outlet.

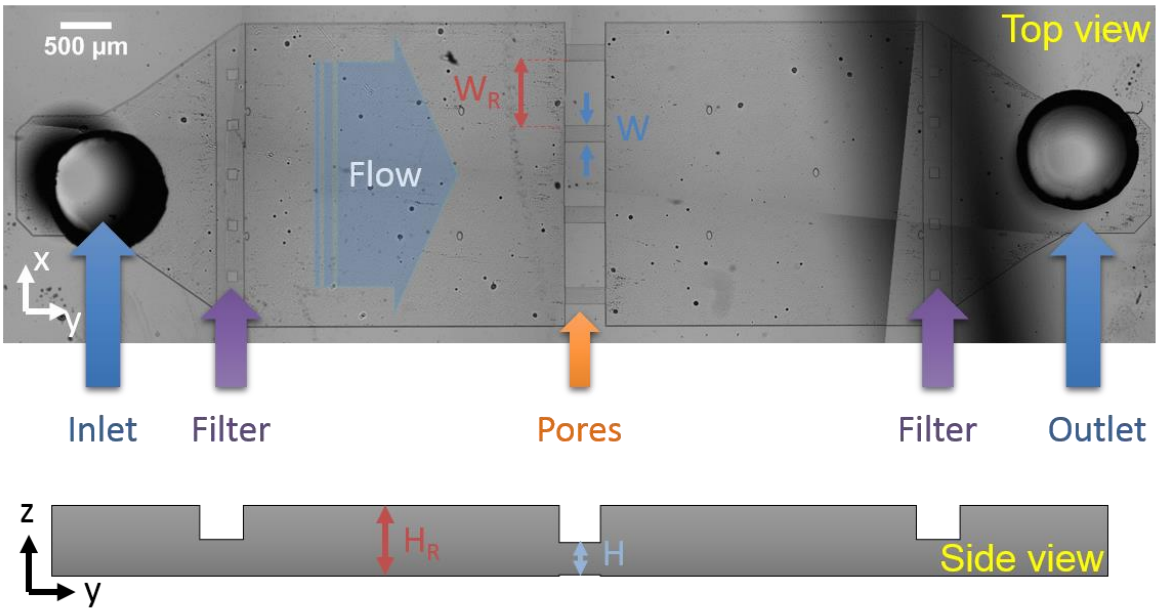

Figure 34: Top and side views of a typical 2d device. The tube coming from the stock solution of particles is connected in the inlet hole. Particles first pass through a filter that blocks particle with a diameter larger than the height of the pore. Particles then flow through the main channel which is long enough to ensure a regularisation of the current line, i.e., all the streamlines are parallel when the flow get closer to the pore entrance. All the particles that enter into a pore of width W and height H also come from the reservoir of width W_R and height H_R, the zone just upstream of the pore. Particles that are not captured go into a disposal vial, connected to the outlet.

The characteristic lengths of such a pore are its width W and height H. The width and the height of the reservoir for each pore (i.e the distance between two channels) are W_R and H_R. We flow through this device dilute suspension of polystyrene microparticles with a diameter D=0.9 H (Figure 35). This is partly due to the limitations of the soft lithography technique but it also far more convinient to image all along an horizontal slot with a constant height. Even at the beginning of the experiment, we deposit the same number of particles within the pore and in the main channel (Figure 35-image 1). As new particles enter into the device, we can see the formation of a clog and aggregates, respectively within the pore and in the main channel. Thus, the probability to capture a particle depends mainly on the most confined dimension or length scale, which is the vertical one in our case. In this configuration, the aggregates and the clog growth are coupled. Indeed, particles that are captured by the growing clog have to first flow through the aggregates and thus follow tortuous and always changing flow paths. Moreover, at the end of the clogging process, the clog is located within the main channel and not in the pore (constriction). In this configuration, it is thus clear that we cannot study properly the clog formation as the time goes on within the constriction.

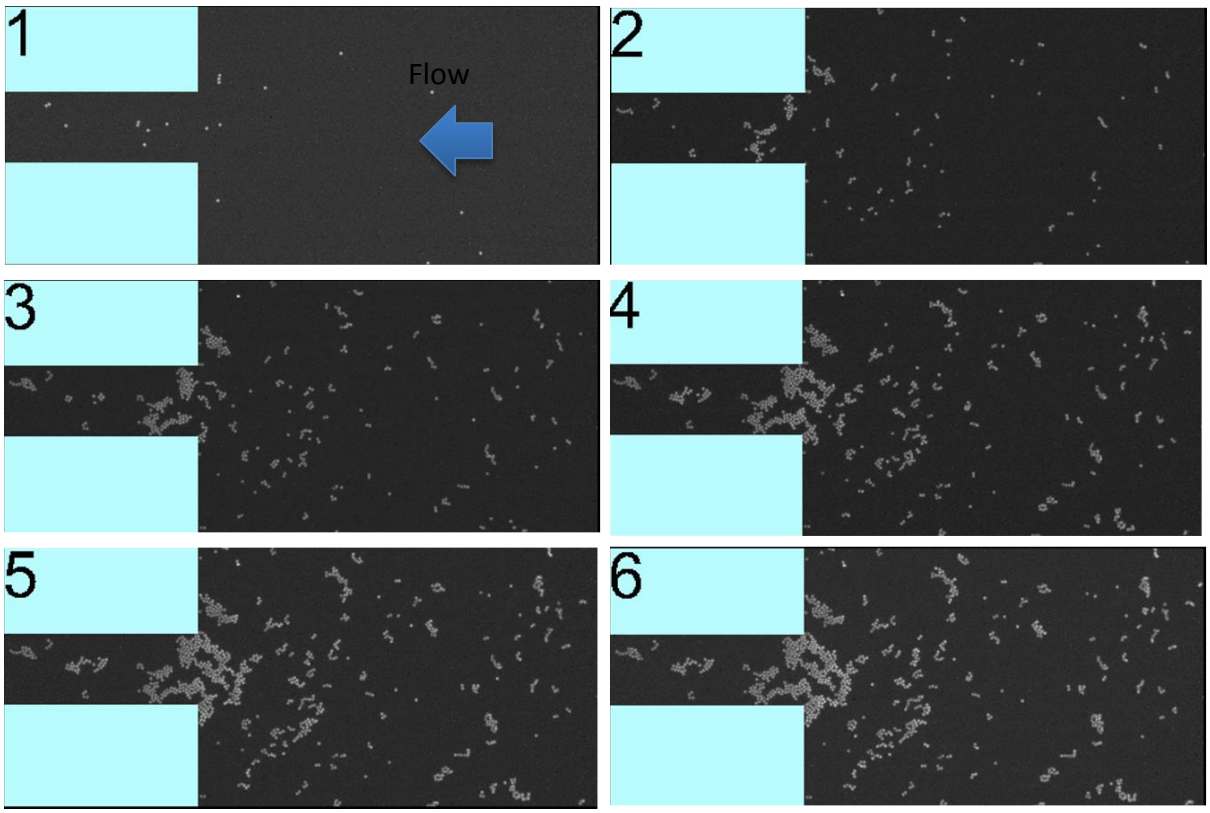

Figure 35: Consecutives images of a clog formation within a constriction in a 2d channel (the main channel height is equal to the pore height H=1.2D, D being the particle diameter). Blue rectangles represents the wall of the channel. Deposition of particles occurs everywhere and the clogging (image 6) occurs in the reservoir and not in the channel.

In order to prevent the deposition of particles and the subsequent aggregates formation, upstream of the constriction, we decided to increase the height of the main channel, keeping the pore height constant (Figure 36-A). We get this device by using two-level channels, which add extra steps in the lithography. In this new device set-up, as the flow is less confined within the main channel, the probability to capture particles within this zone drastically drop down and all the particles now deposits within the pore (Figure 36-B). As one can see on Figure 36-B, for the same flow rate, the value of H_R changes the morphologies and thus the growth history of the clog. With the smaller reservoir height (left), lot of particles deposit downstream within the pore without connection to the final clog, which is located close to the entrance of the pore. With the higher reservoir (right), the clog also forms within the pore, but further down from the pore entrance, and fewer particles are invading the channel prior clogging. We have not study in further details the influence of the reservoir height on the pore clogging, mainly by lack of time. We decided to work with the smaller reservoir height, with $H_R \approx 3H$, for two main reasons; (i) it is easier to build-up the smaller reservoir height with almost straight vertical walls (Figure 36-C), and (ii) we can image all the particles, irrespective of their position in the z direction, which enter within the pore. The side view of the chosen device is shown on Figure 36-C. The entrance of the pore exhibits an asymetric vertical constriction, between the top and the bottom parts, and a symetric horizontal one, on both sides from the middle of the pore. In

the next paragraph we will study the influence of all the other geometrical features of the pores, H, W, W_R and H_R, on the final clogging morphology. Thanks to the soft lithography process, we are able to change those one independently.

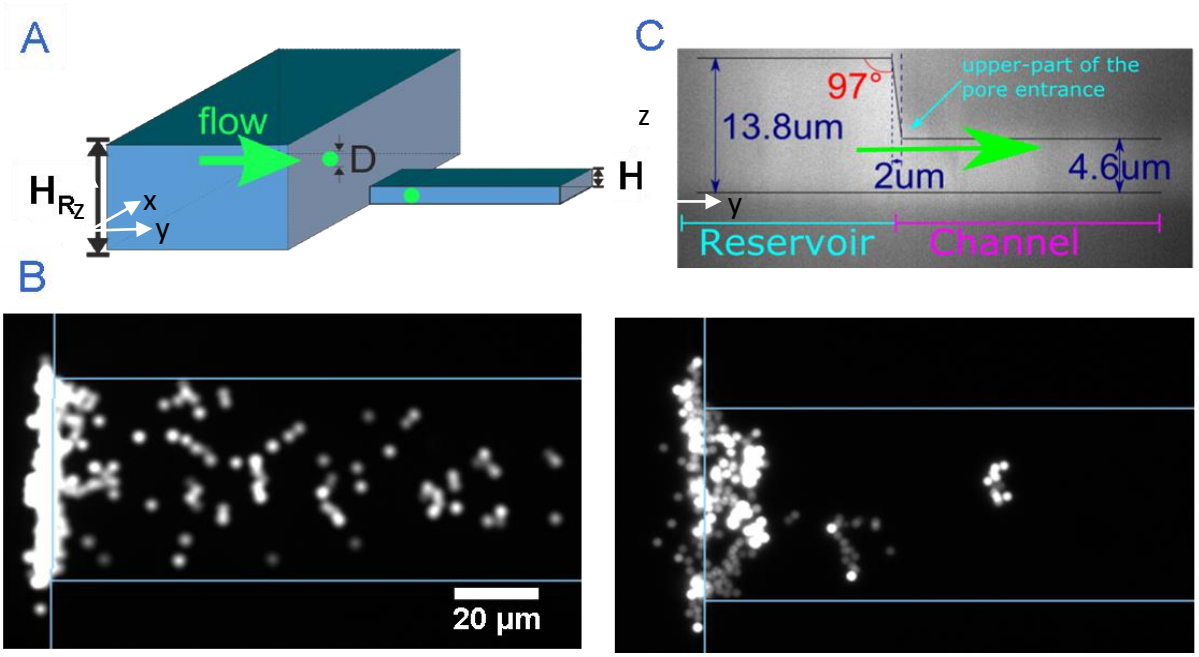

Figure 36: A-3D scheme of the geometry of the 2D constrictions. A reservoir of height H_R corresponding to 3 particle diameter, and width W_R, is placed upstream of the constriction (height H and width W).B- Clog morphologies in a device with H_R=14.5µm (left) and 50µm (right) at the same flow rate (Q=2.6µL/min). C- Side view of the pore entrance: Confocal z-slice reconstruction of a pore. The white shiny signal corresponds to the interior of the channel. It shows relative heights of both reservoir and channel and the steep passage from the reservoir to the highly confined channel. Green arrow indicates the flow direction.

2. Geometrical and flow rate effects

We identified two different morphologies of clog for all the geometrical parameters and flow rates, based on the penetration length of the particle deposit within the pore from its entrance. In a first regime, we call "*line*", clog forms at the entrance of the pore (Figure 37-A). All particles are located near the vertical constriction (Figure 36-C), corresponding to the abrupt transition zone between the reservoir to the pore. Particles lie in a band within the pore of width equal to at most three particle diameters. In a second morphology called "*invasion*", the clog forms further down within the pore, at a distance L from the pore entrance, called thereafter "*clog length*" (Figure 37-B). There are various ways to define this length from the pore entrance (refer to appendices A), because the clog front is not flat. We may choose the maximum length, which is related to the particles that is the furthest from the pore entrance (magenta square), the mean length in the front line (dashed red line) or the maximum density within the front line (red line). It is worth noting that, whichever method we use; there is always a clear distinction between the two regimes for all the parameters.

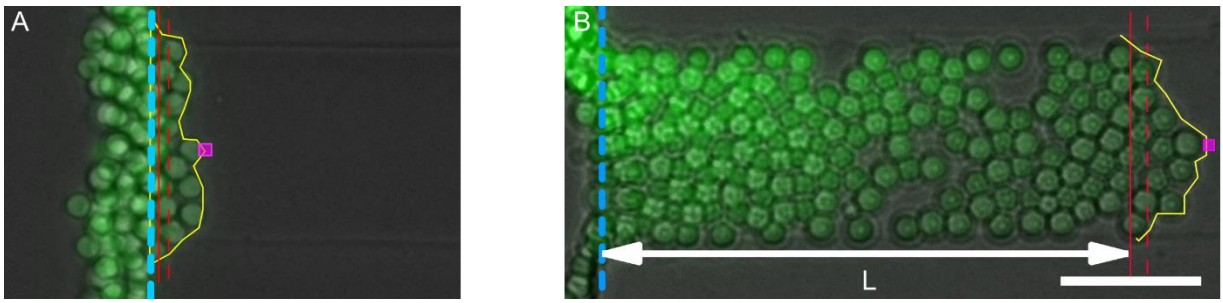

Figure 37: Clog of a W=28 µm pore by 4 µm PMMA in W=28 µm channel. Line (A) and invasion (B) morphologies. Dashed blue line is the constriction entrance. Yellow stroke defines the clog's front line. Dashed red line is the average length of the line front. Continuous Red line is the maximum density line in the clog's front line. Magenta square is the maximum penetration length. Scale bar is 20 µm.

The first natural geometrical parameter that we can vary is the width of the constriction W. However, we have also to consider in the same time the width of the reservoir, W_R, which is just upstream of the constriction and corresponds to the distance between two constrictions (Figure 36). Indeed, the reservoir influences the flow properties at the pore entrance, by changing the shape and spatial repartition of the fluid streamlines, and thus also the transport properties and the capture of the particles at the pore entrance. Instead of W, we will consider thereafter the ratio W_R/W. We observe that, for a given ratio, there is a transition between the two morphological regimes from a critical flow rate thereafter called Q_C (Figure 38, triangles). For the smaller flow rates, in the line regime, L varies very slowly with Q from one particle diameter D up to 2-3 D. In contrast, for the higher rates above Q_C, the invasion regime is characterised by a steep increase of L with Q. It is worth noting that for the smaller width W and the highest Q, the value of L is more than three times greater than W.

Now, if we use a constriction with a different width W, while keeping constant the ratio W_R/W, we observed that the transition between the two regimes takes place for the same Q_C (Figure 38-A, squares). Moreover, the two curves superimpose in the line regime, thus the clog length follow the same variation with the flow rate in this regimes. This is confirmed on the Figure 38-B for a given flow rate below Q_C and three different value of W. Even though the transition between the two regimes seems to occur around the same Q_C, the length of the clog L in the invasion regime increases linearly with W (Figure 38-B).

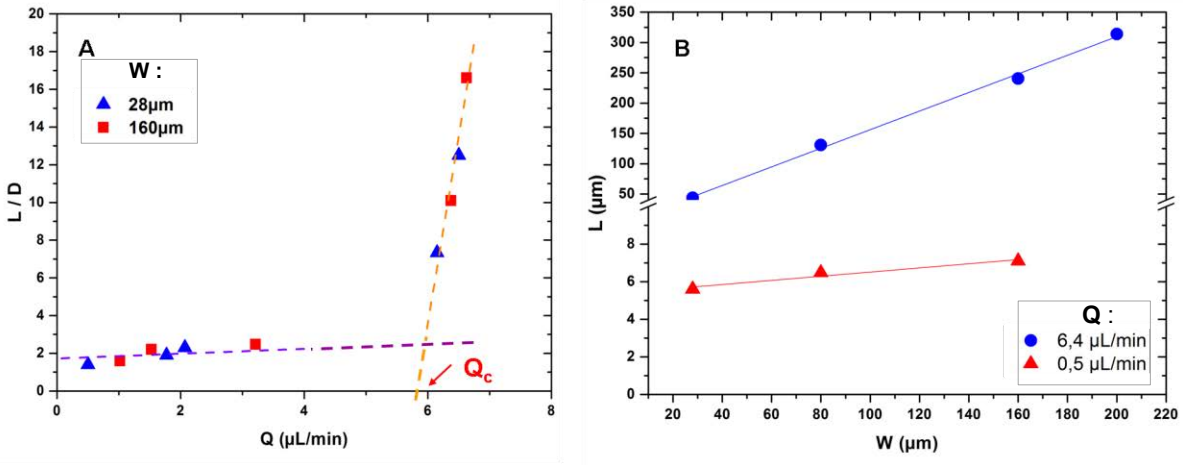

Figure 38: A-Evolution of the clog length, scaled by the particle diameter, L/D, with the flow rate for two different pore widths W (28 and 160 µm) keeping W_R/W=4. The purple and the orange dashed lines (guide for the eyes) correspond to the line and invasive regimes, respectively. The interception of the two lines gives the position of the critical rate Q_C. B-Clog length dependence on the channel's width (W) at fixed W_R/W =4 for two flow rates corresponding to the line regime (0.5 µL/min) and the invasion regime (6.4 µL/min). The two lines are linear fits with slope 1.53 (blue) and 0.01 (red).

Figure 39.A shows the evolution of L with Q for two ratios W_R/W, keeping this time the constriction width W constant. Once again, for both ratios there is the line regime for lower flow rates (Figure 39 image B and D), with a very slow increase of *L* with *Q*, from 2D to 3D. However, the critical rate Q_C and is not the same for both geometries. For the greater width ratio, we enter in the invasion regime for a smaller value of Q_C, and in the invasion regime, the linear variation of L with *Q* is steeper. It is worth mentioning that there is a lot of particles deposition prior pore clogging for the larger width ratio, in both morphological regimes (Figure 39- D-E). Particles that do not belong to the clog deposit all along the pore length, forming sometime very large aggregates (Figure 39-E). In contrast, for the smaller width ratio, we have almost no particle deposition a head of the clog front (Figure 39-B-C).

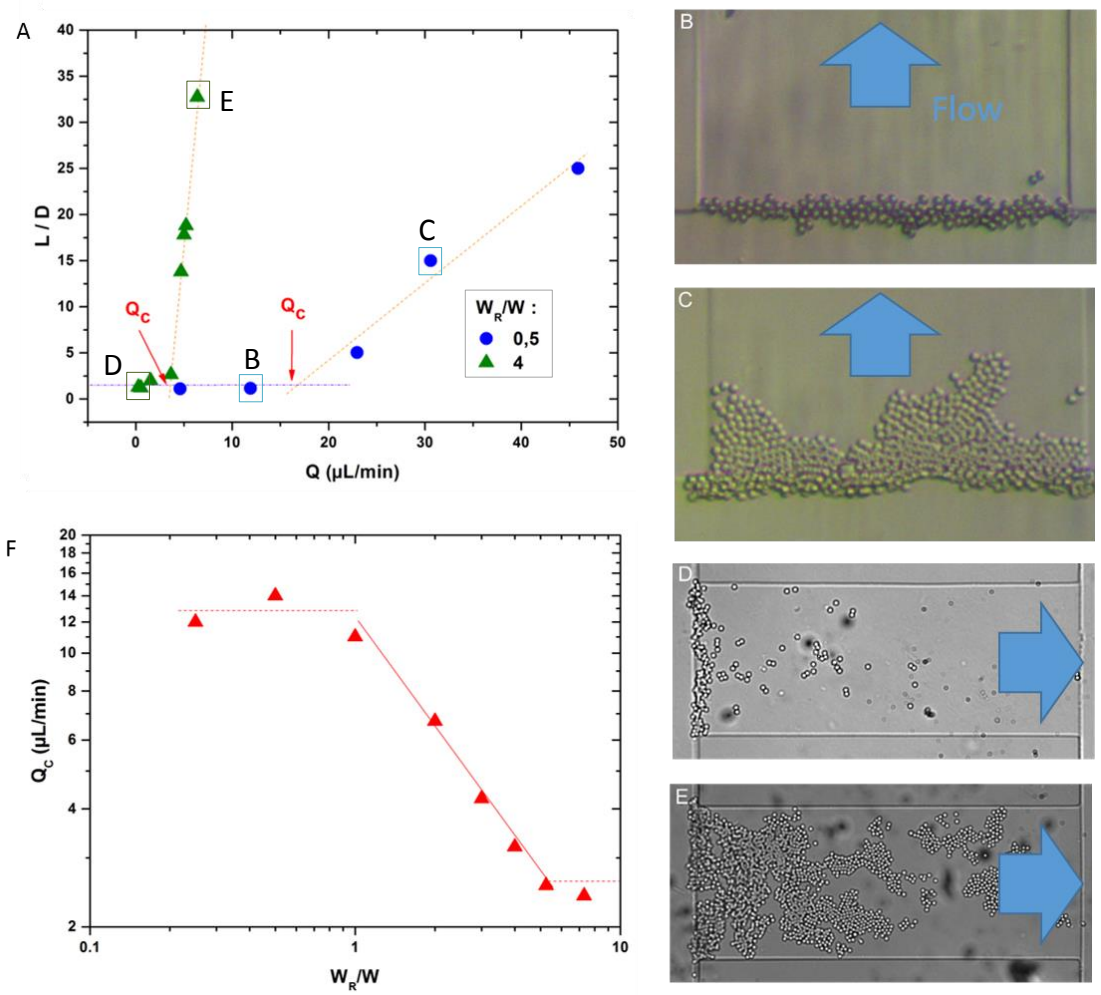

Figure 39: A- Clog's length in particle diameter (L/D) as a function of flow rate (Q) for two different ratio of reservoir with channel width (W_R/W). Transition between line morphology and invasion of the channel occurs at a critical flow rate labelled Qc. B, C, D and E are the images corresponding to the labels in the graph A. For B-C and D-E the width of the pore is 160 µm. F- Evolution of the critical flow rate (Q_C) separating the line and invasion regimes with the ratio between reservoir width and channel width (W_R/W). The continuous line is an inverse power law of the width ratio and the two dotted lines on both sides are guides for the eyes.

We have further investigated the variation of the critical flow rate Q_C with width ratio W_R/W (Figure 39). We clearly see three regimes. For reservoir smaller that the pore, $W_R/W < 1$, Q_C is constant and equal to 12 µL/min. In the intermediate regime, for $1 < W_R/W < 5$, Q_C decreases as the inverse of the width ratio. Finally, for $W_R/W > 5$, Q_c goes back constant, with a value ten times smaller than in the first regime, i.e., Q_c is around 1.2 µL/min.

Finally, we have varied the height of the pore, keeping it below two particle diameters. This condition ensures the "2d" confinement of the particles, i.e. two particles cannot pile up within the pore height. In Figure 40, we plotted the variation of L with the flow rate for two heights, H/D=1.15 and H/D=1.75. In those two "extreme" cases, the results are similar and both curves perfectly overlap perfectly.

Therefore, the height of pore modifies neither the clog morphology nor the variation of the clog length with the flow rate, and the value of Q_C.

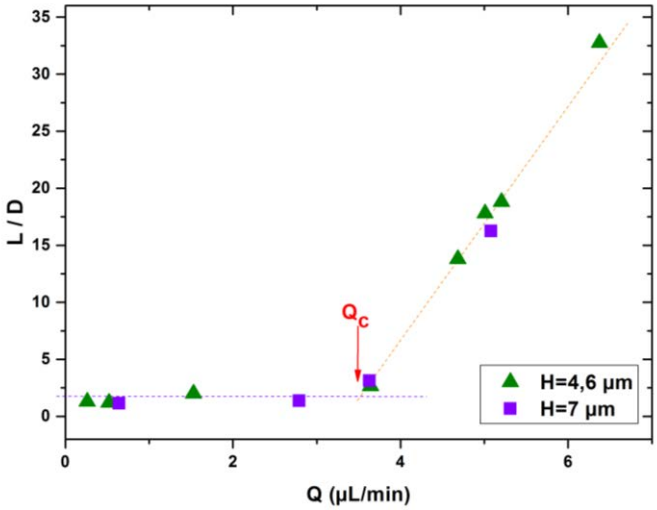

Figure 40: Variation of *L/D* with the flow rate *Q* for two different heights of the pore (H=4.6 and H=7 µm).

a. Phase diagram

We can gather all the data we obtained on a single graph where we plot the ratio of widths as a function of the flow rate (Figure 41). In this graph, we clearly distinguish four zones. At the lowest rates (hatched zone I), there is no deposition of particle within the channel, thus clog cannot be formed. In this regime, colloids are still slowly advected but we cannot neglect the diffusion. The flow cannot push enough the particle towards the wall to overcome the repulsive (electrostatic) barrier. At the highest rates, there is also no particle deposition (zone IV).

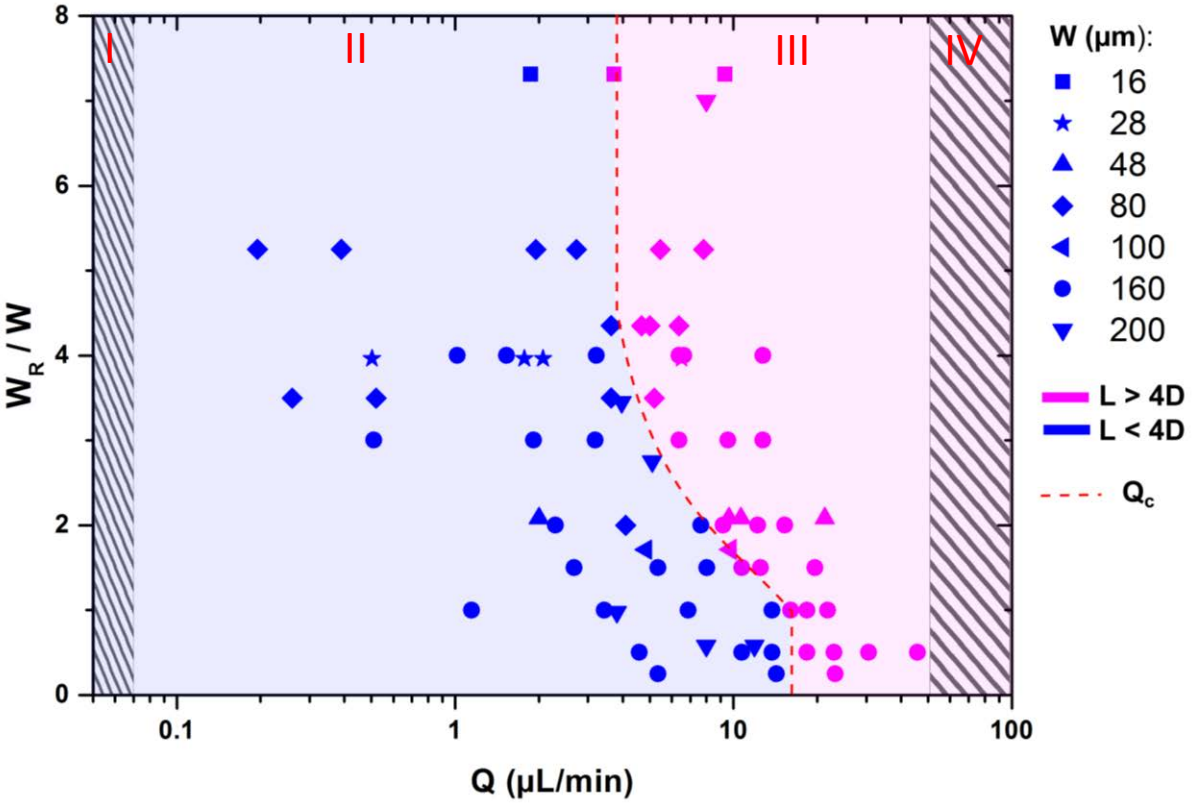

Figure 41: Phase diagram of 2d clogging for D=4 µm PMMA particles. Blue points are line type clogs (clog length L<4D, zone II). Magenta points are invasive clogs (clog length L>4D, zone III). The dashed red line is the critical flow rate Q_c. Hatched zones correspond to areas of no particle deposition (zones I and IV).

However, in this case, the flow is strong enough that it can detach a particle from the wall, i.e. to pull out the particle of the attractive part (van der Walls) of the DLVO potential. In the best case, we may have partial and temporary deposition for such high flow rates. In between those to extreme regimes, we can effectively clog the pore. Within this clogging regime, clogs formed in channels with the same ratio W_R/W at the same flow rate will exhibit the same morphology, irrespective of the value of the channel or reservoir width. It worth mentioning that at the frontier between the two clogging regimes, the critical flow rates Q_c depends on the value of the ratio of widths and follows the same behaviour as previously observed in Figure 39-F. In general, the greater the ratio the smaller is Q_C. When the pores are close to each other, ($W_R/W<1$) the values of Q_C are the greatest. In this case, the dominating morphology is the line, the invasion regime occurring only on a limited range of flow rate. On the opposite, when the pore are far of each other, for $W_R/W >5$, the invasion regime occurs most often and for the smallest value of Q_C. In the following, we will see the geometrical features of the pore affects the filtering efficiency.

3. Filtering efficiency of the pore

In the previous paragraph, we have looked at the final state of the clogging process, which has allowed us to distinguish two main morphologies of clogs. In the present section, we will determine on the overall clogging process, that is, from the first deposited particle up to the clog, how the pores progressively fill up as particles flow through them. Thanks to an automated XY stage and a high speed confocal, we are able to image up to ten different channels of the same device every 30s. We also use colloidal suspensions with a very low volume fraction ($\phi \approx 10^{-5}$), which enables us to image the deposition of almost each single particle within each pore. Those experiments provide information on the deposition rate of the particles and their precise location in three dimensions.

Let us start by investigate the variation of the deposition rate for a pore of width (W) as the flow rate (Q) changes. We can see in the Figure 42-A, that the number of deposited particles, N_p, increases linearly with the number of particles N that have passed through the pore at a given time t, irrespective of the Q value. We can estimate N using the following expression [3]:

$$N = \frac{tQ\phi}{V_p} \qquad (3)$$

With *Q* the flow rate, ϕ the volume fraction and V_P the volume of a particle. Therefore, and in first approximation, we obtain a constant deposition rate of particles, which corresponds to a unique probability of deposition of particles, P, defined as the ratio between N_p and N, for each Q. We can also easily determine the number of particles that have passed through the pore prior the pore clogging, N* (Figure 42-B). While $Q<Q_C$, N* increases moderately with the flow rate, and seems to levels-off around Q_C, but, as soon as $Q>Q_C$, N* increases much more rapidly. Typically, N* is ten to forty times bigger in the invasion regime than in the line one, even though the number of particles within the effective clog, i.e., those which belong to the clog front, increases by a factor of two or three when we go from the line to the invasion regime.

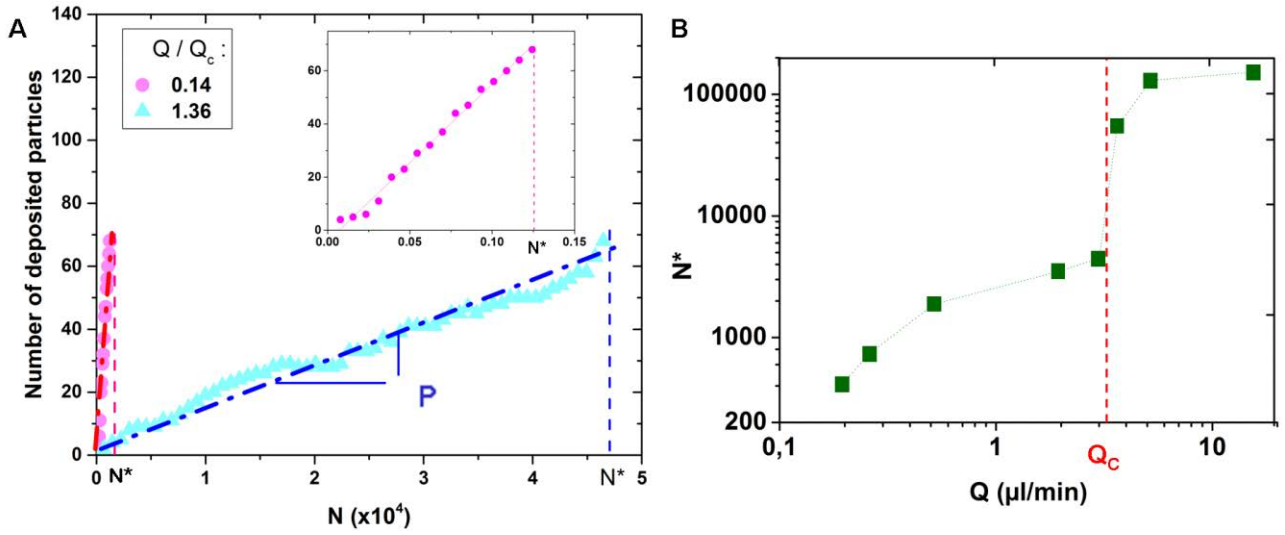

Figure 42: A- Evolution of the number of deposited particles, N_p, with the number of particles that flew through the pore, N, for two flow rates, one below (circles), and one above Q_C (triangles). The two dashed-dotted lines are linear fits with a slope of $6x10^{-2}$ in the line regime and $1.4x10^{-3}$ in the invasive regime. The two vertical dashed lines correspond to N* for each rate. Insert: zoom in of the curve for Q/Q_c=0.14. Channel dimensions are W=80µm and W_R/W =3.5. B- Evolution of N* with the flow rate in a W=80 µm channel. The vertical dashed line corresponds to the critical flow rate Q_C.

The evolution of P with the scaled flow rate, which is also inversely proportional to N*, is plotted on Figure 43. This particle deposition probability is clearly not the same depending on whether we are in the line or in the invasion regime. P is of the order of 0.01-0.1 in the first regime whereas its value drops down quickly by many orders of magnitude with Q above Q_C (inset).

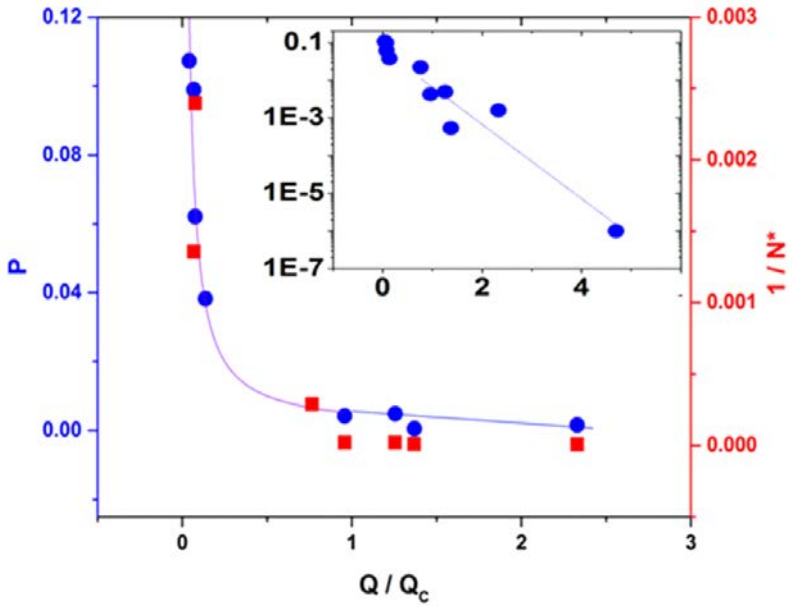

Figure 43: Variation of particle deposition probability *P* (circles) and 1/N* (squares) with the scaled flow rate Q/Q_c. The blue curve is an exponential fit with a decay constant equal to 0.08. Insert: P vs. flow rate in "log-lin" plot.

When we change the width of the pore *W*, keeping the ratio W_R/W constant, we still obtain a constant deposition rate for each width (Figure 45-A), but obviously, the number of deposited particles to clog the pore increases with *W*. We observe that N* increases quadratically with W in the invasion regime (Figure 44-B). More surprisingly, it seems that the deposition rate is the same, irrespective of the width, all the data in Figure 44-A following the same curve. Actually, there is a very slight increase of P with the pore width W (Figure 44-A, inset), but we can neglect it.

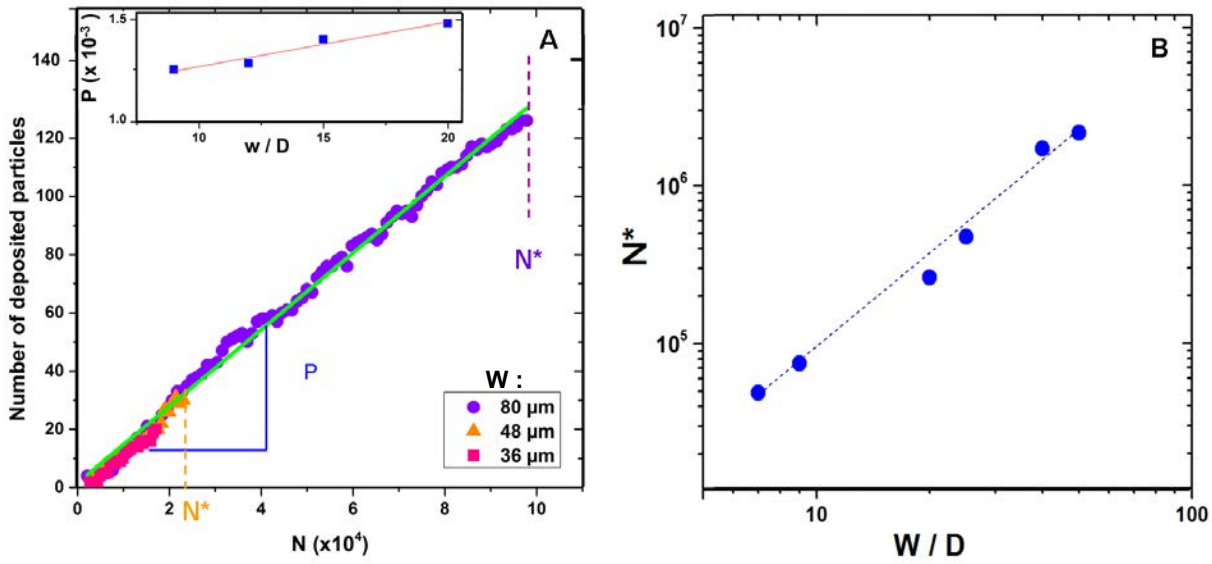

Figure 44: A- Variation of N_p with N in the invasion regime for different pore widths (W=36, 48 and 80 µm) at Q/QC = 1.5. The line is a linear fit with a slope of $1.32x10^{-3}$. Insert-Variation of P (x 10^{-3}) with the rescaled width of the pore W/D .The line is a linear fit with a slope of $2x10^{-5}$. B-Variation of N* with the rescaled pore width W/D. The dotted line is a quadratic fit such as $N^*=1022(W/D)^2$.

Figure 45-A shows the influence of the reservoir width on N*. At a given flow rate, we find that N* increases with W_R/W (Figure 45-A, inset), i.e., when the reservoir zone upstream of the pore is larger, we need to flow more particles through the same constriction to clog it, which corresponds to a decreasing of the probability of particle capture with the reservoir width.

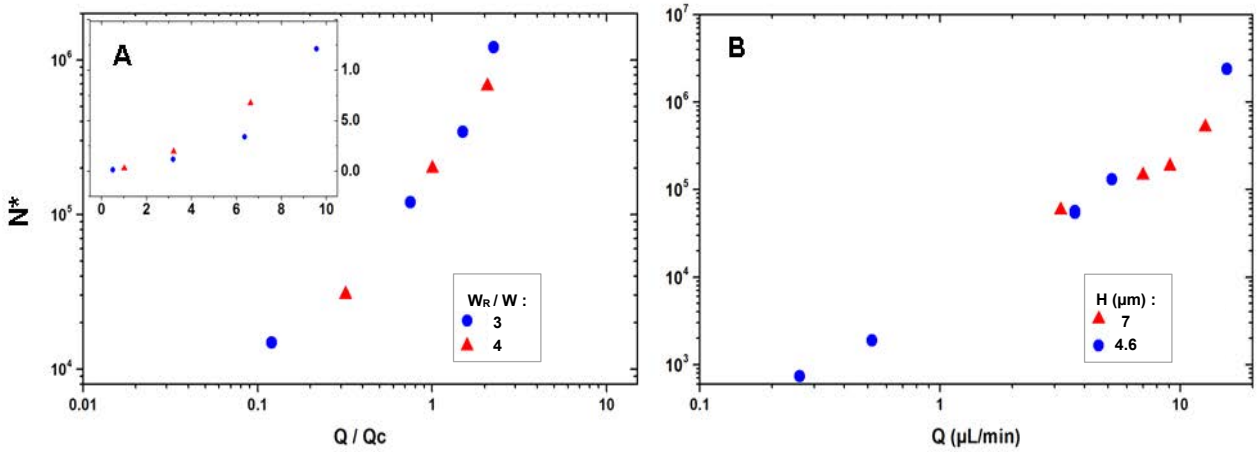

Figure 45: A- Variation of N* with the flow rate Q, normalized by the critical flow rate QC, for two ratio of widths (W=160µm). Inset: N* vs. Q for the same conditions. B- Evolution of the number of particle flowing through the pore prior to clogging with the height of the channel. We used the same experimental conditions as in the Figure 40.

When we rescale the flow rate by the critical value Q_C for each geometry, we get a single master curve of the evolution of N* with the flow rate for the different width ratios (Figure 45-A). Therefore, the spatial repartition of particles, i.e. where they are coming from (just in front of the pore entrance or from both sides in the reservoir zone), and the streamlines upstream of the pore entrance seem to matter. Finally, we looked at the impact of the height of the pore on N*. We measured the evolution of N* with flow rate at fixed ratio W_R/W for two different heights: H=4.6 µm and H=7 µm (Figure 45-B), which are the same conditions we used in Figure 40. Here, again we get a single curve of N* vs. Q for both heights, and thus the same deposition rate.

To briefly sum up this last part, we have considered only the deposition rate of the particles within the pore. It turns out that this rate is constant irrespective of experimental conditions. This can lead us to consider only one type of capture mechanism. The pore walls capture particles, as they encounter the pore entrance. Moreover, we get two distinct regimes for the evolution of N* with all the geometrical features and the flow rate, which perfectly correspond to the two morphological regimes, line and invasion identified earlier. However, a closer look provides some hints that the situation is not that simple, and the link between the deposition rate and the clogging is not straightforward. We have plotted on Figure 46 the evolution of the number of particle deposited N_P with N for three runs in the same experimental conditions. Once again the deposition rate is constant and we get almost the same N*. However, we can see on the images corresponding to the end of the clogging process for each trial that not all the particles partake to the clog formation. For instance, in the first run (Figure 46 image 1), 30 % of the deposited particles are isolated individuals deposited down in the pore, a head of the clog. In contrast, for the second and third runs (Figure 46 images 2 and 3) this population of particles represents only 2 to 4% of the captured particles. Moreover, the shape of the clog is different in each case, even if the clog length is about the same for all. It is worth

mentioning that the particles that belong to the clog front are not always in contact. If the space in between two particles is lower than a particle diameter then we can consider that this local part of the pore is clogged. Therefore, the pore clogging in all confinement seems to be the result of a combination of two mechanisms: (i) deposition of single particles, which remain alone (no contact with the others), and (ii) growth of small aggregates. We do not know at that point, how particles can form those aggregates. This poses the questions of the interaction between two or more particles.

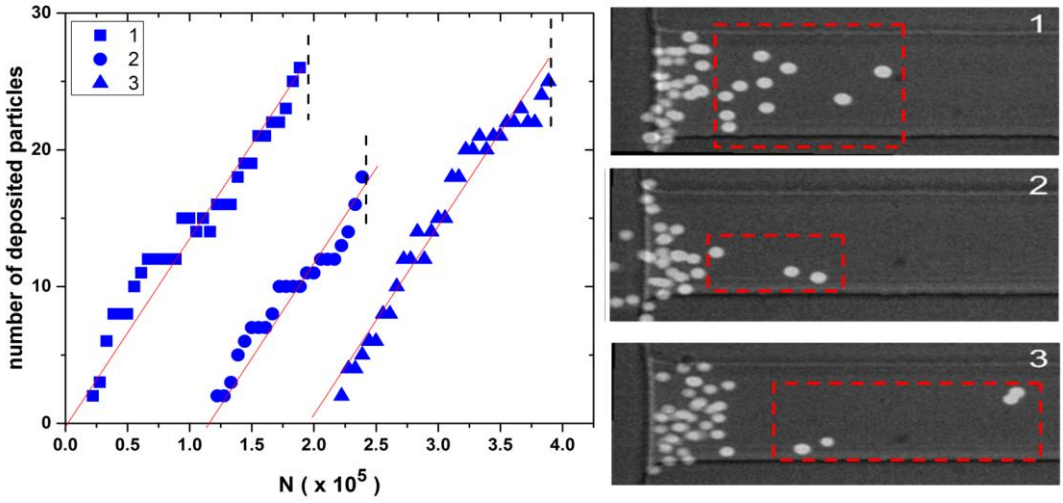

Figure 46: Evolution of N_p for three trials with the same conditions (W=36µm, invasion regime). Each curve corresponds to an image of the final structure of the clog, with the same number as a label. Red lines are linear fits with the same slope of 1.2x10-3. Curves 2 and 3 have been purposely shifted towards the right, starting respectively at N(x 10^5) =1 and 2. The dashed rectangles correspond to particles deposited further down within the pore and which do not belong to the clog front.

Another aspect of the particles interaction can be seen on Figure 47, which gathers consecutive images of the clog formation in the line regime. We form a line of particles at the pore entrance at the beginning of the process up to image 3 (“120 s”), where the upper half of the pore is almost free of particles whereas the lower starts to be crowed. We also observe that two particles deposit further down in the pore, outside of the capture zone corresponding to the line regime (in between the two green lines). This occurs when the average distance between the particles at the entrance, along the line, is about 1.5 particle diameter D. For such a distance, we cannot ignore the hydrodynamic interactions between the particles that form the discontinuous line at the pore entrance and the ones that flow through the pore entrance by the small corridors (see to the two arrows on image “120 s”). In the following, we will first detail all the mechanisms, at the particle scale, which are responsible of the particle deposition and aggregation under flow. In a second time, we will expose how those mechanisms lead to the pore clogging.

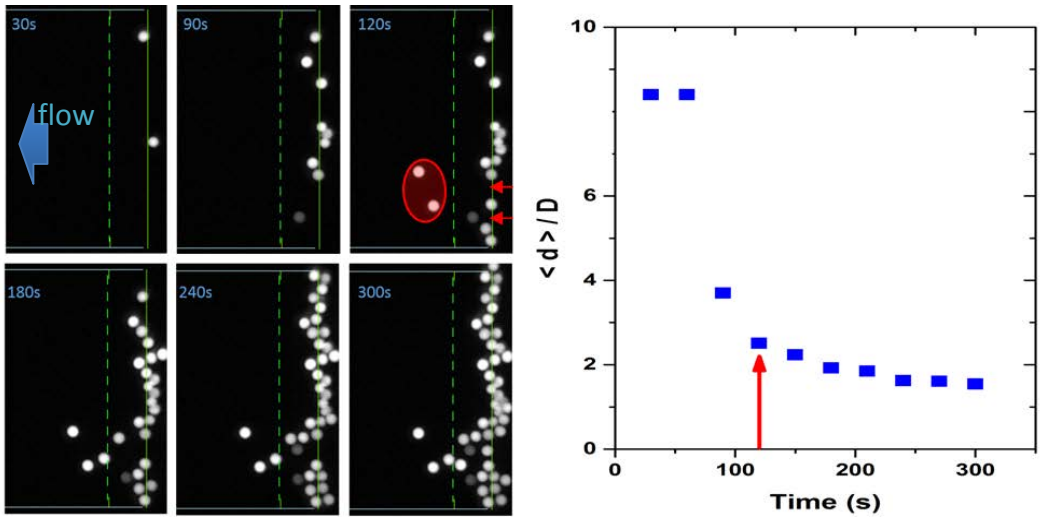

Figure 47: (Left) Images of the formation of a line clog at Q/Qc=0.076. Particles are captured at the entrance of the pore and deposit from the vertical constriction (green continuous line) and over a distance equal to three particle diameters 3D (up the dashed green line). At 120s we notice the deposition further down in the pore than the capture zone associated with the entrance (red circle).The two particles come from the two flow paths (two arrows) This invasion corresponds also to the red arrow in graph on the right. (Right)- Evolution of the mean distance between particles, from the particle centres with the time.

B. Growth mechanisms and characteristics at particle scale

1. Direct interception by the pore wall

Particles first deposit at the entrance of the pore in the two morphological regimes. A priori, a particle can deposit either on the top or on the bottom part of the pore entrance (Figure 48-A). In order to visualize where these captures take place and from where a particle that gets captured comes from, we have designed another microfluidic device. In this peculiar device (Figure 48-B), there is only one constriction which is within a horizontal plane, and the channel has the same height everywhere. We have studied the particle motion in the middle height plane to avoid side effects. We indeed observed two capture positions. The particles are either captured by the curved part or by the flat part of the constriction, at the pore entrance (Figure 15-C). In both cases, particles do not go across the channel to deposit on the opposite side. They apparently follow fluid streamlines up to their capture.

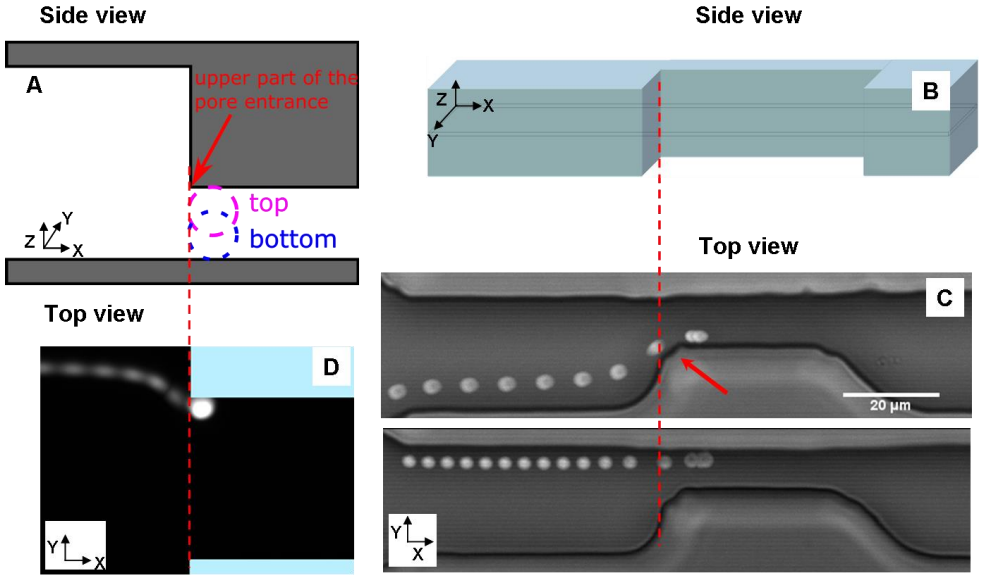

Figure 48: LEFT: Regular device as in figure 3.A- Scheme of the two possible positions of particle capture at the entrance of the pore, by the vertical constriction: curved part (top) and flat part (bottom) of the channel. D- Capture of a particle by the lateral wall within the pore. RIGHT: B- Scheme of the device used to visualise the particles trajectory before their captures. C- Top view of the particle trajectory with a frame rate of 8000 fps. Capture by curved part of the pore (top) and the flat part (bottom). For both devices, the red arrow points to the curved part of the constriction in both devices and the dashed lines correspond to the pore entrance.

We also identified another capture zone in the regular device as in Figure 36. Particles that come from both sides of the pore follow curved streamlines, in the XY and in the XZ planes, just upstream of the pore entrance and get captured near the side walls inside the pore (Figure 48-D). From the analysis of the particle trajectories within the reservoir, we can easily distinguish where the particles come from, either from the sides or from the centre part of the reservoir (Figure 49-A and B). All the particles coming from one of the sides of the reservoir have their trajectories that pass within a zone, adjacent to the lateral pore wall, with a width W_{SIDE} (Figure 49-A), inside the pore. The trajectories of the other particles, which flow through the pore entrance from the centre part of the reservoir, spread on the remaining part of the pore entrance width, that is, $W\text{-}2W_{SIDE}$. The fact that particles within this zone cannot reach the lateral walls of the pore is due to the hydrodynamic interaction (HI) of the particle with the pore edge. In Figure 49-B, we can see that a particle, which is just at the limit between the side and the centre zone, follows a straight-line like trajectory far from the pore entrance but eventually avoids the pore edge zone by turning around it. The horizontal shift from its initial horizontal position in the reservoir is equal to W_{SIDE}. As the particle positions within the centre part of the reservoir depart from the pore edge, the corresponding trajectories curve less in the vicinity of the pore entrance. The length of the HI, and thus the value of $W_{SIDE,}$ depends primarily on the width W_R and the height of the lateral pore wall that is in between two pores. We report on Figure 49–C the variation of W_{SIDE} with W_R, for a fixed reservoir height. W_{SIDE} increases linearly from 1.5D up to 2.7D with W_R. The width of the pore is always greater than the height of the pore, thus

the probability of particle capture by the bottom and top parts of the constriction in the centre zone is more important.

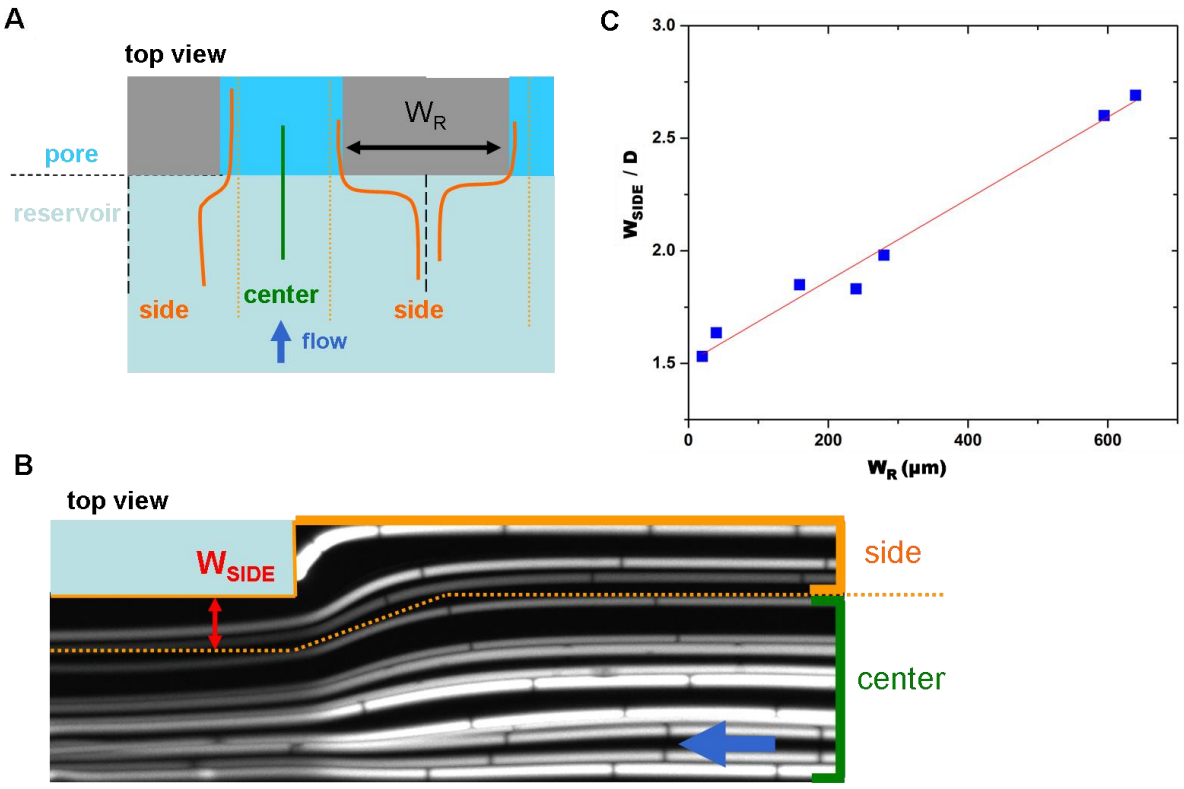

Figure 49: A- schematic of the different zone in the vicinity of the pore entrance. B- Image of the half width of a pore at its entrance with an overlay of different particle streamlines. Particles above the dotted orange line belong to the side part. The others, below the line are part of the centre zone. The streamline just below the dotted line is curved when it gets closer to the pore entrance and it is shifted below from its initial position of a quantity WSIDE when it enters into the pore. C- Variation of WSIDE with the size of the reservoir WR. The line is a linear fit with a slope of 0.0069.

Finally, thanks to the streak image analysis, we can unambiguously establish the link between the initial 3d position of a particle, within the reservoir zone, and its final position, after being captured by one of the pore walls. We have four spatial zones of interest: the top and the bottom capture zones (Figure 50, "side view") and the location within the reservoir, sides or centre (Figure 50, "top view"). In Figure 50, we have plotted the z-position of the centres of several particles within the reservoir and their final distance from the pore entrance, *y*, for various flow rates. Firstly, we can see that top and the bottom capture zone are both adjacent to a horizontal wall. Secondly, particles do not cross the reservoir as they get captured, i.e., a particle captured at the top (bottom) wall of the pore comes from the top (bottom) part of the reservoir. Moreover, those zones do not spread up to the middle of the reservoir, in height. Thus, no particle that come from the zone with z in between 5 and 9µm, centred on the middle height of the pore, are captured by either horizontal walls. The bottom wall capture is observed only at low flow rates ($Q < 0.5\ Q_C$) while the top one occurs for all flow rates. For all particles, there is no unique relationship between their final position within the

pore, y, and their initial altitude within the reservoir, *z*. For the same *z*, we can get different values of *y* within the pore. This likely comes from the fact that the velocity profile is parabolic within the pore, i.e. not whether the particles within the reservoir are close to the top or to the bottom, they are captured within a distance from the entrance *y=3D*, as long as they come from the *centre* zone. Particles that come from both sides of the pore can actually deposit further down within the pore, up to 6-7D. Those latter ones are captured by the horizontal walls of the pore and not by the lateral walls. It is worth noting that the range of altitude of the captured particles decreases with the flow rate.

For instance, for $Q/Q_C = 0.52$, deposition altitudes lies between 9 and 11. 5 µm whereas for $Q/Q_C = 5.15$, it is in between 11.5 and 12 µm. We will give more details in the following. Finally, we do not see a progressive invasion of the pore as the flow rate increases, i.e., there is no difference in the final "y" capture position, whether the flow rate is below or above its critical value. There is just a slight increase of the average value of *y* with the flow rate, which is consistent with the linear variation of the average position of the clog front with Q (see Figure 38-A).

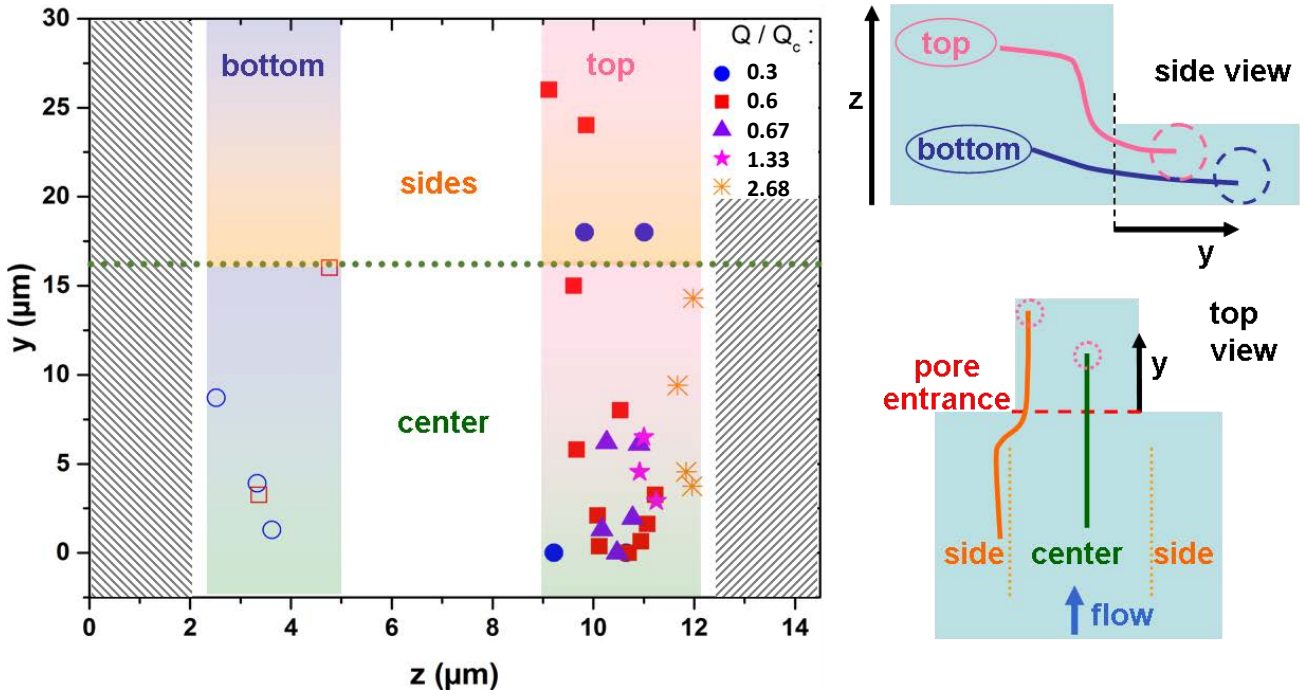

Figure 50: (Left) Distance of deposition (y) of the particles captured by direct capture from the pore entrance, in function of their previous altitude (z) upstream in the reservoir, for various flow rates. The green dotted line (y=4D) corresponds to the end of the deposition area of the line regime. Points above this line are particles captured within the band of width W_{SIDE}, along one of the lateral walls of the pore. Below this line, particles are captured by the top and bottom walls. The hollow and the plain symbols correspond respectively to the capture by the bottom and the top part of the constriction. The two hatched zones on both sides are forbidden regions because of steric hindrance (Right) Side and top schematic views of the capture trajectories in the different zones within the pore.

The width of the pore being always greater than its height, most of the particles that get captured by the top/bottom part of the pore come from the centre zone within the reservoir. We thus focus on these capture modes. We have computed With COMSOL the flow within the pore to get the fluid streamlines, within this centre zone, which correspond to particle streamlines, at least far upstream of the pore entrance. We have represented the streamlines below and above the critical flow rates Q_C, and we can see that they are the same except that they do not correspond to the same fluid velocity in each case (Figure 51-Top). It is worth noting that we can found curved streamlines that could correspond a priori to the trajectories followed by the particles that get captured at the curved part and the flat part of the pore entrance in Figure 48-C. In particular, we do observe in the bottom part just upstream of the pore entrance, that some fluid streamlines get curved downward because of the asymmetry of the entrance. Those ones thus correspond to the trajectories leading to the particle capture by the bottom flat part. We also provide the velocity profile for different positions, within the reservoir, which is followed by the pores in the bottom part of this figure. Those profiles remain parabolic up to 20 µm upstream of the entrance. For smaller upstream distances, they become asymmetrical, the fluid going faster on the bottom part of the channel.

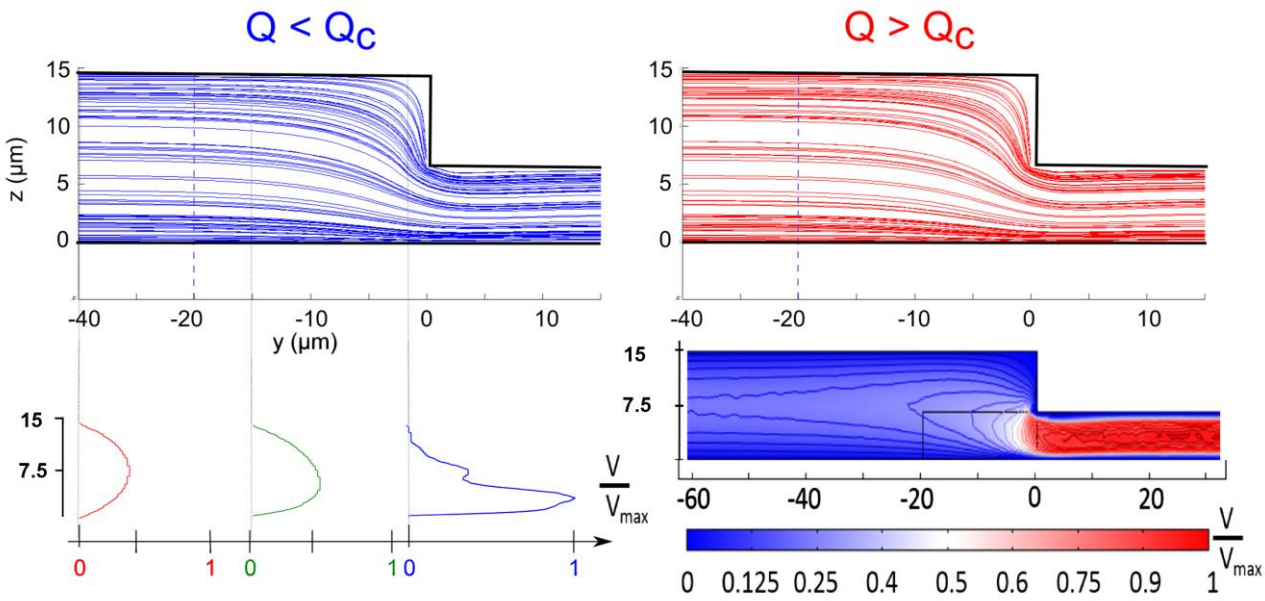

Figure 51: Top- Computed fluid streamlines for $Q<Q_C$ (left) and $Q>Q_C$ (right). The vertical dashed line on each graph corresponds to the distance (20µm from the entrance) from which the velocity profile is no more parabolic and starts to be influenced by the constriction. The flow is going from the left to the right. Bottom- Evolution of the velocity profile at different positions upstream of the pore entrance: at 40 µm (red) 15 µm (green) and 2 µm (blue). The profiles are scaled by the maximum velocity in the pore zone, VMAX (left). Rescaled Velocity map V/V_{MAX} (right).

From the image analysis of the strikes, we can determine the trajectories of the particles that get captured on the top and the bottom part at the pore entrance. On Figure 52, we have superimposed those trajectories with the fluid streamlines we obtain from COMSOL. Far from the pore entrance, particles follow fluid streamlines that are all parallels. In the top part of the channel, when we

approach the entrance streamlines start to bend downward whereas the particle still goes straight. Thus, the particle departs from the streamline followed until that place in order to go towards lower speed zones. The particle eventually goes downward too when it is about to touch the pore wall. The particle has to move because of its finite size and once again crosses fluid streamlines. The particle is the closest to the pore wall as it enters into the pore. Thus, it gets likely captured by the wall at that place. However, the low frequency of the light modulation we used to get the streak lines does not allow us to capture precisely this location. Anyway, the accuracy in the z-position with this technique is about to 120 nm; distance which is greater than the width of the attractive part of the DLVO potential. In the bottom part, both the particle and the fluid streamlines bend downward but again the trajectory of the particle deviates from the fluid streamline to get into contact with the bottom wall.

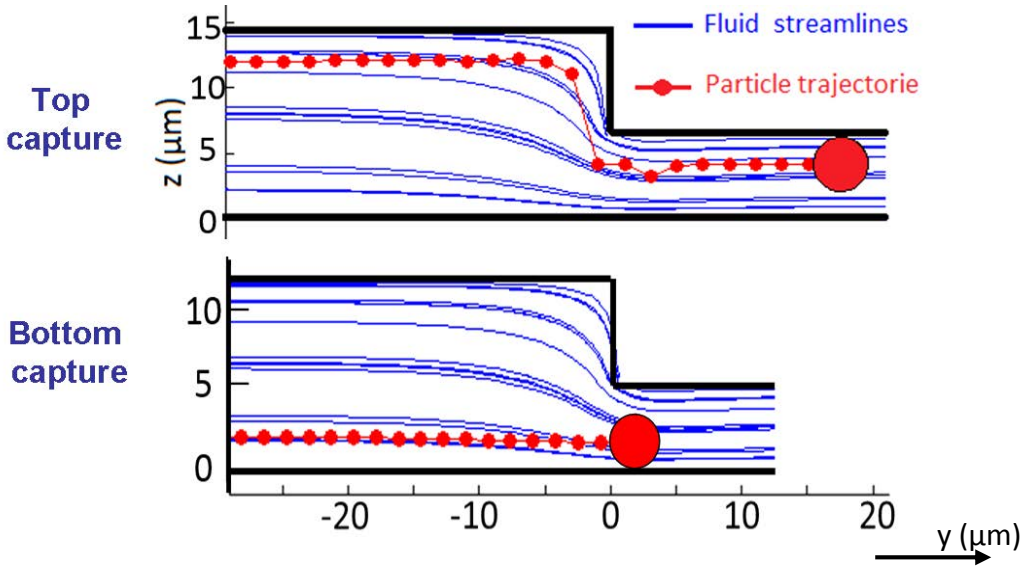

Figure 52: Trajectory of two depositing particles in the z-y plane (dotted red line) overlaid on the fluid streamlines (blue lines), one on the top wall and the other on the bottom one. The particles initially travels along a fluid streamline and cross fluid streamlines approaching the constriction. The flow rate is Q=0.6 µL/min.

From the particle trajectories, we can define the capture zone upstream of the pore from each part of the reservoir, top and bottom. By definition, particles that get captured at the pore entrance have their centre that lies within this zone. This zone is defined far enough upstream of the beginning of the pore, where the particle streamlines remain straight, here at 100 µm from the pore entrance. In Figure 53, we have plotted the evolution with the rescaled flow rate of both, the position of the centre, Z_{CAPT}, and the width, W_{CAPT}, of the capture zone (see insert). For the capture, on the bottom part, Z_{CAPT} increases rapidly with the flow rate (Figure 53-A). Thus, the capture zone departs from the bottom pore surface with the flow rate. At some point, for Q smaller than but close to Q_C, particles that are about to enter into the pore and close to the bottom wall, can still go towards it but they cannot come closer enough anymore to get captured. Thus, no deposition is observed above Q_C. For the capture associated with the upper part of the constriction, Z_{CAPT} decreases linearly with the flow

rate from 2.3 down to 0.5 µm for the highest rate. We do not observe any peculiar change of this quantity when $Q=Q_C$. The width of the capture zone also decreases rapidly with the flow rate from 1.8 µm, for the lowest rate, to 0.18 µm, for $Q=2.5\ Q_C$ and it is constant for higher rates (Figure 53-B). This levelling-off is likely to be an artefact related to our measurement accuracy. Indeed, we cannot measure precisely a z-position lower than 0.12 µm. Actually, W_{CAPT} should still decrease with the rate.

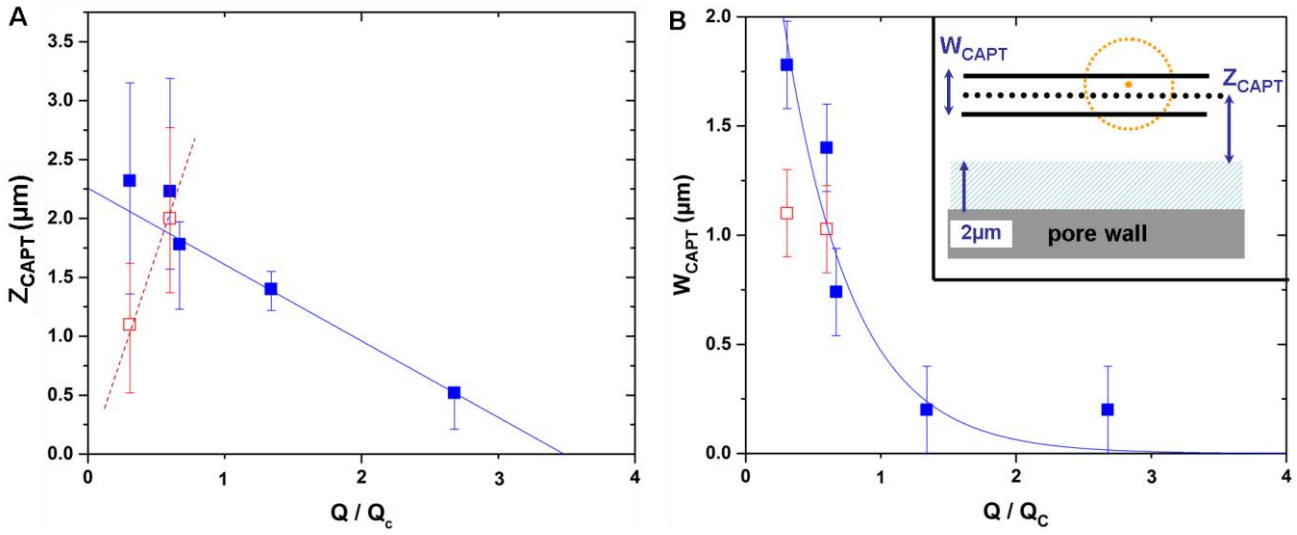

Figure 53: A- Evolution with the rescaled flow rate of the mean altitude of the capture zone, Z_{CAPT}. Full squares are particles depositing on top of the pore and the hollow ones are particles depositing at the bottom. No particles are depositing at the bottom for Q>Qc. The width of the error bar for each rate corresponds to the width of the capture zone, W_{CAPT}, whose evolution with the rate is also reported in B. The continuous line is a linear fit with a slope of 0.36. The dashed line is a guide for the eyes. B- Evolution of the width of the capture zone with the rescaled flow rate. The line is an exponential fit. Insert: schematic of the capture zone. The dotted circle and the hatched blue zone of width 2µm correspond respectively to a particle and the forbidden zone for the centre of a 4µm particle. Thus, when $Z_{CAPT}=0$ the particles are in contact with the pore wall, the bottom one or the top one. The blue curve is an exponential fit such as $W_{CAPT}=3.5\ \exp(-2Q/Q_C)$.

We can also interpret the width of the capture zone as the greatest net vertical distance that a particle can travel towards the wall as it is transported towards the pore entrance and get eventually captured by the wall. When the flow rate is small, particles can "easily" go across the fluid streamlines, which is not anymore true when $Q=2.6Q_C$. In this latter case, the particle which are going to be captured have to be, far upstream of the pore entrance, already really close to the wall.

2. Capture by the walls after interaction

In this section, we consider the influence or the interaction between particles on the deposition within the pore. Actually, as the clog grows, particles flowing in the reservoir eventually encounter immobile particles, which were previously captured within the pore. The repulsive hydrodynamic interactions (HI) between them change the initial trajectory of the mobile particle. In Figure 54-A, the

trajectory of the mobile particle first bends and levels off when the particle first encounters the particle doublet and then turns around the individual that is further downstream. We observe HI also between within the pore (Figure 54-C), but this time the interactions are screened by the pore height (H=1.6D), i.e., for a distance centre to centre higher than 2.6D the trajectory of a mobile particle is not modified by a still one. This HI can also lead to the deposition of a particle depending on the distance between the two objects (Figure 54-B). Indeed, we have a 3d repulsion between particles, and thus the mobile particle is pushed towards the adjacent horizontal wall and comes into contact with it. We cannot quantify with the streak technique those tiny variations of the particle altitude, when the mobile particle is turning around in the same time in the XY plane.

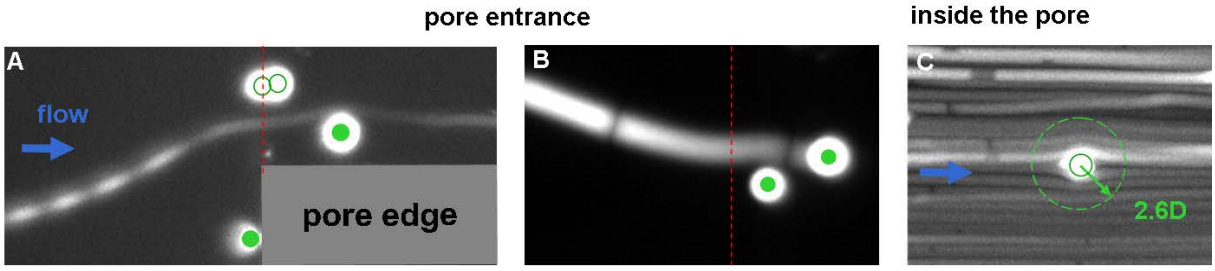

Figure 54: Streak images of the hydrodynamic interaction between a mobile and an immobile(s) particle(s) at the pore entrance (A-B) and further down, within the pore (C). The flow direction is given by the blue arrow, and the particle surfaces and the pore entrance correspond to the green circles and the red dotted lines, respectively. B- The mobile particle turns around the still one and get captured just downstream of it. C- The dashed circle corresponds to the maximum interaction length equal to 2.6 D, centre to centre (1.6D, surface to surface), between the immobile particle in its centre and the flowing ones (white discontinuous shiny lines).

Those binary HI depends a priori on the altitude of the mobile particle and on the distance *dx* between the centres of the mobile and immobile particles, perpendicular to the flow direction and taken within the reservoir zone, well before the two particles start to interact (Figure 55-A). In the Figure 55-B and D, we have plotted respectively the evolution of the distance between the centres of the two particles, d_{final} , when the mobile get captured and stops, with *dx* and the altitude of the mobile particle within the reservoir. In those graphs, we clearly see to mains features. Firstly, binary HI's quasi systematically lead to aggregate (doublet) formation, the mobile particle stopping either in contact with the immobile one, or at a distance d_{final} lower than a particle diameter. This remains true whether this interaction takes place at the pore entrance or occurs further downstream within it (green symbols).

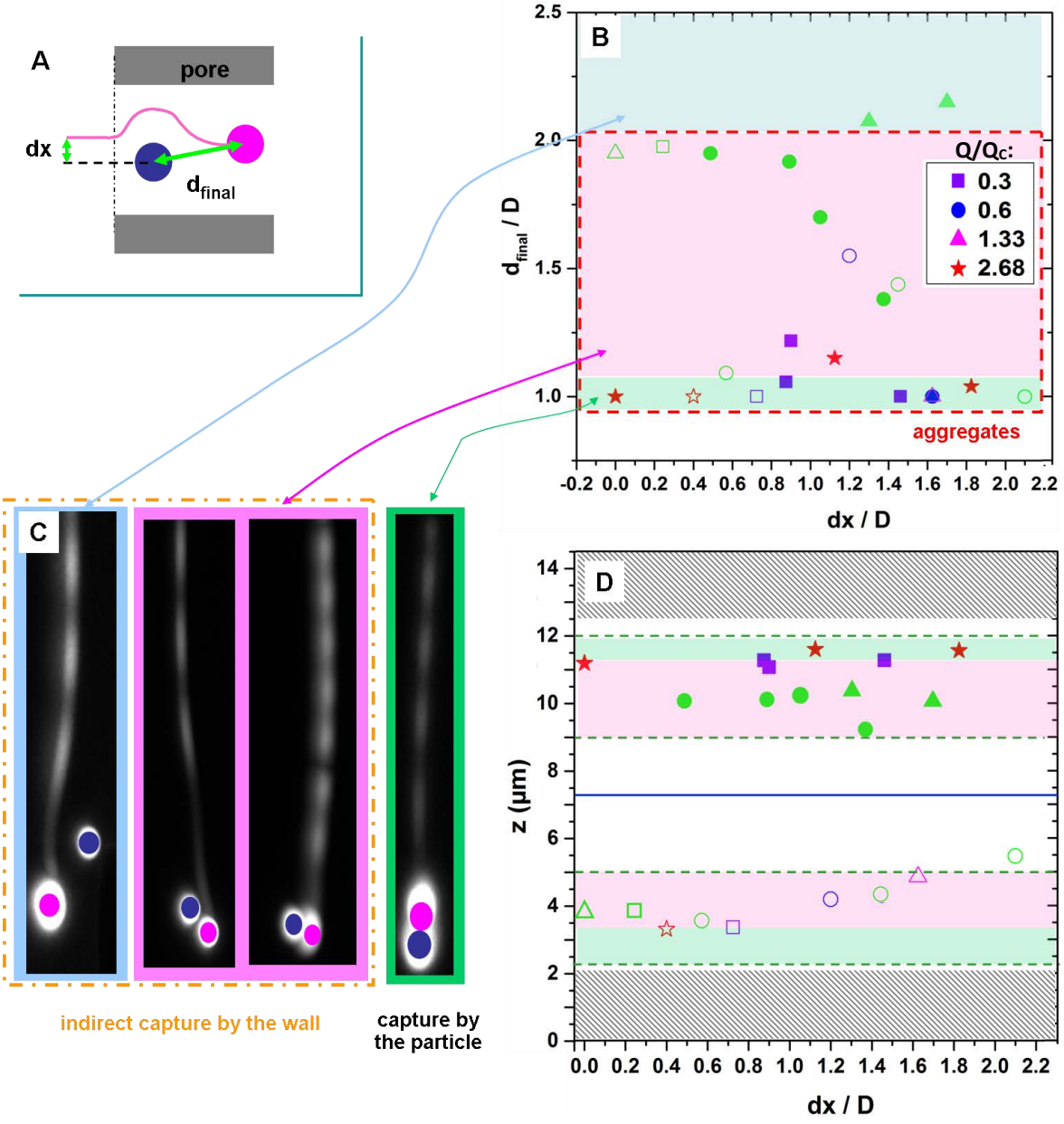

Figure 55: A-Deposition of a particle (pink) close to an immobile one (blue). The length dx is the distance between the two particle centres in the x –direction before they interact. The length d_{final} is the final distance between particles centres after the deposition of the pink one. B-Variation of d_{final}/D with dx/D for various flow rates. The hollow and the plain symbols correspond respectively to particles that come from the bottom and the top part of the reservoir. We have three zones with different colours which correspond to different modes of particle capture. The green one corresponds to the doublet formation when a particle is captured by another one. The pink one is the deposition after an interaction of the flowing particle with an immobile one. The distance between the two particles is smaller than D, thus they form an effective aggregate in 2d. The red dashed area corresponds to the zone for which dx/D is smaller than 2 and in which the two particles from an aggregate, in direct contact or not. The blue one corresponds to the deposition of the flowing particle at a distance greater than 2D of the still one, centre to centre. The green symbol corresponds to particle interacting with particle deposited far from the pore entrance. C- Images illustrating the different capture modes defined in B. The coloured square around the images corresponds to the colour code of B. D-Heights, in the reservoir, of the particles depositing. The altitude of the mobile particles lies within the capture zone defined for the direct capture (green dashed lines).

For the true doublets (particle in direct contact), we observe that the flowing particle stops most of the time at the rear of the still one (Figure 56).

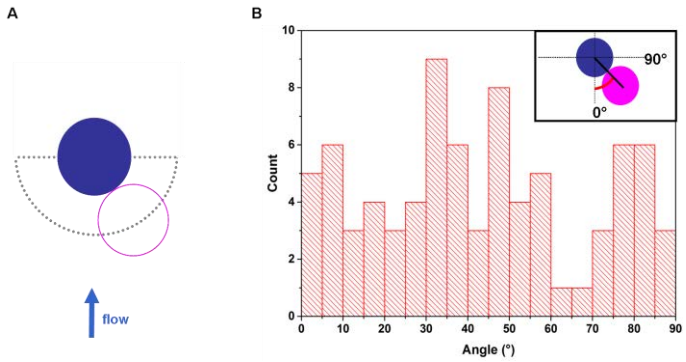

Figure 56: Doublet formation. The grey dotted semi-circle corresponds to the final different positions the flowing particle centre (hollow pink circle) when it is captured by an immobile particle (blue circle). B- Histogram of angle distribution between the two particles according to the flow direction. We do not make any distinction between the right and the left quarter, we add them in order to get only the angle variation in between 0, and 90° (insert)

Secondly, the altitude of the particles that are about to be captured, always lies within the capture zone defined for the direct capture. In particular, we form regular doublets (two particles in contact) only at the pore entrance. In this case, the mobile particles are always very close to one of the horizontal walls within the reservoir, whatever the values of dx and Q. For the other particles which are just a bit further from the wall, we form the other type of aggregate (particles are not in contact) at the pore entrance. For the binary HI well within the pore, it is difficult to establish a relationship between the altitude in the reservoir and D_{final}, since we do not know what the particle altitudes within the pore are. Anyway, we clearly see that their altitude within the reservoir lie at the middle of the capture zone of the direct capture. In most of the cases, those mobile particles end up by forming doublet in which particles are not in contact. This likely comes from a longer range binary HI since the confinement is more important within the pore [75]. Images corresponding to the different capture modes are also shown in Figure 55-C. It is also worth noting that for dx/D> 2.6, we have not observed any indirect particle capture. We suppose that above this value, the HI is screened by the pore height H (dx/D=2.6 corresponds to a distance, surface-to-surface, equals to H).

We have done the same analysis for HI between a mobile particle and an aggregate (Figure 57). Here again, particles coming from either the bottom or the top part of the reservoir lie within the same capture zone that of the particle direct capture by the wall defined in Figure 50 (Figure 57-B). Actually, the capture zone is smaller for the bottom part but we think that it comes from the fact that we do not have data for the highest flow rates (1.33 and 2.68 Q/Q_C). We also get a poor statistics for $Q<Q_C$, because there are not too much aggregates for this range of flow rate. It is worth noting that the vast majority of captured particles that come from the side are located in the top part of the reservoir. Moreover, those particles, after they are captured, increase the size of the aggregate because they become still at a distance smaller than a particle diameter of the aggregate they have interacted with

(Figure 57-A). For particles that come from the centre zone, within the reservoir, we observe that they can deposit far downstream of the aggregate they have encountered, when dx/D_{OBJ} is small. In this case, the bigger the aggregate the more upstream of it the trajectory of the mobile particle is modified, as one can see on the two examples in Figure 57-C. This simply means that the range of the HI increases with the aggregate size.

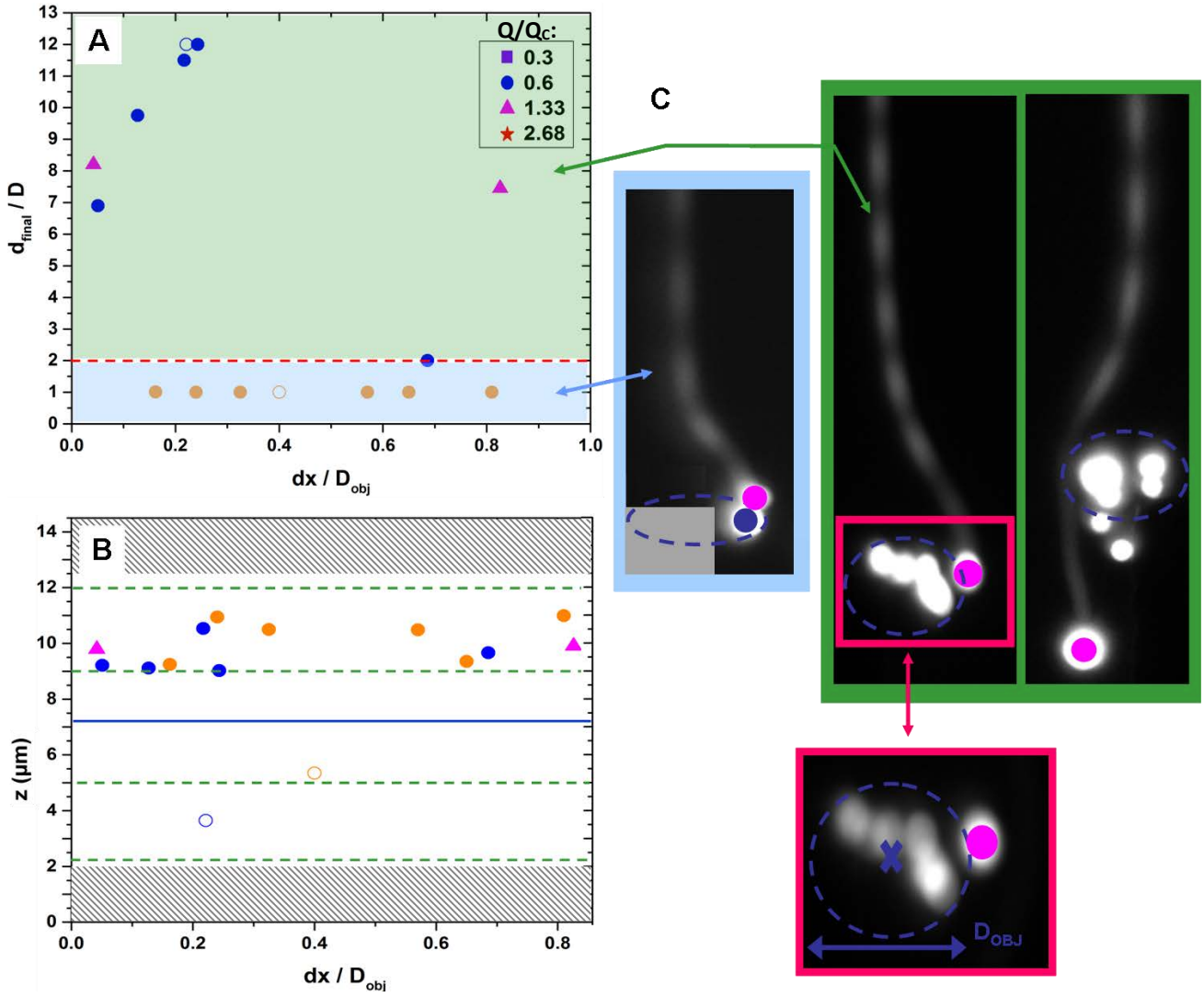

Figure 57: A-Variation of D_{final}/D with dx/D_{obj} for various flow rates. The hollow and the plain symbols correspond respectively to particles that come from the bottom and the top part of the reservoir. The two coloured areas correspond to the two zones within the reservoir, the centre or side ones. The green one corresponds to the interaction of a flowing particle with an object (aggregate) in the centre zone, while the blue one is related to flowing particles coming from the side and interacting with an object, i.e., a particle, or an aggregate, plus the pore edge. B- Altitude of the mobile particle in the reservoir prior to its deposition. The dashed green lines corresponds to the capture zone we identified for the direct capture of particle by the constriction. C-Images of the two zones with the same colour code as in A. A dashed ellipse outlines the object with which the flowing particle interacts. In the side zone (first left image), pore edge (grey rectangle on the bottom left corner) is a part of the object. The capture zone of the middle image is also zoomed in (red rectangle), where we define the centre (cross) and the size of the object, D_{OBJ}. The pink circle is the one that was in motion and thereafter captured by the object.

Now let us look in more details, for the particle-particle interaction that leads to capture, the evolution of mean altitude of the capture zone, Z_{CAPT}, and its width, W_{CAPT}, with the flow rate (Figure 58). We clearly see that on the overall flow rate range, both the mean altitude of the capture zone and its width are greater for the indirect capture mode than for the direct mode. This means that HI between a still particle and a mobile one helps to capture particles which would not have been captured directly by the pore wall otherwise. Moreover, the highest values of the mean altitude and of the width of the capture zone indicate that HI cannot help a flowing particle to go across the channel along its height. Indeed, we have checked for instance that a flowing particle, which was previously located in the top part of the reservoir, will remain closer to the top part of the pore, as it flows through it. Thus, particle-particle HI draws particles near the closer horizontal wall. Actually, this indirect capture event occurs when a flowing particle and a still one are not located on the same part of the channel. For example, a flowing particle that comes from the top part of the reservoir will be pushed towards the top horizontal wall of the pore as it flows close to a still particle deposited on the bottom pore wall, and vice and versa. Therefore, particles that come from either the top or the bottom part of the reservoir will keep moving in the top or the bottom part of the pore, respectively, even though they encounter multiple still particles or aggregates along their path. It's also worth mentioning that we have deposition of particles coming from the bottom part of the reservoir due to the indirect capture mode for all applied flow rates, whereas it is limited to $Q < 0.5Q_C$ for the direct particle capture mode.

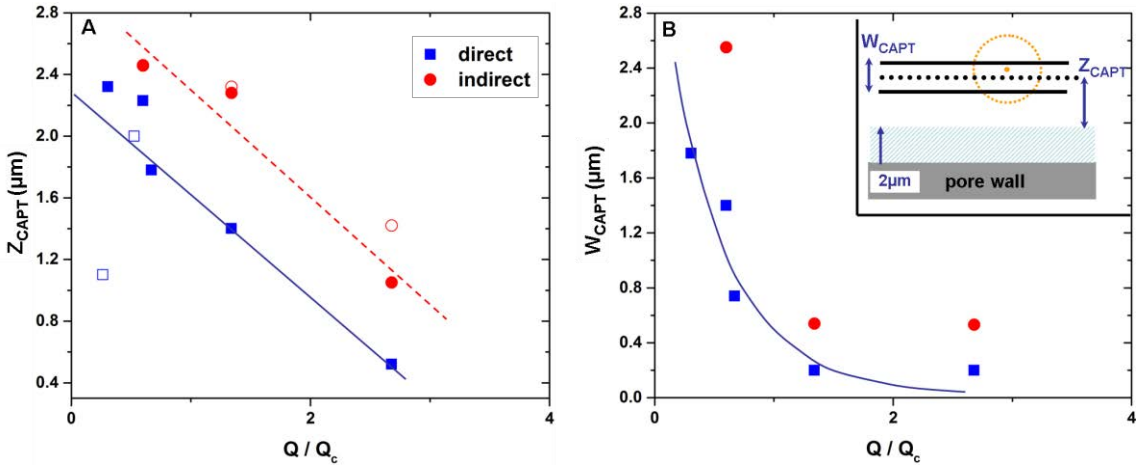

Figure 58: Evolution with the rescaled flow rate of the mean altitude of the capture zone, Z_{CAPT} (A) and its width W_{CAPT} (B), for both direct (blue symbols) and indirect capture (red ones). Hollow and plain symbols are still respectively associated to bottom and top part of the reservoir. A-The line is a linear fit of the data whose parameters are defined in Figure 53. For the indirect capture the value of Z_{CAPT} for the smallest rate is the same for the top and the bottom part, thus we cannot distinguish both symbols. Insert: schematic of the capture zone. The dotted circle and the hatched blue zone of width 2 µm correspond respectively to a particle and the forbidden zone for the centre of a 4 µm particle. Thus, when Z_{CAPT}=0 the particles are in contact with the pore wall.

We have limited ourselves to the binary HI, but the deposition of a new particle within the pore can be even and often more complicated. Indeed, a particle can encounter along its path more than one

object, particle or aggregate, before it gets captured. We gather on Figure 59-A few examples of these multiple complex HI that lead to particle deposition. Moreover, those obstacles exhibit different sizes (from a single particle to large aggregates) and orientations with respect to the flow direction (Figure 59-B).

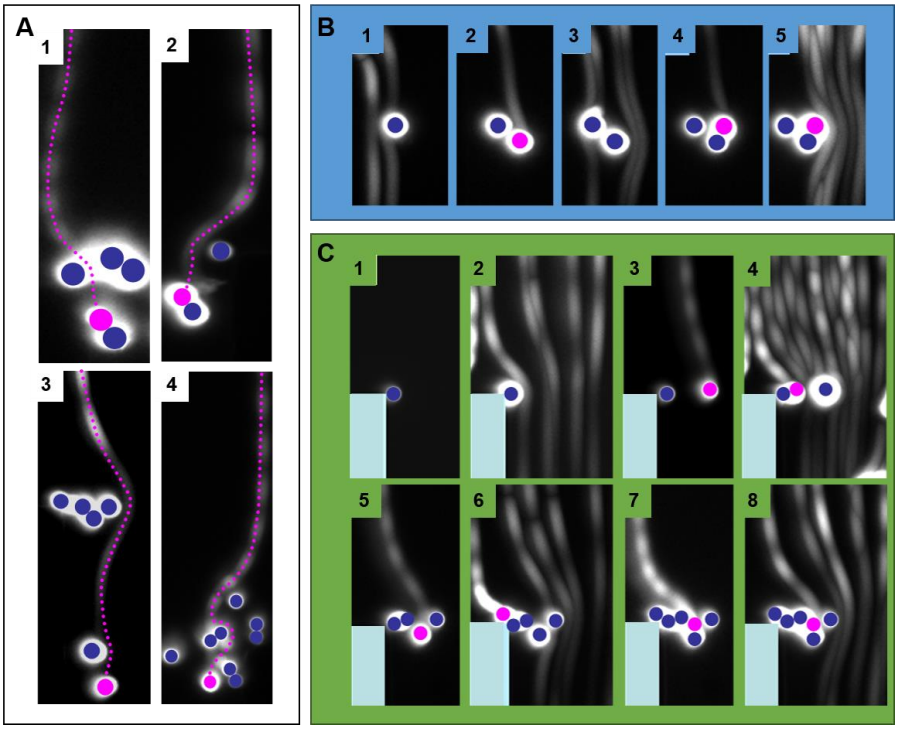

Figure 59: A-Particle deposition (pink circles) after having encountered multiple obstacles (particles or aggregates). The dotted line outlines its trajectory. B, C-Progressive formation of a triplet (B) and a sextuplet (C). Each time a new particle is captured (pink circle) by the aggregate (blue circles), we get on the next image various particle trajectories around the aggregate. In all images, flow direction is from top to bottom.

Finally, this indirect capture mode can also lead to another growing mode of the aggregates (Figure 60). A flowing particle deposits in between two aggregates and in this way creates a single larger aggregate. This merging process occurs more often at the end of the pore clogging.

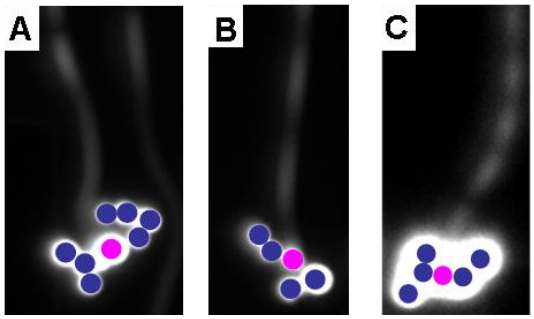

Figure 60: Images of merging aggregates. The pink particle comes and gets captured in between two aggregates (blue particles), forming in this way a larger one.

We can sum up the various cases of deposition, direct or not, based on the final position of a particle within the pore and relatively to a single particle or the closest particle belonging to an aggregate (Figure 61). The direct capture by the horizontal walls concerns only a particle that deposits at a distance smaller than 4D from pore entrance. Moreover, this particle has to be at a distance greater than α=3 of the closest particle (with α being the distance centre to centre to the closest particle rescaled by the particle diameter D). When α<2 we consider that the new particle partakes to the aggregate growth. For 2 $\leq\alpha<$ 2.2 or $\alpha>$ 1.5 D_{obj}, the trajectory of the flowing particle was modified respectively by another particle or an aggregate of size D_{obj}. In both cases, the new-deposited particle is considered as an isolate one. The indirect deposition also occurs at the end of the clogging process, in the line regime. In this case, the HI leads to the deposition of the flowing particle at a distance greater than 4D from pore entrance.

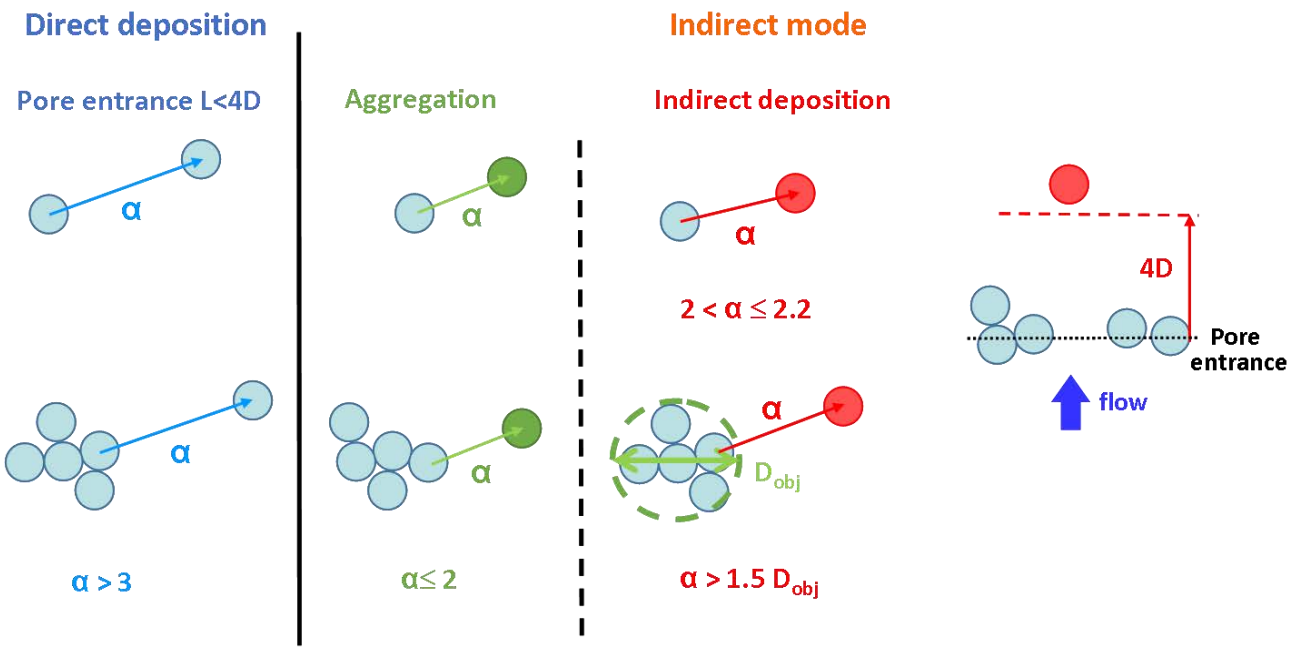

Figure 61: Various deposition mechanisms. α is a rescaled distance with α=1 corresponding to D, a particle diameter or to D_{obj} if the closest object to the depositing particle is an aggregate. This distance allows discriminating between the three types of deposition mechanisms we identified. Particle depositing further than α=3 are capture directly by the constriction and have not interacting with already deposited particles. Particles with α<2 forms an aggregate with the object they interacted with. Finally, particle depositing in intermediates α are deposing after interaction with an object.

C. Statistics of the various deposition mechanisms

1. Capture of a particle by the wall

Now we have identified the different mechanisms of particle capture either by the wall or by an aggregate, we will determine the probability for each of those mechanisms. In the following, we will focus only on one ratio of width, $W_R/W=4$, the same behaviour being obtained for the other ratios. We start with the direct capture of particles by the pore wall. However, usually, when a particle is about to be captured somewhere by the pore wall, other still particles may be present in its vicinity. As we have seen in the previous paragraph, those particles can interact with the mobile particle and thus likely modify its capture probability by the wall. Indeed, we can see on the Figure 62 that the probability to capture a new particle increases if another is already here. In this example, for a given Q, the probability becomes constant only when the distance between the new captured particle and the still one is greater than one particle diameter D.

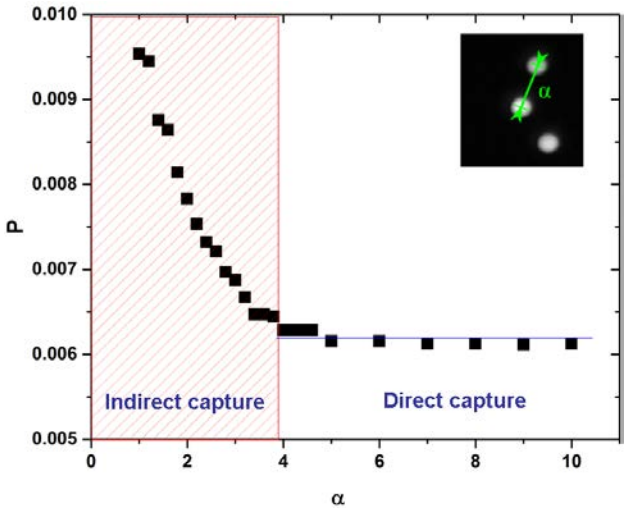

Figure 62: Evolution of the probability of deposition of a particle as a function of the distance of another one, rescaled by the particle diameter D. Insert: definition of α, which corresponds to the distance centre to centre between two adjacent particles.

Therefore, below this critical distance, called thereafter α_C, we have an indirect capture by the wall, while beyond α_C, the particle capture is not modified by another still particle and does depend only on the particle-wall interaction, i.e., a direct capture by the wall. This latter probability is directly linked to the width of the capture zone within the reservoir. Assuming a uniform density over the whole height of the reservoir this probability should be simply the ratio between the flow rate in the capture zone and the total flow rate [3]:

$$p = \frac{Q_{Capture}}{Q_{total}} = \frac{W_{capt}W_R}{H_R W_R}\frac{v_{capt}}{v_{total}}$$

$$p = \frac{Q_{Capture}}{Q_{total}} = \frac{W_{capt}}{H_R}\frac{v_{capt}}{v_{total}}$$

where, v_{capt} and v_{total} are the mean velocities in the capture zone and the overall height of the reservoir. The velocity dependence comes from the parabolic shape of the velocity profile along the z-direction. In particular, as the capture zone gets closer to the pore surface when the flow rate increases (Figure 51), the velocity within this zone decreases and thus reduces the probability.

We determined the probability density along the z-direction and we found that this one is not a constant. Actually, there are preferred locations, one close to the top and the other near the bottom part of the reservoir. We suppose that the particles start to drift towards the horizontal walls from the inlet of the microfluidic device. We calculate that this drift is around 5-20 nm/µm until the particles found a stable position at a fixed distance from the wall equal to a particle radius, surface to surface. Whatever the flow rate, we hardly found particles at the reservoir mid height (Figure 63). We have then taken into account this non-uniform particle spatial repartition in the zone capture from the rest of the reservoir. Therefore, the probability must be corrected by the ratio between the density in the capture zone and the whole reservoir height:

$$p = \frac{W_{capt}}{H_R}\frac{v_{capt}}{v_{total}}\frac{\rho_{capt}}{\rho_{total}} \qquad (4)$$

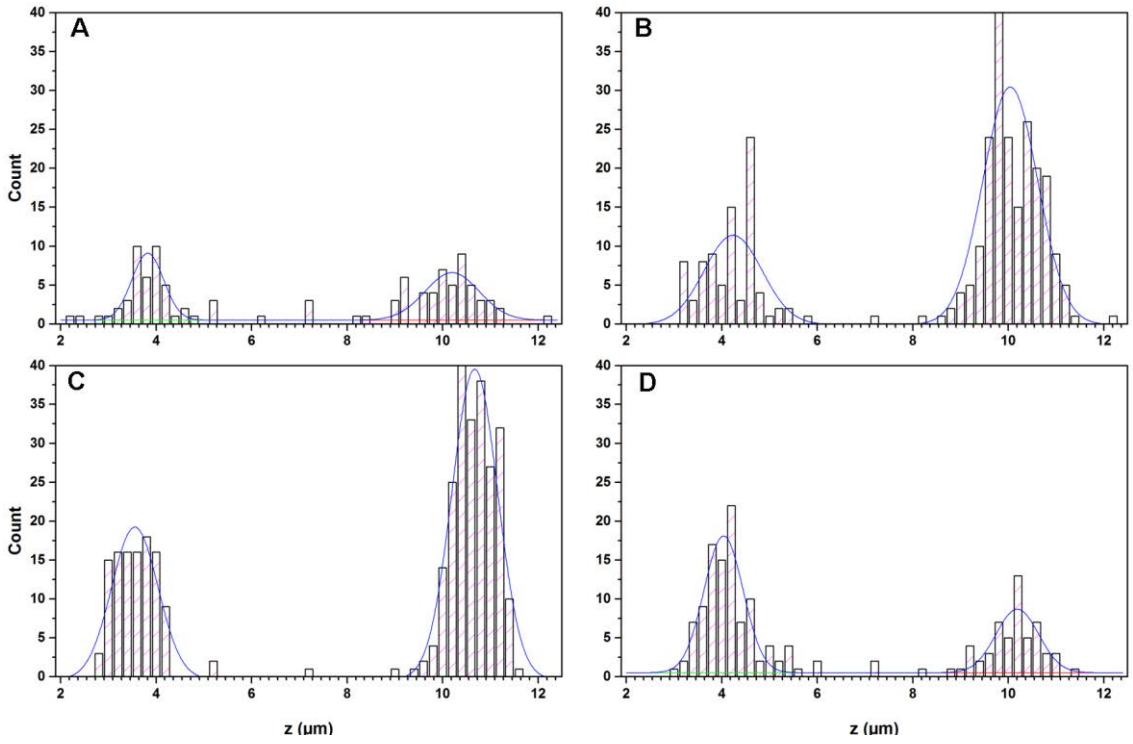

Figure 63: Repartition of particles in the z direction in the reservoir at 100µm from the pore entrance for Q/Qc =0.35 (A); 0.71 (B); 0.92 (C); 1.23 (D). The central zone of the reservoir (the highest speeds) is depleted in all cases. Particles are mainly in two zones centred on z=4 µm and z= 10.5 µm, for all flow rates.

In order to calculate the direct capture probability we used the probability density profile 100µm upstream of the pore entrance, where particles follow fluid streamlines (Figure 64-A). From these profiles, we simply count the number of particles that belong to the capture zone (Figure 53-A) and calculate the ratio of density, which is around 0.08-0.1 for most of the flow, rates (Figure 64-B). The resulting probability is shown on the Figure 65-A (blue symbols).

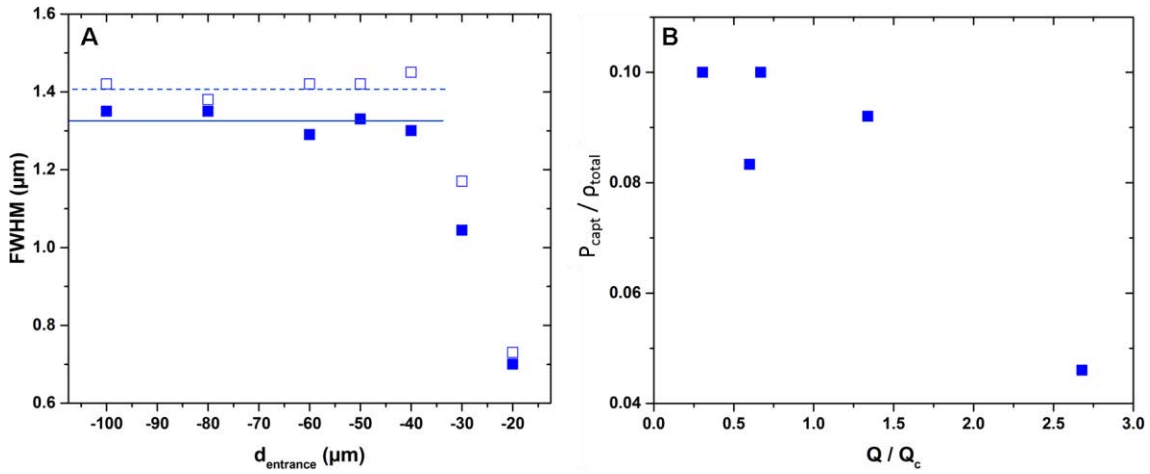

Figure 64: A- Evolution of the full width at half maximum (FWHM) of the probability density for various distances from the pore entrance, for the bottom (open symbols) and the top (plain symbols) parts. The two lines are guides for the eyes. B- Evolution with the flow rate of the ratio between the particle concentration within the capture zone and the total concentration.

We can also obtain this probability thanks to confocal experiments. In this case, the probability is inversely proportional to the average time between two particle depositions (Figure 65, red symbols), the averaging being done on the overall the experiment, up to the clogging. It is worth noting that there is a good agreement between the data coming for the both techniques. We get an exponential decay of the probability with the flow rate, this behaviour being directly linked to the evolution of the capture zone width W_{CAPT}. Indeed, W_{CAPT} decreases exponentially with the flow rate, with the exact same growth rate that of the direct capture probability.

From the confocal analysis, still based on the average time between two particle depositions, we have determined the probability related to the indirect capture (Figure 65-B). Here, we consider only the deposition events that do not lead to the aggregates formation or growth. In this indirect case, the evolution of the probability is not only related to the variation of the width of the capture zone, corresponding to the indirect particle mode, with the flow rate. This probability also depends on the presence within the pore of an obstacle and on its size. Actually, this mode of capture shows up mostly when some aggregates form at the pore entrance. Below $Q<Q_C$, only few particles are deposited by this capture mode at the very end on the clog formation.

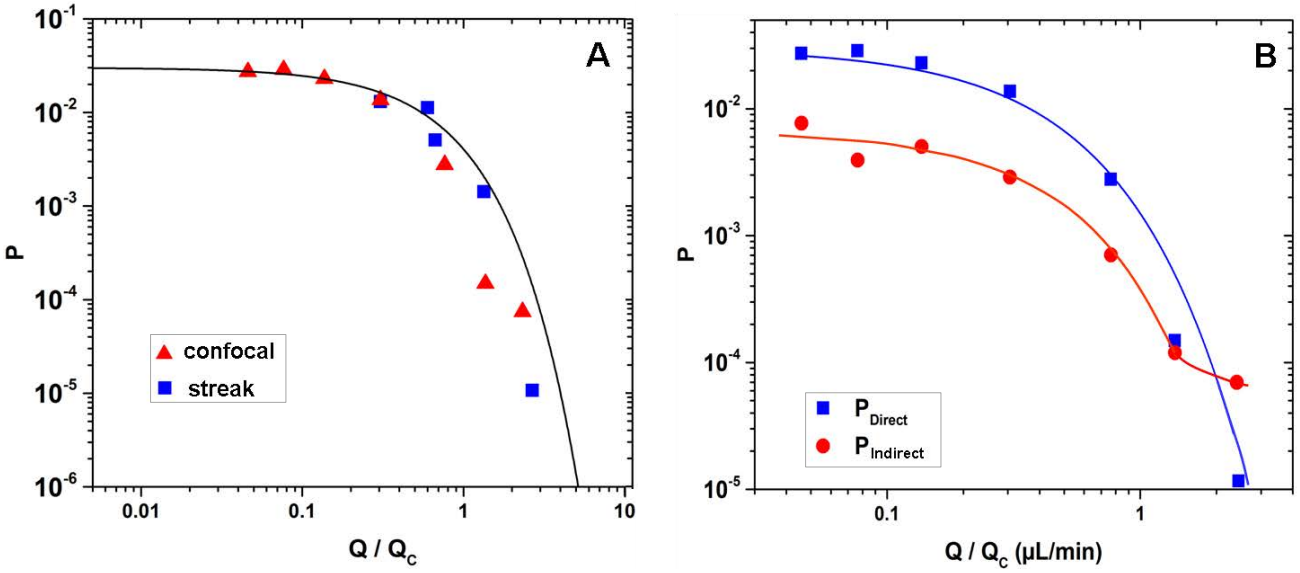

Figure 65: Variation of the probability of direct capture of particle by the pore wall with the rescaled flow rate. The data coming from the analysis of the streak images and the confocal imaging are respectively the blue and the red symbols. The line is an exponential fit of the data coming from the variation of the width of the capture zone and the particle concentration within this zone such as $P=0.024\exp(-2Q/Q_C)$. B- Probability of the direct (squares) and indirect capture (circles) by the pore wall versus flow rate. The two lines are guides for the eyes.

2. Aggregate formation

The probability related to the aggregate growth is determined from the time interval needed to deposit a particle at a distance $\alpha \leq 2$ of (i) another single particle (doublet formation), (ii) the closest particle that belongs to an aggregate. In Figure 66-A, we have plotted, for various flow rates, the evolution of the probability for aggregates of different sizes to grow by gaining one particle. Even for low Q, there is aggregate formation even though those ones remain small and they are never bigger than quintuplets are. It is worth noting that the range of aggregate sizes increases with the flow rate. The aggregate growth rate, directly related to the probability, is the same for all aggregates, irrespective of their size, for each flow rate. This is even more surprising because not all those aggregates have the same shape and their locations within the pore are different. This constant growth rate remains constant as long as aggregates are not too close to each other, and thus they can grow independently. These features likely come from our definition of an aggregate in which particles are not always in contact. This indicates that aggregate growth depends mainly on the flow rate and only on the local properties around the aggregates, at the particle scale.

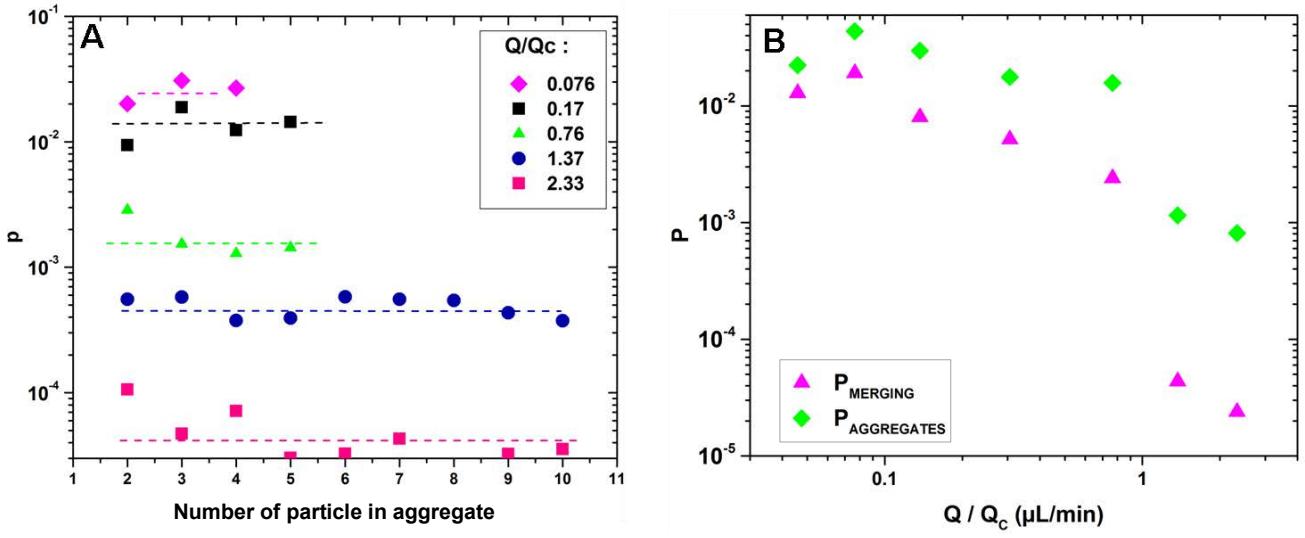

Figure 66: A-Probability of aggregate formation for various flow rates. The dashed lines correspond to the average probability for each flow rate used in B. B-Variation of the average probability to form an aggregates which size in between 2 and 10 (diamonds) and to merge two aggregates (triangles) whatever their sizes, with the flow rate.

It means that binary hydrodynamic interactions, i.e., HI between a particle, at one of the aggregate edges, and a flowing one, which is about to be captured, are responsible of the aggregate growth. Thus, this implies that the flowing particle has to be close enough of the aggregate to be captured by it, as we have seen before (see Figure 55, Figure 56). We have also to consider another growth mode, the merging mode, during which a flowing particle get captured in between two independent aggregates. In Figure 66-B, we have reported the evolution of both the average growth rate of aggregates and the probability of merging two existing aggregates, irrespective of their sizes, with the flow rate. We clearly see that for all flow rates, aggregates grow independently to each other rather than by merging. Actually, the aggregate growth by merging corresponds to the cases where there is not enough room in between two aggregates, i.e. a particle cannot flow in between them and thus makes the connection between them (Figure 60). Therefore, as the pore being filled by particles, we observed first that individual aggregates grow and then, at some point, some of them may merge, likely when we get closer to the end of the clogging process.

Now we have defined the different mechanisms of particle capture and their related average probability, we can try to explain the line-invasion morphological transition at the particle scale.

D. Discussion: Line-invasion transition at the particle scale

The influence of the different capture modes on the line to invasion transition can be first determined by comparing the contribution, in term of average probability on the overall experiment, of all modes, direct and indirect captures by the pore walls, with the flow rate (Figure 67-A). We can as before, distinguish two regimes. Below Q_C, all the capture modes decrease in the same manner, while from the line to invasion transition, that is for $Q=Q_C$, and beyond, the aggregation become the main deposition mode. The aggregation mode decreases more slowly with the flow rate than the indirect single particle capture mode while the direct mode dramatically drops down. We can thus first conclude that the line to pore invasion transition is related to a change of particle capture mode within the pore. We can see it more clearly on the Figure 67-B, where we compare the probability of the direct mode and the total indirect mode, which includes the aggregation, the merging and the single particle capture.

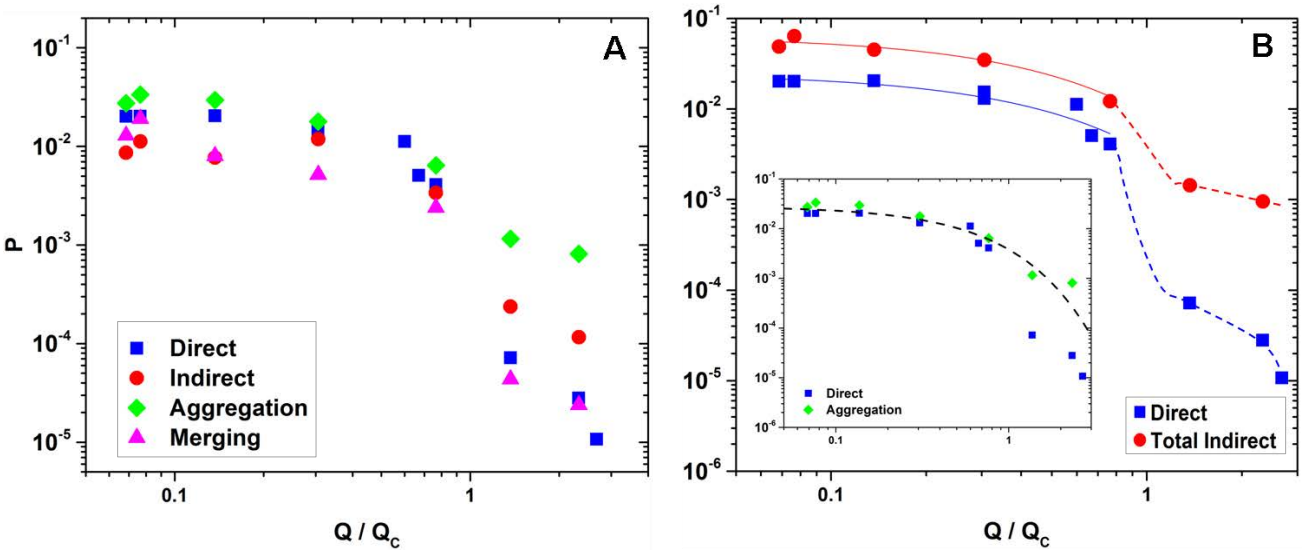

Figure 67: A-Variation of the average probability with the rescaled flow rate for the different capture mechanisms. B-Evolution of the direct (squares) and indirect (circles) capture mode with the flow rate. Thick lines are exponential fits with the same growth rate and dashed lines are guides for the eyes. Insert: same data as in B where we consider only the aggregation mode instead of the total indirect mode.

Below Q_C, both modes, direct and indirect, really evolve in the same way with the flow rate. They follow an exponential decay with Q, i.e., with the same growth rate. This evolution directly comes from the variation of the capture width W of the direct capture with Q (cf. Figure 53). Therefore, in the line regime, particles are captured at the pore entrance, by the horizontal pore walls, with a greater probability, around 2.57 times greater for the indirect mode, i.e. if they get captured in the vicinity of a still particle. Actually, this probability increase is simply related to an increase of W due to the binary HI (cf. Figure 54). For a given flow rate $Q/Q_C=0.3$, W increases of 1.8 µm and the density of particles increases by a factor of 1.45, the capture probability being proportional to both (cf.

Chapter III -C.1-Capture of a particle by the wall). From this calculation, we found that the capture probability due to the indirect mode is greater than that of the direct mode by a factor of 2.66, which is really close to the value we found form the fits of both probabilities just mentioned above (Figure 67-B).

In the invasion regime, above Q_C, the indirect capture mode largely dominates over the direct one, with a probability 25 times bigger. Actually, the aggregates growth dominates the indirect mode. Thus, this simply means that even at the pore entrance very few particles can deposit by direct capture. Instead, some aggregates grow quite faster within the pore, not only at the pore entrance. In the following, we will study in more details the building-up of the clog for each regime.

1. Line regime

Successive images of the particle deposition within the pore, for two flow rates ($0.076Q/Q_C$ and $0.76Q/Q_C$) in the line regime are shown on Figure 68. For the smaller one, the first particles deposit within a zone of width 4D from the pore entrance, corresponding to the direct capture mode (top, image 1). Actually, for such low Q, particles get captured mostly at the very entrance of the pore (image 2).

After the deposition of 5 particles in the same way, doublets are also formed at the pore entrance, still captured by the top wall. As new particles arrive at the pore entrance we form most exclusively aggregate and a discontinuous line starts to show up. In this range of flow rate and for a pore width of 80µm, only 6 to 8 particles in average, at captured by the wall without interacted with a still particle, which is expected. Indeed, in an ideal case where the distance between the captured particles is the same, we cannot have more than 6.7 particles at the line deposited in the direct mode. Otherwise the average distance between particles will be lower than one particle diameter, distance below which a still particle captured at the entrance modify the flow around it, and enhance the capture of the particles that pass within this zone. To sum up, at the beginning of the building up of the clog, we observe direct capture, and then small aggregates form. Their size and growth are rather limited. Most of the time, a doublet or a triplet merged with another aggregate of the same size by merging, when a new particle get captured in between them.

For the higher flow rate (bottom raw), the most of the feature are the same, but we observe than in average particle are deposited further down within the pore, from its entrance. The shape of the clog is still a line but this one is really more tortuous, as we can see on image 6 of both rows. For both flow rates, indirect deposition, particles deposit at a distance greater than 4D from the pore entrance (red circles, in the image 3 in the top and image 1 and 2 in the bottom) is rather limited. Moreover, those particles do not partake to the clog formation. In each case, those indirect deposition events come from the HI between the flowing particle and one or two aggregate present at the pore entrance.

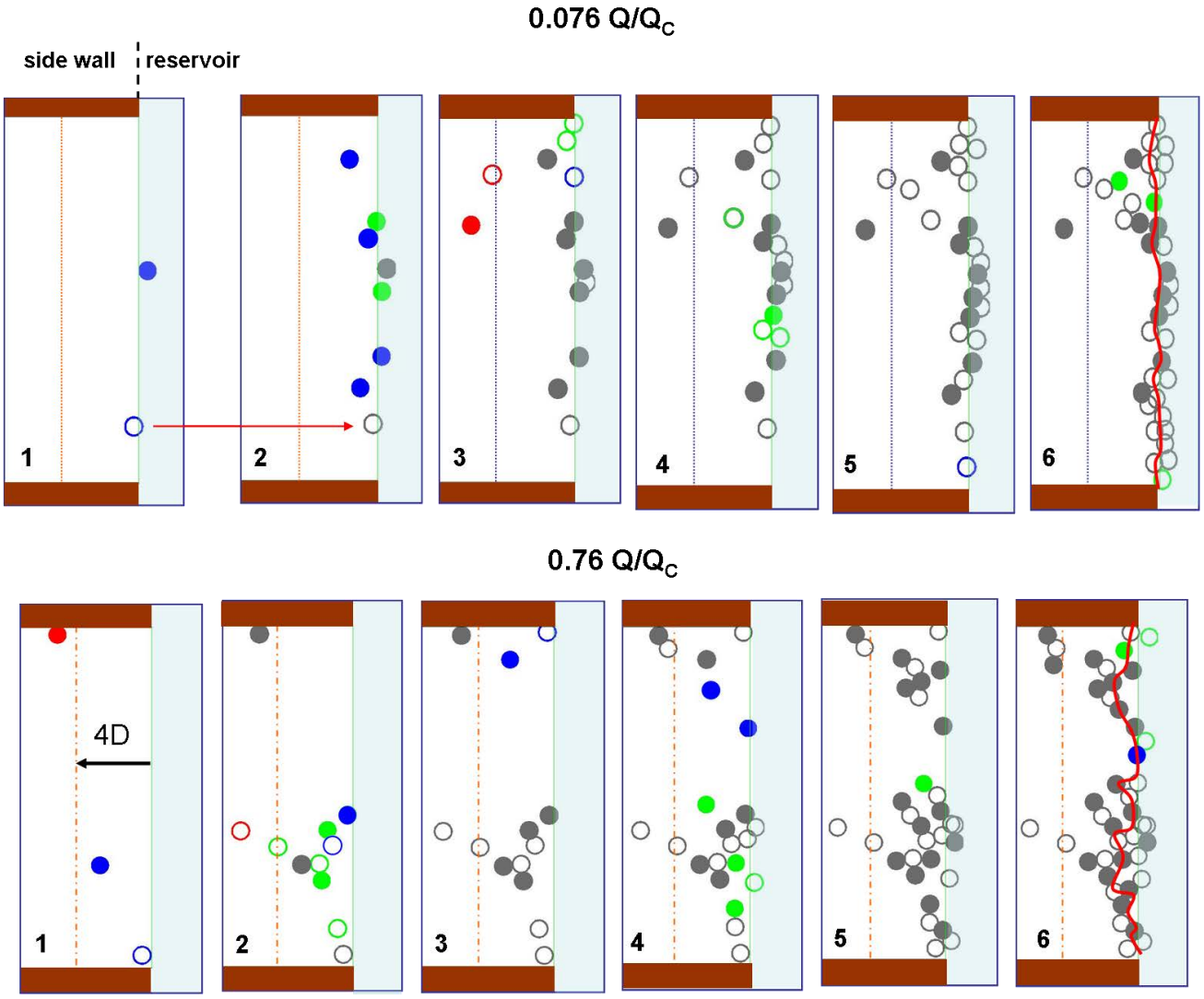

Figure 68: Consecutives images of the clog building up for two flow rates, 0.076 Q/QC (top raw) and 0.76 Q/QC (bottom). The turquoise zone corresponds to the reservoir zone and the two brown rectangles are the lateral pore walls. The colour code corresponds to the one defined earlier on Figure 61. The blue, green and red symbols correspond respectively to the direct capture, the aggregate and the indirect capture mode. The grey particles correspond to the ones that were previously deposited. The plain and the hollow symbols are respectively for the particles captured by the top and the bottom walls

2. Invasion regime

The progressive clog building up in the invasion regime is shown in Figure 69. Here, the situation is quite different. Even at the beginning of the experiment, there are very few particle depositions within the pore entrance. We hardly see more than two to three particles captured directly by the horizontal walls at the pore entrance, that is, without having interacted with another particle or an aggregate. Moreover, those particles stop within the pore with their centre lying in average at a distance from the pore entrance equals to 2.5D (Figure 70-A). In this case, the HIs between particles do not take place at the pore entrance anymore but rather entirely within the pore. Once a particle deposits whether at the pore entrance or further down within the pore, an aggregate rapidly grows at that place (Figure 69). As Figure 70-B shows, this growth is mainly due to binary HI with a short distance. Indeed, in this graph we have plotted the probability to capture a particle at a distance *d* of another one that was just captured.

This probability decreases rapidly and exponentially with the *d*, and from d=0.6D there is no particle capture anymore due to the binary HI. Beyond this distance, this HI still modifies the trajectory of the flowing particle but does not lead to its capture by the wall. Therefore, for $Q=Q_C$, because the mean position of the particle centre captured directly is equal to 2.5D, a flowing particle that enters within the pore, will start to interact with this immobile particle at a distance from the pore entrance (4-5 µm) beyond which the fluid velocity is constant. Finally, it is worth noting that the short range of the binary HI within the pore also explains why we found that the aggregate growth for a given Q is constant irrespective of the aggregate size (cf. Figure 66). Indeed, when a particle is captured by an aggregate, it stops at a distance smaller than D from one of the aggregate edges. Thus, the flowing particle interacts only with the particle located at this edge in order to be captured.

As we have seen before (cf. Figure 58), particles that encounter another particle or an aggregate and are captured have their centre that lies within the capture zone W_{CAPT} in the reservoir. In the invasion regime, W_{CAPT} decreases very slowly with Q and is far greater than the one associated to the direct capture. From the equation (4) (cf. Chapter III -C.1), we can calculate the average probability to be captured by an aggregate within the pore. We found that this probability decreases also slowly from $4x10^{-3}$ down to $2x10^{-3}$ when we twice the value of Q for $Q>Q_C$, values which are good agreement with the average probabilities we found from the confocal measurements (cf. Figure 67-B, red points above Q_C).

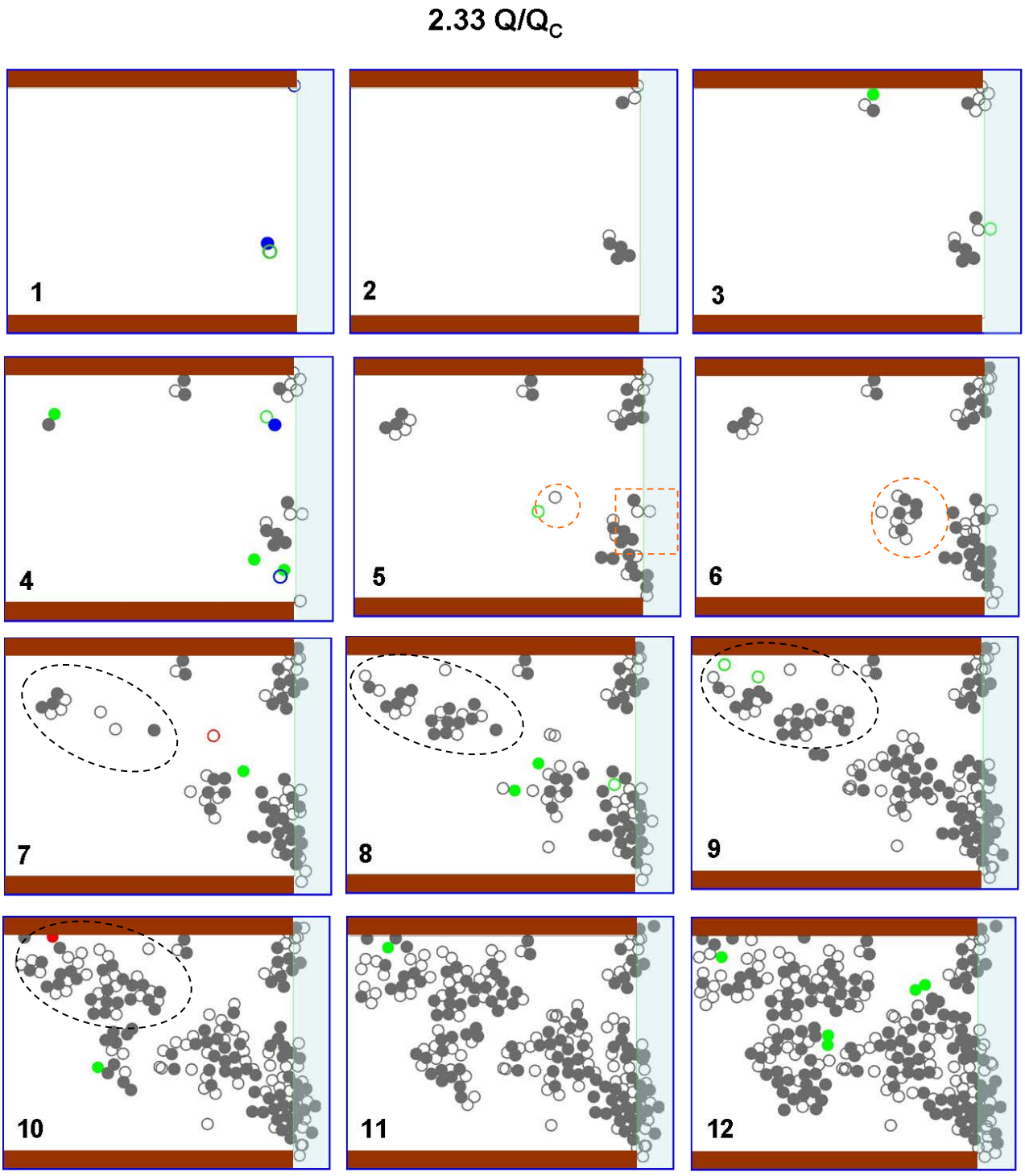

Figure 69 : consecutives images of the clog building up for a flow rate of 2.33 Q/Q_C. Refer to the Figure 68 for all the details of this figure.

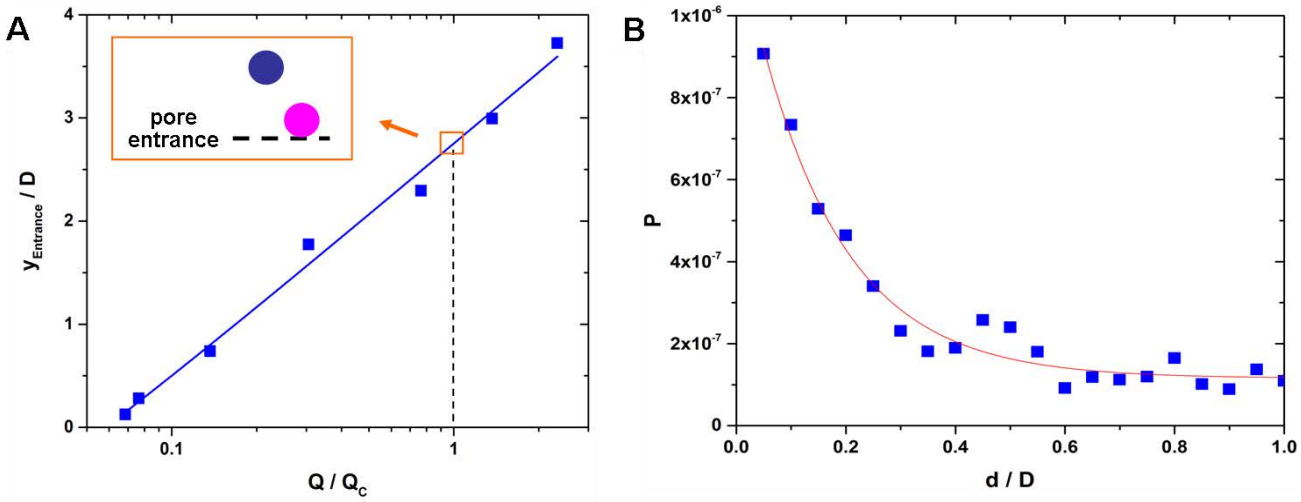

Figure 70: A- Average position from the pore entrance rescaled by D of the particle capture directly by the horizontal walls of the pore. The line is a logarithmic fit such as $y_{Entrance}$ / D = ln(15Q/Q_C + 0.09). For Q=Q_C, a flowing particle (pink circle) comes into the pore before interacting with the still one (blue circle). B- Probability to deposit a particle at a given distance d/D of a particle which was just captured. The line is an exponential fit such as P=1.15x10^{-7} + 5.9x10^{-4} * exp(-6.3 d/D).

Actually, this calculated probability is also an average value on the overall clogging process. It is likely overestimated at the beginning of the process and underestimated at the end. Indeed, this calculation is based only on the binary HI, which occurs more often at the beginning of the pore clogging than near the end of the process, where the flowing particles predominantly interact with aggregates. Moreover, we supposed that there is always a still particle along the path of the flowing one. This latter assumption is less valid at the beginning of the pore clogging than at the end.

A last feature of the binary HI concerns the z-position of the two particles. We can observe on images of figure 36 that roughly speaking there is the same number of particles captured at the top wall and at the bottom one. This is confirmed by the analysis of the confocal images on the altitude of the particles within the pore for Q>Q_C (Figure 71A). In particular, this means that a particle that comes from the top part of the reservoir will be captured in the vicinity of a still particle in contact with the bottom horizontal wall and vice and versa (Figure 71B). We supposed that when a flowing particle and still one are on the same side of the pore, in the vicinity of the same horizontal pore wall, there is repulsion between them, repulsion that leads to a greater departure from the wall of the flowing particle, which thus prevents it to be captured.

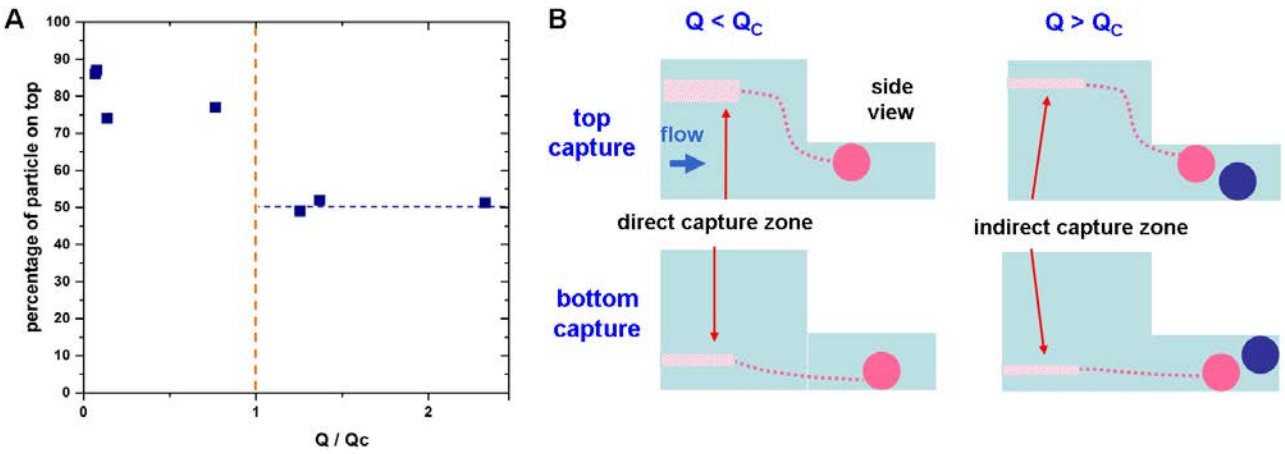

Figure 71: A-percentage of particles captured by the top wall of the pore as a function of the flow rate. B-Schemes of the main capture mode for the line ($Q<Q_C$) and in the invasion regime ($Q>Q_C$).

In the invasion regime, aggregates grow more rapidly than single particle is captured at the pore entrance (cf. Figure 67). As they grow, aggregates also modify the trajectories of an increasing number of particles, which enhances the indirect deposition of single particles further down within the pore. For instance, the two isolated particles within the dotted circle in images 5 likely get captured after having encountered with the two aggregates that lie within the dotted rectangle at the pore entrance. Those two isolated particles, in turn capture other particles and new aggregates start to grow. The two particles of image 5 become an 11 particles aggregate within the dotted circle on image 6. Therefore, during the clog's building up, we have mainly indirect single deposition and aggregate growth. Another typical example of the progressive invasion of the pore is also shown on Figure 72. There is an aggregate that grows at the pore entrance (rectangle Figure 72a) and allows a particle to be captured further downstream within the pore (circle in b). Hereafter, this particle captures other particles and forms an aggregate (Figure 72 images b to c). Interestingly, this aggregate grows in the direction opposite to the flow, until it grows enough, becomes big enough, to merge with the previous aggregate located at the pore entrance, and thus forms a unique aggregate (rectangle in Figure 72 image d). In turn, this aggregate allows the indirect particle deposition even further down within the pore and the growth of other aggregates still opposite to the flow direction (aggregate within the orange ellipse in Figure 72 images d and e). We see a similar behaviour far from the pore entrance on Figure 69 within the black dotted ellipse (Figure 69 images 7 to 10). The aggregates grow first independently in this way at various places within the pore and eventually they get in contact with the others.

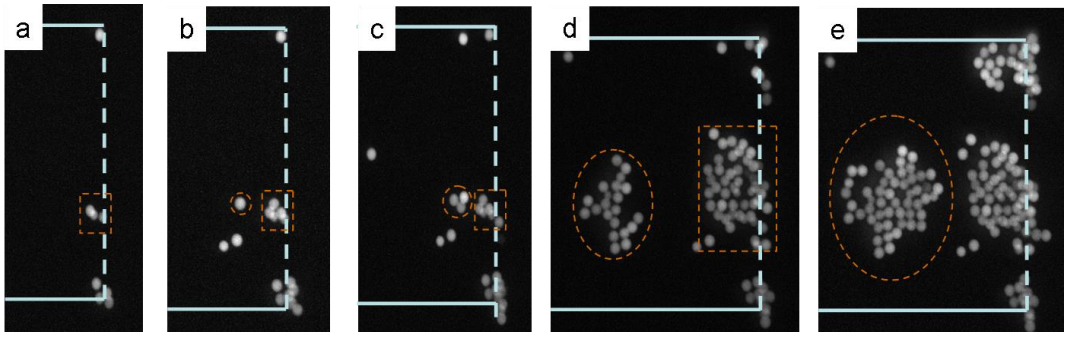

Figure 72: Images of particles deposited within the pore in the flow direction and from the pore entrance.

3. Influence of the reservoir

We have determined earlier that the channel geometry, upstream of the pore, can modify the value of Q_C (cf. Figure 39-F, Figure 41). We found that for $W_R/W<1$, Q_C is the greatest. For those values of the width ratio, most of the particles come from the centre zone and get deposit close to the pore entrance. Only few isolated particles are deposited further downstream of the clog (Figure 39-C). The situation is quite different when the size of the reservoir becomes greater than that of the pore. The critical rate Q_C becomes simply proportional to W_R/W and we observed that well below Q_C the number of particles deposited far from the entrance is roughly equals to the number of particles that form the clog at the entrance (Figure 39-D). We may conclude that particles that come from the sides of the pore contribute more on the pore invasion than the particles that flow through the centre zone. The proportionality between Q_C and the width ratio would mean that the number of particles deposited far from the entrance increases linearly with W_R. Actually, side particles first get stuck on the opposite corners at the pore entrance and thus do not partake to the pore invasion. They form here aggregates that decrease the pore width W. For $Q<Q_C$, this aggregates growth is rather limited because particles coming the centre zone get captured more rapidly at the pore entrance, forming the line-shaped clog. After having formed an aggregate on each corner, the new particles coming from the side zones enter into the pore and can get captured further downstream, if they encounter a still particle or an aggregate. However, those latter ones do not partake to the clog formation. In the line regime, the aggregate growth within the pore is less rapid than the growth of the line at the pore entrance.

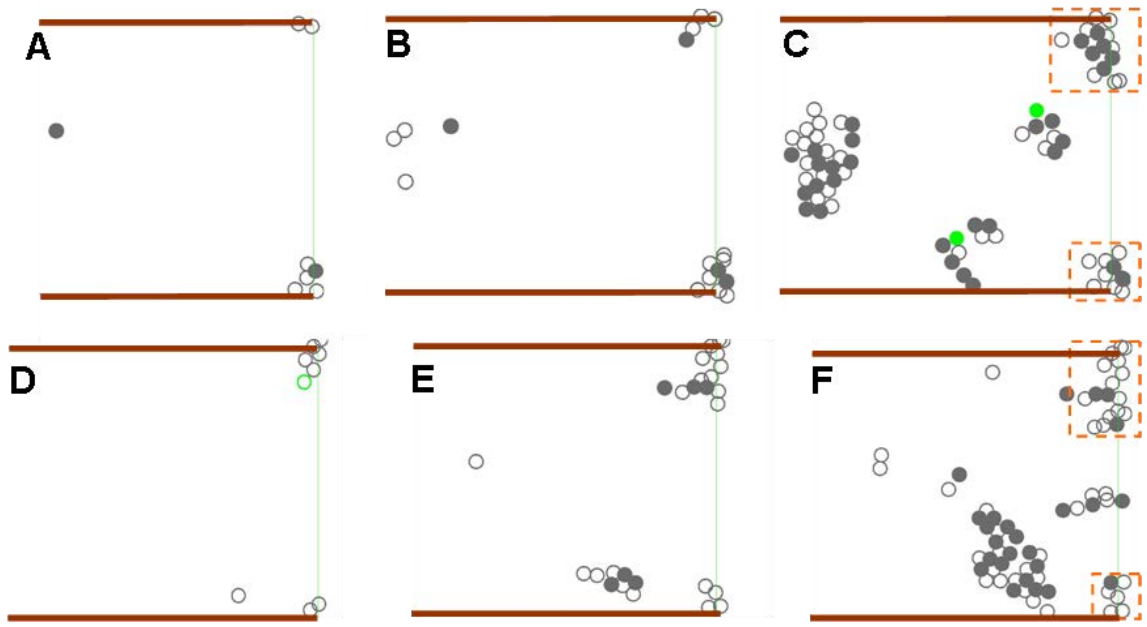

Figure 73: Two examples (top: A-C and bottom: D-F) of early times of the clog formation for Q=2.33 Q_C, with W_R/W=4.

By contrast, for $Q>Q_C$, the situation is reversed. The aggregates grow on both corners of the pore entrance more rapidly than on its centre part (Figure 73 A-B, D-E) and they can easily clog 40 to 50% of the pore entrance at the beginning of the pore clogging. This significant reduction of the pore width leads a decrease of the capture probability by the centre part of the pore entrance and thus to an effective increase of W_R. For instance, in Figure 69 and Figure 73, the width ratio initially equals to 4, at the beginning of the experiment, is twice very quickly and seven-eighths of the particles that enter into the pore come from both side zones. Those particles will not be captured at the pore entrance because as they turn around the two aggregates on both sides of the pore and they also get pushed away from the pore wall. It is worth mentioning that this situation is also true if a big aggregate is located at the middle of the pore entrance (Figure 72 C-E). Moreover, the reduction of the section at the pore entrance results in an increase of the particle velocity at that place, which in turn decreases greatly the width of the capture zone (cf. Figure 58) and thus the direct capture probability at the pore entrance as well. After they enter into the pore, the particles that come from the side will partake to the aggregate growth further downstream. To sum up, for $W_R/W<1$, the invasion regime starts for higher Q_C values, and most of the aggregate growth even though it occurs within the pore, it takes place close to the pore entrance. For $1<W_R/W<4$, the greater the width ratio the sooner the invasion regime shows-up. The number of particles deposited further downstream within the pore increases with the width ratio and thus the aggregates grow faster. For $W_R/W>4$, Q_C becomes almost constant. In this case, particles can be captured almost everywhere within the pore except at the pore entrance and the pore clogging occurs even further down from the pore entrance.

E. Conclusions

In this chapter, we have provided a comprehensive study of the clogging of a pore with its height slightly greater than the particle diameter. We have been able to do it only because we used in parallel two imaging techniques. The fast confocal set-up helps us to get enough statistics on the particle capture events and on their position in *3d*, whereas the streak technique allows us to capture the dynamics and the trajectory of the deposited particles. We showed that, depending of the flow rate and the width ratio between the pore and the reservoir zones, clogging of a very confined pore gives rise to a rich phase diagram. We found in particular that there is a morphological transition of the clog front. For low flow rates, as expected, particles get stuck at the pore entrance forming a line shaped clog whereas for flow rates higher than a critical value, there are particle depositions further down within the pore and the pore being clogged at a distance comparable to the pore width. We have determined all the different particle capture modes, direct and indirect within the pore. When particles come close enough to the pore wall, they can get captured by it (direct capture mode), due to van der Waals interaction. We have shown that the variation of the capture probability associated with this mode with the flow rate is directly related to the evolution of the capture zone within the reservoir with Q. However, once few particles get captured at the pore entrance or further downstream, new particles coming from the reservoir eventually encounter those still ones. In this case, hydrodynamic interactions between them lead to the capture of the flowing particle by the pore wall (indirect capture mode). This is also in this way that aggregates can be formed and grow within the pore. Finally, we show that the transition between those two regimes with the flow rate corresponds to the competition between the direct and the indirect capture mode. The clogging in the line regime is related to the direct capture closer to the pore entrance. Even if some particles get deposited beyond the pore entrance, the clog is formed more rapidly at this place. In the invasion regime, the direct capture mode becomes less probable and most of the particles are used to form and grow aggregates within the pore, due to the indirect capture mode.

Chapter IV - Clogging in a 3d pore

We now consider a channel geometry with a lower confinement along the height than previously, allowing to stack more than one particle in this direction (Figure 12-C, Figure 74) forming thus a “3d” pore. In order to form a clog in this case, unlike in the 2d one, particles will have not only to interact with the surfaces of the pore but also with each other. The build-up of a clog in this geometry will thus imply some new mechanisms that where not expressing in the 2d case.

In this chapter, we will first investigate the formation of clogs in a 3d pore at the pore scale. It will allow us to determine the geometrical and hydrodynamic conditions under which we can observe the formation of clogs. In a second part, we will study the clogging phenomenon at the particle scale. We will investigate the structure of a clog from 3d reconstructions after its formation. Finally, we will investigate the clog formation at the particle scale. It will allow us to identify the different mechanisms leading to the formation of the clog.

A. General Features at pore scale

In this part, we will present the main features of the clogging phenomenon at the pore scale. This coarse description of the clogging process is a necessary step prior to the investigation of the clogging mechanisms at the particle scale. Our aim is to determine what the main features that lead to the clog formation are. We separately investigate the influence of the pore geometry, the confinement, the hydrodynamic conditions (by applied pressure variation) and the ionic strength of the solution, on the clogging process at the scale of a single pore/constriction. We perform all those investigations on the clog after its complete build up within the pore, the clog structure being thus fixed.

1. Geometrical and flow conditions to observe clogging

The model porous media we used to investigate the clogging in 3 dimensions consists of an array of 30 parallel long pores/constrictions of square cross section of width W (Figure 74), i.e. the pore height H is equals to the pore width W. We choose this type of geometry as it was reported in previous studies [3], [47] to ease the formation of clogs. Upstream of each constriction there are one or two reservoirs. This configuration ensures, firstly, that colloids in a clogged channel do not overflow into the adjacent channels. Secondly, clogging a pore does not modify the streamlines in the vicinity of the other pore entrances.

We also checked that no reservoirs were full of particles at the end of each experiment. We flowed the suspensions by imposing a controlled pressure difference across the device. When five channels out of 30 were clogged, we considered that the experiment was over. In this

way, we have not modified significantly the flow rate during the experiment, and we can consider each clogging event as independent.

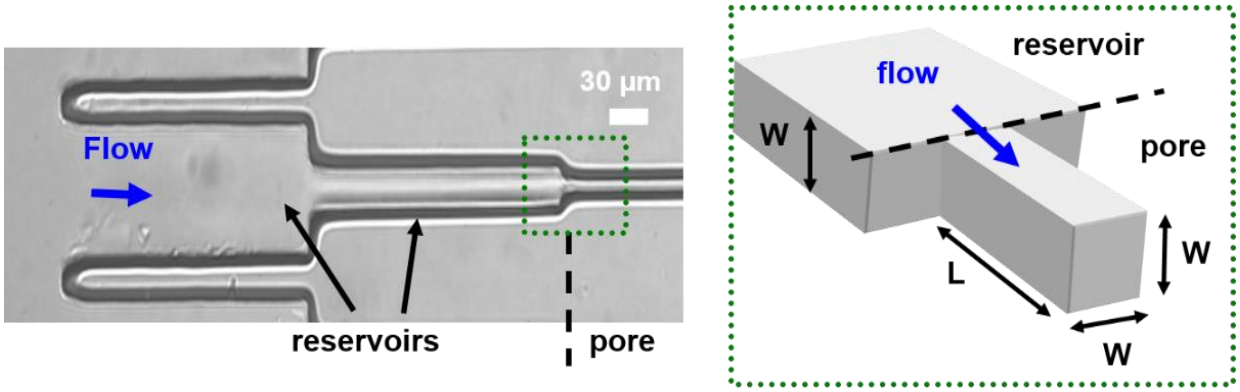

Figure 74: Scheme of the 3D geometry in top (left) and side (right) view. The blue arrows indicate the flow direction. Particles flow through two consecutives reservoirs prior entering into the pore/constriction. There is a factor of three between the width of the smaller reservoir and the pore one, and also between the larger and the smaller reservoirs.

We flow within this channel a solution of particles previously filtered to ensure their monodispersity. We also sonicated the solution during 30 min prior to each experiment to ensure that no aggregates could be found in the solution prior to the injection in the device.

The volume fractions we use ($\phi=10^{-6}-10^{-3}$) allows a flow of a single particle at the time in the channel. Like Wyss et al.[3] we can estimate that, even with local fluctuation of concentration particles, cannot arrive simultaneously at the entrance of the pore and then we cannot observe formation of bridge like observed by Bacchin et al. [47]. However, we observe a deposition of particles inside the pore as a one by one process (Figure 75). Therefore, in the following, we will adopt the point of view developed by Wyss et al. and we will assess the clogging efficiency by measuring the time to form a clog. Using eq. (3) (cf. Chapter III -A.3) we can estimate the number of particle that has flown through the pore prior the clogging, N*. The different steps of clog formation in an elongated channel are shown in images of Figure 75. Deposition of particle firstly occurs at the entrance of the pore (Figure 75-a). The capture of particle at this location is due to the compression of streamlines created by the constriction. Particles following a streamline far from the pore approaching the pore entrance moves relatively to the fluid and can thus approach the pore surface. If this movement brings the particle close enough to the region where the van der Waals force dominates (10-50nm from the wall) it can be captured.

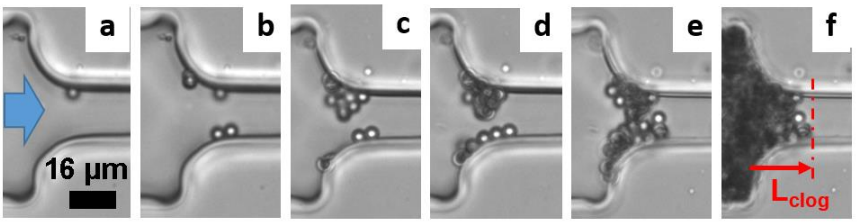

Figure 75: Chronology of clog formation. The deposition first occurs at the entrance of the pore (a) and deposits close to the top and bottom plates of the pore (a-b). Deposition keeps on in the vicinity of the already deposited ones. After the clogging of the pore (f) we can measure the length of the clog, L_{clog}. Blue arrow on a indicates the flow direction.

The second particle deposition (Figure 75-b), on the same side of the channel, occurs upstream of this first particle very close to it and so on for the others. Shortly thereafter, particles are also captured in the corners and on the top and the bottom surface (Figure 75-b). Once the first layer of particles has spread over a distance of the order of W inside the pore, particles start to accumulate on top of this layer (Figure 75-c). In this way, some aggregates grow toward the centre of the pore until it clogs. At the end of this process, when the pore is completely blocked, we can measure the length of the clog, L_{clog}, and in average $L_{clog} \approx W$.

In this type of geometry, firstly, we verify that the volume fraction of the particles in solution does not influence the clogging efficiency as showed by Wyss et al. We measured the time to form a clog in a 15 µm channel with 3 µm polystyrene particles with solutions of particle volume fraction ranging from $\phi=5x10^{-6}$ up to 10^{-4} (Figure 76-A). Over this range, the time of clog formation is inversely proportional to the volume fraction. Therefore, the number of particle flowing through the pore prior to clogging remains constant. Thus, the particle volume fraction is of no influence on the clogging efficiency.

Secondly, we look at the influence of the hydrodynamic conditions on the clogging efficiency. We flow D=3 µm polystyrene particles in a pore of width W=21 µm by applying a pressure drop ranging from 1 up to 600 mbar and measure the time of clog formation (Figure 76-B). Over this pressure range, the particle Reynolds number evolve from $5x10^{-5}$ up to $4x10^{-3}$, remaining thus in the limit of low Reynolds number. We observed two clogging regimes. In the first one, ranging from 1 mbar to 20 mbar, the mean time for a clog to form decreases as particles are bring more rapidly in the pore therefore, the clogging efficiency remains constant. The number of particle flowing through the pore prior to the obstruction does not evolve with the applied pressure. We also observed that the length of the clog does not evolve with the pressure in this regime. In the second regime, above 20 mbar, applying a larger pressure reduces the clogging efficiency, N* rises as well as the length of the clog. In this regime, we observe peculiar behaviour of the particle depositing. Particles roll on the surface and can also be detached. We have not investigate that into more details. In the following, we run all experiments in the first pressure regime where the clogging is independent of the

applied pressure. This allows us to use a pressure range corresponding to a flow rate range in the device Q=1 to 30 µL/min.

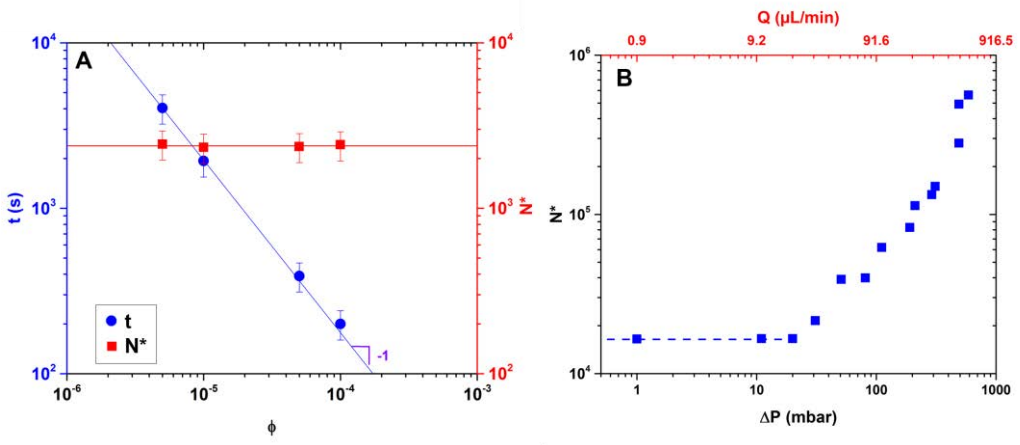

Figure 76: A- Influence of the particle volume fraction (ϕ) on the clogging time (●) and N*(■). Increasing the volume fraction decreases the time to form a clog. The evolution of t with ϕ follows a -1 power law (blue line is power -1 fit). The clogging time is inversely proportional to the volume fraction therefore N* does not depends on ϕ over the range we used (red line is a constant fit of N*) B- Evolution of the number of particle flowing through the pore prior to clogging with the applied pressure drop. Over a range from 1mbar to 20mbar N* remains constant.

2. Influence of the pore geometry

a. Pore length

We have established that clogging occurs at the entrance of an elongated pore. Now, the first geometrical feature of the pore that we can vary is the length of the constriction. We will determine more specifically the influence of the geometry of the pore entrance on the clogging properties. We start by modifying the pore length. We designed pores consisting of two circular sections at both ends and a flat part in the middle (Figure 77-B). We varied the length of the flat part, L_{flat}, from 0 (no flat part) up to 220 µm. Changing this geometry parameter is quite similar to changing the radius of curvature of the collector in analogy with classical particle capture theory (cf. §Capture of a particle by a solid surface)

We flow 4 µm polystyrene particles in those pores of width W=30 µm at a volume fraction of $4x10^{-3}$ and measured the time of clog formation N* (Figure 77). For each geometry, that is, for each constriction length, we adapted the input pressure to get the same hydrodynamic conditions in all cases, i.e. the flow rate Q is fixed. When there is no flat part in the pore (Figure 77- A, B-a), the pore walls are hemi-cylindrical with a radius of curvature about the size of the particle. In this geometry, we do not observe clog. After 5 hours of experiment about $2x10^8$ particles has flown through the pore and only a dozen of particles deposit on the pore walls. Those particles are captured in the corners formed by the top or the bottom plates with the lateral walls. We do not see further deposition on the pore walls or on top of the already deposited particles. In this case, the flow is rapidly changing from converging to diverging. Far

away from the pore, a particle follows a streamline, but at the constriction entrance, the streamlines must be compressed and force the particle to move relatively to the fluid. In this way, a particle can approach the pore surface and eventually get captured. From the middle of the constriction, the situation reverse, the channel starts to widen and the streamlines expand. As a result, the particles move away from the wall. This almost constant change in translational velocity associated with the hemi-cylindrical pore does not allow particles to deposit effectively on pore surface and thus does not lead to clogging of the pore.

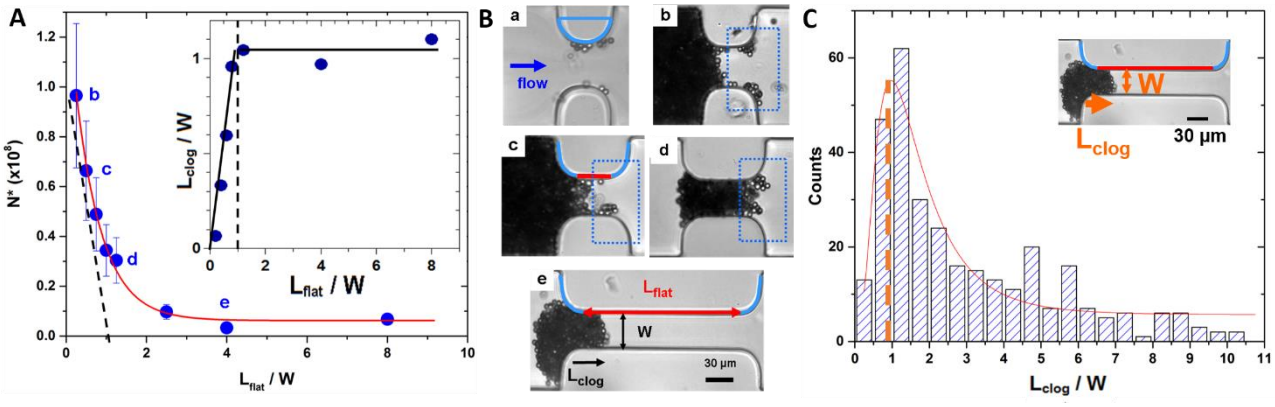

Figure 77: Influence of the constriction length. A- Number of particles flowing through the pore, N*, vs. the length of the straight part of the channel (L_{flat}) with images corresponding in B. Inset: Evolution of the clog length with the flat part of the pore. When the flat part is smaller than the channel width, the length of the clog increases until it reach a plateau value around W when L_{flat}=W. a- No clogs are formed when L_{flat}=0, image of the final deposition in a channel without flat part after 5h of experiment; b-e- images of the clogs formed for different sizes of the flat part of the channel (L_{flat}/W= 0.25 (b); 0.54(c); 1.25(d); 4(e)) . C- Histogram of the clog's length for 312 clogs made with 4 µm particles in W=30 µm channel. Red Line is a Log-Normal fit centered around L_{clog} = W (orange dashed line) and with standard variation of 0.63.

By increasing the length of L_{flat} up to 6 µm (1.5 particle diameter, Figure 77B-b) clogs can now show up with $N^* \approx 10^8$. The flat part, in between the two curved ones, is thus a "necessary" geometrical feature for the clog formation. Here again, there are only few particles captured at corners of the outlet part of the constriction, from the place where the particle velocity starts to decrease for the other values of L_{flat} (zone within the dotted rectangles in Figure 77-B-b-d). The flat part ensure that the particles that get closer to the wall can eventually get captured before they can move away from it, because they do not feel the expansion part of the pore. Indeed, in the flat part of the pore, the translational velocity of the particle reaches a constant value and is no more influenced by entrance or exit, at least over the length necessary for a particle to get captured. Figure 78 presents the different steps of the clogging of such a short pore. Particles are first captured at the pore entrance, at the very beginning of the flat part. Hereafter, there are particle depositions all along the pore within the corners (Figure 78 a-b).

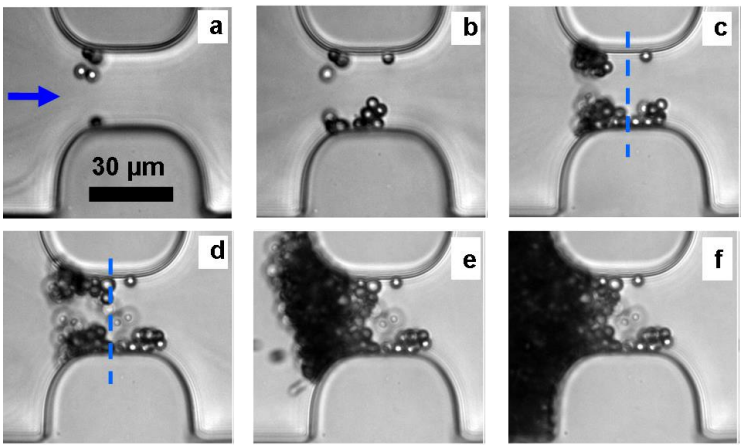

Figure 78: Images of the different construction steps of a clog in a pore with small L_{flat}=0.4W. Blue arrow on a indicates the flow direction, the dashed blue line on c and d indicates the middle of the pore. a-b: deposition of the first particles at the pore entrance within the corners. c-d growth of two aggregates on the opposite sides of the pore on the entrance half the pore. Those aggregates grow until they finally merge and clog the pore (e-f).

Then two aggregates grow on the opposite face within the first half of the pore (on the left of the dotted line in Figure 78 c-d), whereas no additional particles get captured within the second half of the pore, where the velocity starts to decrease. Those aggregates grow towards the centre of the pore until they get in contact, clogging in this way the pore (Figure 78 e-f). As L_{flat} increases, the clog invades the flat part of the pore and the length of the clog, L_{clog}, increases linearly with the length of the constriction while L_{flat}<W (Figure 77-A-insert). The plateau value we measured for L_{flat}>W, is $L_{clog} \approx$W. We determined this length for numerous clogs (for 4 µm particles in a W=30 µm and L_{flat} = 220 µm channel, Figure 77-C). We found that indeed the length distribution follows a log-normal law centred at the channel's width with a low probability of occurrence at length larger than 2W.

In the same time, the number of particles that flow through the constriction prior to the pore blocking, N*, decreases exponentially with L_{flat} (Figure 77-A), until L_{flat} >2-3W. Below this value of L_{flat}, the clog build-up is affected by slowing down of the particle velocity at the outlet part of the constriction (zone within the dotted rectangles in Figure 77B-b-d), as some particles belonging to the clog, at its front, deposit within this zone. For L_{flat} >3W, referred as a "long pore" hereafter, the clog front location departs from the pore outlet and N* becomes constant. It is worth mentioning that N* decreases by a factor of twenty from the shortest to the longest L_{flat}. Thereafter, experiments will always be performed in pores with flat part long enough to ensure the same clogging conditions. In this geometry, the penetration length of the clogs seems directly related to the channel width, which is thus the next parameter we will vary.

b. Pore width

In the previous paragraph, we have seen that in average L_{clog}=W. To further investigate this relationship, we measured systematically L_{clog} for various W and particle sizes D. To get significant statistical data, we must image about a hundred clogs. In order to measure L_{clog} for several pores in the same image we decided to use a low magnification objective. On images taken within such conditions, we identify L_{clog} as the end of the dark region forming the clog (top inset in Figure 79-A).

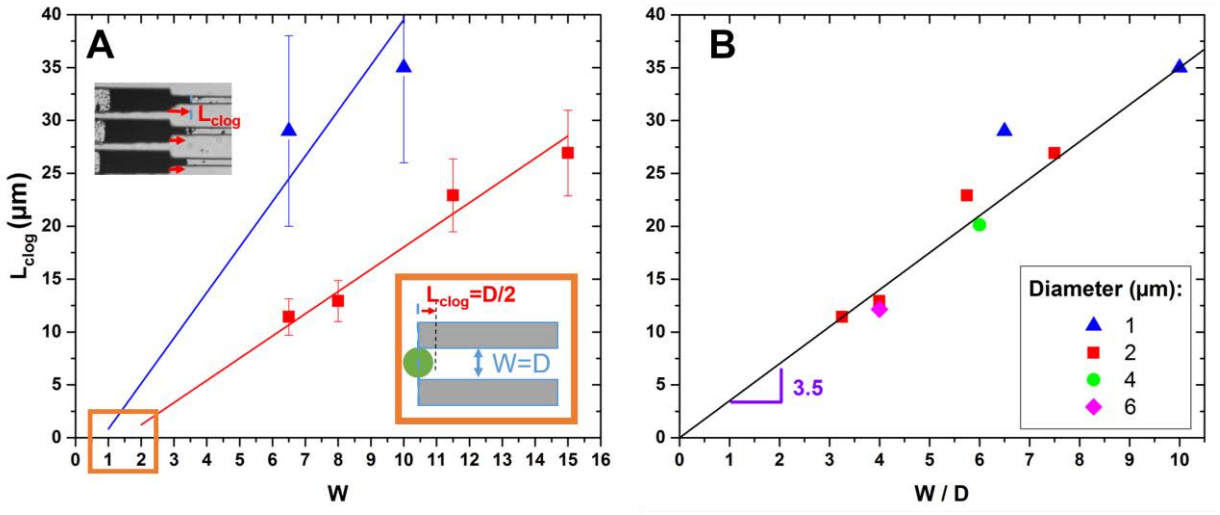

Figure 79: Evolution of the clog length (L_{clog}) with the pore width W. A- L_{clog} vs. W for D=1µm (▲) and 2µm particles (■). Lclog evolve linearly with W, with a slope depending on D. Lines are linear fits with a slope equals to 4.3 and 2.1 for 1 and 2 µm particles, respectively. The interception at W=D is D/2 as illustrated by the inset. B- By rescaling the pore width by the particle diameter (W/D), L_{clog} follows a linear master curve with a slope 3.5.

We varied W between 5 µm up to 24 µm and D from 1 to 6 µm, and measured L_{clog} for each of these geometries. In all the different geometries, we applied a pressure drop leading to the same hydrodynamic conditions in the pore. We observe that L_{clog} evolves linearly with W for each particle size, the larger the pore is and the longer the clog gets (Figure 79-A). However, the slope of this evolution is changing with the size of the particle flowing through the pore. For 1 µm particles, the length of the clog increases faster with W than for 2 µm particles (Figure 79-A). Extending the linear fit to W=D is consistent with a penetration of a single particle up to its radius as illustrated in the bottom-right inset of Figure 79-A. If we consider the confinement of the particles in the channel (W/D) instead of the channel width as parameter, all data collapse on a master curve where $L_{clog}=L_1 W/D$ with L1=3.5 µm. This value L_1 is close to the average particle diameter. The key parameter to clog length is thus the confinement W/D.

We also measured the number of particles flowing through the pore prior to clogging, N*, for different ratios W/D, using several combination of D (2<D<10 µm) and W (5<W<30 µm), (Figure 80). For a given ratio W/D, with different W and D, we always found the same value

of N*. As expected, working with higher degree of confinement increases N*, i.e., we need more particles to clog a larger pore. However, we found that N* increases very rapidly with W/D and follows a power law such as:

$$N^* \propto \left(\frac{W}{D}\right)^7$$

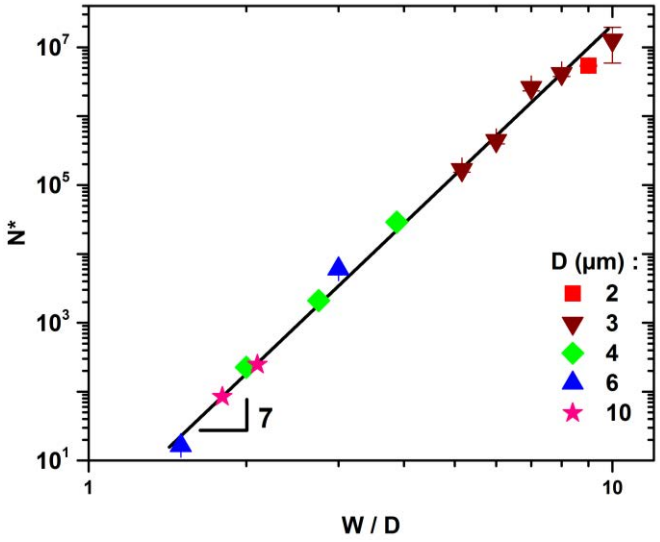

Figure 80: Evolution of the clogging efficiency with the confinement W/D. Particles are polystyrene particles of different sizes corresponding to the different symbols. The red line is a power law fit with power 7.

In the following, we will see how those parameters, L_{clog} and N*, are influenced by the DLVO forces and the hydrodynamic conditions for a fixed geometry of the pore.

3. Influence of colloidal forces

The two colloidal forces that might influence the clogging are the electrostatic repulsion (Chapter II -A.1.iii), preventing particles to aggregates and approach each other, and the van der Waals force (cf. Chapter II -A.1.i) responsible for the adhesion of particles on the surface and between each other. As the electrostatic repulsion prevents particle from approaching one another or the surface, it seems like the main parameter to vary first. We can vary the electrostatic repulsion by adding electrolytes to the suspending solution. This salt addition screens the surface charges of the particles, thus reducing the repulsion. The electrolyte concentrations we used were below the critical coagulation concentration (CCC_{PS}=0.07 M) of the suspension to prevent from particle aggregation in the bulk. We added $5x10^{-2}$ M of NaCl in the solution of polystyrene particles (PS) we used previously and measured the N* evolution with W/D (Figure 81-A). We get the same behaviour as before, where we added no salt, i.e. N* is still a power law 7 of W/D. But now, for each W/D, N* is smaller than without salt. A $5x10^{-2}$ M NaCl solution reduces N* by a factor of almost 10. It is worth noting that the salt addition does not lead to any significant modification of L_{clog}. We also varied the ionic strength of the PS solution more finely from 10^{-4} to $5x10^{-2}$ M (Figure 81-C). We still observed

the same reduction of N* as the electrolyte concentration increases, for each W/D. We can therefore rescale the N* taking into account a parameter λ such as $N_{rescale} = \lambda N^*$. In doing so, the curve with and without salt superimpose on a single master curve (Figure 81-C). The rescaling factor λ varies linearly with the salt concentration C_{NaCl}, the higher the salt concentration, the larger λ is (the smaller N*). We reported the rescaling factor for each concentration on Figure 81-D.

We are also able to vary the complete DLVO interactions, using a different type of particles, the PMMA particles. Indeed, the two types of particles have really different refractive indexes (n_{PS}=1.59; n_{PMMA}=1.49) and surface charges (zeta potentials: ζ_{PS}=30-35 mV; ζ_{PMMA}=70 mV) leading respectively to different van der Walls forces and electrostatic repulsions. Changing the particle type implies also a change in the suspending solution, in order to meet the criterion of density matching. We used a mixture of solvent with a higher viscosity for the PMMA particles than for the PS ones. We took care of changing the pressure drop accordingly to this viscosity change, to ensure the same hydrodynamic conditions for all the particle types. We observed, as before, the same power law increase of N* with W/D (Figure 81-B). This scaling law seems thus to be quite robust and does not depend on the particle type. However, the clogging is far more rapid with PS particles than with PMMA. For the same W/D, there is a factor of ten between the N* values obtained with the two particle types. We also measured the average clog length. For PMMA particles, L_{clog} is larger than for the PS particles: $L_{clogPMMA} \approx 2.4W$ whereas $L_{clogPS} \approx W$. Once again, the salt addition does not modify L_{clog} in the PMMA case, while we still observe a decrease of N*. It is worth noting that increasing the salt concentration, up to 5×10^{-2} M, in the PMMA suspension almost leads to the same evolution of N* with W/D found for the PS suspension without salt added.

Finally, we have modified the attractive part of the DLVO potential by changing the refractive index (n) of the suspending fluid. Doing so with the PS particles is rather difficult because of their density (1.055 g/cm^3). Indeed, to meet the density match criterion, we have to add a solvent with a density a bit higher than that of the water, which does not allow the use of solvents with refractive indexes quite different of that of the water. PMMA particles being much denser than the PS ones (1.18 g/cm^3), we can more easily use different suspending media that still fulfil the density matching criterion. We used a solution of 29% of sucrose (n=1.38) and a solution of 64% of urea (n=1.42). The change of solution modifies the Hamaker constant (van der Walls forces) from $A_{PMMA\text{-}29\%Sucrose} = 1.21 \times 10^{-20}$ J to $A_{PMMA\text{-}64\%Urea} = 7.87 \times 10^{-21}$ J, a 1.5 variation equals to the difference between PS ($A_{PS} = 1.88 \times 10^{-20}$ J) and PMMA in 29% of sucrose. Once again, whatever the suspending medium for the PMMA particles, the variation of N* with W/D are the same (Figure 81-B). The depth of the attractive well is thus not responsible of the large deviation in N* between PS and PMMA. Finally, we observed that $L_{clogPMMA}$ was not modified when we changed the suspending fluid.

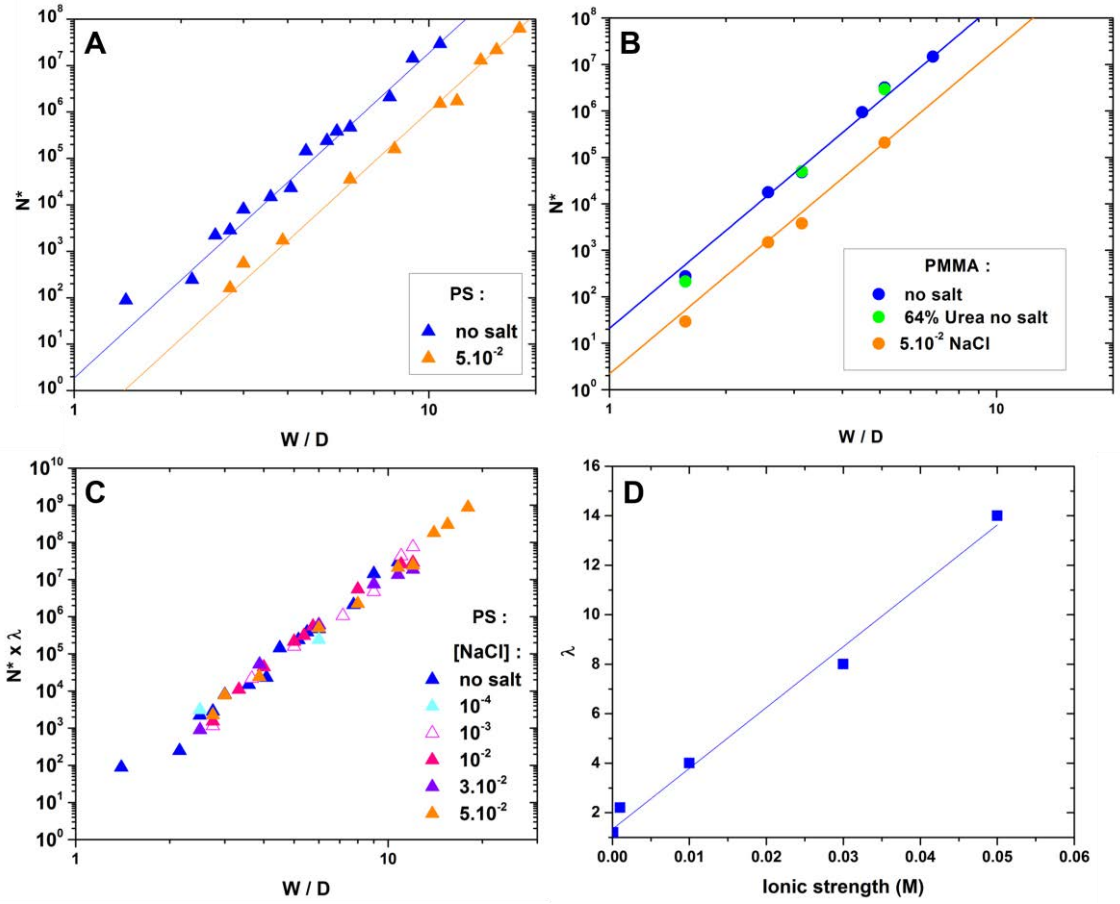

Figure 81: Colloidal forces influence. A- Evolution of the clogging efficiency with confinement for polystyrene particles suspended in a solution of water and heavy water (45%-55% in weight) with and without addition of NaCl. B- Similar to A for PMMA particles suspend in a mixture of water urea and glycerol (23%, 37% and 30% in weight respectively) and a mixture of water and sucrose with and without addition of NaCl. In A and B lines are power fit with exponent 7 and with coefficient N_0^* =3.96 (▲); 0.23 (▲); 20.7 (●); $5x10^{-2}$ (●). C – Data of A (and other NaCl concentration values not shown in A for clarity) rescaled by a factor λ. D- Evolution of the rescaling factor λ between N*=f(W/D) without salt and with addition of salt vs. the ionic strength of the polystyrene particles solution. Blue line is a linear fit with slope equals to 245.

B. Clog structure

We have defined up to now the properties of the clog formation at the pore scale from bright field microscopy. In the following, thanks to the confocal imaging, we will study the clog formation at the particle scale. In a first part, we will look at the details of dynamic of the clog building up and determine its structure after its formation. We restricted ourselves to a high confinement case, H/D=3, mainly because the number of particle to clog the pore, N*, is small (of the order of 10^4) and the criterion of refractive index matching is less restrictive (see just below). In a second part, we will consider only the structure of the clog for lower confinement, H/D=6, once the clog is already formed. In this case, in order to be able to localize precisely individual particles within the bulk, we need to find a trade-off between the size of the channel in the z-direction and the refractive index matching between the particles and the solvent. 1.8 µm PMMA dispersed in a solution of 37% (in weight) of urea, 30% of glycerol and water was the best compromise we found. This mixture reduces the index mismatch between

the particles and the solution without suppressing completely the van der Waals forces needed to get both, inter-particle and particle-wall adhesions, (n=1.42, A=7.87x10^{-21} J). Moreover, we used a channel of height H=11 µm, to limit the number of particle stacking in the z direction. Above this height, the laser comes across too many particles (interfaces) that diffract the laser and do not allow determining the position of the particles within the pore. The chosen device has a width equals to 9 µm. We studied twenty-one clogs formed in the same hydrodynamic conditions, with a high particle charge and eleven ones with ionic strength of the suspension equals to 0.15 M, corresponding to very low particle surface charge.

1. Growth dynamics in high confinement

a. Geometrical features of the pore

In the following set of experiments, we investigate the clogging of D=4 µm PMMA particles in a rectangular section pore with fixed geometrical features (Figure 82). The microfluidics device we use to this end consists of a series of parallel constrictions of width W=16 µm corresponding to 4D. They are connected to each other by a reservoir of width W_R three times larger allowing the independency of all channels (cf. Chapter IV -A.1) on the overall experiment. The height of the device, H, is kept constant on the whole device and corresponds to 3D.The volume fraction of particles in solution is $\phi=5x10^{-5}$. The flow conditions are also kept constant, by applying a pressure drop ΔP=30 mbar, corresponding to the pressure range where N* and the length of clog are independent of the pressure (cf. Chapter IV -A.1).

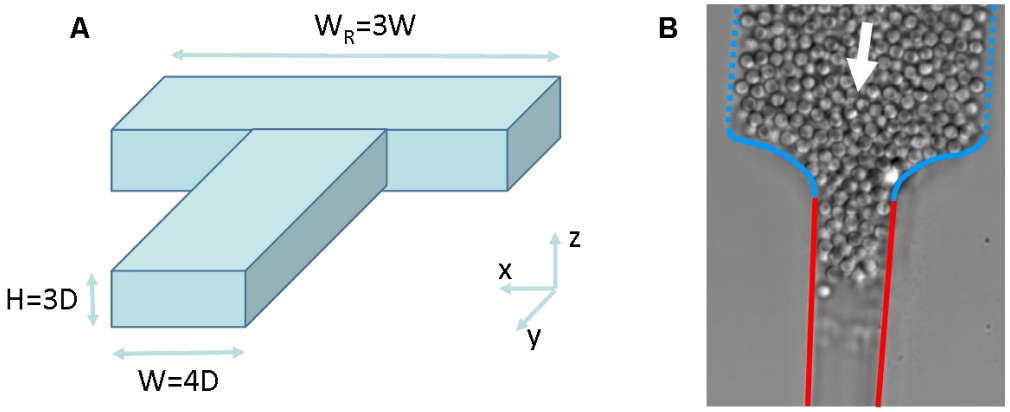

Figure 82: A-Geometry of the pore. B-Top view image of the pore clogged. The blue dotted lines and the red ones correspond to the reservoir edges and to the flat sides of the pore, respectively, while the curved part of the pore entrance are outlined by the blue continuous lines. The arrow points to the flow direction.

b. Building up of a clog at the pore scale

The use of high speed confocal allowed us to image in three dimensions, by z-stacking, the clog formation on ten different channels with a rate of 1 minute between each z-stacks. We image each channel individually by z-stacking and move between them using a motorized

stage. It allows us to monitor the deposition of particles in the pore along time. By using the equation 3 in (Chapter III -A.3) we can link the time with the number of particles that has flown through the pore. We thus reported the evolution of the number of particles deposited in the pore as a function of the particle that has flown through the pore (N) for four different channels under the same conditions (Figure 83). Unlike in the 2d case (cf. Figure 42) the successive deposition of particles does not follow a simple linear evolution with the time. Instead, we have here a two steps process (green and red dashed lines in Figure 83), each following a nearly linear evolution in time. The first step of clog construction (green dashed line) lasts the longer and presents the shallower slope. The deposition slope is between $2.2x10^{-3}$ and $6.8x10^{-3}$. Actually, the curves are not smooth: there are rising-up parts followed by inactivity periods where no particle deposits. The second step (red dashed line), is by far quicker. The slope is about 7 times larger than in the previous regime varying between $1.4x10^{-2}$ and $4.8x10^{-2}$. It starts at the end of the clogging process until the complete blocking.

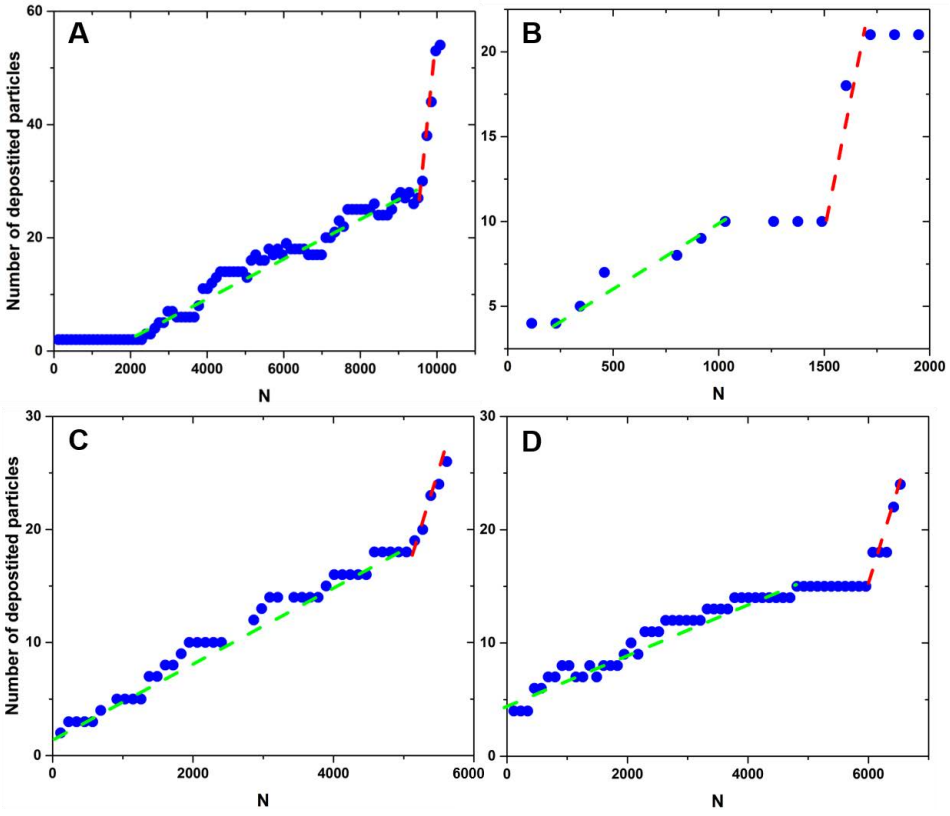

Figure 83: Evolution of the number of particles deposited in the pore for four different channels as a function of the particle flown through the pore N. Experiment is run in a W=16µm H=12µm channel with 4µm particles with ϕ=5.10-5 and ΔP=30mbar. Even though clogs where formed under the same flow and geometry conditions deposition curves and the clog structure are different.

In Figure 84, we have shown a progressive 3d build-up of a clog, corresponding to the particle deposition curve of Figure 83-A. Particles are first deposited at the pore entrance, close to the corners, and thereafter we form small aggregates in which all particles share a contact with the pore walls. From $N=9.5x10^{3}$, particles start to be captured by other individuals, i.e., the

capture involves inter-particle interaction rather than a particle-surface one (yellow arrow). It is worth noting that this peculiar moment also corresponds to the transition between the two regimes. This feature is quite robust and thus observed in the three other examples. In the remaining part of the pore clogging, particles deposit either on the second layer or at the rear of the clog, at the pore entrance. In the next paragraph, we will look in more details the different mechanisms that lead to the pore clogging at the particle scale.

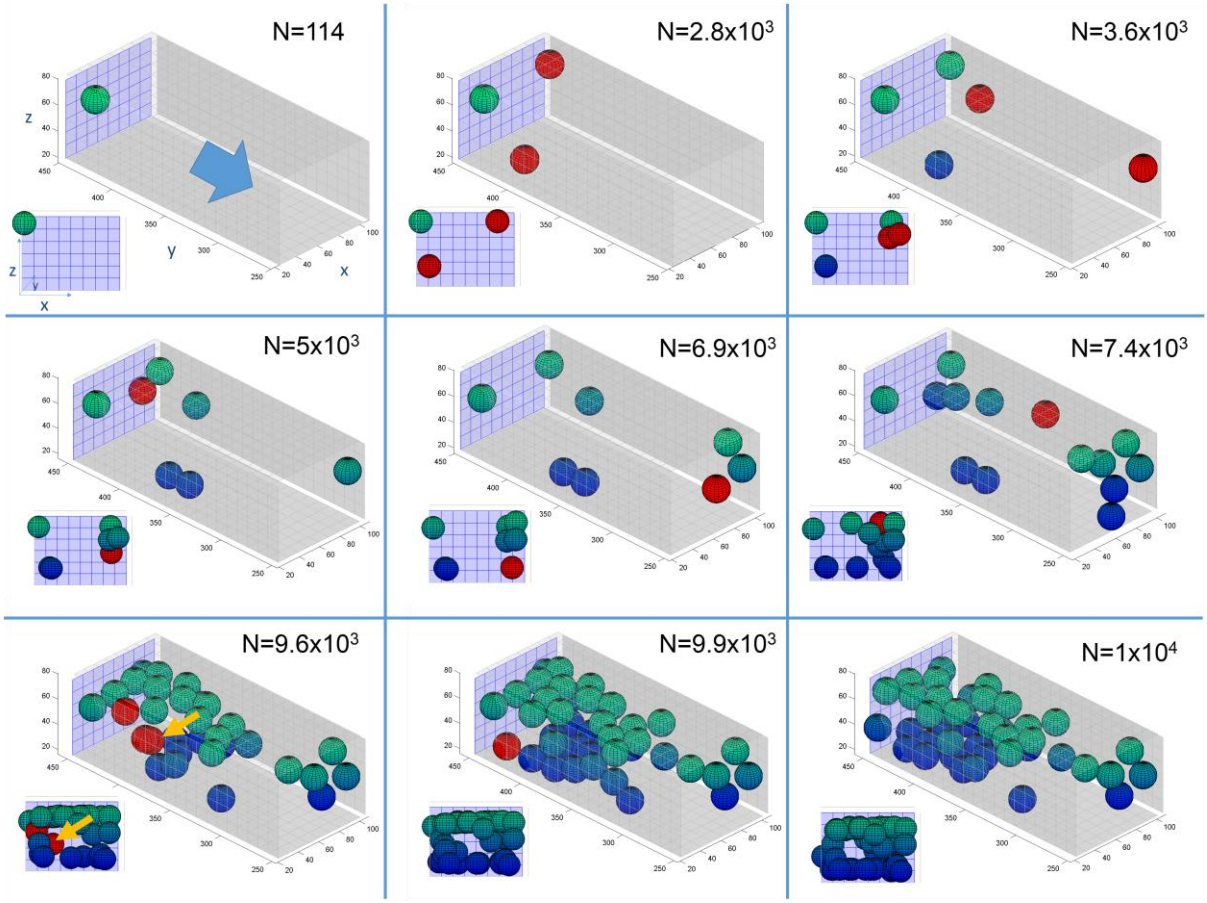

Figure 84: 3d images of the Successive particle depositions, which correspond to the deposition curve in Figure 83-A. The blue plane represents the pore entrance and the grey ones the four pore walls. The blue arrow indicates flow direction. The first particle deposits in the top left corner of the channel (N=114). Next particles deposit on the other corners (N=2.8x10^3). Other Particles then deposit onto the pore walls until N=9.6x10^3 where a particle deposits on top of the first particle layer. We provide on each image a projected view, perpendicular to the flow direction, in order to better visualize the clog inward building up. The red particles are the freshly captured ones, whereas the blue to green ones correspond to the older ones, captured from the bottom to the top, respectively.

c. Different mechanisms of particle capture by the pore walls

i. Direct capture by the wall

The simple and the first mechanism that shows up at the beginning of the pore clogging is the particle capture by the pore walls; we called, in the previous chapter, the “direct capture”.

Due to the pore geometry, we do not get the same conditions of particle capture on all the pore surfaces (Figure 85). Indeed, there is a symmetric constriction only on the lateral sides of the pore, the pore height being constant. Therefore, we expect to see a greater deposition on the lateral walls than on the top and the bottom ones ([3] and Chapter III -). We must then treat the top and the bottom walls (blue zones) separately from the lateral walls (orange zones). We will also consider the case of the corners (green zones) separately. In the following, we will keep using the colour code defined in Figure 85 for those three different zones within the pore cross section.

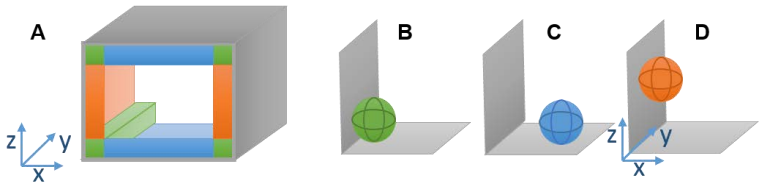

Figure 85: A- Scheme of the three different zones of deposition onto the walls of the pore. Particles can deposit on the corners of the pore (green area, B); on the top and bottom plates (blue area, C); or on the sidewalls (orange area, D).

Confocal imaging allows us to determine precisely the deposition length from the pore entrance, L, of the first particle captured directly by the pore wall, and the wall(s) with which the particle is in contact (Figure 86). All the particles start to deposit from the beginning of the flat part of the pore entrance, just after the curved part, up to 4D further within the pore (Figure 86-main). Strikingly, the vast majority of the particles are stuck in the corners (Figure 86-inset). Only few particles are captured by the sidewalls while the bottom and the top ones capture no particle. The deposition length for the direct capture is in good agreement with what we have found in the 2d part (cf. Chapter III -B.1). Moreover, the capture in the corners suggests that we have also an uneven particle distribution along the pore height, within the reservoir, like in the 2d case (cf. Figure 50), since the height of the pore is the same (H=3D). The probability related to this direct capture mechanism is around 10^{-3}.

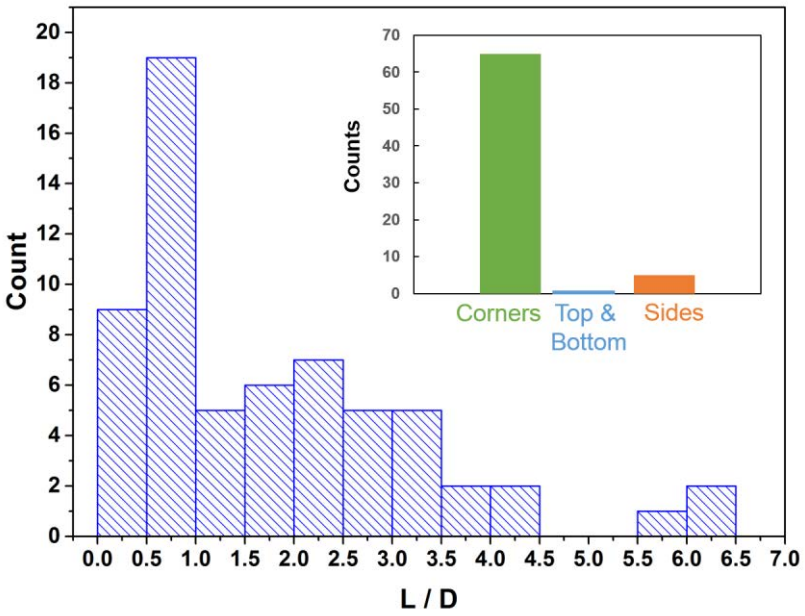

Figure 86: Distribution of the positions of the particles captured directly by the pore walls. Inset: repartition of the captured particles between sides of the pore.

ii. Indirect capture by the constriction

As just mentioned above, the direct particle capture occurs mainly in the pore corners. Once a particle gets in that place, it modifies the flow around it over a distance we can estimate to be around 1.5D from its surface [76]. This implies that we cannot have direct capture of particle in the two corners of the same side of the pore (Figure 87-A), since the channel height is only equals to 3D. The first deposited particle is thus able to modify the trajectory of the second particle on the same lateral side (yellow particle in Figure 87-A). Therefore, in a given cross section at the pore entrance, we can have direct capture particle only on one corner of both lateral sides of the pore, at a distance centre-to-centre equals to 3D or 3.6D. When this is indeed the case, almost no other particle can enter into the pore without having its trajectory modified (Figure 87B-C). This example is purely qualitative, however it put forward the fact that from the very beginning of the experiment, the vast majority of the particle captures will be indirect, i.e., result from hydrodynamic interactions with still particles.

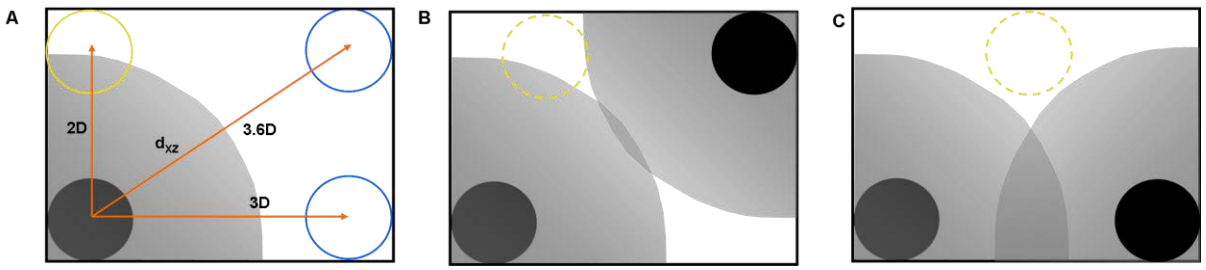

Figure 87: A-Cross section of a pore with a particle captured in a corner (black), and three possible positions in the remaining corners. Only the top and bottom right corners can capture a particle without having any hydrodynamic interaction with the black one. All new particles that will come from the grey zone around the black particle will have their trajectory modified by the black one. B-C- Hydrodynamic influence of two particles captured on corners. The hollow yellow circle are shown in C indicates that only within a narrow zone of cross section particle trajectories are not modified.

We reported on Figure 88-A the distance in the flow direction y, between a new deposited particle and the closest immobile one, versus their distance in the xz section. We observed that once a new particle deposit, it is quasi systematically in the vicinity of another still one, at a distance smaller than a particle diameter, surface to surface. Indeed, in all the experiments we performed, only 7 particles over 170 deposited were at a distance greater than D (yellow and green particles in Figure 88-A-D). Some of those particles (yellow ones) can be deposited up to 4D upstream from the still particle (yellow volume in Figure 88-B). As in the 2d chapter, they undergo indirect deposition without forming an aggregate and are captured on the sides of the pore but not on the corners (yellow circles in Figure 88-C, D). Other particles can also flow over a still particle captured in a corner, which then acts as a local constriction. This kind of particles are enlighten in Figure 91 as green points and can be identified by their difference in height with the still one corresponding to the pore height (Figure 88-C-D). We reported on Figure 88-B the volume in which particles get captured (direct capture in purple and indirect in yellow) around a particle stuck in a corner, since we show that this is the first location of capture at the pore entrance. We see that the particle in this zone influences almost half of the pore (grey zone in Figure 87A). Thus, all particles entering into the pore, either from above the still particle and up to the top wall, or from the side of the still particle, up to the middle of the pore, along its width, will be captured.

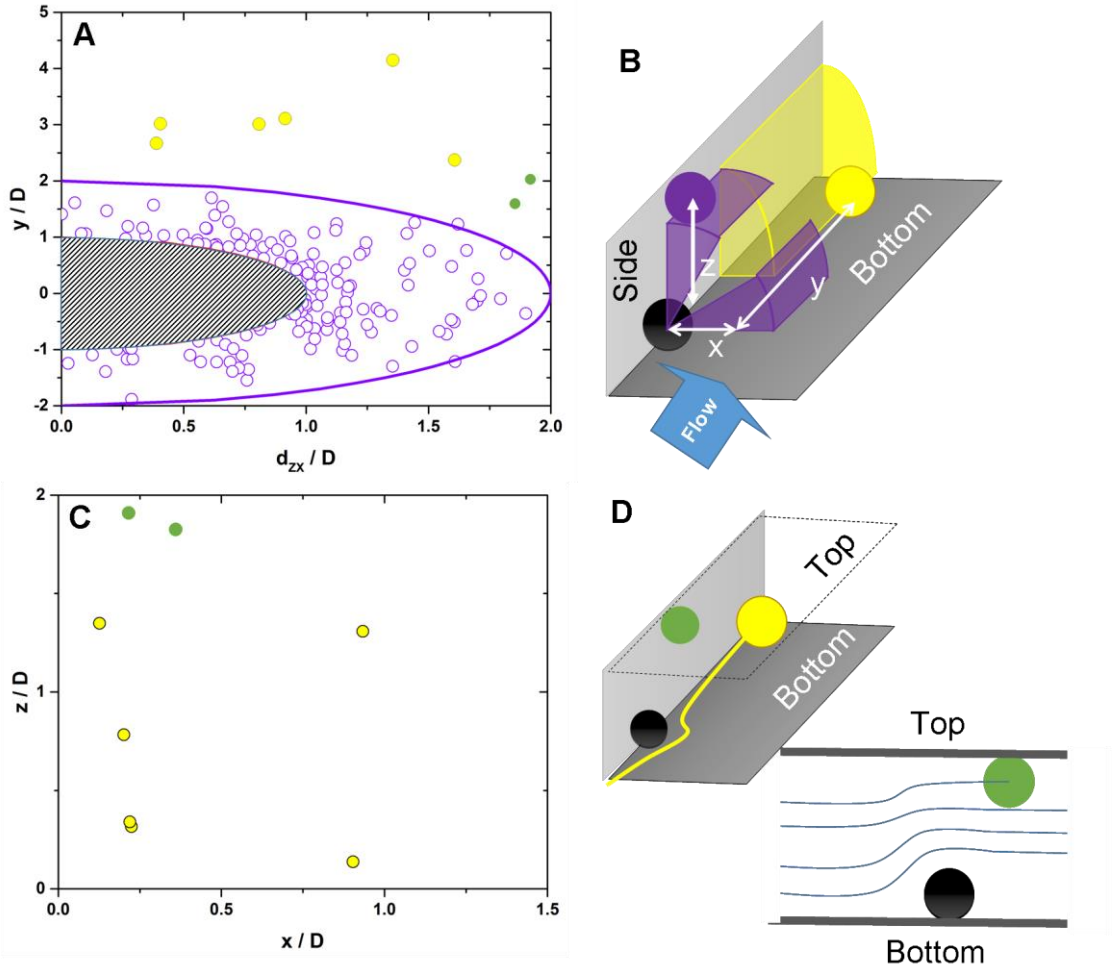

Figure 88: Characteristics of the deposition onto the walls after interaction with a particle already deposited on the pore. A- Distance of deposition downstream from the still particle (y) vs. the distance in zx plane. The black hatched area is the location of the particle already sitting on the pore walls. The area delimited by the violet circle arc is the aggregation zone where final distance between the two particle is d_{zx}<2D and -2D<y<2D. Most of the particles depositing after interaction are depositing in this zone. Eventually some particles will deposit further away from the still particle (yellow and green points).B- Illustrate the measured distances and the zones of influence of the already deposited particle (black). Particle depositing in the violet area forms an aggregate with the first one. Particle depositing in the yellow area deposits after interacting with the still one. C- Detail of x and z distances between still particle and depositing one in the yellow zone in B. Yellow points correspond to particle depositing after crossing the immobile particle directly as pictured in D. Green points correspond to particle depositing on the corner opposite to the still particle but on the same lateral wall. Such particles experience a local constriction in height due to the still particle as illustrated in D. D- Scheme of the 2 cases identified in B.

Let us focus now on the main mode of particle deposition that leads to aggregate growth. Almost every new-deposited particle within the pore forms an aggregate with a still particle or an aggregate. As defined earlier (cf. Chapter III -C.2), we get a true aggregate or an effective one, depending whether or not the two particles are in contact within a doublet, for instance. The new deposited particles that lead to the aggregate growth are represented by the purple points in Figure 88-A, which thus correspond by far to the majority of the captured particles. Therefore, the still particles within the pore act as attractors for the other ones, which flow in their vicinity. We can easily identified the different aggregates within the pore and study

their growth rate over time. In all cases, there are two to four aggregates, at most, that grow in the same time, but only one or two are responsible for the clog formation. A typical clog formation is shown on the Figure 89, which corresponds to the deposition curve shown in Figure 86B. The different particle colours correspond to different aggregates. We clearly see that from the beginning of pore filling (N=114) that two isolated particles are deposited on one vertical wall (blue particle) while a first aggregate starts to grow on the opposite wall (purple particles). The doublet keeps growing until it catches one of the isolated (blue) particle ($N=1.14x10^3$). As mentioned just above, all new particles that get captured partake to the growth of this aggregate during almost all the clogging build-up. However, a second aggregate (pink particles), a doublet, also starts to grow near the end of the clogging process ($N=1.26x10^3$). This occurs when a flowing particle get captured in the vicinity of the second isolated particle, deposited right at the beginning of the experiment. The main aggregate, as it grows, merges with this latter small aggregate. Once the main aggregate covers enough surface of the pore, particles starts to deposit on top of this first particle layer ($N=1.49x10^3$). This moment corresponds to the beginning of the second step of the particle deposition in Figure 83-B. Finally, the main aggregate spreads all over the cross section and all particles, deposited in the pore, are included into this unique aggregate ($N=1.6x10^3$).

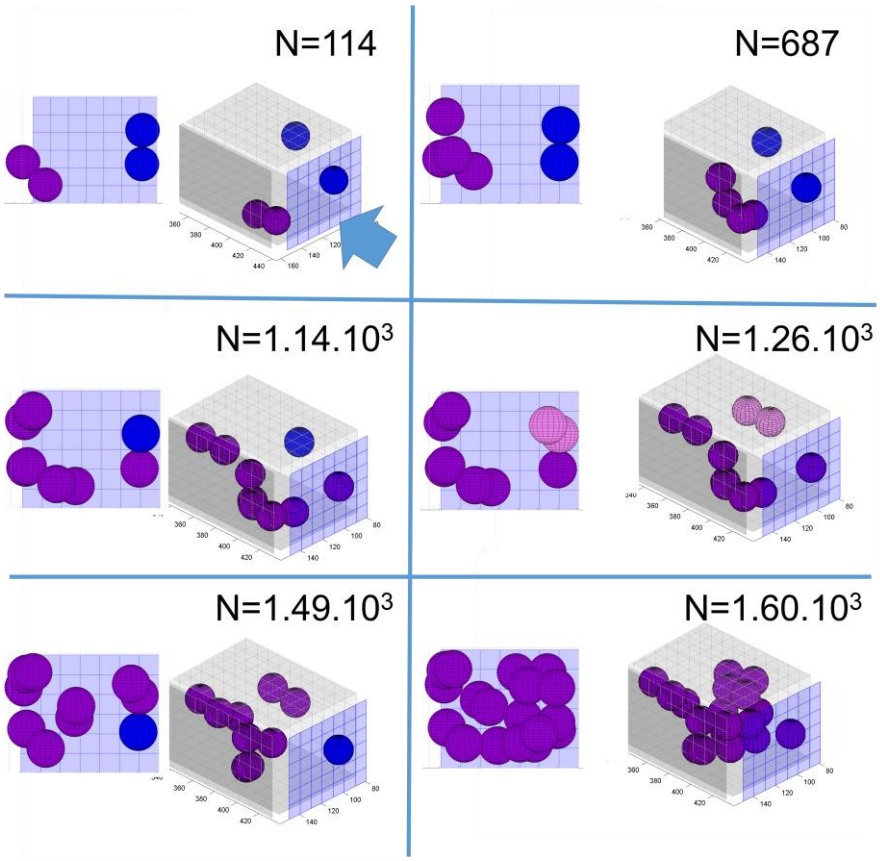

Figure 89: 3d images of a clog build up, from the top left corner to the bottom right one, corresponding to the deposition curve in Figure 83-B.

We may also look at the stability of the particles within the first layer (Figure 90-A), to complement and detail the data about the relative particle position of Figure 88-A. Only 3% of total numbers of particle are really isolated ones, deposited on the sides and not in the corners. All the other particles partake to an aggregate, a true or an effective one: 34% have only one contact with the pore surface and form effective aggregate, while 63% are in direct contact with the pore wall and at least with one particle. We may conclude that, even though we deal with colloidal particles, those ones cannot have a stable position under flow if they have only one contact with the surface. We indeed observe that sometimes still particle detach from the surface or they moves slowly, likely rolling on the surface. We also observed more frequently this slow rolling phenomenon during the clogging of the 2d pores. However, the image acquisition rate is not high enough to get a decent statistics of the conditions and of the rate of such detachment. It seems that the particle capture in the close vicinity of another one, or near an aggregate, even though they are not in contact, helps the newly captured particle to remains attached on the pore surface.

It is also worth noting that particles captured by the aggregates generally deposit further downstream within the pore as the aggregates grow. In this way, the first layer of particles invades progressively the pore, from its entrance. We have plotted in Figure 90-B the distribution of the deposition lengths for all the particles captured by the indirect mode. We clearly see that most of the particles are located near the pore entrance, i.e., for L/H or L/W≈1. This means that in average the cross section of the pore is the most reduced in those places and hence the final step of the clog takes place here. Moreover, the tail of the distribution, L/D=7, (L/W≈2.3) corresponds to the average length of the first layer at the end of the clogging process. Therefore, the location of the clog is closer to the pore entrance than the front of the first particle layer. It is worth noting that from bright field images used earlier in the pore scale part study (cf. §a, we cannot have access to the structure of the clog. We are able to get only the overall length of the clog, which we have called L_{clog}. In the pore scale part, L_{clog} corresponds actually to the length of the first particle layer. Indeed, for the PMMA particles we found in average that L_{clog}=2.4W.

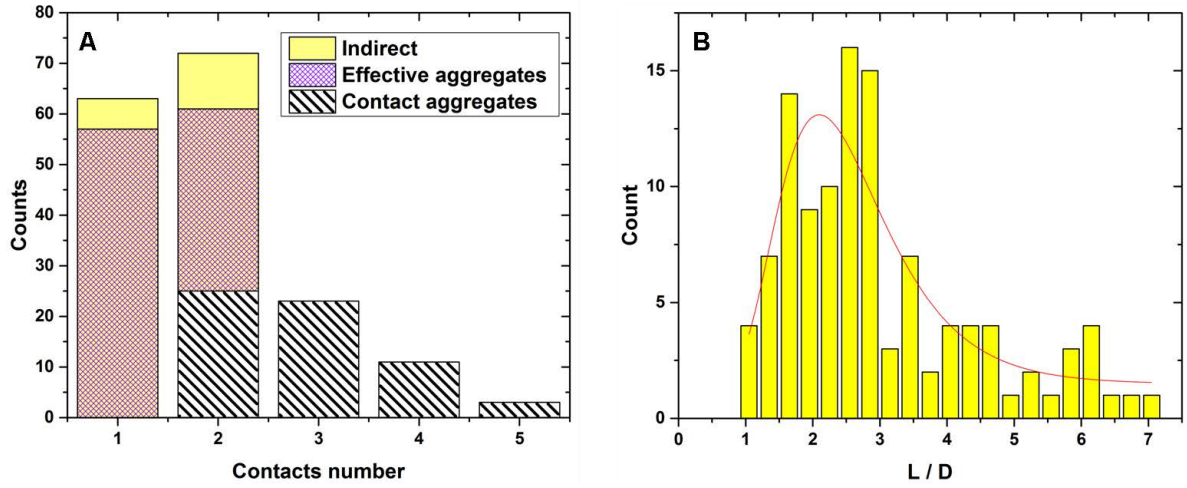

Figure 90: A-Distribution of the coordination number for the particles belonging to the first layer. B-Distribution of the deposition length from the pore entrance of the particle captured after having interacted with a particle or an aggregate. The red line is a log-normal fit of the data peaked around 2L/D, which corresponds to 0.7H.

d. Deposition onto the first particle layer

The second step of the clog formation consists in the deposition of particle on both, the pore wall and the top of the first monolayer, in contact with the pore walls. This final step is the faster of the clogging process and always starts by the deposition of a particle on top of other particles exclusively, that is, this new captured particles has no contact with the pore surface (Figure 91 A and B). The four sides of the pore do not have to be fully covered to observe the particle deposition on the second layer The particle neither gets stuck where the cross section is the narrowest but it can be captured everywhere within the pore. As soon as two to three particles cover the pore surface locally, in such a way that no other particle can be lodged within the remaining place on the pore surface, in between those particles, then a particle can deposit on top of other individuals (Figure 91-B). In other words, the new particle is captured by an aggregate; it thus simply partakes to the growth of this aggregate. Therefore, there is no difference between the deposition in the first layer or in the second layer of particles. In both case it corresponds to the growth of aggregates, even the growth of very small ones such as doublets (last three examples of Figure 91-B). Finally, it is worth noting that in this second deposition step, we capture in average the same number of particles in the first and in the second layer. Thus, in this step, aggregates grow by filling the available gaps in their vicinity, irrespective of their location within the pore. Either the main aggregate grows inward from one corner and fills a pore cross section up to the clogging, or it spreads along the pore in both direction, along or opposite to the flow, before growing toward the centre and eventually clogs the pore.

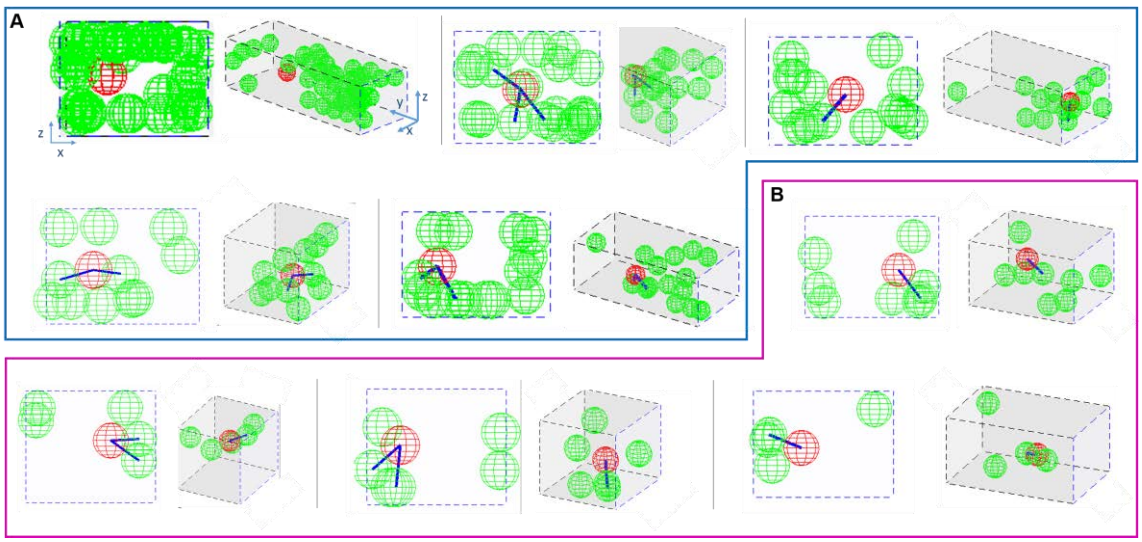

Figure 91: Surface of the pore coverage, by the green spheres, when the first particle (red sphere) deposits on top of those particles for all the experiments. The blue lines correspond to the direct contacts of the red particle with those in the first layer. For each experiment, we have both, a projection of all particles in a same plane (left) and a 3d view of the forming clog (right) where the flow goes from the right to the left. When the red particle get captured either two to three pore surface are fully covered (A) or at least there is an aggregate on the pore wall (B).

We also measured the number of contacts of the new particles deposited on top of other particles (Figure 92). The contact number is in between one and four. Contrary to the first layer deposition case, 35% of the particles are in contact only with another individual. We do not know if those particles remain and are not detached, later on, by the flow, the particle deposition being quite fast at the end of the clogging process. Moreover, since several particles get captured in the same time and we cannot track the position of each particle unambiguously.

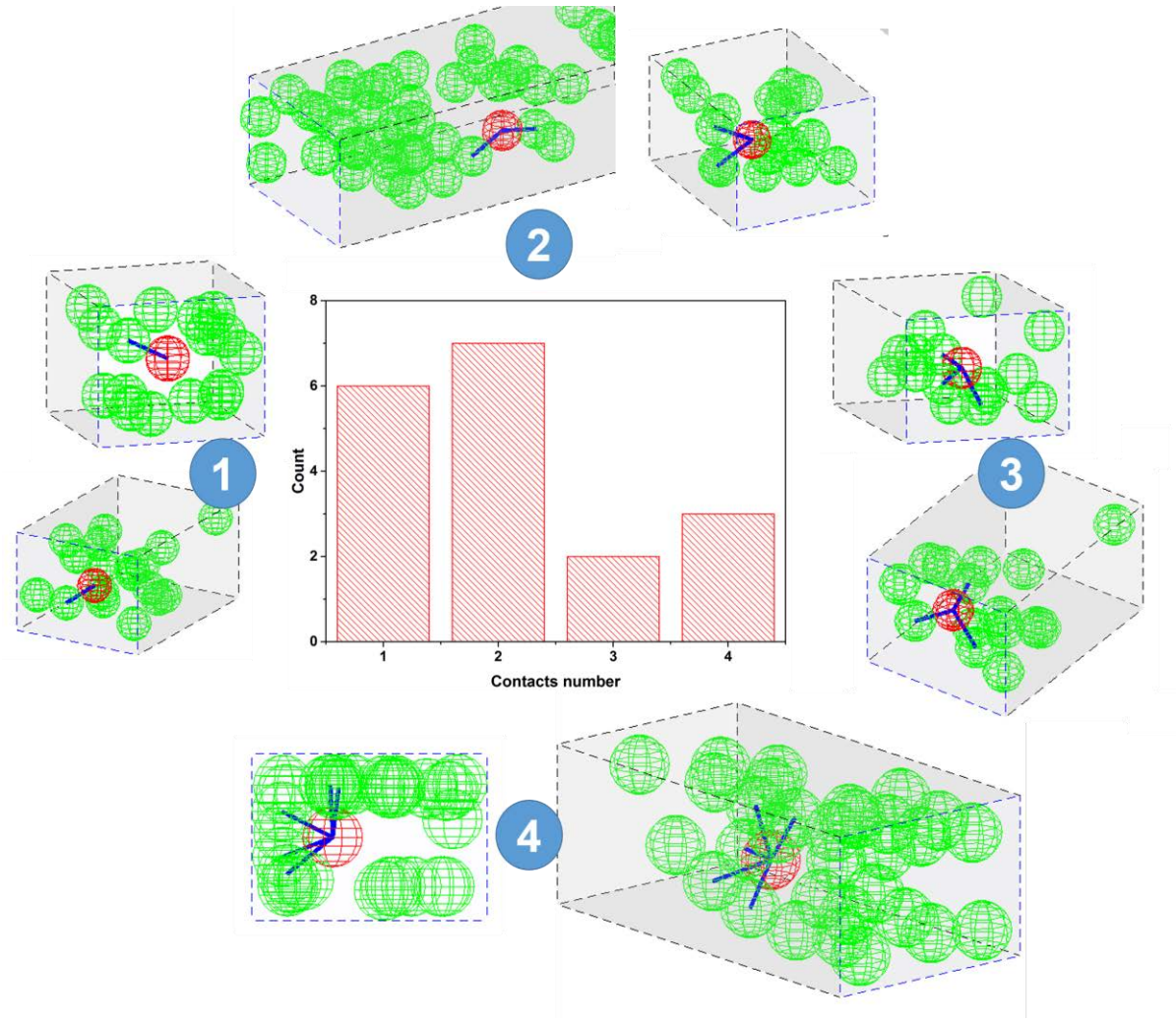

Figure 92: Distribution of the coordination number of the particle deposited in the second layer. We identified particles with 1 to 4 contacts, the most probable one being 2 contacts. Each case of contact number is illustrated by two examples with 3D images of the whole pore. The colour codes are the same as in the previous figure.

2. Final clog structure in high confinement

We analysed the structure of the clog at the particle scale for this high confinement case W/H= 3. In the Figure 93-A, we have plotted the evolution of the average volume fraction of clog, ϕ_{clog}, within a particle diameter width slices, from the pore entrance up to the head of the clog. The entire build-up of this clog is shown in Figure 84. There is an increase of the volume fraction from 2-3% up to 40% over a length equals to 2.3H from the pore entrance. In average, for such a high confinement, the length of the clog is consistent with the one we found in the pore scale study for lower confinement (L_{clog}≈2.4H for H/D=5) but it is a bit smaller, L_{clog}≈2H. For a distance, from the pore entrance, greater than H the volume fraction increases from 0 to 20% or so. This corresponds to a partial coverage of the pore surface. Thus, a higher confinement obviously implies that the spatial repartition of the particles on the pore wall has a greater impact on the volume fraction of the clog. For the distance lower than H, ϕ_{clog} increases up to reach 40% at the pore entrance. In this zone, there are most of

particles captured within the second layer, “in the bulk”. The average value of the volume fraction is a bit higher than for H/D=6 (Figure 93B). This result has to be confirmed by getting more statistics.

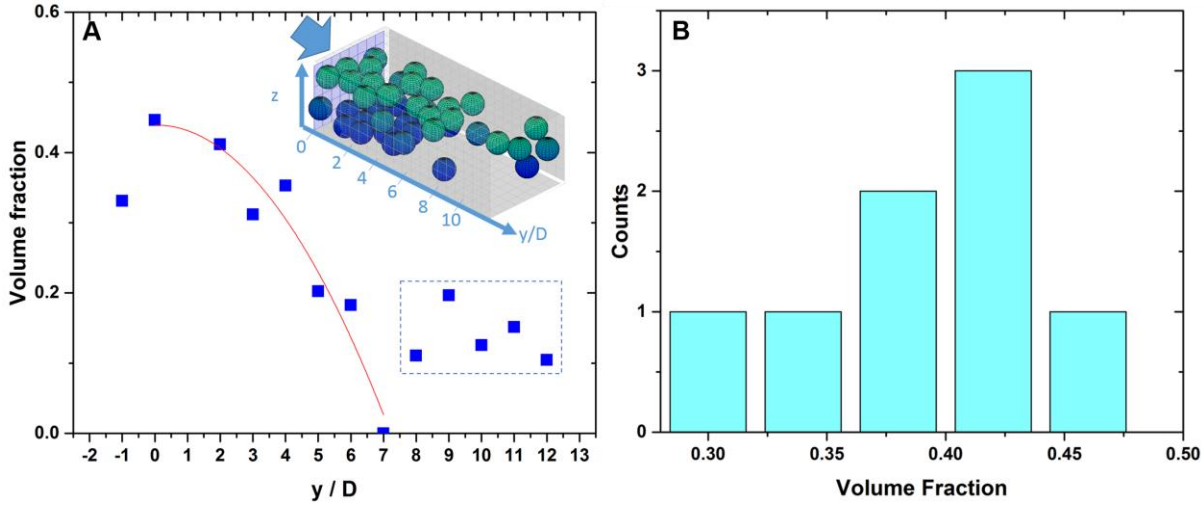

Figure 93: A-Evolution of the volume fraction within the pore along the flow direction. We calculate the volume fractions in a volume of WxHxD, i.e. the cross section of the pore along a length of D. The red line is a second order polynomial fit such as $y/D=0.44+5x10^{-4}\phi-8.5x10^{-3}\phi^2$, and is here as a guide for the eyes. Particles that belong to the clog are in between 0< y/D<7. For y/D>8 there are one aggregate and one isolated particle that do not partake to the clog. B-Volume fraction distribution for all the experiments.

We have also plotted all the contacts within the clog from a length equals to 4D from the pore entrance in Figure 94. To identify the contacts shared by a particle we have to define a threshold length between the particle and the surrounding ones or the pore wall. We choose a distance of 1.1D centre to centre as the limit to contacts. This 0.1D allowance on the particle diameter correspond to an uncertainty of 1 pixel on each particle diameter (1pxl =0.204 µm in our optical set-up). We make sure that this 10% allowance on the particle apparent size was robust and that the results obtained with this criterion was invariant over small variations (1.05 to 1.15D). In the example show in Figure 94, most of particles on the top and the bottom surfaces are connected to the pore surface but also to other particles in their surroundings. At the head of the clog, within the cross section between the distance 3D and 4D from the pore entrance (Figure 94-C-1), the various aggregates connect one another. Nevertheless, when we go towards the entrance, to the adjacent cross section (Figure 94-C-2), there is a continuity in network of the contacts all around the pore surface. In those first two cross sections, some places remain where particles could go through, in principle. Even closer to the entrance (Figure 94-C-3), we get the densest cross section of the clog and the remaining surface is smaller than the projected surface of a particle. From the view in Figure 94-B, we clearly see that there are also connections between the particles that belong to the various cross sections.

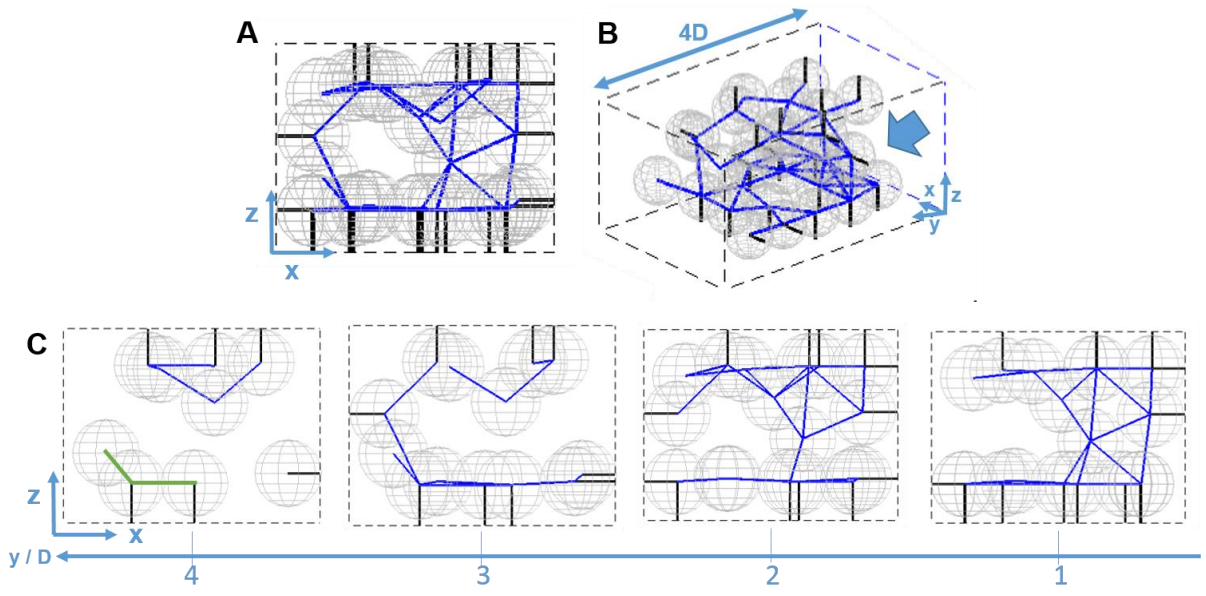

Figure 94: Sectioning of the clog shown on Figure 93-A. A- Projection in the pore cross section of the clog over its size Δy_{clog} (cf. Figure 93-B) i.e. 4D. Dashed line represents the pore walls. Blue lines represent the contacts between particles. Black lines represent contacts between particles and walls. B- 3d view of A. Flow is along y axis. C- Illustration of the sectioning shown in D. The 4D length is divided in cross sections of length 2D along the flow direction. D- Cross sections of the clog, from the head of the clog (downstream, image y/D=4) to its end (upstream, image y/D=1). The different links colours correspond to particles connected to each other in the section sorted by contact aggregate size. Inter-planar links are not consider here, but in A were they are, we see a single link colour indicating that all particles are connected. y-coordinates of the centre of the slice are indicated below each images.

3. Final clog structure in lower confinement

In this section, we investigate the final structure of a clog formed in a square cross section (H=W) channel of width W=11 µm with D=1.8 µm PMMA particles, i.e. W/D≈6. First, we investigate the structure of clogs formed without any modification of the particles surface charges. Hereafter, we do the same with addition of electrolytes in the solution.

a. Particles with high surface charges

We imaged clogs after their formation by performing a confocal z-stack. Therefore, the particle location in the clog can be determined in 3d; and an example of a clog is shown in Figure 95-A. From the location of the particle centre, we are able to measure the volume fraction of the clog, ϕ_{clog}. We did this along the flow direction within a particle diameter width slices, starting from the furthest deposited particle toward the pore entrance as illustrated in Figure 95-A. The volume fraction evolves from a background level around 2-3%, due to two to three particles captured on the pore surface at the front of the clog, up to a plateau around 33% (Figure 95-B). This increase of the volume fraction spreads over a length roughly equals to the pore width W. In a first approximation, we may consider that length corresponds to the clog, and thus it indicates that the clog build-up within a volume of the order of W^3. The plateau value of ϕ_{clog} is low and reflects a very loose, gel like, structure consistent with the

results obtained from sedimentation studies with micrometre particles [77]. We can have a better understanding of the structure of the clog by looking inside its different cross sections (Figure 96-D). As we might expect, in the cross section corresponding to the maximum value of ϕ_{clog}, at the beginning of the plateau, there is not enough room to let a particle go through the pore (Figure 96-D3). Moreover, the maximum value of the coordination number, which is the number of contacts of a particle with its neighbours, is found within this peculiar slice. All those details are thus consistent with our definition of the spatial spreading of the clog (L_{clog}=W). However, a closer look on both, the internal structure and contact network, can lead to another definition of the clog. Indeed, we observe on Figure 95-C that there is a first increase of the average coordination number up to the peak just mentioned above. Within this zone (Figure 96-D1-3) few aggregates are not in contact within each cross section. At the peak or close to it, one aggregate span on the overall cross-section of the pore (Figure 96-D4). After this peak, toward the pore entrance, even though the volume fraction seems to slightly oscillates around a constant value, the coordination number decreases over a distance also equals to W.

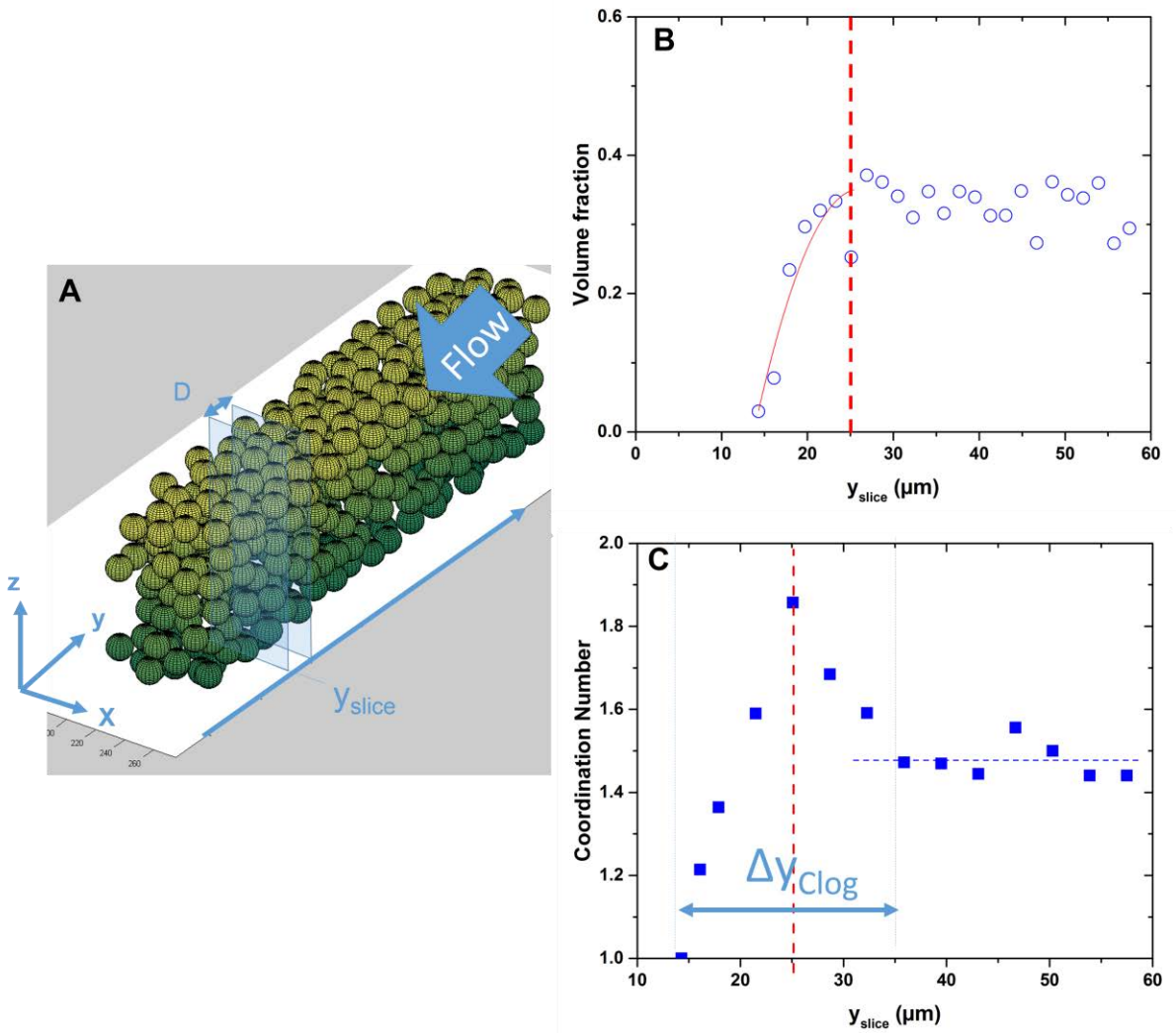

Figure 95: Clog structure for D=1.8µm particles in a W=11µm pore. A- 3d recontruction of the particle forming the clog after its formation from confocal imaging. B - Evolution of the clog volume fraction in a slice of width D along the flow direction from the head of the clog to the end of the particles accumulation (upstream direction). Slices in which the volume fraction is calculated is illustrated on A. The volume fraction evolve from a low noise level (due to the deposition of few particles downstream of the clog that are not part of the clog itself) to a plateau value on a distance about the size of W. This evolution is fitted by a 2nd order polynome ($y=bx+cx^2$,red curve) with parameters b=0.12 c=-2.3x10^{-3}. C- Evolution of the mean coordination number of particles in the slices defined in A. Red dashed line corresponds to the maximum in volume fraction (B). We define the size of the clog as the width of the peak in coordination number: Δy_{clog}.

Even if we have still a main aggregate, which spans over half of the cross section (Figure 96-D4-6), others are non-connected. Moreover, there is a significant place, free of particle, in between those aggregates. At a distance greater than W, from the peak towards the pore entrance, the coordination number levels off to 1.5. Therefore, the clog span over a length around 2W rather than W. This is consistent with the results of the last section in the high confinement case. The aggregates have grown on the pore surface over 2W and they end up by merging and thus clogging the pore at the middle of this zone, or close to it, where the coordination number is the greatest. Thus, in this definition of the clog, the length over which the clog builds up has to be taken into account rather than just the length within which the

volume fraction and the coordination number are the greatest. Upstream of the clog, as ϕ_{clog} remains constant and the coordination number is fixed at a low value. In this zone, the particles close to the pore surface can be captured (Figure 96-E-F). Indeed, those ones do not need to have a high velocity to deposit on the pore walls, the electrostatic barrier to be captured on the walls being small, since the PDMS is almost not charged. For small accumulation length (Figure 96-E and F), behind the clog, the related the hydrodynamic resistance remaining small, we can still capture particles within the second layer of particle (relies only on inter-particle interaction).

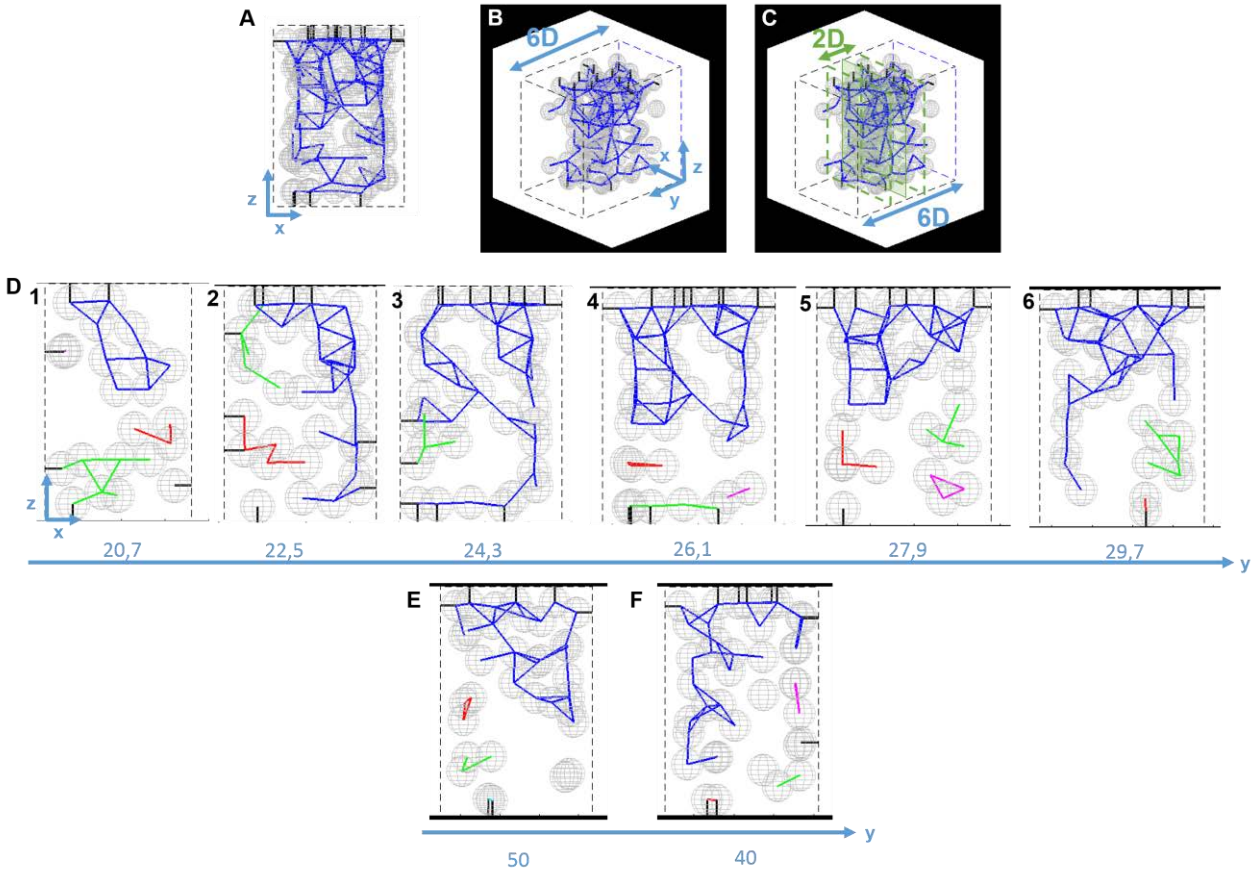

Figure 96: Sectioning of the clog shown on Figure 95. A- Projection in the pore cross section of the clog over its size Δy_{clog} (cf. Figure 95-B) i.e. 6D. Pore walls are represented in dashed line. Blue lines represent the contacts between particles. Black lines represent contacts between particles and walls. B- 3d view of A. Flow is along y axis. C- Illustration of the sectioning shown in D. The 6D length is divided in cross sections of length 2D along the flow direction. D- Cross sections of the clog, from the head of the clog (upstream, image 1) to its end (downstream, image 6). The different links colours correspond to particles connected to each other in the section sorted by contact aggregate size. Inter-planar links are not considered here, but in A, where they are, we see a single link colour indicating that all particles are connected. y-coordinates of the centre of the slice are indicated below each images. E and F – Sections in the accumulation area upstream of the clog at 50 and 40 µm in the y direction respectively.

We can confirm that such repulsive colloidal glass follows the clog, in which most of the particles experience irreversible contact, by performing a simple unclogging experiment (Figure 97). We have formed a clog at a given pressure difference and we have let the particles accumulate at the rear of the clog until they start to invade the reservoir zone (Figure

97, first image). At that moment, we released the pressure and we clearly see that there is a uniform front of decompaction within the reservoir. All the particles that were just behind the effective clog just leave the place in the opposite direction of the flow (1st raw: from the second image up to the last one). Only individual particles and some aggregates in contact with the pore wall, all located behind the clog, do not move. The particles that belong to the clog also do so (particle within the dashed rectangle of length 2W).

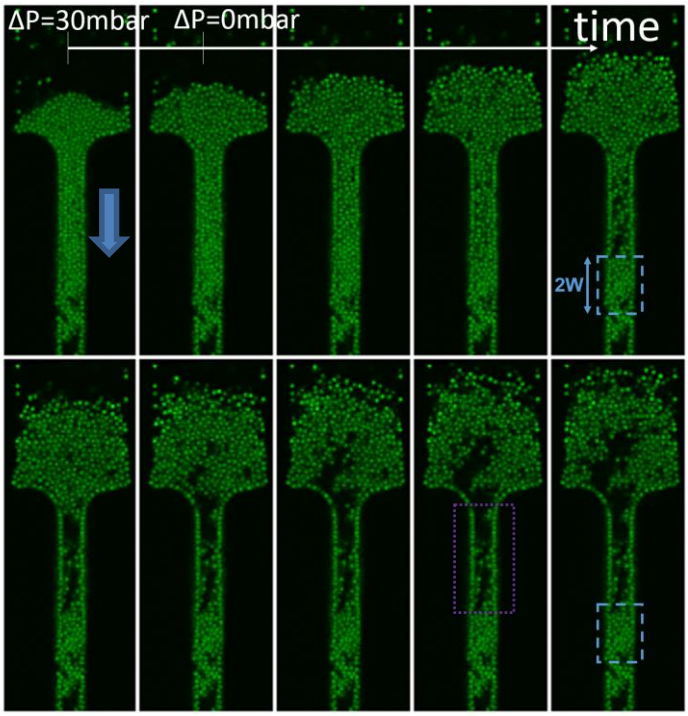

Figure 97: Consecutive images of a clog dislocation after pressure release. On the second image, the pressure applied to form the clog is released to 0. The particles that accumulated behind the clog starts to flow from the pore, as a concentrated solution. It leaves the clog intact and we can see its real extension in the pore (about 2W) as illustrated by the blue dashed rectangle on the last images of each rows. We can also note remaining aggregates on the pore walls upstream of the clog (purple dotted rectangle). Blue arrow indicates the flow direction.

We also provide other examples of clog structures in the Figure 98. Sometimes aggregates can be formed further downstream within the pore and do not finally partake to the clog, this latter being formed closer to the pore entrance (Figure 98-A). However, for those aggregates, the increase of volume fraction is very similar to what we have found for a regular clog (Figure 95, Figure 98-B). Moreover, those aggregates grow over a distance about 2W. Thus, those observations strengthen the idea that various aggregates grow and get connected to clog the pore. This could also explain why the final structure of the clog is so loose. When the clog formation takes place closer to the pore entrance than usual (Figure 98-B), we can get a higher average ϕ_{clog}. This likely comes from the fact that (i) the aggregates grow partly on the curved part of the pore entrance; (ii) the width of the pore is greater.

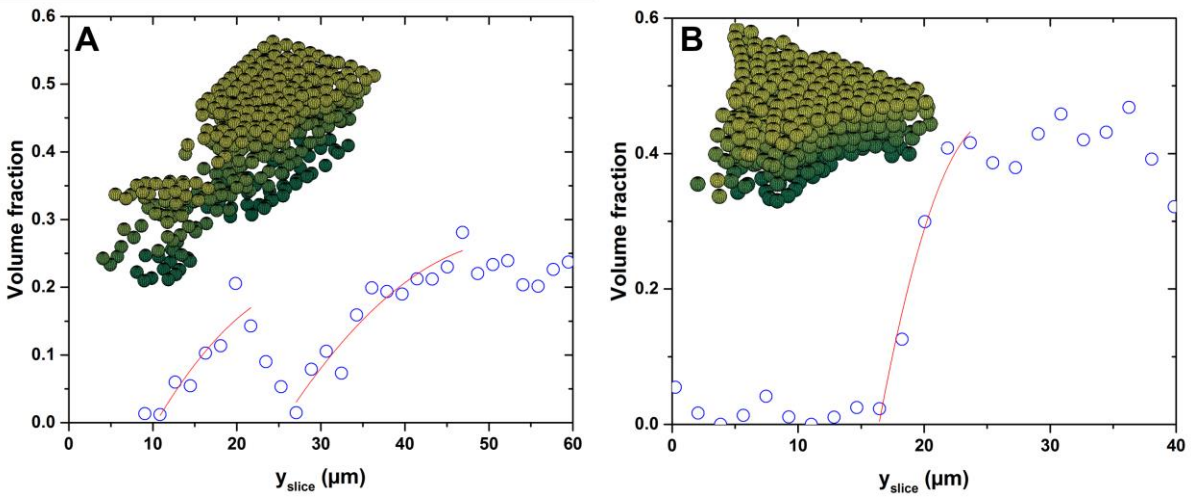

Figure 98: Evolution of the clog volume fraction (cf. Figure 95) illustrating the lowest volume fraction value we found (A) and the highest (B). A- We see a first increase of the volume fraction due to an aggregate formed downstream from the clog, this evolution follows the same type of polynome that the clog itself. It results in a lower final volume fraction at the clog. B- The clog is located closer to the entrance than the average clog. The construction of the clog on such a short extension results in a highest volume fraction of the clog.

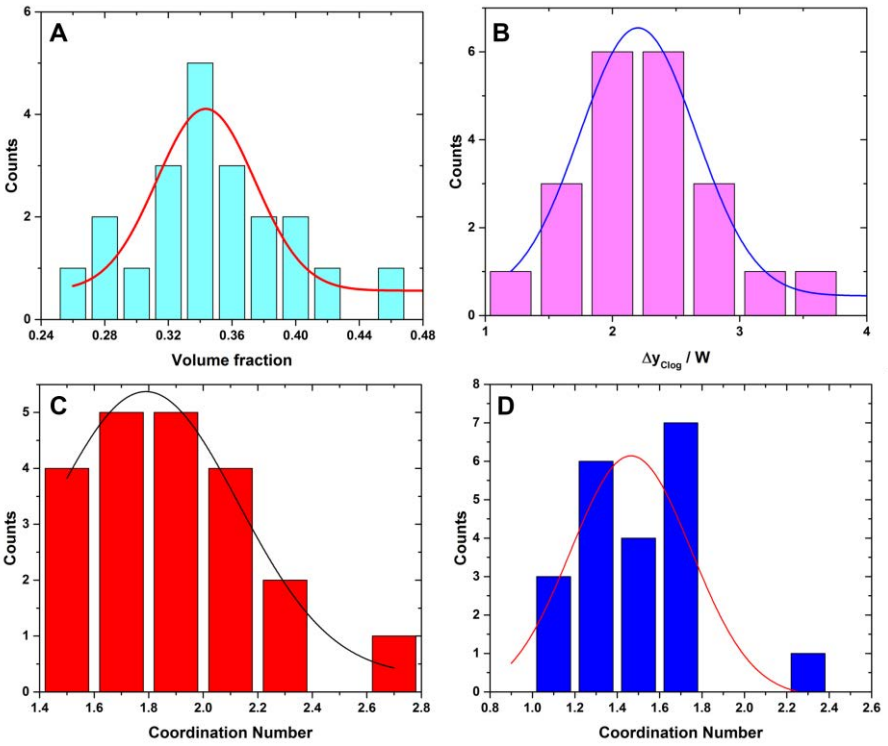

Figure 99: Statistics on clog structure descriptors. A- Distribution of the maximum volume fraction of the clogs. It follows a Gaussian distribution centred on 0.34 with a standard deviation of 0.06. B- Distribution of the clogs sizes. It follows a Gaussian distribution centred on 2.2 with standard deviation of 0.9. C- Distribution of the particles mean coordination number at the peak (cf. Figure 95-C). It follows a Gaussian distribution centred on 1.8 with standard deviation 0.67. D- Distribution of the particles accumulating behind the clog mean coordination number. It follows a Gaussian distribution centred on 1.46 with standard deviation 0.57.

No features of the clog structure change too much from one clog to another. We found that the average coordination number and the clog volume fraction at the peak (highest ϕ_{clog}) are

equal to 1.8 and 34% (Figure 99-A and C) while the length of the clog is around 2.2W (Figure 99-B). At the rear of the effective clog, the average coordination number is equals to 1.5 (Figure 99-D). As we have shown before (cf. Chapter IV -A.3), the addition of electrolytes in the solution increases the clogging efficiency. In the next section, we will see how this affects the structure of the clog.

b. Particles with screened surface charges

We now investigate the structure of the clogs in the same pore geometry (W=H=6D), with the same suspension, but with a high salt concentration (0.15 M). Here, the surface charge of both, the pore wall and the particles, are largely screened, since we are close to the critical coagulation concentration (CCC=0.2 M). An example of the clog formed in these conditions is shown in Figure 100-A. The evolution of the volume fraction follows the same trend as before, i.e. when we added no salt, but the increase of ϕ_{clog} spreads over a greater length, roughly equals to 1.7 W (Figure 100-B). Moreover, the value of ϕ_{clog} at the plateau is also higher and is around 0.4, which corresponds to an increase of 15% in respect to the former case, without added salt.

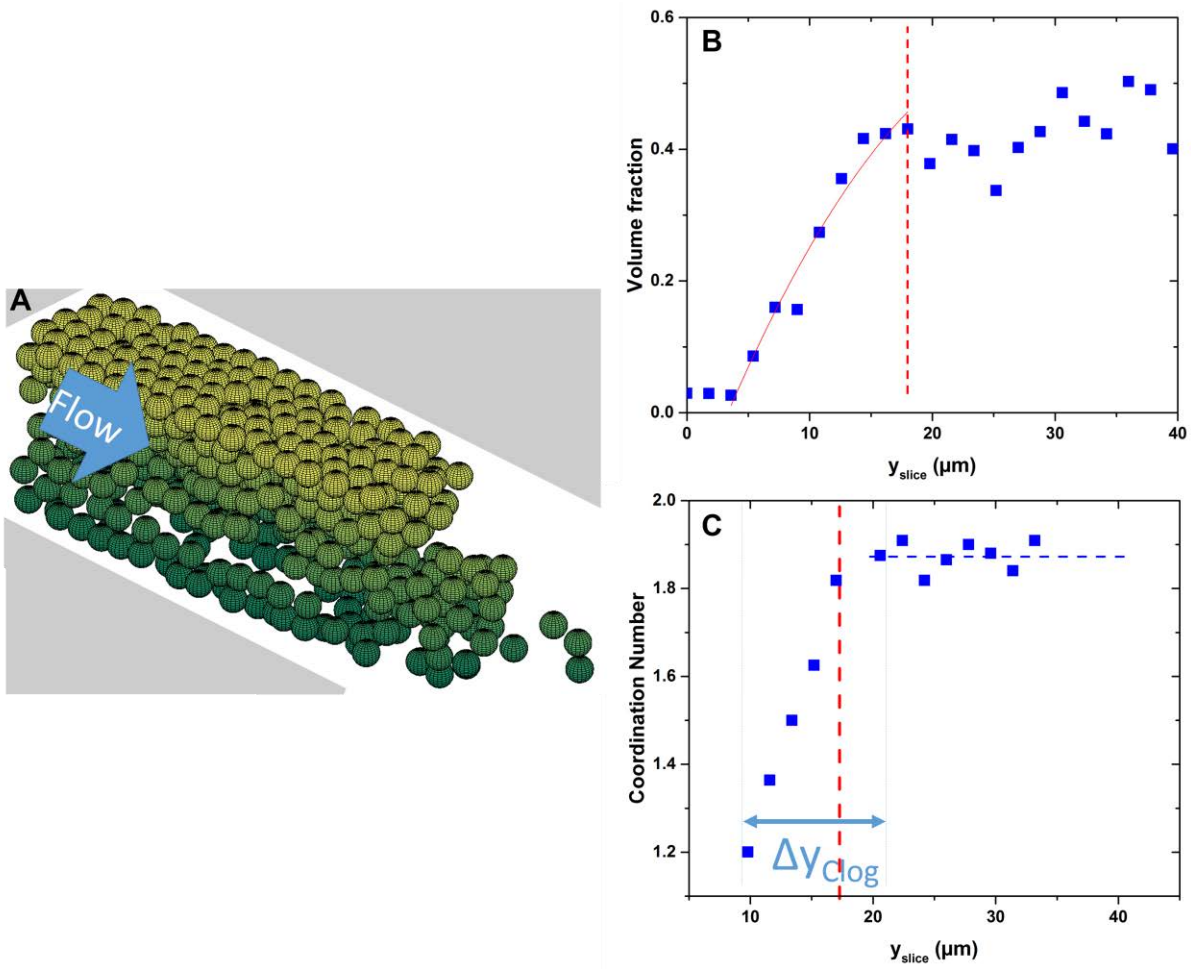

Figure 100: Structure of a clog formed with an addition of 0.15M NaCl in solution. A- 3d image of the clog from confocal images. B- Evolution of the particle volume fraction in the clog along the flow direction as illustrated in Figure 95-A. C- Evolution of the particles mean coordination number.

The coordination number also reaches its maximum, around 1.9, at the very beginning of the plateau, and it does not change as particles accumulate at the rear of the clog (Figure 100-C). Therefore, when the suspension exhibits a high salt content, even though the maximum value of ϕ_{clog} is greater, we have a slower increase of ϕ_{clog} over the clog length. Those new features of the clog obviously lead to another clog structure than before (Figure 101). In front of the clog, few isolated particles correspond to the background level of the volume fraction around 2-3%. At the clog front, we do not have various tiny aggregates as before but rather a big one which is more compact (Figure 101-A). A bit deeper into the clog (Figure 101-C6), there are two compact aggregates, one which fills almost entirely half of the top part while the other fills half of the bottom one. At the densest part of the clog, once again, only one aggregate spans over the all cross section (Figure 101-C5). After this part, still towards the pore entrance, (Figure 101-C6 to C1) the main aggregate almost fills half of the pore, in the top part, while only the vicinity of the pore surface is covered by particles in the other half, in the bottom. We also observed isolate particle within the bulk with no contact that thus jiggle, due to the Brownian motion (Figure 101-D and E).

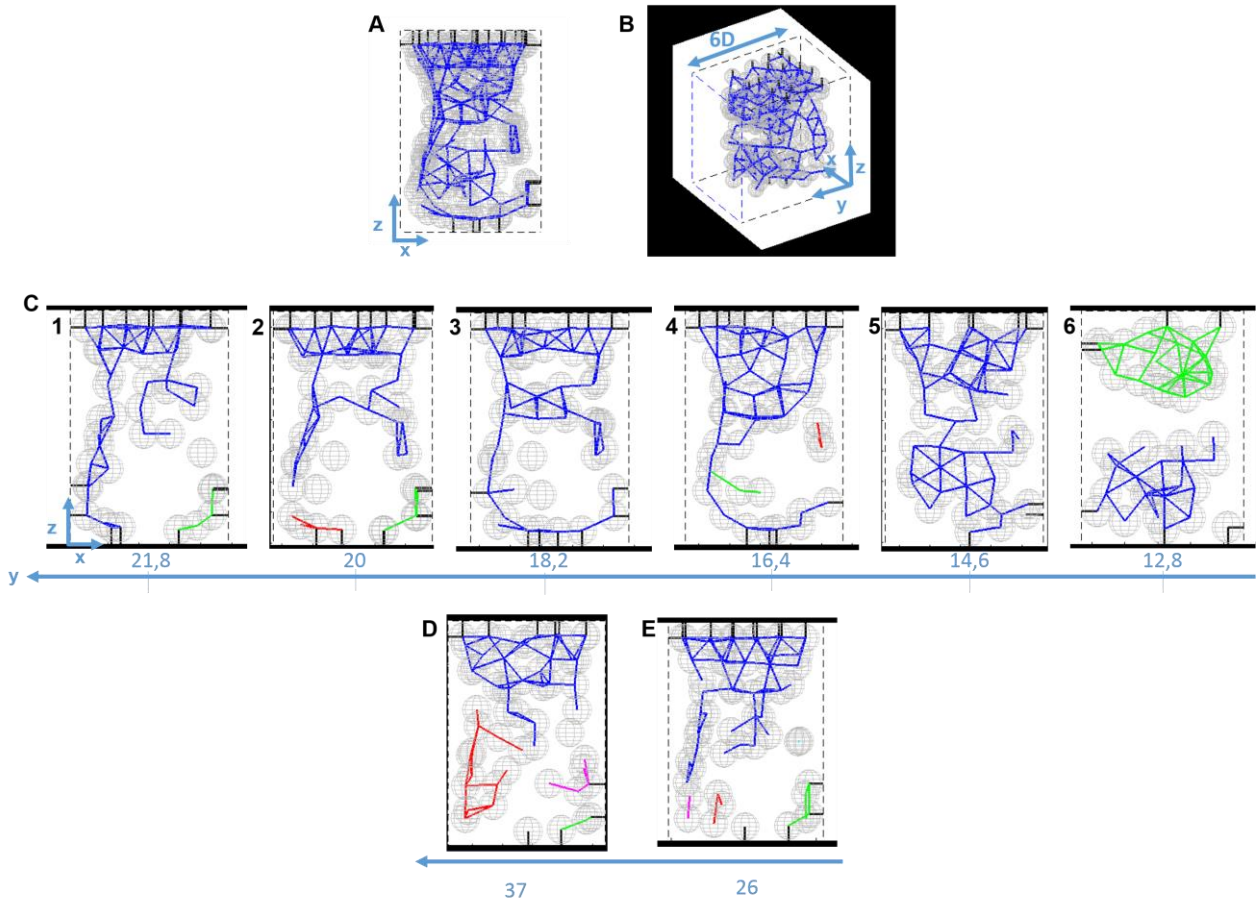

Figure 101: Sectioning of the clog shown on Figure 100, as described in Figure 96. D and E – Sections in the accumulation area upstream of the clog at 37 and 26 µm in the y direction respectively.

Here contrary to the previous case, the formation of aggregate is still possible well upstream of the clog front. Those aggregates are more compact and they can easily grow inward the pore. This is directly related to the high ionic strength of the suspension. When the particles get towards rear front of the clog, they can go closer than before to the various aggregates that lie on the pore surface and get captured, since there is almost no repulsion. Moreover, the particle capture requires a very low particle velocity to overcome those small electrostatic barriers (probably around 20-100 K_BT, with K_BT the thermal energy). Therefore even if the particles pile up over a rather long distance within the pore, which results in a high hydrodynamic resistance and thus low particle velocities, the aggregate growth is still possible.

All the features discussed above are also quite robust (Figure 102). For such high salt content, the average volume fraction is around 41% (Figure 102-A) while the clog length is equal to 1.7W (Figure 102-B). Since the formation of aggregates is usually possible, we found that the distribution of coordination number looks like the same at the peak, at the beginning of the plateau (Figure 102-C) or deeper within the pile up of particles (Figure 102-D). Still this quantity is a bit higher in the plateau than everywhere else.

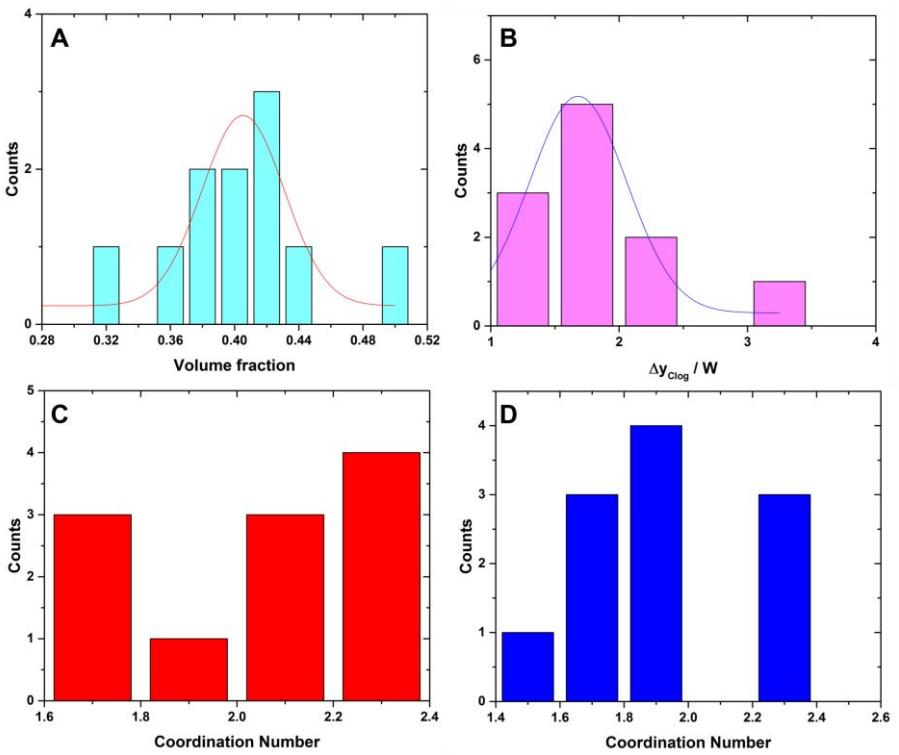

Figure 102: Statistics on the features of the clog structure with an ionic strength of 0.15 M NaCl. A- Distribution of the maximum volume fraction of the clogs. It follows a Gaussian distribution centred on 0.40 with a standard deviation of 0.05. B- Distribution of the clog length. It also follows a Gaussian distribution centred on 1.68 with standard deviation of 0.75. C- Distribution of the particles mean coordination number at the peak (cf. Figure 100-C). The mean value is 2.01 with a standard deviation of 0.26. D- Distribution of the particles accumulating behind the clog mean coordination number. The mean value is 1.91 with standard deviation 0.29.

C. Discussion

By gathering the pore scale and the particle scale data, we can determine the different steps of formation of a clog. Here, we focus only on the long pore, in which clogs easily show up. At the beginning of the clogging process, particles always get captured at the very entrance of the pore, where the particles accelerate. Those particles also get mainly in the corners of the pore, where the particles also experience quick change of fluid velocity as they get closer to the pore wall. Those capture zones are also often observed since this is the place, within a pore cross section, where the shear flow is the lowest. It is thus the most stable position under flow for a still particle within the pore. This notion of stability under flow is quite important to understand the clog formation. The particle capture requires that the pressure drop across the pore is high enough to overcome the repulsive electrostatic barrier. Therefore, we cannot observe formation of clog without applying a pressure drop as the Brownian motion is not sufficient to allow particles to stick to each other. We have always worked below the CCC, and then there is no spontaneous aggregation. On the opposite, a too large pressure drop imposes a torque on a still particle large enough to overcome the adhesive van der Waals force. We can estimate a critical fluid velocity for which the torque exerted by the drag force

on a still particle can remove it from the pore wall [78]. We must consider two typical cases: either the particle is stuck on the pore surface or it is on another particle. In order to detach the still particle, the torque exerted by the drag force (TD) has to be greater than the torque related to the van der Waals force (TvdW) either between the particle and wall, or between particles, respectively (Figure 103).

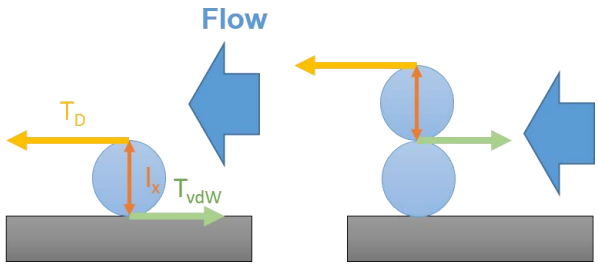

Figure 103: Hydrodynamic torque acting on a deposited particle. Left: particle deposited on the pore wall. Right: particle deposited on top of another particle.

We easily deduce the critical fluid velocity to detach the still particle in both cases from the torque balance. In both case we get:

$$T_D = T_{vdW}$$

$$F_D \times l_x = F_{vdw} \times l_x$$

where l_x is the lever arm of the Torque (for particle stuck vertically l_x=D) as illustrated on Figure 103. From this expression, we easily obtain the following ones:

$$F_D = F_{vdW}$$

Particle-Wall :

$$6\pi\eta D U_{C\,p-w} = \frac{AD}{12h^2}$$

$$U_{C\,p-w} = \frac{A}{72\eta h^2}$$

Particle-Particle :

$$6\pi\eta D U_{C\,p-p} = \frac{AD}{6h^2}$$

$$U_{C\,p-p} = \frac{A}{36\eta h^2}$$

We have shown that there are two regimes of clogging. In the first one, both the L_{clog} and the N* are constants, whereas in the second regime L_{clog} and N* increase. An example of the variation of N* with the applied pressure is shown the Figure 104-A. For this example, the first regime occurs within a limited pressure range (0.1-20 mbar). In this regime, the hydrodynamic torque is not able to detach particle neither on the pore surface nor on top of other particles (Figure 104-A). The fluid velocity near the surface and on top of the first layer, at least, is always smaller than the critical values mentioned above in this regime (Figure 104-A). In contrast, in the second regime, from its beginning, the fluid velocity is higher than the two critical one needed to detach particles captured on top of the first layer. Thus, we can deposit

particles on the pore surface but not form more than a monolayer. Increasing the pressure by a factor five (around 100 mbar), allows the flow to remove all the particles from the pore wall. Actually, we still observe clog formation in the second regime, because there are other positions within the pore where particles can stay still under flow and aggregates can be built up from those place. For instance, as we mentioned at the beginning of this paragraph, corners are stable positions for the particles. Another reason of stability in this zone is the fact that the particles here have two contacts with the wall. Thus, the fluid flow has to be stronger to remove those ones.

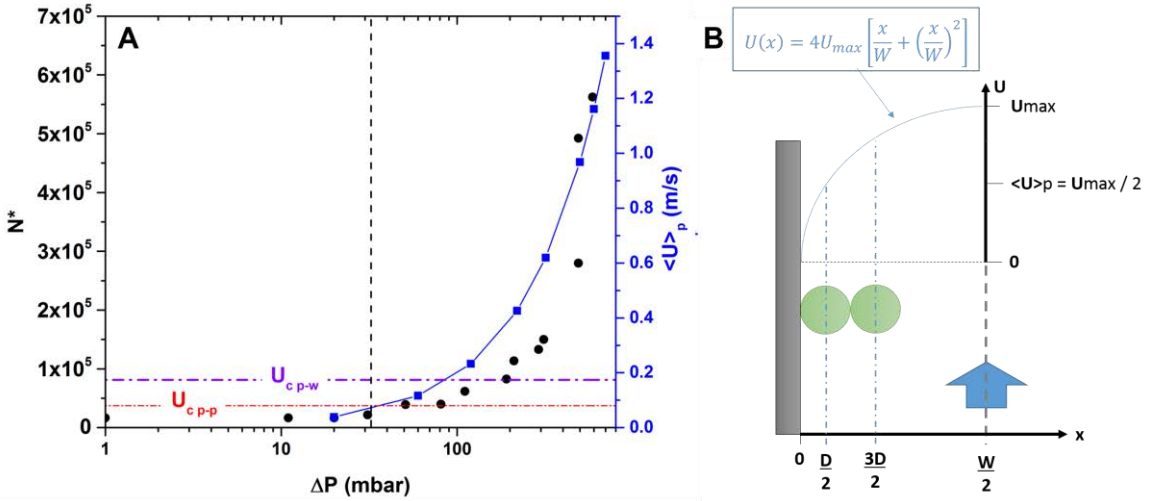

Figure 104: A-Evolution of N* and the mean measured velocity of the particles with the applied pressure drop. The particle velocities increase linearly with the pressure drop. The dashed red line corresponds to the critical velocity to remove a particle deposited on another one. The dashed-doted purple line is the critical velocity to remove a particle deposited on the pore surface. B- Fluid velocities experienced by the particles. The velocity profile is parabolic with its maximum value at the centre (W/2). We can relate the velocity in any x position to the average velocity we measured by the equation shown on the scheme and the fact that the average velocity is half the maximum velocity. Particle removed from the wall have their centres at D/2 from the wall and particles on top of another one will have its centre at 3D/2.

From those features of the particle deposition within the pore, we can provide some general findings on the evolution of L_{clog} and of N* in both clogging regime. In the second one, for the higher applied pressure, L_{clog} increases simply because particles on the pore surface are more stable than those on the top of the first layer of particles are, since the adhesive torque is higher on the pore surface. Then we will capture more particles on the pore surface before depositing a particle on top of those ones. Moreover, we have shown that still particles modify the flow around us in such way that flowing particles will be stuck preferentially in their vicinity (cf. Chapter IV -B.1.ii). We show that this is how aggregates start to grow from the pore surface. We thus suppose that aggregate will mainly grow only on the pore surface over longer distance in the second regime. On the other hands, since there are less and less stable positions for the particles under flow, as the pressure increases, N* has to increase.

Indeed, the particles that will partake to the growth of the aggregates will necessarily have the maximum possible number of contacts with other individuals to remain stuck under flow. This means that a greater number of particles have to flow along the forming aggregates before there are ones that meet the local stability criteria. It is worth mentioning that particles can also move slowly on the pore surface, i.e., they roll. This motion will also modify the aggregate growth. All those features of the particle deposition in the second regime likely lead to the building up of clog with a structure different to what we get in the first regime. We think that those structures will evolve with the pressure, which is not really true in the first clogging regime.

Now let us focus only the first regime for which most of the data of this chapter is devoted. For a high confinement, we were able to follow the dynamic of the building up of the clog. We show that few aggregates grow mainly on the pore surface until they merge and only one grows and invades the remaining space within the pore up to the clogging. In average, those aggregates spread along the pore surface over a length a bit greater than 1.5W before a particle gets captured on top of this first layer. In the following, the aggregates keep spreading along the pore until $L_{clog} \approx 2W$ and grow towards middle of the pore. In this building up, all the new captured particles always stopped in the vicinity of the aggregates. We think that the same mechanism remains true for the building up of the clog in lower confinement (cf. Chapter IV -B.3). Unfortunately, we get only the structure of the clog once this latter is already formed. However, we suppose that several aggregates start to grow from the corner, and they "catch" particles. As they grow, some of them get connected until a main aggregate clogs the cross section of the pore. Despite the fact that the degree of confinement is twice smaller (H/D=3 up to H/D=6), we observe similar features of the final structure. Even though, L_{clog} increases from 2W to 2.2W, this evolution is consistent with an increase with W/D. Thus, for the PMMA particles, L_{clog} increases with W/D in the exact same way that the PS particles did (Figure 79-B). The volume fraction ϕ_{clog} decreases from 40 to 34%. In both cases, we still have a gel like structure, i.e. a rather loose structure. On the other hands, as expected, there is an increase of this number when the pore becomes larger, $N^*=A(W/D)^7$. Wyss et al. [3] also found a power law scaling but with a four power. This likely comes from the fact that they used the raw suspension within which there always are few particles with a size quite larger than the mean particle size [38]. In their case, the pore clogging is a two steps process. There is first aggregates growth on the wall of the pore until the remaining cross section of the pore is about the size of the few big particles present in the solution. Very recently, Sauret et al. [39] have confirmed this scenario with the same geometry used by Wyss. They have shown that if there are big particles, with a particle volume fraction of 10^{-6}, within a suspension of small particles, with a particle volume fraction of 10^{-3}, all the pores of the device are eventually clogged by the bigger objects. In our monodisperses case, the steeper increases of N^* with W/D is thus quite natural since, during the aggregate growth from the pore wall,

more particles have to be used to clog the pore. Here, we also found that there are two distinct contributions to the variations of N* with W/D:

$$N^* = f(DLVO) \times g\left(\frac{W}{D}\right)$$

where f depends on the salt content and g relies only on purely geometrical considerations.

$$N^* = N_0 \times \frac{C_{DLVO}}{[NaCl]} \times \left(\frac{W}{D}\right)^7$$

where N_0 is the N* for W/D=1, $[NaCl]$ is the concentration in NaCl in the solution and C_{DLVO} is a constant depending on the particle properties.

We do not know where this power seven of the function g comes from. We can suppose this rather steep increase is related to growth rate of the aggregate and thus to the probability of particle capture by them. Indeed, we have seen in the chapter on 2d for instance, that the width of the capture for a given flow rate does not change when the channel becomes wider or higher, whereas the capture probability decreases quite rapidly since it is the ratio between of the capture width over the channel height (width).

The other contributions of N*, f (DLVO) is better understood. Whatever the salt concentration and the particle type (PS or PMMA), the geometrical features of the clog at the pore scale do not change significantly, in particular the width and the length of the clog. Therefore, N* corresponds to the number of particles to be used to form a clog in a fixed volume in between W^3 and $2W^3$, irrespective of the salt concentration. From the study at the particle scale, we found that the structure of the clog is quite similar even though some differences remain. In particular, the average clog volume fraction goes from 34% to 41% when the ionic strength increases from 0 to 0.15, which is close to critical coagulation concentration. Since both the clogging volume and the average clog volume fraction are roughly the same, we can conclude that the probability of the particle capture by the growing aggregates increases with the ionic strength. We have thus to use less particles to form almost the same clog structure in the same clogging volume when $[NaCl]$ increases, N* decreasing linearly with $[NaCl]$.

D. Conclusion

In this chapter, we have provided a general picture, both at the pore and at particle scale, of the clogging process by colloidal particles of a 3d pore. The pore scale approach, based on bright-field microscopy, has allowed us to determine the influence of the pore geometry, the hydrodynamics and the colloidal forces on the clogging process. We observed that slight modifications of the geometry of the pore entrance could dramatically change the clogging ability of the pore. We showed that for clogging to occurs, the pore must be long enough, never smaller than W, the width of the pore cross section. This length corresponds to the

lateral extension, along the pore, of a stable clog under flow. We showed that such stable clog require that a fixed number of particles N* has to pass through the pore prior its clogging. In the following, we studied the evolution of those two parameters, N* and Lclog with the other relevant parameters, namely the hydrodynamics and the colloidal forces. Starting with the hydrodynamics, we observed a first regime of low pressures where N* and L_{clog} remain constant, irrespective of the pressure. In contrast, in the second clogging regime, for a higher-pressure range, both quantities increase with the pressure. We focus mainly of the first clogging regime hereafter and we showed that L_{clog} and N* increase with the degree of confinement W/D, linearly and far more steeply, as a power law 7, respectively. On the other hands, the modification of the repulsive part of the DLVO potential leads to the greater change of N*. A higher repulsion between the particles corresponds to a higher value of N*: N* increasing linearly with ionic strength of the suspension for each confinement. However, the evolution of N* with W/D does not change. We thus conclude that there were two independent contributions to the variation of N* with the confinement, the first one being purely geometrical while the second is related only to the DLVO potential. Zooming in at the particle scale, thanks to high-speed confocal microscopy, we have been able to show that indeed the structure of the clogs, obtained for very different ionic strength conditions, is almost the same. The rapid change of N* with the ionic strength is related to the probability of capture of the particles by the growing aggregates. For high ionic strength, close to the critical coagulation concentration, the repulsive barrier is tiny and thus the hydrodynamic drag needed to overcome this barrier is rather small, which facilitates the particle capture. In the opposite, for very low ionic strength, the barrier is high and the capture probability is small, since our particles, PS and PMMA, exhibit naturally high surface charge.

We were also able to capture the dynamics, at the particle scale, of the clog building up for a high confinement (H/D =3). We identified two steps of formation of the clog. The first step consists in the deposition of particle on the pore walls. We found that the clogging process starts with the direct capture of particles by the wall at the pore entrance. As soon as two or three particles were deposited here, the indirect capture dominates. Thus, all new particles that enter within the pore will eventually encounter the still ones at the entrance. In this case, hydrodynamic interactions between those two particle categories lead to the capture of the flowing one by the pore wall (indirect capture mode). In this case, the hydrodynamic interactions mainly lead to the particle deposition in the vicinity of the still particle. Therefore, as soon as new particles are captured within the pore one of the aggregates grows. We found that few aggregates first grow and, as the time goes on, they get connected and only one main aggregate dominates the clog build-up. Once it extends in the pore over a length close to the pore height (the more confining length scale), the deposition on top of the first monolayer of particles, in contact with the pore wall, starts. We indeed observed that the deposition of the first particle on that monolayer corresponds to the beginning of the second and last step of the clog build-up. During this regime, the particle capture rate increases since

the available cross section of the pore is rather reduced. Finally, we confirm that for a higher confinement, the average volume fraction is a little more important than for the lower confinement case studied before (H/D=3 vs. H/D=6). This is mainly because, in high confinement, most of the particles depositions take place on the pore walls, where the local volume fraction is the highest possible one. Whatever the degree of confinement, clogs always exhibit a loose, gel-like, structure, resulting from the aggregates growth.

Chapter V - Conclusions and outlook

A. Conclusions

In this thesis, we have performed experimental studies on the successive depositions of micron colloidal particles at the entrance of a pore that leads to the clogging. Thanks to the soft lithography techniques, we have been able to study the clogging process in various confinements and with different pore geometries in a single pore. We were able to describe this process at the pore and at the particle scale. We determined the features of the different steps of the clog build-up using high-speed confocal. This process starts with the deposition of particles onto the pore walls. Then aggregates form until they get connected to each other and eventually clog the pore.

In the Chapter III -, we have studied the features of the particle deposition on the pore wall, which corresponds to the first step of the clogging process. At the very beginning of this process, a first particle deposits at the pore entrance. This corresponds to a direct interception of the particles by the pore walls (called direct capture mode). We captured the 3d dynamics (position and velocity) of these deposition events using streak technique, which consists of a periodic modulation of the fluorescence signal. This allowed us to determine the probabilities associated with this capture. We show that this probability is proportional to the width of capture zone, upstream of the pore entrance. The width of this zone decreases exponentially with the flow rate. The confocal microscope provides additional data on both, the frequency of such deposition events and the precise 3d location of the particles at the pore entrance. In this way, using these two techniques, we have been able to obtain a reasonable statistics, which allowed us to determine precisely the capture probability of a particle by the pore wall. We also showed that particles deposit usually on the corners, when the height of the pore becomes higher than two particles diameters. We think that particles stay there because they are more stable under flow, since they share two contacts with the pore walls. However, we do not know why they systematically deposit in those places. The use of the streak techniques for lower confinement will likely give an answer to this question.

However, the direct capture of particles by the pore wall is limited since we work in a relatively high confinement. Indeed, as soon as there are few isolated particles captured at the pore entrance, they modify the trajectories of all new coming ones (indirect capture mode). Those binary hydrodynamic interactions lead to an increase of the capture probability, whatever the degree of confinement. The capture of new particles always takes place in the vicinity of a still one. Thus, still particles act as collectors or as local constrictions, which enhances the particle capture. This is the way that aggregates form and grow from the pore surface. In very high confinement, for $H/D<2$, since all the particles are captured only on the two horizontal pore walls, the aggregate growth does not require that particles are in contact within an aggregate.

For lower confinement, aggregates first grow by spreading over the pore wall and, at some point, particles are captured on top of this first particle layer. This transition depends only on the magnitude of the adhesive forces of the particles on the pore surface. Variations of the ionic strength of the suspension do not modify the length of this monolayer of particles, in contact with the pore wall, since it is weakly charged.

Only few isolate aggregates grow in the same time within the pore. However, quite rapidly, one aggregate grow faster than the others do, by capturing new particles that flowed in its vicinity, or by merging with other aggregates. This remains true, irrespective on the degree of confinement.

We observe that the aggregate growth keep going on until the aggregates spread over a length, in the flow direction, roughly equals to the width of the pore, W. At that point, all the aggregates merge as a single one and clog the pore. This lateral spreading of the aggregates is needed to get stable structure of the clog under flow. This was confirmed by studying systematically for the PS particles, from bright field images, the length of the clog, L_{clog} from the pore entrance. Actually, we found that $L_{clog} \propto W/D$, for $1.5 < W/D < 10$. We showed that such stable clogs require that a fixed number of particles N* has to pass through the pore prior its clogging. We observed that this number increases very rapidly with the degree of confinement, i.e., $N^* \propto (W/D)^7$. Those two features, N* and L_{clog} constant, corresponds to the first clogging regime, on which we mainly focussed in this work. In a second regime, for a higher-pressure range, both quantities increase with the pressure.

We have also investigated the influence of the colloidal forces on the N* and L_{clog} in the first clogging regime. The uses of solvents with different refractive indexes, which enable us to get different adhesive properties of the particles, leads to a modification of the L_{clog}, while it does not affect the variation of N* with the degree of confinement. By contrast, the modification of the repulsive part of the DLVO potential does not modify L_{clog}, while it greatly changes the value of N*. A higher repulsion between the particles corresponds to a higher value of N*: N* increases linearly with ionic strength of the suspension for each confinement. However, the evolution of N* with W/D does not change. We thus conclude that there were two independent contributions to the variation of N* with the confinement, the first one being purely geometrical while the second is related only to the repulsive part of the DLVO forces. Thanks to the confocal imaging, we have been able to determine the influence of the particle repulsion on the final structure of the clog, at the particle scale. We also showed that the structure of the clogs, obtained for very different ionic strength conditions, is almost the same. Clogs always exhibit a loose, gel-like, structure, resulting from the aggregates growth. We observe that, within the densest part of the clog, an aggregate spans the overall cross section of the pore. Within this cross section, the average volume fraction goes from 34%, for very low ionic strength (raw suspension without added salt) up to 40%, for a high ionic strength, close to the critical coagulation concentration. From those measurements, we have

been able to conclude that the modification of N* with the ionic strength is related to the capture probability of the particles by the growing aggregates. For high ionic strength, the repulsive barrier is tiny and thus the hydrodynamic drag needed to overcome this barrier is rather small, which facilitates the particle capture. In the opposite, for very low ionic strength, the barrier is high and the capture probability is small, since our particles, PS and PMMA, exhibit naturally high surface charge.

B. Outlook

Our experimental study helps to identify, more clearly, how the dynamics of clogging process and the structural properties of the clog depend on the pore geometry, the confinement, the hydrodynamics conditions and the colloidal forces. However, many aspects of the clogging remain partially unexplored.

Particle capture and trajectory

In the 2d clogging chapter (cf. Chapter III -), we were able to get the trajectories of the particles that eventually deposit. However, this measurement was unable to get more than the particle position within the reservoir zone, upstream of the pore entrance, prior to their capture. It would be interesting to use of a fluorescence signal modulated at a higher frequency that would allow getting the entire trajectory of the particle, from the reservoir, up to its capture at the pore entrance. From those precise trajectories, we could also determine the hydrodynamic interaction between a still particle and a mobile one, within the pore, which leads to the indirect capture obtained when $Q>Q_C$, in the invasion regime. Finally, this will help us to quantify the influence of the aggregate porosity and shape in 2d on the motion of a nearby flowing particle, since we will have access to the velocity variations of this mobile particle. In midterm, the use of the streak techniques would also be beneficial to the study of the clogging process in a 3d pore, even though it will be far more difficult to use and to analyse the data that will get out of it.

Colloidal forces

To complete the work in the 2d chapter, we could investigate the influence of the colloidal forces on the various phenomena involved in the clogging process. First, modifications of the van der Waals force will have a direct impact on the range of pressure accessible to capture particles by the pore wall but also to detach those from the wall. The higher the particle adherence and the wider the pressure range of stable deposition is. It would be interesting to check whether changing this quantity will change other aspects of the clogging like the dynamic of the particle capture, for instance. The variation of the other part of the DLVO potential, the repulsion one, seems to be more promising. We have done some preliminary experiments where we tune the repulsive barrier by adding electrolytes. Preliminary experiments are carried out in W=36 µm channels with D=4 µm PMMA particles in a solution

of 0.05 and 0.1 M of NaCl with hydrodynamic conditions of Q/Q_C=1.1, thus in the invasion regime. This addition of salt leads to a faster pore clogging, as we observed in the 3d case. The addition of 0.1M of NaCl in the solution reduces N* by a factor 4.5 (Figure 105–B). This means that, even though we increased a lot the ionic strength of the suspension, the average probability to capture a particle by the pore wall increases only by this 4.5 factor. This is due to the very low surface charge of the PDMS. However, this moderate increase of the capture probability changes more drastically the deposition length within the pore. We observed that the deposition length within the pore increases linearly, at first glance, with the ionic strength (Figure 105–A). This could mean that the width of the capture zone of the indirect capture is greater. A still particle within the pore will help more particles that flow nearby to be pushed towards the pore wall and be captured. More precisely, particles at a greater distance, from the still one, than before are captured. Therefore, the growth of aggregates within the pore is more pronounced when the salt concentration increases. Moreover, even though we need less particles to clog the pore, the number of particles deposited within the pore prior clogging is far more important (Figure 105-C-D). On the other hands, this would also indicate that the colloidal forces might influence the regimes of clogging we established for the 2d clogging (line and invasion ones). Especially, we would expect the critical flow rate Q_C to be different with the addition of salt. Our preliminary results seem to show that the value of Q_C decreases with the electrolyte concentration. To fully capture the influence of the colloidal forces, this pore scale investigation should be carried out with the PS particles as well to investigate any influence of the van der Waals forces, and for a range of pressure allowing to cover a line in the phase diagram (Figure 41) for a given geometry (i.e. given W_R/W).

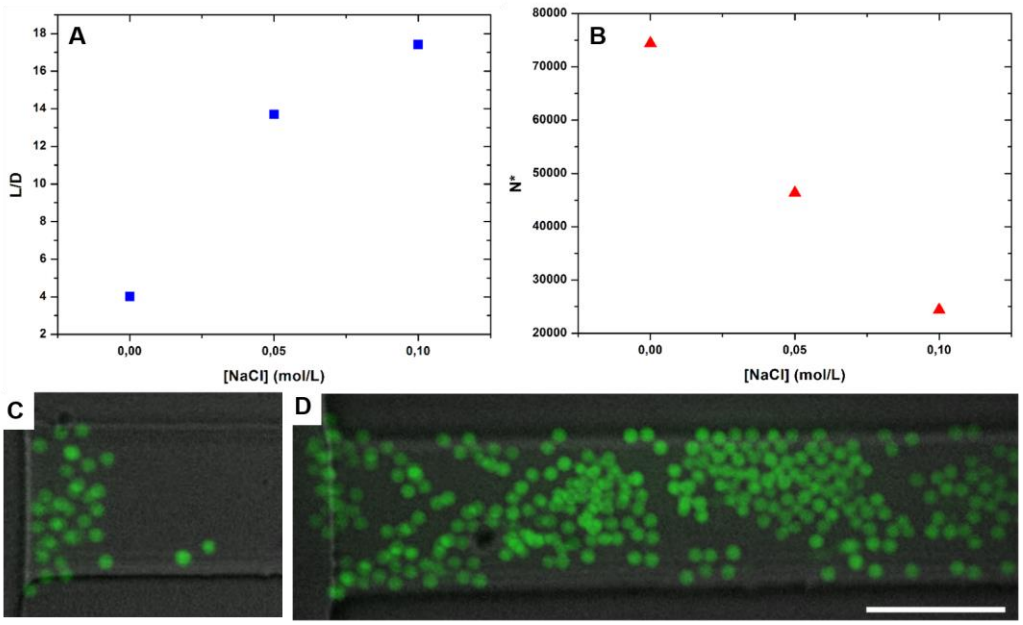

Figure 105: Influence of ionic strength on clogging at pore's scale in W=36µm channel at Q/Qc=1.1. A- Evolution of the clog's length with salt concentration; B- Evolution of the number of particle flowing through the channel prior to clog with salt concentration; C- Image of a clog without addition of salt; D- Image of a clog at 0.1M of NaCl. Scale bar = 20µm.

The influence of the attractive part of the potential, in the 3d case, has not been studied yet. However, our preliminary results (Figure 106) indicate that, since the very beginning of the clogging process, the attractive forces between the particles and the pore wall have a deep impact on the repartition of the particles within the pore. When the particle-wall van der Waals forces are important, like for PS particles in water/D2O mixtures, (Figure 106-A), as soon as particles cover the pore walls, over a length equals to W, aggregates can grow on top of it and eventually clog the pore, as we have seen before (cf. Chapter IV -C). For the PMMA particles in a solution of 29% of sucrose (n=1.38), the van der Waals force are 1.5 times smaller than in the PS ones. In this case, we observed that particles on the first layer spread over a length about to 2.4W at the end of the clogging process (Figure 106-B). Finally, when we lower the adhesive forces by another 1.5 factor, by dispersing PMMA particles in a solution of 64% of urea (n=1.42), the dynamics of deposition are quite different even though the applied pressure is the same (Figure 106-C). From the beginning of the deposition process, particles is captured on the pore wall over a length 10 times larger than W (Figure 106-C images a-c). In this first step, all the particles are captured almost exclusively at the corners of the pore walls. We observed that particles could be removed from the surface before some others are captured in their vicinity. When the pore is clogged, the length of the first layer is around 5W while the denser part of the clog is around 2.5W. For the last two examples, L_{clog}, or at least the length of the first particle layer, is doubled while N* remains the same (cf. Chapter IV - A.3, Figure 81). We clearly see here that a greater number of particles have to pass through the pore before forming the first layer of particle, when the adhesive torque is smaller. Therefore, the structure of the aggregates that grow on this first layer, and thus the clog structure, will also be modified. It would be interesting to investigate this stability issue as the clog is forming, from confocal imaging. This has to be done with an initial volume fraction of particles such that a single particle gets captured at a time, on the growing aggregates. In these conditions, we can check if a captured particle will (i) always stay definitively on the growing aggregate, (ii) modify the stability of the aggregates on top of which it is deposited.

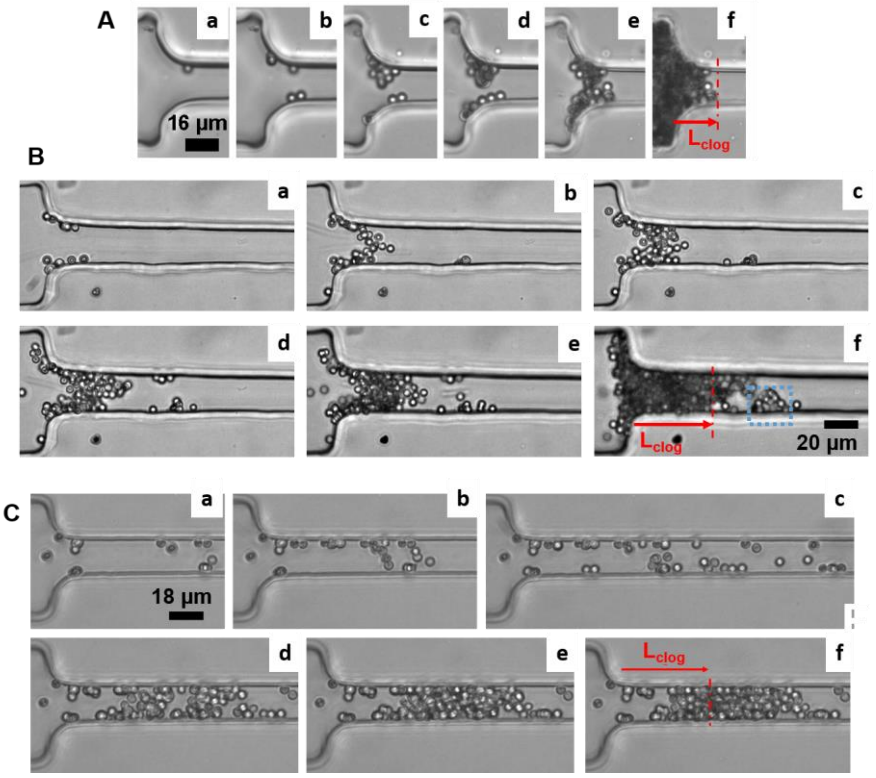

Figure 106: Successive images of clog build up. A- 4µm PS particles in solution of H2O/D2O in a W=16 µm pore (cf. Figure 75). B- 4 µm PMMA particles in a solution of 29% of sucrose in a W=24 µm pore. C- 4 µm PMMA particles in a solution of 64% of urea in W=18 µm pore.

In general, the dynamics of the clog building- up in low confinement conditions remains to be studied. Typically, with W/D>5-6 we will insure that the pore surface will have less influence on the aggregates growth. In the first step of the clogging process, it will be interesting to determine the structure of the aggregates while they stay independent of each other. We also want to determine the growth rate of such aggregates. Hereafter, the same kind of studies has to be performed with colloidal suspensions exhibiting different ionic strength. We want to see how the local structure is modified by the addition of salt, since we have seen that the average volume fraction of the clog increases with ionic strength.

Towards the clogging of a 2d porous medium

In this manuscript, we have worked within a single pore, completely independent of the others. A natural extension would be to work in a 2d network of interconnected pores, with a well-known pore size distribution. In these conditions, it would be interesting to study how the clogging of a peculiar pore will modify the flow on the neighbouring pores and will and change the clogging features of the other pores. It would be interesting to study the clogging at the porous medium scale, i.e. in which conditions and how, the whole porous medium gets eventually clogged. This kind of studies could also be performed with different pore geometries, slender pores vs. rounded ones, for instance and with different length of the porous medium. The colloidal forces and the hydrodynamic conditions have to be modified,

as well. It is worth noting that such extension will require a very large amount of time since the clogging phenomenon has to be studied at the porous medium scale, at the pore scale but also at the particle scale.

Bibliography

[1] C. Tien and B. V. Ramarao, *Granular Filtration of Aerosols and Hydrosols*. Elsevier, 2011.

[2] T. Nagatani, “The physics of traffic jams,” *Rep. Prog. Phys.*, vol. 65, no. 9, p. 1331, Sep. 2002.

[3] H. Wyss, D. Blair, J. Morris, H. Stone, and D. Weitz, “Mechanism for clogging of microchannels,” *Phys. Rev. E*, vol. 74, no. 6, Dec. 2006.

[4] M. D. Haw, “Jamming, Two-Fluid Behavior, and ‘Self-Filtration’ in Concentrated Particulate Suspensions,” *Phys. Rev. Lett.*, vol. 92, no. 18, p. 185506, mai 2004.

[5] D. Genovese and J. Sprakel, “Crystallization and intermittent dynamics in constricted microfluidic flows of dense suspensions,” *Soft Matter*, vol. 7, no. 8, pp. 3889–3896, Apr. 2011.

[6] L. Isa, R. Besseling, A. N. Morozov, and W. C. K. Poon, “Velocity Oscillations in Microfluidic Flows of Concentrated Colloidal Suspensions,” *Phys. Rev. Lett.*, vol. 102, no. 5, p. 058302, février 2009.

[7] A. I. Campbell and M. D. Haw, “Jamming and unjamming of concentrated colloidal dispersions in channel flows,” *Soft Matter*, vol. 6, no. 19, pp. 4688–4693, Sep. 2010.

[8] M.-B. L. M, H. J. R, and S. Nicholas, “Particle transport through porous media,” Dec. 1986.

[9] J. N. Ryan and M. Elimelech, “Colloid mobilization and transport in groundwater,” *Colloids Surf. Physicochem. Eng. Asp.*, vol. 107, pp. 1–56, février 1996.

[10] R. Kretzschmar, M. Borkovec, D. Grolimund, and M. Elimelech, “Mobile Subsurface Colloids and Their Role in Contaminant Transport,” in *Advances in Agronomy*, vol. 66, D. L. Sparks, Ed. Academic Press, 1999, pp. 121–193.

[11] P. Knowles, G. Dotro, J. Nivala, and J. García, “Clogging in subsurface-flow treatment wetlands: Occurrence and contributing factors,” *Ecol. Eng.*, vol. 37, no. 2, pp. 99–112, février 2011.

[12] D. Helbing, I. Farkas, and T. Vicsek, “Simulating dynamical features of escape panic,” *Nature*, vol. 407, no. 6803, pp. 487–490, Sep. 2000.

[13] D. Helbing, L. Buzna, A. Johansson, and T. Werner, “Self-Organized Pedestrian Crowd Dynamics: Experiments, Simulations, and Design Solutions,” *Transp. Sci.*, vol. 39, no. 1, pp. 1–24, février 2005.

[14] C. Saloma, G. J. Perez, G. Tapang, M. Lim, and C. Palmes-Saloma, “Self-organized queuing and scale-free behavior in real escape panic,” *Proc. Natl. Acad. Sci.*, vol. 100, no. 21, pp. 11947–11952, Oct. 2003.

[15] A. J. Liu and S. R. Nagel, “Nonlinear dynamics: Jamming is not just cool any more,” *Nature*, vol. 396, no. 6706, pp. 21–22, Nov. 1998.

[16] N. Roussel, T. L. H. Nguyen, and P. Coussot, “General Probabilistic Approach to the Filtration Process,” *Phys. Rev. Lett.*, vol. 98, no. 11, p. 114502, Mar. 2007.

[17] P. G. Lafond, M. W. Gilmer, C. A. Koh, E. D. Sloan, D. T. Wu, and A. K. Sum, “Orifice jamming of fluid-driven granular flow,” *Phys. Rev. E*, vol. 87, no. 4, p. 042204, avril 2013.

[18] D. Helbing, I. J. Farkas, P. Molnar, and T. Vicsek, “Simulation of pedestrian crowds in normal and evacuation situations,” *Pedestr. Evacuation Dyn.*, vol. 21, pp. 21–58, 2002.

[19] I. Zuriguel, A. Janda, A. Garcimartín, C. Lozano, R. Arévalo, and D. Maza, “Silo Clogging Reduction by the Presence of an Obstacle,” *Phys. Rev. Lett.*, vol. 107, no. 27, p. 278001, décembre 2011.

[20] N. Shiwakoti, M. Sarvi, G. Rose, and M. Burd, “Biologically Inspired Modeling Approach for Collective Pedestrian Dynamics Under Emergency Conditions,” *Transp. Res. Rec. J. Transp. Res. Board*, vol. 2196, pp. 176–184, décembre 2010.
[21] D. R. Parisi and C. O. Dorso, “Microscopic dynamics of pedestrian evacuation,” *Phys. Stat. Mech. Its Appl.*, vol. 354, pp. 606–618, août 2005.
[22] A. Janda, I. Zuriguel, A. Garcimartín, L. A. Pugnaloni, and D. Maza, “Jamming and critical outlet size in the discharge of a two-dimensional silo,” *EPL Europhys. Lett.*, vol. 84, no. 4, p. 44002, Nov. 2008.
[23] P. Baveye, P. Vandevivere, B. L. Hoyle, P. C. DeLeo, and D. S. de Lozada, “Environmental Impact and Mechanisms of the Biological Clogging of Saturated Soils and Aquifer Materials,” *Crit. Rev. Environ. Sci. Technol.*, vol. 28, no. 2, pp. 123–191, avril 1998.
[24] J. Gregory and A. J. Wishart, “Deposition of latex particles on alumina fibers,” *Colloids Surf.*, vol. 1, no. 3–4, pp. 313–334, juillet 1980.
[25] X. Li, P. Zhang, C. L. Lin, and W. P. Johnson, “Role of Hydrodynamic Drag on Microsphere Deposition and Re-entrainment in Porous Media under Unfavorable Conditions,” *Environ. Sci. Technol.*, vol. 39, no. 11, pp. 4012–4020, juin 2005.
[26] D. C. Mays and J. R. Hunt, “Hydrodynamic Aspects of Particle Clogging in Porous Media,” *Environ. Sci. Technol.*, vol. 39, no. 2, pp. 577–584, Jan. 2005.
[27] V. Ramachandran and H. S. Fogler, “Plugging by hydrodynamic bridging during flow of stable colloidal particles within cylindrical pores,” *J. Fluid Mech.*, vol. 385, pp. 129–156, 1999.
[28] R. I. Mackie, R. M. W. Horne, and R. J. Jarvis, “Dynamic modeling of deep-bed filtration,” *AIChE J.*, vol. 33, no. 11, pp. 1761–1775, 1987.
[29] D. C. Mays and J. R. Hunt, “Hydrodynamic and Chemical Factors in Clogging by Montmorillonite in Porous Media,” *Environ. Sci. Technol.*, vol. 41, no. 16, pp. 5666–5671, août 2007.
[30] X. Li, C.-L. Lin, J. D. Miller, and W. P. Johnson, “Pore-scale Observation of Microsphere Deposition at Grain-to-Grain Contacts over Assemblage-scale Porous Media Domains Using X-ray Microtomography,” *Environ. Sci. Technol.*, vol. 40, no. 12, pp. 3762–3768, juin 2006.
[31] X. Li, C.-L. Lin, J. D. Miller, and W. P. Johnson, “Role of Grain-to-Grain Contacts on Profiles of Retained Colloids in Porous Media in the Presence of an Energy Barrier to Deposition,” *Environ. Sci. Technol.*, vol. 40, no. 12, pp. 3769–3774, juin 2006.
[32] J.-F. Gaillard, C. Chen, S. H. Stonedahl, B. L. T. Lau, D. T. Keane, and A. I. Packman, “Imaging of colloidal deposits in granular porous media by X-ray difference micro-tomography,” *Geophys. Res. Lett.*, vol. 34, no. 18, p. L18404, Sep. 2007.
[33] D. C. Mays, O. T. Cannon, A. W. Kanold, K. J. Harris, T. C. Lei, and B. Gilbert, “Static light scattering resolves colloid structure in index-matched porous media,” *J. Colloid Interface Sci.*, vol. 363, no. 1, pp. 418–424, Nov. 2011.
[34] C. Scholz, F. Wirner, Y. Li, and C. Bechinger, “Measurement of permeability of microfluidic porous media with finite-sized colloidal tracers,” *Exp. Fluids*, vol. 53, no. 5, pp. 1327–1333, Nov. 2012.
[35] F. Wirner, C. Scholz, and C. Bechinger, “Geometrical interpretation of long-time tails of first-passage time distributions in porous media with stagnant parts,” *Phys. Rev. E*, vol. 90, no. 1, p. 013025, juillet 2014.
[36] K. V. Sharp and R. J. Adrian, “On flow-blocking particle structures in microtubes,” *Microfluid. Nanofluidics*, vol. 1, no. 4, pp. 376–380, Oct. 2005.

[37] M. Auset and A. A. Keller, “Pore-scale visualization of colloid straining and filtration in saturated porous media using micromodels,” *Water Resour. Res.*, vol. 42, no. 12, p. W12S02, décembre 2006.
[38] B. Mustin and B. Stoeber, “Deposition of particles from polydisperse suspensions in microfluidic systems,” *Microfluid. Nanofluidics*, vol. 9, no. 4–5, pp. 905–913, Oct. 2010.
[39] A. Sauret, E. C. Barney, A. Perro, E. Villermaux, H. A. Stone, and E. Dressaire, “Clogging by sieving in microchannels: Application to the detection of contaminants in colloidal suspensions,” *Appl. Phys. Lett.*, vol. 105, no. 7, p. 074101, Aug. 2014.
[40] M. Alaskar, K. Li, and R. Horne, “INFLUENCE OF PARTICLE SIZE ON ITS TRANSPORT IN DISCRETE FRACTURES: PORE-SCALE VISUALIZATION USING MICROMODELS.”
[41] D. Gassara, P. Schmitz, A. Ayadi, and M. Prat, “Modelling the Effect of Particle Size in Microfiltration,” *Sep. Sci. Technol.*, vol. 43, no. 7, pp. 1754–1770, mai 2008.
[42] I. Ben Hassan, C. Lafforgue, A. Ayadi, and P. Schmitz, “In situ 3D characterization of monodispersed spherical particle deposition on microsieve using confocal laser scanning microscopy,” *J. Membr. Sci.*, vol. 454, pp. 283–297, Mar. 2014.
[43] I. Ben Hassan, C. Lafforgue, A. Ayadi, and P. Schmitz, “in situ 3D characterization of bidisperse cakes using confocal laser scanning microscopy,” *J. Membr. Sci.*, vol. 466, pp. 103–113, Sep. 2014.
[44] G. Brans, A. van Dinther, B. Odum, C. G. P. H. Schroën, and R. M. Boom, “Transmission and fractionation of micro-sized particle suspensions,” *J. Membr. Sci.*, vol. 290, no. 1–2, pp. 230–240, Mar. 2007.
[45] V. Ramachandran and H. S. Fogler, “Multilayer Deposition of Stable Colloidal Particles during Flow within Cylindrical Pores,” *Langmuir*, vol. 14, no. 16, pp. 4435–4444, août 1998.
[46] P. Bacchin, A. Marty, P. Duru, M. Meireles, and P. Aimar, “Colloidal surface interactions and membrane fouling: Investigations at pore scale,” *Adv. Colloid Interface Sci.*, vol. 164, no. 1–2, pp. 2–11, mai 2011.
[47] G. C. Agbangla, É. Climent, and P. Bacchin, “Experimental investigation of pore clogging by microparticles: Evidence for a critical flux density of particle yielding arches and deposits,” *Sep. Purif. Technol.*, vol. 101, pp. 42–48, Nov. 2012.
[48] G. C. Agbangla, “Blocage de microcanaux par des particules micrométriques en écoulement : simulations numériques et expériences à l’échelle locale,” phd, Université de Toulouse, Université Toulouse III - Paul Sabatier, 2011.
[49] P. Bacchin, Q. Derekx, D. Veyret, K. Glucina, and P. Moulin, “Clogging of microporous channels networks: role of connectivity and tortuosity,” *Microfluid. Nanofluidics*, vol. 17, no. 1, pp. 85–96, Jul. 2014.
[50] J. Lin, D. Bourrier, M. Dilhan, and P. Duru, “Particle deposition onto a microsieve,” *Phys. Fluids 1994-Present*, vol. 21, no. 7, p. 073301, Jul. 2009.
[51] P. Duru and Y. Hallez, “Capture mechanisms of electrically neutral particles on a microsieve,” *Preprint*, 2014.
[52] J. K. Marshall and J. A. Kitchener, “The deposition of colloidal particles on smooth solids,” *J. Colloid Interface Sci.*, vol. 22, no. 4, pp. 342–351, Oct. 1966.
[53] N. Ryde, N. Kallay, and E. Matijević, “Particle adhesion in model systems. Part 14.—Experimental evaluation of multilayer deposition,” *J. Chem. Soc. Faraday Trans.*, vol. 87, no. 9, pp. 1377–1381, Jan. 1991.

[54] C.-H. Ko and M. Elimelech, “The ‘Shadow Effect’ in Colloid Transport and Deposition Dynamics in Granular Porous Media: Measurements and Mechanisms,” *Environ. Sci. Technol.*, vol. 34, no. 17, pp. 3681–3689, Sep. 2000.
[55] Z. Adamczyk, B. Siwek, M. Zembala, and P. Belouschek, “Kinetics of localized adsorption of colloid particles,” *Adv. Colloid Interface Sci.*, vol. 48, pp. 151–280, avril 1994.
[56] P. R. Johnson and M. Elimelech, “Dynamics of Colloid Deposition in Porous Media: Blocking Based on Random Sequential Adsorption,” *Langmuir*, vol. 11, no. 3, pp. 801–812, Mar. 1995.
[57] J. F. Brady and G. Bossis, “Stokesian Dynamics,” *Annu. Rev. Fluid Mech.*, vol. 20, no. 1, pp. 111–157, Jan. 1988.
[58] M. Whittle, B. S. Murray, J. Chen, and E. Dickinson, “Simulation and Experiments on Colloidal Particle Capture in a Shear Field,” *Langmuir*, vol. 16, no. 25, pp. 9784–9791, décembre 2000.
[59] J. H. Schenkel and J. A. Kitchener, “A test of the Derjaguin-Verwey-Overbeek theory with a colloidal suspension,” *Trans. Faraday Soc.*, vol. 56, no. 0, pp. 161–173, Jan. 1960.
[60] V. Ramachandran, R. Venkatesan, G. Tryggvason, and H. Scott Fogler, “Low Reynolds Number Interactions between Colloidal Particles near the Entrance to a Cylindrical Pore,” *J. Colloid Interface Sci.*, vol. 229, no. 2, pp. 311–322, Sep. 2000.
[61] R. G. M. van der Sman, “Drag force on spheres confined on the center line of rectangular microchannels,” *J. Colloid Interface Sci.*, vol. 351, no. 1, pp. 43–49, Nov. 2010.
[62] A. Espinosa-Gayosso, M. Ghisalberti, G. N. Ivey, and N. L. Jones, “Particle capture and low-Reynolds-number flow around a circular cylinder,” *J. Fluid Mech.*, vol. 710, pp. 362–378, 2012.
[63] L. A. Spielman and S. L. Goren, “Capture of small particles by London forces from low-speed liquid flows,” *Environ. Sci. Technol.*, vol. 4, no. 2, pp. 135–140, 1970.
[64] O. Goldberg, “Köhler illumination,” in *The microscope*, vol. 28, pp. 15–22.
[65] M. C. Jenkins and S. U. Egelhaaf, “Confocal microscopy of colloidal particles: Towards reliable, optimum coordinates,” *Adv. Colloid Interface Sci.*, vol. 136, no. 1, pp. 65–92, 2008.
[66] Minsky, M, “Microscopy Apparatus,” 3013467, 1957.
[67] J. C. Crocker and D. G. Grier, “Methods of digital video microscopy for colloidal studies,” *J. Colloid Interface Sci.*, vol. 179, no. 1, pp. 298–310, 1996.
[68] A. Fage and H. C. H. Townend, “An Examination of Turbulent Flow with an Ultramicroscope,” *Proc. R. Soc. Lond. Ser. A*, vol. 135, no. 828, pp. 656–677, Apr. 1932.
[69] T.-S. Wung and F.-G. Tseng, “A color-coded particle tracking velocimeter with application to natural convection,” *Exp. Fluids*, vol. 13, no. 4, pp. 217–223, Aug. 1992.
[70] N. E. Huang, Z. Shen, and S. R. Long, “A NEW VIEW OF NONLINEAR WATER WAVES: The Hilbert Spectrum1,” *Annu. Rev. Fluid Mech.*, vol. 31, no. 1, pp. 417–457, 1999.
[71] S. Shen, E. D. Sudol, and M. S. El-Aasser, “Control of particle size in dispersion polymerization of methyl methacrylate,” *J. Polym. Sci. Part Polym. Chem.*, vol. 31, no. 6, pp. 1393–1402, 1993.
[72] W. C. K. Poon, E. R. Weeks, and C. P. Royall, “On measuring colloidal volume fractions,” *Soft Matter*, vol. 8, no. 1, p. 21, 2012.
[73] Y. Xia and G. M. Whitesides, “Soft lithography,” *Annu. Rev. Mater. Sci.*, vol. 28, no. 1, pp. 153–184, 1998.

[74] M. T. Khorasani, S. Moemenbellah, H. Mirzadeh, and B. Sadatnia, “Effect of surface charge and hydrophobicity of polyurethanes and silicone rubbers on L929 cells response,” *Colloids Surf. B Biointerfaces*, vol. 51, no. 2, pp. 112–119, Aug. 2006.

[75] T. Beatus, T. Tlusty, and R. Bar-Ziv, “Phonons in a one-dimensional microfluidic crystal,” *Nat. Phys.*, vol. 2, pp. 743–748, 2006.

[76] G. C. Agbangla, É. Climent, and P. Bacchin, “Numerical investigation of channel blockage by flowing microparticles,” *Comput. Fluids*, vol. 94, pp. 69–83, May 2014.

[77] K. J. Dong, R. Y. Yang, R. P. Zou, and A. B. Yu, “Role of Interparticle Forces in the Formation of Random Loose Packing,” *Phys. Rev. Lett.*, vol. 96, no. 14, p. 145505, avril 2006.

[78] S. Torkzaban, S. A. Bradford, and S. L. Walker, “Resolving the Coupled Effects of Hydrodynamics and DLVO Forces on Colloid Attachment in Porous Media,” *Langmuir*, vol. 23, no. 19, pp. 9652–9660, 2007.

List of figures

Résumé

La formation de bouchon est un problème récurrent et presque inévitable lors de l'écoulement de solutions diluées dans des milieux poreux. Actuellement, on ne sait pas comment, à partir du processus initial de déposition de particules à la paroi, ces dernières s'accumulent dans le pore et finissent par le boucher. L'idée générale de ce travail est d'étudier la dynamique de formation de bouchon lors l'écoulement de particules colloïdales au sein de matériaux poreux modèles (canaux microfluidiques). Nous décrivons dans un premier temps, les différents phénomènes physiques impliqués dans la capture de particules et dans l'agrégation colloïdale. Nous faisons également une brève présentation des différentes techniques d'imagerie utilisées dans ce travail et des méthodes de préparation des solutions colloïdales ainsi que des dispositifs microfluidiques.
Le troisième chapitre est consacré à l'étude du processus de colmatage en situation de fort confinement (2d). Nous avons identifié deux régimes de colmatage (régime de « ligne » et « d'invasion »). Nous avons ensuite déterminé les processus de capture de particules à l'origine de ces deux régimes, à l'échelle de la particule. Nous avons montré que le processus de colmatage correspond à un phénomène d'auto-filtration. Alors que les premières particules sont capturées de manière « directe » par les parois du pore, la déposition de toutes les suivantes résulte systématiquement d'une interaction avec ces dernières.
Finalement, nous avons abordé le colmatage de pore 3d, dont la hauteur est égale à la largeur du pore. Nous avons fourni une description détaillée de l'ensemble du processus de colmatage, à l'échelle du pore et de la particule. Nous avons déterminé les conditions d'adhésion des premières particules à la paroi du pore, les propriétés de croissance des agrégats, ainsi que la manière dont ils se connectent pour obstruer le pore. Nous avons montré que cette dynamique de formation conduit à une structure finale de bouchon très ténue.

Abstract

Clog formation is a recurring and almost inevitable issue when dilute solution of particles flows in porous media. Currently, we do not know how, from the initial process of particle deposition on the pore wall, particles accumulate in the pore leading to its blocking. The main idea of this work is to study the dynamics of the clog formation, when colloidal particles flow through a single pore (microfluidics channels). In a first part, we describe the various physical phenomenon involved in the particle capture and the colloidal aggregation. We also describe briefly the imaging techniques used in this work as well as the colloidal solution and micro-fluidics chips preparation.
The third chapter is devoted to the study of the clogging process in high confinement (2d). We identified two clogging regimes ("line" and "invasion"). We then studied the underlying capture mechanisms, at the particle scale, related to both clogging regimes. We showed that the blockage process corresponds to a self-filtration process. The first particles are captured "directly" by the pore walls, while the deposition of all the following ones systematically results from hydrodynamic interactions with those first still particles.
Finally, we addressed the clogging of a 3d pore, in which the height of the pore is equal to its width. We gave a detailed description of the whole clogging process at the pore and at the particle scale. We provided the conditions for the adhesion of the first particles on the pore walls, the properties of subsequent aggregates growth, and how the aggregates eventually merge in order to block the pore. We showed that this dynamics of formation leads to a very loose clog structure.